Measurement, Modeling, and OFDM Synchronization for the Wideband Mobile-to-Mobile Channel

A Dissertation
Presented to
The Academic Faculty

By

Guillermo Acosta-Marum

In Partial Fulfillment
Of the Requirements for the Degree
Doctor of Philosophy in Electrical Engineering

School of Electrical and Computer Engineering
Georgia Institute of Technology

May, 2007

Measurement, Modeling, and OFDM Synchronization for the Wideband Mobile-to-Mobile Channel

Approved by:

Dr. Mary Ann Ingram, Advisor
School of Electrical and Computer Engineering
Georgia Institute of Technology

Dr. Peter H. Rogers
School of Mechanical Engineering
Georgia Institute of Technology

Dr. Ye Li
School of Electrical and Computer Engineering
Georgia Institute of Technology

Dr. Aaron Lanterman
School of Electrical and Computer Engineering
Georgia Institute of Technology

Dr. Thomas G. Pratt
Georgia Tech Research Institute
Georgia Institute of Technology

Date Approved:

To my beautiful wife Claudia, the love of my life,

and to my son Memo, the joy of our lives.

ACKNOWLEDGEMENTS

First and most importantly, I would like to thank my advisor, Dr. Mary Ann Ingram, for trusting me and helping me achieve one of my major milestones of my life. Working for Doctor Ingram has enriched my life not only in the academic sense. Her achievements, her work ethics, and her keen eye for every important detail have been an inspiration throughout all the years I have worked with her. She has been more than a mentor. She has opened her arms to me and my family, and she has a very special place in our hearts. I also want to express a very special gratitude to Dr. Thomas G. Pratt without whom this project could have not happened.

I would also like to express my gratitude to Dr. Ye Li for all his valuable input and comments during the time he was my co-advisor and for being part of the reading committee.

It has been a very long trip. There are so many people to thank, but I would like to start by thanking all the people from the *Consejo Nacional de Ciencia y Tecnología* (CONACYT) who had faith in me and gave me the opportunity to come back to school. I am also very grateful to all the insitutions and companies that helped finance this project. This project received support from the National Science Foundation (NSF), Georgia Insitute of Technology, and Arinc. My special thanks to Mr. Broady Cash.

Many are the collegues who helped me through all these years. My deepest gratitude goes to all of them. In particular, I want to thank Dr. Weidong Xiang, Nathan Jones, Mark Wheeler, Brett Walkenhorst, Jeng-Shiann Jiang, Kathleen Tokuda, Lu Dong, Vikram Arreddi, and Anh Nguyen.

I want to thank my friends Roberto Uzcategui, John Gibby, and Dr. Ricardo Villalaz for all the good conversations. Finally, my deepest love goes to my wife Claudia and my son Memo. You have been my loyal partners in this adventure. I could not have done it without you. I love you both.

TABLE OF CONTENTS

LIST OF TABLES

LIST OF FIGURES

SYMBOLS AND ABBREVIATIONS

ADC	Analog-to-Digital Converter
AWGN	Additive White Gaussian Noise
BER	Bit Error Rate
BPSK	Binary Phase Shift Keying
BS	Base Station
BW	Bandwidth
CAZAC	Constant Amplitude Zero Autocorrelation
CCD	Charge-Coupled Devices
CDF	Cumulative Distribution Function
CIR	Channel Impulse Response
DA	Data Aided
DAB	Digital Audio Broadcasting
DAC	Digital-to-Analog Converter
DARPA	Defense Advanced Research Projects Agency
DSP	Digital Signal Processor
DSRC	Dedicated Short Range Communications
DVB	Digital Video Broadcasting
FFT	Fast Fourier Transform
FIR	Finite Impulse Response
FMCW	Frequency Modulated Continuous Waveform
FPDP	Front Panel Data Port
GTRI	Georgia Tech Research Institute
HMT	Handheld Multimedia Terminal

IBOC	In-Band On-Channel Digital Audio Broadcasting
ICI	Inter-Carrier Interference
IEEE	Institute of Electrical and Electronics Engineers
IF	Intermediate Frequency
IFFT	Inverse Fast Fourier Transform
IR	Impulse Response
ISI	Inter-Symbol Interference
LOS	Line of Sight
MA	Moving Average
MAC	Medium Access Control
MD	Maximum Delay
MIMO	Multiple Input Multiple Output
ML	Maximum Likelihood
MLS	Maximum Length Sequence
mph	Miles per hour
MS	Mobile Station
MTM	Mobile-to-Mobile
NDA	Non Data Aided
NLOS	Non-Line of Sight
NTP	Need to Purchase
OFDM	Orthogonal Frequency Division Multiplexing
PAR	Peak-to-Average Power Ratio
PDF	Probability Density Function
PDP	Power Delay Profile
PER	Packet Error Rate

PHY	Physical Layer
PN	Pseudo-Noise
ppm	Parts per million
PSD	Power Spectral Density
PSDU	Physical Layer Service Data Unit
RF	Radio Frequency
RMS	Root Mean Square
RTM	Roadside-to-Mobile
SARL	Smart Antenna Research Laboratory
SAW	Surface Acoustic Wave
SC	Switched-Capacitor
SISO	Single Input Single Output
SNR	Signal to Noise Ratio
STDCC	Swept Time-Delay Cross-Correlator
UMTS	Universal Mobile Telecommunication Systems
US	Uncorrelated Scattering
λ	Wavelength
WAVE	Wireless Access in Vehicular Environments
WDMR	Wideband Digital Mobile Radio
WSS	Wide-Sense Stationary
WSSUS	Wide-Sense Stationary Uncorrelated Scattering

SUMMARY

Wireless communication services tend towards “anywhere” and “everywhere” capabilities. Many of the available services require a stationary base station to provide links between mobile stations. Wideband mobile-to-mobile (MTM) communications might allow future digital broadband mobile services with a reduced infrastructure investment. There is also a growing interest from the military in wideband MTM communications for tactical applications. Another one of these conceived services is dedicated short range communications (DSRC), which is a short to medium range service that supports both Public Safety and Private operations in roadside to vehicle and vehicle-to-vehicle communication environments. The DSRC standard uses orthogonal frequency division multiplexing (OFDM).

Wideband measurements of the mobile-to-mobile channel, especially of the harshest channels, are necessary for proper design and certification testing of mobile-to-mobile communications systems. A complete measurement implies that the Doppler and delay characteristics are measured jointly. However, such measurements have not previously been published.

The main objective of the proposed research is to develop channel models for specific scenarios from data obtained in a wideband mobile-to-mobile measurement campaign in the 5.9 GHz frequency band. For this purpose we developed a channel sounding system including a novel combined waveform. In order to quantify and qualify either the recorded channel or the proposed generated channel, we developed a simulation test-bed that includes all the characteristics of the proposed DSRC standard. The resulting channel models needed to comply with the specifications required by hardware

channel emulators or software channel simulators. From the obtained models, we selected one to be included in the IEEE 802.11p standard certification test. To further aid in the development of software radio based receivers, we also developed an OFDM synchronization algorithm to analyze and compensate synchronization errors produced by inaccessible system clocks.

CHAPTER 1

INTRODUCTION

Wireless communication services tend towards “anywhere” and “everywhere” capabilities. Most of the available services require a stationary base station (BS) to provide links between mobile stations (MS). There is a growing research interest for wideband MTM communications that might allow future digital broadband mobile services with a reduced infrastructure investment. Dedicated broadband communications to vehicles could open the doors for either the transformation of industries such as broadcasting or the creation of new services. There is also a growing interest from the military in wideband mobile-to-mobile communications for tactical applications such as the handheld multimedia terminal (HMT) developed for the Defense Advanced Research Projects Agency (DARPA), which is based on the development of the Tactical Internet, a data channel also used for routing information to identify positions of friendly forces [90]. Another one of these conceived services is DSRC, which is a short to medium range service that supports both Public Safety and Private operations in roadside-to-vehicle and vehicle-to-vehicle communication environments [6].

DSRC services aim to provide a broadband channel to and between moving vehicles. The vehicle-to-vehicle channel is of interest for emergency notification (such as when an emergency vehicle approaches an intersection), as well as for other intelligent transportation applications [9], [22], [41], [53], [84]. As with many other communications services, a reliable channel characterization or model is essential in the design of new equipment and research on the vehicle-to-vehicle channel is still needed. In general, the

MTM channel differs from the cellular (fixed-to-mobile) channel, not only because both the transmitter and receiver may be moving, but also because MTM applications typically use lower transmitter antenna heights and therefore experience more scattering near the transmitter [6], [86]. Narrow-band measurements to obtain fading statistics have been reported for MTM channels in various environments [48], but the worst-case channel is often of particular interest, especially when safety is a concern. For OFDM with a relatively small number of subcarriers, which is the modulation format being considered for DSRC, doubly selective fading (*i.e*. time and frequency selective fading) is expected to be a feature of a difficult or bad channel [85] and is the focus of this dissertation.

Many papers on vehicle-to-vehicle channel characterization address a “platooning” application, which enables vehicles to travel at high speeds in close proximity. In a platoon, the typical channel is a line-of-sight (LOS) signal path over relatively small transmitter-receiver separations ranging from 1 m to 40 m [41], [84]. These channels usually exhibit small delay spreads, *e.g.*, RMS delay spreads less than 40 nS [22], [25]. In contrast, for an emergency-notification application, transmitter-receiver separations may be significantly larger than within a platoon, and vehicles, buildings or other structures may block the LOS path. These conditions may lead to larger delay spreads, as suggested by fixed-to-mobile urban measurements [44]. In that work, with antenna heights as low as 1.6 m, delay spreads were reported to increase with transmitter-receiver separation. Delay spreads were also observed to increase when the LOS path was blocked [44]. These factors motivated us to try to find sites in Atlanta, Georgia that exhibit large delay spreads since we consider that such sites will provide the most challenging environments for MTM communications.

The major contribution of this dissertation is the development of non-separable, *i.e*., joint delay spread-Doppler, wideband MTM channel models from a statistical modeling

of empirical data obtained from two measurement campaigns. To our knowledge, measurements of the type presented in this dissertation, *i.e*. per-tap Doppler spectra for the MTM channel, where both vehicles are in motion, have not been presented before. We carried out the first measurement campaign, which we will refer to as Phase One, in the 2.4 GHz frequency band. Phase One consisted of two periods. For Period One, our objective was to find sites with the worst-case delay in the Atlanta Metropolitan Area. For Period Two, we measured the joint delay-Doppler characteristic of the sites found in the previous period. We performed the second measurement campaign, Phase Two, in the 5.9 GHz frequency band. For Phase Two, our objective was to measure joint delay-Doppler characterisitics in specific scenarios as required to develop a proposed channel model to be included in the IEEE 802.11p standard certification test. The model parameters obtained from the channel measurements were the number of taps and the relative time delay, path loss, amplitude statistics, and Doppler spectral shape for each tap. For the model development, we chose similar scenarios from both phases. We started our model development using the methodology found in the literature [51] and applying it to the data of Phase One. To validate or quantify this initial approach, we developed a system to compare the obtained model with the original recorded data. We found this available methodology to be quite limited. In particular, it fell short of incorporing the wide dynamics with respect to the bit error rate (BER) encountered in the recorded channel. We needed to outgrow these limitations to develop a methodology that allowed us to create practical channel models useful in either commercial channel emulators or simulation systems with a performance closer to that of the recorded channel.

OFDM has been selected for many wideband communication systems, including DSRC. Much research effort has been focused on its synchronization, which is one of its major weaknesses. For this matter, we are extending the analysis of synchronization off-

sets to generate a degradation function that includes all of them. Previous works have focused on subsets only [65] or have made approximations to reduce the expression complexity [50]. Also, the literature is vast on OFDM synchronization algorithms, but few of them focus on fixed or inaccessible clocks. We present a joint data aided (DA) and non-data aided (NDA) synchronization algorithm that combines and upgrades existing ones to synchronize when the clock is inaccessible.

The structure of the thesis is as follows: In Chapter 2, we provide a background on mobile channel modeling, a review of channel sounding techniques, statistical channel parameter extraction, and OFDM synchronization algorithms. In Chapter 3, we proposed a thorough OFDM synchronization offsets analysis, and we propose a synchronization algorithm useful to identify the synchronization performance in each of the steps of the development of an OFDM system. In Chapter 4, we present a detailed analysis of the specifications, limitations, and performance of our developed wideband sounding systems. In Chapter 5, we describe the two phases of our measurement campaigns. In Chapter 6, we present our approaches to channel modeling. In Chapter 7, we present six channel models for six different scenarios. We also present the results of the performance of these models using the prototype equipment and the channel emulator. Finally in Chapter 8, we summarize the contributions of this dissertation, and we suggest the future work that can be developed from our results.

CHAPTER 2

BACKGROUND

A major prerequisite for the design of future wideband digital mobile radio (WDMR) systems or the optimization and extension of existing WDMR systems is a thorough knowledge of the propagation characteristics of the mobile radio channel. Because of the complexity of the propagation phenomena and because of the statistical nature of the radio channel parameters, a reliable channel characterization can be based only on appropriate channel measurements. In this chapter, we present an overview of the channel modeling fundamentals and an overall look at the available channel sounding techniques. We also offer a general description of the existing techniques to combat synchronization problems in OFDM.

2.1 Channel Modeling

For the required IEEE 802.11p standard certification test MTM models, we will ignore the large scale fading; therefore, we will concentrate our efforts in small scale fading phenomena.

2.1.1 Small Scale Fading

We start with the analysis with a description of the parameters that produce the small scale fading. We begin by expressing a passband-transmitted signal as follows:

$$s(t) = \Re\left(u(t)e^{j2\pi f_c t}\right) \tag{2.1}$$

where $u(t)$ represents the complex baseband signal. The Doppler shift modifies the carrier frequency according to the relative velocity of the transmitter-receiver pair. This modification is

$$\begin{aligned} f &= f_m \cos\left(\theta\left(t\right)\right) + f_c \\ &= f_D\left(t\right) + f_c \end{aligned} \tag{2.2}$$

where $f_m = v_m / \lambda_c$ is the maximum Doppler frequency, which is a function of the maximum relative velocity V_m, λ_c is the wavelength of the arriving plane wave, and $\theta\left(t\right)$ represents the angle of incidence of the wave front arriving at the antenna. For a line-of-sight (LOS) transmission (no bounces), the received signal becomes

$$x_{LOS}\left(t\right) = \Re\left(u(t)e^{j2\pi f_m \cos\left(\theta(t)\right)t} e^{j2\pi f_c t}\right) \tag{2.3}$$

for which the complex baseband signal is

$$r_{LOS}\left(t\right) = u\left(t\right)e^{j\left(2\pi f_m \cos\left(\theta(t)\right)t\right)}. \tag{2.4}$$

Analyzing one bounce or τ-delayed path, the passband signal is

$$x\left(t-\tau\right) = \Re\left(u(t-\tau)\alpha e^{j2\pi f_m \cos\left(\theta(t-\tau)\right)(t-\tau)} e^{j2\pi f_c (t-\tau)}\right) \tag{2.5}$$

where α is the complex reflection coefficient, and the complex baseband is

$$r\left(t-\tau\right) = u\left(t-\tau\right)e^{j\left(2\pi f_m \cos\left(\theta(t-\tau)\right)(t-\tau)+2\pi f_c \tau\right)}, \tag{2.6}$$

but since the terminals are moving, the time delay τ and reflection coefficient α should be functions of time to give

$$r\left(t-\tau\left(t\right)\right)=u\left(t-\tau\left(t\right)\right)e^{j\left(2\pi f_m\cos\left(\theta\left(t-\tau(t)\right)\right)\left(t-\tau(t)\right)+2\pi f_c\tau(t)\right)}. \tag{2.7}$$

If we consider a multipath trajectory, we can index the time delay and reflection coefficient and add up the total effect to give

$$x\left(t\right)=x_{LOS}\left(t\right)+\sum_{n=1}^{L}\Re\left(u(t-\tau_n\left(t\right))\alpha_n\left(t\right)e^{j2\pi f_m\cos\left(\theta\left(t-\tau_n(t)\right)\right)\left(t-\tau_n(t)\right)}e^{j2\pi f_c\left(t-\tau_n(t)\right)}\right) \tag{2.8}$$

where L indicates the number of paths. The multipath complex-baseband signal becomes

$$r\left(t\right)=r_{LOS}\left(t\right)+\sum_{n=1}^{L}u\left(t-\tau_n\left(t\right)\right)\alpha_n\left(t\right)e^{j\left(2\pi f_m\cos\left(\theta\left(t-\tau_n(t)\right)\right)\left(t-\tau_n(t)\right)+2\pi f_c\tau_n(t)\right)}. \tag{2.9}$$

As we can see in (2.9) the small scale variations encountered in a mobile-to-mobile transmission produce a very complex expression. In order to provide useful description or model, we need to somehow define, measure, calculate, or estimate the four parameters: L, $\tau_n\left(t\right)$, $\alpha_n\left(t\right)$, and f_m [75].

2.1.2 Basic Model and Popular Statistics

The multipath fading for a channel manifests itself in two effects [37]:

- Time spreading (in τ) of the symbol duration within the signal, which is equivalent to filtering and bandlimiting.
- A time-variant behavior (in t) of the channel produced by the motion of the receiver, transmitter, changing environment, or movement of reflectors and scatterers.

The random fluctuations in the received signal caused by fading can be modeled by treating the channel impulse response (CIR) $h(\tau,t)$ as a random process in *t*. Since the components of the multipath signal arise from a large number of reflections and scattering from rough or granular surfaces, then by virtue of the central limit theorem, the CIR can be modeled as a complex Gaussian process. At any time *t,* the probability density functions of the real and imaginary parts are Gaussian. This model implies that for each τ the ray is composed of a large number or unresolvable components. If $h(\tau,t)$ has zero mean, then the envelope $R(\tau,t)=|h(\tau,t)|$ has a Rayleigh probability density function (PDF). If it has a nonzero mean, which implies the presence of a significant specular component, then the envelope has a Ricean PDF. While the PDF of the CIR describes the distribution of the instantaneous values of the CIR, the temporal variations are modeled by an appropriate autocorrelation function or, equivalently, by the power spectral density of the random process in the *t* variable.

2.1.3 Scattering Function

Bello [11] introduced a model for the multipath channel that includes both the variations in *t* and τ. The time-varying nature of the CIR is mathematically modeled as a wide-sense stationary (WSS) random process in t with an autocorrelation function

$$R_h(\tau_1,\tau_2,\Delta t)=E\left[h^*(\tau_1,t)h(\tau_2,t+\Delta t)\right]. \tag{2.10}$$

In most multipath channels, the attenuation and phase shift associated with different delays can be assumed uncorrelated; this is the uncorrelated scattering (US) assumption, which leads to

$$R_h(\tau_1,\tau_2,\Delta t)=R_h(\tau_1,\Delta t)\delta(\tau_1-\tau_2). \tag{2.11}$$

(2.11) embodies both the WSS and US assumptions, and it is referred to as the WSSUS model for fading. This autocorrelation function is denoted by

$$R_h(\tau,\Delta t) \equiv E\left[h^*(\tau,t)h(\tau,t+\Delta t)\right]. \tag{2.12}$$

It is apparent from (2.12) that the WSSUS model can be represented in either the time domain or the frequency domain by performing a Fourier transform on one or both of the variables *t* and τ. From the engineer's point of view, it would be useful to have a model that simultaneously provides a description of the channel properties with respect to the delay variable τ and a frequency-domain variable (Doppler frequency) ν. We obtain this model by Fourier transforming the autocorrelation function in the Δt variable:

$$S(\tau,\nu) = \int_{-\infty}^{\infty} R_h(\tau,\Delta t)e^{-j2\pi\nu\Delta t}d\Delta t. \tag{2.13}$$

$S(\tau,\nu)$ is called the **scattering function** and is perhaps the most important statistical measure of the random multipath channel. It is a function of two variables: τ (delay) and a frequency-domain variable ν called the Doppler frequency. We can see from (2.13) that ν is the dual variable of Δt, hence it captures the rapidity with which the channel itself changes. From the scattering function, we can obtain some of the most important relationships of a channel, which impact the performance of a communication system operating over that channel. One of these is the **power delay profile (**PDP) is defined as

$$p(\tau) = R_h(\tau,0) = E\left[\left|h(\tau,t)\right|^2\right], \tag{2.14}$$

which represents the average received power as a function of delay τ. We can derive $p(\tau)$ from the scattering function via

$$p(\tau) = \int_{-\infty}^{\infty} S(\tau, \nu) d\nu. \tag{2.15}$$

For an ideal channel and assuming that we could transmit an ideal impulse, $p(\tau)$ would be a single impulse with an amplitude reduction that follows the inverse square law, and it would represent the energy received for a specific time window, which also translates into a specific local area. For a mobile channel and also for a transmitted ideal impulse, the delay-power profile would show a collection of attenuated ideal impulses forming clusters in short times after the first one. This type of response is a result of multipath propagation. For any mobile service, the usual design is for the base station (BS) or transmitter to cover a particular area of service; therefore, the mobile station (MS) or receiver can receive energy or signals from many different trajectories. For each trajectory, there is a path length and phase differences. The PDP is a description of the received energy as a function of delay τ, or a description of the time it takes to the channel to clear after it is excited by an impulse. In other words, knowledge of $p(\tau)$ helps answer the question "For a transmitted impulse, how does the average received power vary as a function of time delay, τ?" [74].

Another function that is useful in characterizing fading is the Doppler power spectrum, which is derived from the scattering function through

$$S(\nu) = \int_{-\infty}^{\infty} S(\tau, \nu) d\tau. \tag{2.16}$$

$S(\nu)$ characterizes the time variation of the channel produced by the motion between the transmitter and the receiver.

For the case of mobile radio with a stationary base in a two-dimensional propagation geometry, an array of uniformly spaced scatterers around the MS, all with equal magni-

tude reflection coefficients, but independent, randomly occurring phase angles, is a widely accepted model. This model is referred as the dense scatterer channel model [35] and is commonly known as the Jakes model. For this model, the Doppler power spectrum is

$$S(\nu) = \frac{1}{\pi f_m \sqrt{1 - \left(\frac{\nu}{f_m}\right)^2}}, \quad |\nu| \le f_m. \tag{2.17}$$

This assumption that the angle of arrival of a received plane wave is uniformly distributed random variable seems plausible for urban environments, but it is not so valid for rural or suburban environments. The Doppler spectrum described by (2.17) has to be regarded as an average power Doppler profile over many environments considering a fixed velocity magnitude [2]. One consequence of this assumption is that the results do not depend on the mobile's direction of travel. In addition, the Doppler power spectrum is symmetric. Conversely, a *non*-uniform distribution of the angle of arrival will skew the Doppler spectrum [68]. For example, if the angle of arrival is biased in the direction of the base station, then the Doppler power spectrum will be skewed toward $+f_m$ when the mobile is moving toward the base and skewed toward $-f_m$ when mowing away from the base.

Another consequence of the Jakes model assumption is *delay/temporal separability*. A channel is described as **separable** if and only if

$$S(\tau, \nu) = S(\nu) p(\tau). \tag{2.18}$$

If the scattering function can not be separated or factored this way, the channel is called **non-separable**. Many analyses of OFDM and often channel measurement approaches

assume a separable model for simplification [46], [68]. However, some wideband standard models, such as COST 231, which models the universal mobile telecommunication system (UMTS) channel, assume a non-separable model. Part of the contribution of this dissertation are measured non-separable models for the MTM channel.

2.1.4 MTM Model

In this section, we present a brief summary of the analytical studies of the MTM channel models. Akki and Haber [7] published the first study in 1986. It was not until the recent past years that the subject rose again, and three other papers were published [63], [86], [88]. These papers are discussed below.

In [7], Akki and Haber follow the idea that multipath fading manifests as a time spreading of the symbol within a signal, which is equivalent to filtering; therefore, a statistical model for the MTM channel can usually be based on a transversal filter structure with a limited number of taps [7], [13]. Their analysis is as follows. For a transmitted signal at frequency f_c with complex envelope $u(t)$, the received signal $r(t)$ is given as:

$$r(t) = \Re\left(\sum_{i=1}^{L} Q(\alpha_{1i}, t) u(t - \tau_i) e^{j 2\pi f_c (t - \tau_i)} \right) \tag{2.19}$$

where

$$Q(\alpha_{1i}, t) = r_i e^{j[2\pi (f_{D1i} + f_{D2i}) t + \phi_i]}. \tag{2.20}$$

$Q(\alpha_{1i}, t)$ is defined as a complex Gaussian process with magnitude r_i equal to the envelope of the received signal for angle of arrival $\alpha_{1i} \pm \Delta\alpha/2$. $\Delta\alpha$ is the incremental angle around the angle of arrival α_{1i} that defines the region where the receiver captures signals coming from scatterers or reflectors. L is the number of these signals. f_{D1i} and f_{D2i}

are independent Doppler shifts produced by the movement of the receiver and transmitter respectively and $\phi_i = \phi_i' - \left(f_{D1i} + f_{D2i}\right)\tau_i$ where ϕ_i' is a uniformly distributed random variable and τ_i is the mean delay. Assuming frequency flat fading conditions, the baseband received complex envelope is [63]

$$g(t) = \sum_{n=1}^{L} \exp\left[j\left(2\pi\left\{f_1 \cos\left(\alpha_n\right) + f_2 \cos\left(\beta_n\right)\right\}t + \theta_n\right)\right] \tag{2.21}$$

where f_1 and f_2 are the maximum Doppler frequencies with respect to a stationary observer for the transmitter and receiver respectively, and α_n and β_n are the angles of departure and angles of arrival of the n^{th} path measured with respect to the transmitter and receiver velocity vectors respectively.

Based on this finite tap model [7], the time correlation function for a Rayleigh distributed complex envelope assuming uniform scattering and two vehicles in motion is

$$\begin{aligned} R_v(\Delta t) &= \sigma_1^2 J_0(2\pi f_1 \Delta t) J_0(2\pi f_2 \Delta t) \\ &= \sigma_1^2 J_0(2\pi f_1 \Delta t) J_0(2\pi a f_1 \Delta t) \end{aligned} \tag{2.22}$$

where $J_0(\bullet)$ is a zero-order Bessel function of the first kind, σ_1^2 is the received power, and where $f_2 = af_1$ with $0 < a < 1$ [7]. The Doppler spectra $S(\nu)$ is obtained by Fourier transform of the time autocorrelation function $R_\nu(\Delta t)$ of the complex envelope assuming uniform 2-D scattering and omni-directional transmit and receive antennas:

$$S(\nu) = \frac{\sigma_1^2}{\pi^2 f_1 \sqrt{a}} K\left(\frac{1+a}{2\sqrt{a}} \sqrt{1 - \left(\frac{\nu}{(1+a)f_1} \right)^2} \right) \tag{2.23}$$

where $K(\bullet)$ is a complete elliptic integral of the first kind. A plot of Doppler spectra for different values of a is shown in Figure 1 [63]. The statistical properties associated with this model are further analyzed in [8] to show that the level-crossing rate of the envelope for the vehicle-to-vehicle case increases compared to the fixed-to-mobile case by a factor of $\sqrt{1+(V_2/V_1)^2}$, where V_1 and V_2 are the velocities of the mobiles. The average fade duration $\bar{\tau}$ is reduced by a factor of $\sqrt{1+(V_2/V_1)^2}$ compared to the fixed-to-mobile case.

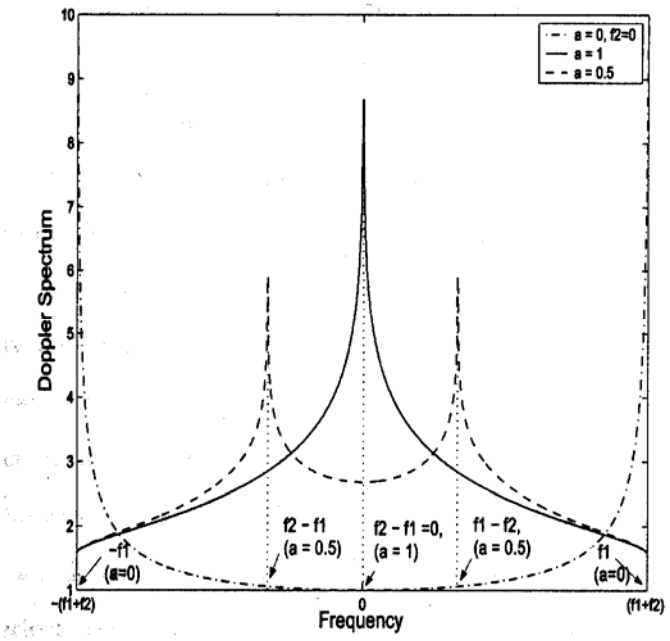

Figure 1: Doppler spectrum for MTM and cellular channels (a=0) [63].

In [87] and [88], Wang and Cox derived the power spectrum for the two dimensional non-LOS case assuming both the transmitter and receiver are moving at the same speed. The derivation consisted of a convolution (in frequency) of the classical spectra, *i.e.*, the classical spectrum represents a fixed transmitter and moving receiver. Again, the resulting double-mobility Doppler power spectrum is a complete elliptic integral of the first kind, where the Jakes model is a special case. For their analysis and instead of us-

ing a factor multiplying either Doppler frequency, they defined the *degree of double mobility* as follows:

$$\alpha = \frac{\min(V_1, V_2)}{\max(V_1, V_2)}, \quad 0 \le \alpha \le 1 \tag{2.24}$$

where $\alpha = 1$ is *full double mobility* and $\alpha = 0$ is *single mobility*. Although they did not give a derivation for the case where transmitter velocity is not equal to receiver velocity, they indicated that as the velocity of the transmitter increases from zero, the vertical asymptotes of the Jakes model move inward. At "full" mobility, when the transmitter and receiver velocity are equal, the vertical asymptotes merge at the center of the spectrum. In essence, they arrived to the same spectral shapes as the ones shown in Figure 1, but they just provided analytical derivations for the extreme cases. They also suggested that for a fixed maximum Doppler shift, the closer the system is to the full mobility case, it results in smaller RMS and effective Doppler spread, hence slower fading [87].

The next 2-D study is [63]. Here, Patel introduces the concept of a "double-ring" mobile-to-mobile scattering environment. This "double-ring" model defines an individual ring of uniformly spaced scatterers for both the BS and the MS, which causes each transmitted path to undergo two reflections, one for each ring. For this model, the baseband received complex envelope is proposed as:

$$g(t) = \sum_{n=1}^{N} \sum_{m=1}^{M} \exp\left[j\left(2\pi \left\{ f_1 \cos(\alpha_n) + f_2 \cos(\beta_m) \right\} t + \theta_{nm} \right) \right] \tag{2.25}$$

where index *n* refers to paths traveling from transmitter to the *N* scatterers located on the transmitter ring, and index *m* refers to the paths traveling from the *M* scatterers on the receiver ring to the receiver. The statistical properties of this model match those of the

transversal filter model previously described, e.g., its time correlation function is also given by (2.22).

Finally, we found just one 3-D study in [86]. Here, the Doppler spectrum for a WSS MTM channel with NLOS 3-D multipath distributions was derived via Fourier transform of the time-autocorrelation function of the channel transfer function. The derivation uses the PDF for the angle of multipath arrival, the PDF of the intrinsic multipath scattering distribution weighted by an antenna radiation function, and the Doppler frequency shift for each component. This Doppler spectrum was evaluated numerically for coherent and square law detection assuming an antenna radiation function for a vertical half-wave dipole antenna. Examples are shown in Figure 2 and in Figure 3

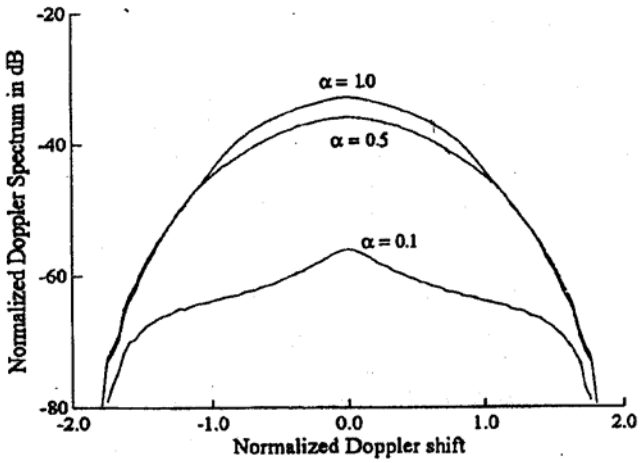

Figure 2: Normalized Doppler spectrum for a mobile-to-mobile link as a function of normalized Doppler shift for different values of the ratio α=fd1/fd2 (coherent detection) [86].

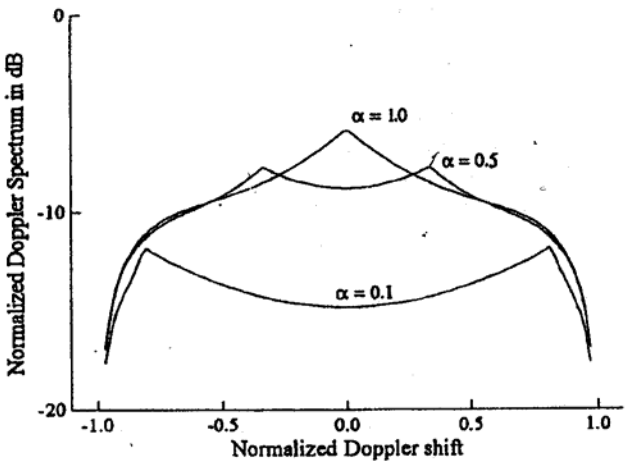

Figure 3: Normalized Doppler spectrum for a mobile-to-mobile link as a function of normalized Doppler shift for different values of the ratio α=fd1/fd2 (square law detection) [86].

2.1.5 Measured MTM Doppler

One paper [48] contained the flat-fading measurements of vehicle-to-vehicle Doppler shown in Figure 4 for urban and highway environments. In Figure 4, the total power of each spectrum was normalized to one so that the plots represent the probability density function of the Doppler frequency f_D. It was noted that the Doppler spectrum for the highway environment was broader than the urban case, as expected since higher relative velocities occur more frequently in the highway scenario leading to a larger Doppler spread. Symmetric peaks related to “overtaking situations” are noted for both urban and highway scenarios.

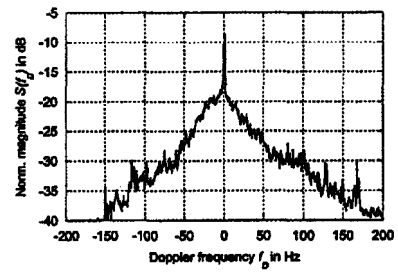

(a) Urban

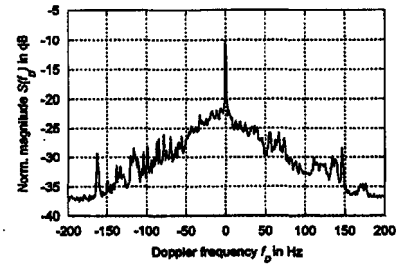

(b) Highway

Figure 4: Flat-fading Doppler measurements in [48].

The measured spectrum resembles the theoretical spectrum for *a=1* in Figure 1, although the measured peak is much taller. It also resembles the spectrum on the first tap of our measured freeway data. Other examples of measured spectrum from the literature are shown in Figure 5 [91]; these measurements were for a fixed-to-mobile environment but represent a subset of what might be encountered in the MTM case.

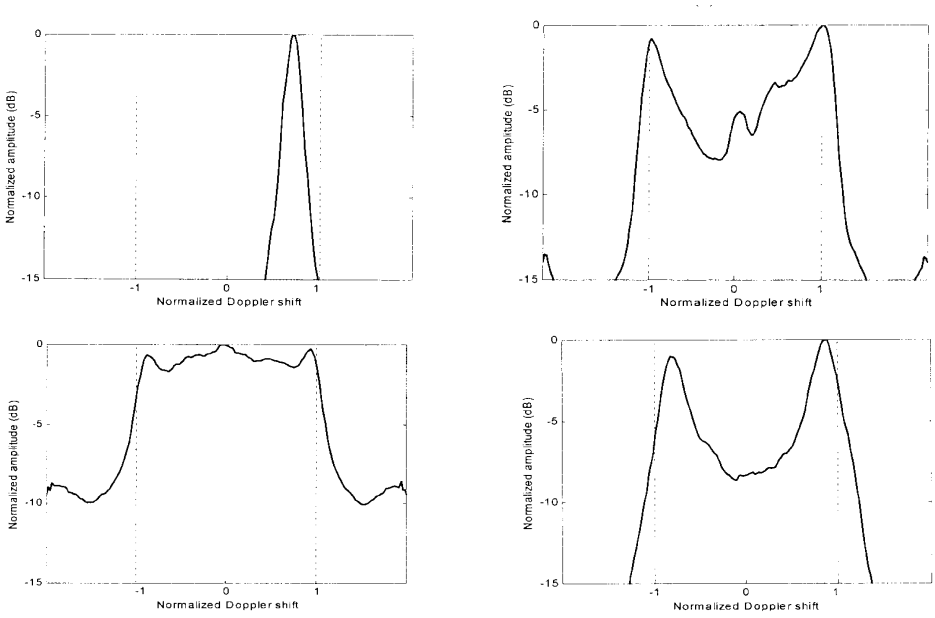

Figure 5: Examples of Doppler spectra measured in a fixed-to-mobile environment [91].

Maurer also considered an analytical expression for level-crossing rate that was based on the assumption of a Gaussian Doppler spectrum. This expression was compared to fast fading measurements and results indicated that a Gaussian Doppler spectrum was a good approximation in a 15 dB range near the mean value but a larger deviation between theoretical and measurements outside of this range indicated Doppler spectra other than Gaussian would be appropriate**.** Based on the analysis and measurements cited above, we expect a variety of Doppler spectra in our MTM measurements.

2.2 Channel Sounding

The mobile radio channel within a certain bandwidth of interest can be completely characterized by its complex time-variant impulse responses (IRs). The measurement equipment must be able to record the IRs with a sufficient length in time and to fulfill the sampling theorem with respect to the Doppler shift (*i.e.* record at least two IRs per Hertz

of the maximum Doppler frequency). For system related investigations (e.g., simulations with stored channel data), a measurement bandwidth equal to the system bandwidth is sufficient. For the development of (wideband) deterministic or statistical propagation models, a very large bandwidth for channel measurements is desirable in order to gain as much detail as possible to enable the understanding of the propagation phenomena (e.g., identification of scatterer locations) and support the modeling approaches. However, propagation measurements with large bandwidths produce a huge amount of data. Narrowband measurements are much simpler to carry out and handle. They are appropriate if we require only narrowband information. This is particularly the case for all types of path-loss modeling [39].

We find in [64] one of the most cited classifications of the available channel sounding techniques where we can fit most of the published works in the last decade. The techniques are classified as narrowband or wideband and as time- or frequency-domain approaches.

2.2.1 Narrowband Sounding Techniques

The most common narrowband technique is to excite the channel using an unmodulated RF carrier (single tone). Large variations are then observed in the amplitude and phase of the received signal, these variations are a result of the random phase additions of signals arriving over many scattered paths. Through the years, models like the Jakes [28] have shown reasonable agreement with single tone measurements of the fading envelope. One can also perform narrowband Doppler spread measurements by either recording the channel induced frequency and/or phase modulation of the RF carrier or by direct observation of the modulation using a spectrum analyzer.

2.2.2 Wideband Sounding Techniques

The evolution of communications systems has dramatically increased the demand for wideband measurements. There are a number of different approaches to wideband sounding. In the proposed research, at least two of these approaches will be used to measure the mobile-to-mobile channel. In this section, we review several techniques, beginning with the oldest technique of tone-sweeping. We next describe a superior multi-tone approach, which we will use as a benchmark. To this benchmark, we will compare several time- and frequency-domain sounding methods, including periodic pulse sounding, pulse compression, chirp sounding, and an OFDM approach. In each case, we will examine what parameters would be needed to approach the performance of the multi-tone approach.

2.2.2.1 Tone Stepping

The first wideband measurement attempts relied on sweeping the RF spectrum using the simple tone technique. In this technique, we step the tones across a band of frequencies to measure the channel frequency transfer function. Using a vector network analyzer, we can measure the magnitude and phase of the forward transmission gain S_{21} as if we were exciting a test circuit (in this case the RF channel) with a single sine wave. This is repeated for a number of equally spaced frequencies within the bandwidth of interest. Frequency domain channel sounding using network analyzers has two major drawbacks. First, stepping a synthesizer over a large bandwidth in small steps is time consuming, and secondly, it is impossible to make mobile measurements due mainly in part to the strict timing reference requirements, which can be accomplished only through a wired system. On the other hand, it provides the best multipath resolution and very small storage requirements. For example, J-S. Jiang [38] used a 500 MHz bandwidth centered at 5.8 GHz with 401 stepping points and a recording time of six seconds. Such

a bandwidth provides a PDP resolution of two nanoseconds, which corresponds to four wavelengths.

As we can imagine, the tone stepping method is too slow for mobile channels. A faster alternative would be to perform a real-time frequency domain channel measurement by exciting all frequencies simultaneously and attempting to process and/or record the reception in real-time. There are two techniques available. The first one uses a swept frequency (chirp) signal instead of single tone stepping, but the frequency sounding is still sequential. The other one uses a multi-tone signal, and at this time, the RUSK™ [13] channel sounder is the best representative of this technique, which is also known as frequency domain correlation processing. For both techniques to work in mobile channels, they require at least real-time recording of baseband complex symbols.

2.2.2.2 The RUSK™ Multitone System

Up until now and to our best knowledge, the state of the art sounding system is the RUSK™ system. We will briefly describe this system to have a benchmark to compare the other available techniques. In the RUSK™ system, a signal is sent that includes a complete set of single tones with $f_0 = 1/t_p$ Hz of separation. The maximum bandwidth of the system is 240 MHz, which produces a 3.12 ns resolution. The system has three different repetition periods (IR lengths), $t_p = 6.4; 25.6; 102.4\,\mu s$. The system captures the signal with an eight bit 640 MHz analog-to-digital (ADC) converter. The system is capable of recording at a rate of 320 MByte/s using four disk arrays in parallel controlled by a proprietary interface. All the previous description is about how the system overcomes the first drawback of the network analyzer system: speed of measurement. To overcome the second one, which allows for mobile measurements, the system relies on calibrated Ru-

bidium frequency generators. We shall describe the characteristics of these frequency generators in later chapters when we discuss our synchronization method.

There are other alternatives for wideband channel measurements. In the next four sections we present an overview of the time- and frequency-domain sounding methods where we show the advantages and disadvantages for each one along with the required specifications to obtain a similar performance of that of the RUSK™ system previously described.

2.2.2.3 Periodic Pulse Sounding Method

The CIR is by definition the convolution of the channel response with an ideal pulse (*i.e.*, infinite magnitude and zero duration). Since there is no such thing as an ideal pulse, whatever we can measure is only an approximation to the real CIR. On the other hand, this is a simple channel sounding technique to rapidly determine the power delay profile of any channel by just detecting the envelope of the received signal and displaying it on a high speed oscilloscope. The probing signal is a pulse of width T_p with repetition period T_R. The smaller the pulse width is compared to the delay spread of the channel the better we can resolve the individual multipath components assuming that the period exceeds the maximum delay spread, τ_m. Of course, the shorter the pulse, the larger the required null-to-null bandwidth $BW = 2/T_p$ for a power spectrum envelope of the form $\left[\frac{\sin(f-f_c)T_p}{(f-f_c)T_p}\right]^2$. This system is highly sensitive to noise and to interference, and it requires a high peak-to-average power ratio (PAR) to provide adequate detection of weak echoes [27]. We can detect phase and Doppler shifts using a coherent detector instead of the envelope detector, but the system loses its simplicity and real time capability.

2.2.2.4 Pulse Compression Techniques

To overcome the large dynamic range requirement imposed by the high PAR, we use pulse compression techniques. The theory of linear systems [62] contains the basis for all these techniques as follows: if white noise $n(t)$ is input to a linear system, and if the system output $y(t)$ is cross-correlated with a delayed replica of the input $n(t-\tau)$ then the resulting coefficient is proportional to the IR of the system $h(t)$ evaluated at the delay time τ. We will show this below. Let

$$E\left[n(t)n^*(t-\tau)\right] = R_n(\tau) = N_o\delta(\tau) \tag{2.26}$$

where $R_n(\tau)$ is the autocorrelation function of the noise, and N_o is the one-sided noise power spectral density. The cross-correlation of the system's output is

$$\begin{aligned} E\left[y(t)n^*(t-\tau)\right] &= E\left[\int h(\lambda)n(t-\lambda)n^*(t-\tau)d\lambda\right] \\ &= \int h(\lambda)R_n(\tau-\lambda)d\lambda \\ &= N_0 h(\tau) \end{aligned} \tag{2.27}$$

We now need to use an approximation to white noise. We can do it by using maximum-length pseudo-random binary sequences, which are deterministic signals with noise-like or pseudo-noise (PN) characteristics. These sequences possess excellent periodic autocorrelation properties and can be easily generated using linear feedback shift registers. The general form of one transmitted MLS is

$$\sum_{n=0}^{N-1} a_n g(t-nT_c)\cos(2\pi f_c t) \tag{2.28}$$

where $\{a_n\}_{n=0}^{N-1}$ is the MLS with $a_n \in \{-1,+1\}$. T_c is the "chip" or element period, the pulse $g(t-nT_c)$ is rectangular with width T_c, and $N = 2^p - 1$ is the length of the sequence.

The exponent p is the order of the Galois-field primitive polynomial that generates the sequence. The first thing we notice is that the MLS is performing a binary phase shift keying (BPSK) of a carrier with frequency f_c; therefore, we expect a similar spectrum, $\left[\frac{\sin(f-f_c)T_c}{(f-f_c)T_c}\right]^2$ and bandwidth $BW = 2/T_c$ to the pulse sounding case. Once again, the resolution of the system is given by T_c, and T should exceed τ_m, but in this case T is also a function of the dynamic range, $20\log(N)$, of the signal.

We might consider two main design or performance goals for any channel sounding system: real time processing or information and real time storage or recording. As an hypothetical example, let us try to obtain the specifications for a MLS system that matches the RUSK™ system described previously. We have a 240 MHz bandwidth and $T = 25.6\,\mu s$. First, we would like the maximum resolution $T_c = 2/(240\,\text{MHz}) = 8.33\,\text{ns}$, then, we want the maximum dynamic range that allows the repetition rate. In this case, $T/T_c = 3072$; therefore, we need to choose between an order 11 (*N*=2047, *T*= 17.0 μs, & 66 dB) and an order 12 (*N*=4095, *T*= 34.0 μs, & 72 dB) MLS. We choose the latter. Let us talk about real time recording first. We need at least a 580 MHz ADC. Since we have chosen the MLS with 72 dB of dynamic range, it would be logical to match it with at least a 12-bit ADC. This will mean that we need a two-byte word for each quadrature sample or four bytes per complex sample. The required recording speed is 2.32 GByte/s. Assuming that there exists a hard disk array that can match the PCI-X bus (latest server interface bus), we can only achieve 1.064 GByte/s; therefore, there are trade-offs to solve among dynamic range, repetition rate, and resolution. For this example, we can first perform some processing before recording. We could combine the complex samples into a three byte word and decimate by two, which will reduce the speed to 720 MByte/s. This speed can fit into the PCI-X bus, but it will probably require an array of 16 of the

fastest hard drives to match the speed. As we can see, even with the latest technology, real time recording is hard and expensive.

For real time processing, let us start by looking at the discrete-time correlation operation as follows:

$$R_{xx}(n) = \frac{1}{N}\sum_{k=0}^{N-1} r_{I\,or\,Q}(n)\,a(k) \tag{2.29}$$

where $r(n)$ is the received baseband quadrature signal, and $a(k)$ is the stored MLS. For each complex baseband sample, we need 2*N* operations, which for our example translate into 4.42 TFLOPS, way out of the reach of even the most powerful DSP. Therefore, in cases like our example, it makes more sense to bias the design efforts towards recording capability for off-line or post-processing.

In case of continuous-time processing, there are two main techniques to perform the correlation process. The first one is the **convolution matched-filter technique** where a filter is designed to match the sounding waveform. This means that the filter must match the specific MLS by implementing a transversal or finite impulse response (FIR) filter with a MLS used as the tap weights. CMOS switched-capacitor circuits (SC), charged-coupled devices (CCD), and surface-acoustic wave (SAW) technologies are all viable solutions for this task. SAW devices are most suitable for high-frequency operation while the others are preferable in digital CMOS compatible solutions [61]. Such a system will operate in real time, but the recording requirements do not change. Also, the performance of practical SAW devices is limited by their own deficiencies. Specifically, long sequences are difficult to obtain, and the generation of spurious acoustic signals that along with other inherent imperfections cause time sidelobes to appear at the output of the filter. These sidelobes reduce the sensitivity to weak echoes.

The second technique is the **swept time-delay cross-correlation** (STDCC) method. This method focuses on real time processing and data reduction to allow recording. For real time processing, a local MLS is generated and mixed with the incoming signal usually at IF. This requires a stable synchronization, which once again is usually achieved by means of a Rubidium generator. In a sense, we have to duplicate the whole transmitter generator, but there is a big problem. It is not just a matter of running the two generators in parallel; we cannot achieve the correlation function this way. What we will need to do is to start the local MLS at least every delay lag chosen as the system resolution, which is of course clearly unrealistic since it would require a huge bank of generators. There is an alternative that not only allows real-time correlation, but it also reduces the recording requirements. This idea dates back to 1972 [21] and relies in a time-scaling of the IR estimate [81]. To explain the time-scaling, we start by looking at an ideal discrete-time signal illustrated in Figure 6. By ideal, we mean as if we were able to process the sequences digitally with perfect synchronization. Here we show the first elements of the transmitted sequence with elementary or chip period T_c, the sequence generated at the receiver with a chip period T_{cr}, and the period T_{ps}, where we have a maximum value for the correlation between the two sequences. As we can see, the period of the receiver sequence is slightly longer than the transmitted period. We can easily accomplish this by offsetting the reference generators by a small amount. There will be an instant when the first elements of two sequences align at $t = 0$. From this instant, they will start separating or offsetting at a rate $\Delta = N\left(T_{cr} - T_c\right)$ for each sequence repeti-

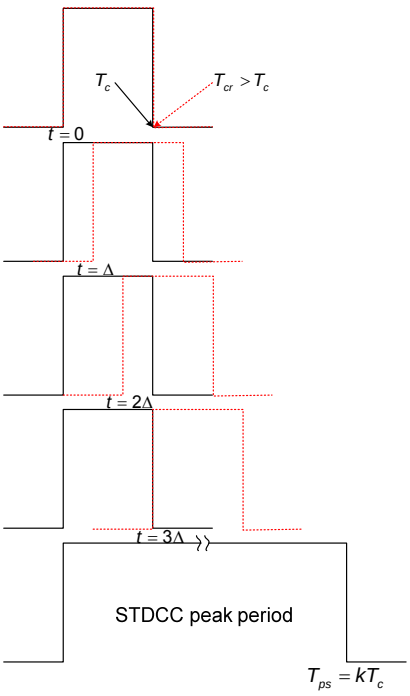

Figure 6: First elements of transmitted and locally generated sequences shown for three transmitted sequence repetition cycles.

tion cycle $T_{rep,TX} = NT_c$. If we consider the trailing edge of the receiver's sequence first element as the correlation instant (*i.e.*, the sampling instant), we can fit T_c/Δ correlation instants before the sequences have to align again. Therefore, both sequences will sustain correlation for a period $T_{ps} = kT_c$ where $k = T_c/(T_{cr} - T_c)$ is the slide factor. We have indeed extended or time-dilated the correlation period to $T_{rep,STDCC} = kT_{rep,TX}$, and the resulting output will resemble a pulsed signal with pulse width T_{ps}, repetition rate $T_{rep,STDCC}$, and amplitude N. For each reflected path, the receiver's sequence will correlate in the same manner; therefore, the delay spread measurement obtained will also be time-dilated. To obtain the original or real delay spread, we have to scale the measurement dividing by k. As we mentioned before, the correlation operation is usually performed at IF in the STDCC systems using a mixer to multiply the signals followed by an integrator.

The equivalent baseband operations is as follows: we start with just one transmitter sequence and one receiver sequence aligned at $t = 0$

$$\begin{aligned} s_{TX}(t) &= \sum_{n=0}^{N-1} a_n g(t - nT_c) \\ s_{RX}(t) &= \sum_{k=0}^{N-1} a_k g'(t - kT_{cr}) \end{aligned} \tag{2.30}$$

where g' has width T_{cr}. During the correlation period, the receiver sequence advances at Δ intervals

$$s_{RX}(t,m) = \sum_{n=0}^{N-1} a_n g(t - nT_{cr} - m\Delta); \tag{2.31}$$

therefore, the output of the correlator is

$$\begin{aligned} c(m) &= \int_0^{NT_c} s_{TX}(t) s_{RX}(t,m) dt \\ &= \sum_{n=0}^{N-1} \sum_{k=0}^{N-1} \int_0^{NT_c} a_n a_k g(t - nT_c) g'(t - kT_{cr} - m\Delta) dt, \end{aligned} \tag{2.32}$$

which is reference to the transmitter chip period T_c. The maximum value of the correlation will occur when the sequences' overlapping is a maximum as we can see in the top graph of Figure 6. Since the areas will start overlapping from the left for the next alignment instant, the resulting shape of $c(m)$ is a triangular pulse similar to the convolution of two rectangular pulses as we describe in Figure 7.

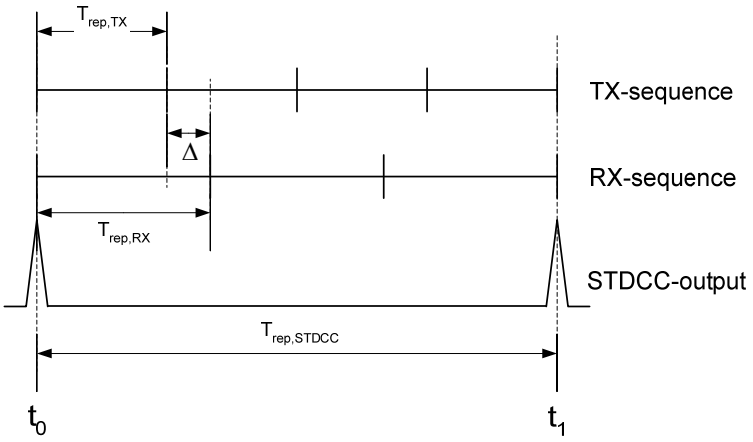

Figure 7: Transmitted sequence and locally generated sequence alignment period [81].

Let us now analyze the performance of a STDCC system. Following our previous example, we have $T_c = 2/(240\,\text{MHz}) = 8.33\,\text{ns}$, $N = 4095$, and $T = 34.0\,\mu\text{s}$. Since the correlation is now done in time domain with hardware elements, we have to focus only on the recording parameters. With a $k = 5800$, the sampling frequency reduces to $fs = 100\,\text{kHz}$, which requires a recording speed of 300 kByte/s for the same 12-bit ADC, well within the reach of many available digitizer boards. The system satisfies the processing and recording requirements, but the repetition period increases proportionally to $T_{rep,STDCC} = 197.2\,\text{ms}$, which practically limits its use to static channels since the maximum allowable Doppler frequency reduces to approximately 2.5 Hz.

2.2.2.5 Chirp Sounding

So far we have seen that bandwidth and power efficiency are two desirable goals in a sounding system. The chirp or frequency modulated continuous waveform (FMCW) sounding technique allows ample control to attain these goals. In this method, we use a frequency modulated signal as the transmitted signal. Frequency modulation has constant power; therefore, we can avoid power deficiencies such as the ones produced by

large PAR. The transmitted baseband signal is usually a linear frequency modulated continuous signal of the form

$$s(t) = A\cos\left(\omega_H t + \beta t^2/2\right) \tag{2.33}$$

where A is the signal amplitude, $\omega_H = 2\pi f_H$ is the initial frequency, and $\beta = \partial\omega/\partial t$ is the rate of frequency variation. This signal has an almost constant spectrum over the swept bandwidth in contrast to the square sinc shape of the STDCC. Its multipath resolution is $1/BW$, and its unambiguous Doppler coverage is $\pm 1/2T$.

At the receiver, the chirp signal is compressed by either a matched filter in a similar manner to the sliding correlator, *e.g.*, via SAW filters, but with the same limitations and advantages as before. Another way to measure the individual time delays of the multipath arrivals is to combine the received signal with the transmitted signal using a mixer. This homodyne signal contains frequencies, called beat frequencies, which are proportional to the time delays of the multipath arrivals. Since this method requires strictly identical chirp-signal characteristics and simultaneous synchronization in both transmitter and receiver, homodyne reception is highly desirable, but it limits the use of the system to static measurements. Once again, using highly stable Rubidium reference generators, we can achieve heterodyne reception.

The output of this detection method is compressed in frequency but not compressed in time. The required bandwidth at the output of the detector is determined by the product of the sweep rate and the maximum expected time delay of the farthest echo. This results in an important reduction in bandwidth without a significant reduction in the effective repetition rate of the sounder. The disadvantage of the chirp sounder is that the

compressed pulse has high sidelobes, which can be reduced by weighting [69]. Let us consider a delayed signal as follows:

$$r(t) = B\cos\left(\omega_H (t-\tau) + \beta (t-\tau)^2/2\right). \tag{2.34}$$

The output of the mixer would be

$$r_{mx}(t) = \frac{AB}{2}\left(\cos\left(\beta\tau t - \frac{\beta\tau^2}{2} + \tau\omega_H\right) + \cos\left(\beta t^2 - \beta\tau t + \frac{\beta\tau^2}{2} + 2\omega_H t - \tau\omega_H\right)\right). \tag{2.35}$$

If we low-pass filter to ω_H, we obtain

$$r_{bb}(t) = \frac{AB}{2}\cos\left(\beta\tau t - \frac{\beta\tau^2}{2} + \tau\omega_H\right). \tag{2.36}$$

So the beat or difference frequency $\beta\tau$ uniquely determines the propagation time. If we use a spectrum analyzer, we can obtain a real time measurement of path delays. Following the same design specifications we have $\beta = \frac{240\ \text{MHz}}{25.6\ \mu\text{s}} = 9.375$, this means that the generator must be capable of sweeping 240 MHz every $25.6\ \mu\text{s}$. Its delay spread resolution is 4.16 ns, and its maximum Doppler frequency is 19.531 kHz.

In contrast to the STDCC where the compression relies on the maximum Doppler frequency reduction, here the compression relies on the longest delay spread reduction. If we were to record the channel response with a $\tau_m = 25.6\ \mu\text{s}$, we would need at least a 540 MHz ADC; on the other hand, a reasonable $\tau_m = 2\ \mu\text{s}$ reduces the required ADC frequency to 37.5 MHz, which is in the range of many available recording systems. We achieve this compression in the design parameters of the detector output filter. In addition, by offsetting the center frequency of this filter, one correlator would suffice to pro-

vide both range and Doppler information without having to obtain quadrature components.

2.3 Channel Emulation

As we have mentioned before, wideband synthetic models of the mobile radio channel are required for mobile radio system design and optimization. We can categorize systems where we can use the aforementioned models as follows: The first and usually most expensive one is the **hardware channel emulator**. As an example, we present a block diagram of an IEEE 802.11g throughput testing using a channel emulator in Figure 8. In Figure 9, Figure 10, and Figure 11, we present the required input parameters to perform a channel emulation experiment with the Spirent™ TAS 4500, which we can consider a standard in the industry. As we can deduce from these figures, we require the following parameters:

1. Number of taps or paths
2. Relative time delay per tap
3. Relative path loss per tap
4. Amplitude statistics or modulation per tap
5. Doppler spectrum shape and parameters per tap

With the appropriate parameters, the channel emulator provides a convenient, thorough approach for testing wireless communications equipment by emulating the delay, fast and slow fading, and path loss characteristics of RF mobile communication channels. The effectiveness of this system is as good as the channel model.

The second option is **software simulation** of communication channels. This is the cheapest and most accessible option. As with the previous system, its effectiveness depends on the channel model. The third option is called the **stored channel approach**.

This is also an expensive and time consuming option since it requires physical channel measurements, large storage capacity, and high processing power. Of the three systems, this one is the only accurate representation of the channel. Basically, a channel model may be thought of as a representation, in mathematical or algorithmic form, of the transfer characteristics of any contiguous subset of the general block diagram of the system under study. This representation is generally not based on the underlying physical phenomena, but rather on fitting external (empirical) observations [37]. In other words, the design of the channel model is an open procedure (*i.e*. there is not a unique method), but standardization and cost optimization are desirable goals. In Figure 12, we show the required input parameters for two of the most common software channel models. We can observe that the previous parameter list is valid; therefore, we can define the estimation of these parameters from our measurement campaigns as the major contribution of this thesis.

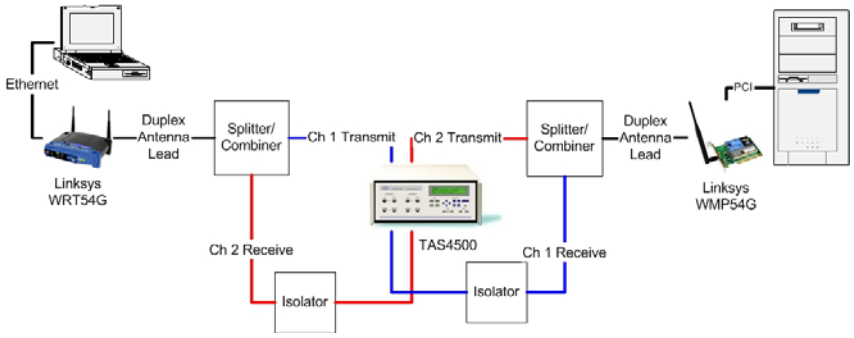

Figure 8: Channel emulator setup for IEEE 802.11g throughput testing.

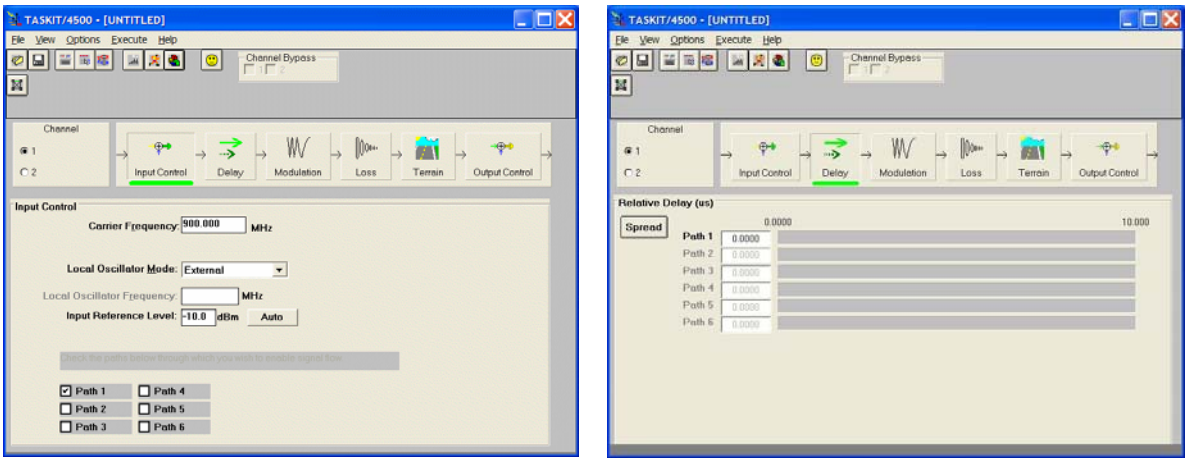

(a) (b)

Figure 9: Spirent TAS 4500 hardware channel emulator parameters setup: (a) number of taps and (b) delay per tap.

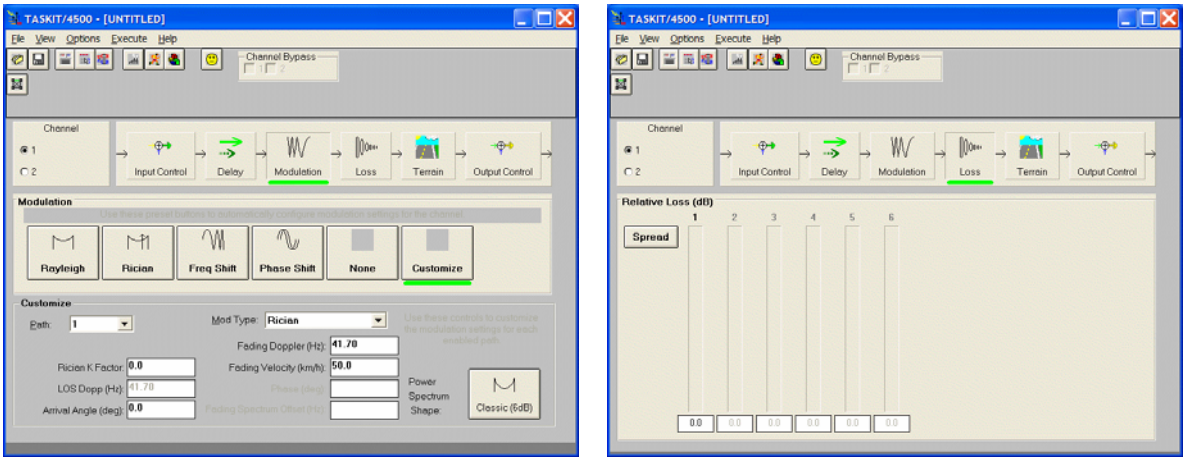

(a) (b)

Figure 10: Spirent TAS 4500 hardware channel emulator parameters setup: (a) Doppler parameters per tap and (b) power per tap.

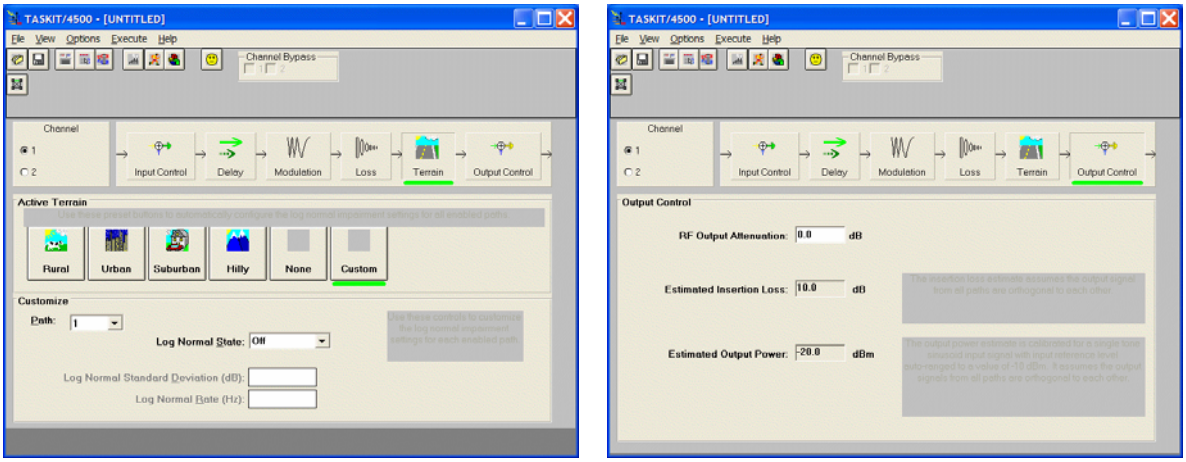

(a) (b)

Figure 11: Spirent TAS 4500 hardware channel emulator parameters setup: (a) large-scale fading per tap and (b) output power adjustment.

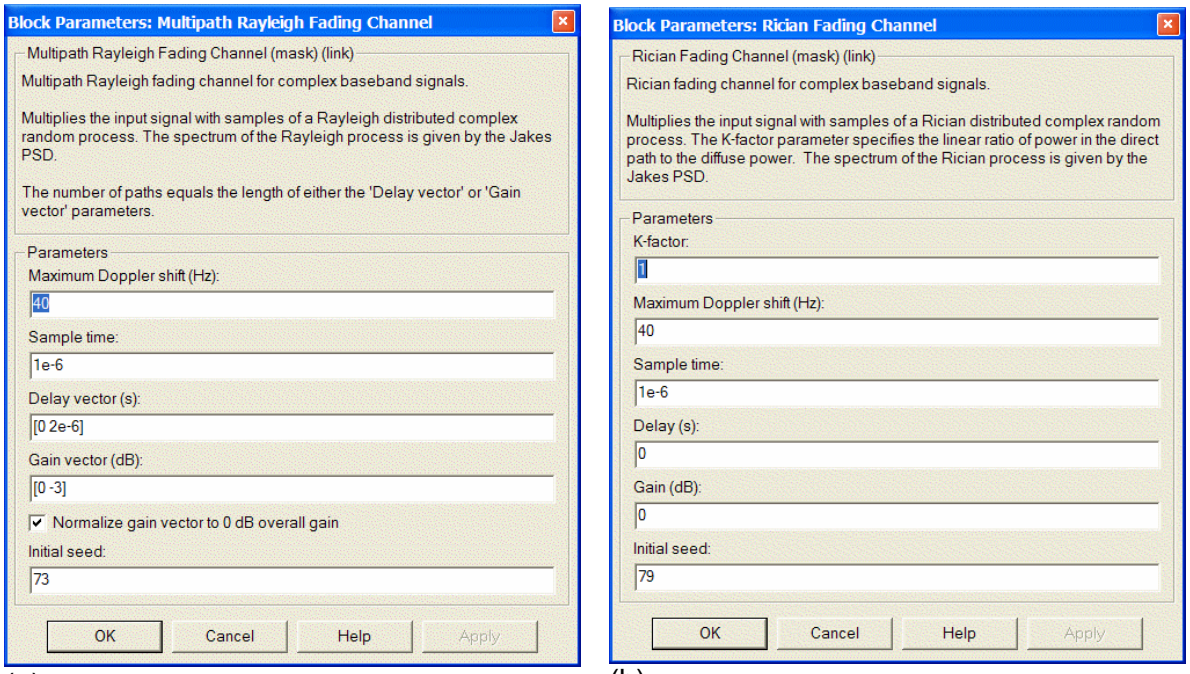

(a) (b)

Figure 12: Matlab™ Simulink™ software channel models: (a) multipath Rayleigh and (b) Rician fading.

The synthetic models presented in the previous section are based on a transversal filter structure with a limited number of taps. Measurements support this approach, because the number of significant paths with time-varying amplitude is constant assuming WSSUS conditions [11], [51]. For each tap, we need to obtain the required parameters.

We now present a methodology for their derivation from channel measurements [43], [51]. The first step in extracting the model is to separate the fast from the slow fading characteristics. We can obtain the slow fading by obtaining the local average power [45]. For this, we require uncorrelated samples of the IR over an appropriate distance that will average out the short-term fading and will not smooth out the long-term fading. This length is usually in the range of 20 to 40 wavelengths (λ), and a sampling at $0.8\,\lambda$ is usually enough to achieve uncorrelated samples. We calculate the PDP by averaging the magnitude squared of the IR over the distance,

$$P(n\Delta\tau) = \frac{1}{Q}\sum_{k=0}^{Q-1}\left|h_{norm}\left(n\Delta\tau, k\Delta t\right)\right|^2 \qquad 0 \le n \le N-1 \tag{2.37}$$

where $k\Delta t$ is the fixed observation instant of the *k*-th single IR, *Q* is the total number of IRs, and h_{norm} indicates short-term fading only. Next, we determine the significant part of the PDP by discarding all parts that are more than 35 dB down from the strongest path.

Let L be the length of the significant part of the PDP divided by $\Delta\tau$. Let M be the number of taps in the model, such that M < L. The L samples are divided into M groups. If the result $L/M = I$ is not an integer, samples with zero amplitude are added to the end of the PDP. The tapped delay value in each group is found by [51]

$$\tau_m = \frac{\sum_{n=i_m}^{i_m+I-1} n\Delta\tau \cdot P\left(n\Delta\tau\right)}{\sum_{n=i_m}^{i_m+I-1} P\left(n\Delta\tau\right)} \quad \text{for} \quad 0 \le m \le M-1 \tag{2.38}$$

where i_m is the sample number at the start of each group. The delay of the first tap is $\tau_0 = 0$. Knowing the delay position of the tap, we can obtain the tap magnitude as follows:

$$P_m\left(\tau_m, k\Delta t\right) = \frac{1}{I}\sum_{n=i_m}^{i_m+I-1} P\left(n\Delta\tau, k\Delta t\right). \tag{2.39}$$

We determine the Rice factor for each tap using the moment-method [1], [29] as follows:

$$\begin{aligned}
G_k &= \left|h_m\left(\tau_m, k\Delta t\right)\right|^2, \quad k = 1,\mathrm{K}\ ,Q \\
G_a &= \frac{1}{Q}\sum_{k=1}^{Q} G_k \\
G_v &= \sqrt{\frac{1}{Q}\sum_{k=1}^{Q}\left(G_k - G_a\right)^2} \\
\left|V\right|^2 &= \sqrt{G_a{}^2 - G_v{}^2} \\
\sigma^2 &= G_a - \left|V\right|^2 \\
K_{Rice} &= \frac{\left|V\right|^2}{\sigma^2}.
\end{aligned} \tag{2.40}$$

Finally, we use the Welch algorithm to estimate the Doppler spectrum per tap.

2.4 OFDM Synchronization Algorithms

In Section 3.1, we will present a quantitative measure of the problems encountered in the OFDM synchronization process. According to this measure, we need to find, estimate, or minimize the frequency, symbol timing, and sampling frequency offsets for any type of OFDM transmission; and we need to diminish the effect of the Doppler spread and delay spread for high mobility channels. We shall attempt to describe the developments and techniques we have found in the literature that deal with each of the problems. We can start by mentioning that there is a common structure in most of the synchronization techniques. The techniques are usually divided in two steps or phases: acquisition and tracking, and they can be performed in a NDA or DA manner. In the former step, a coarse estimate of the parameters to control is obtained, and in the latter, the errors are minimized. This process is illustrated in Figure 13. As with many other communications processes, there exists a trade-off between overhead and complexity; therefore, many of the techniques combined NDA and DA algorithms for time and frequency synchronization. Another common trend in the techniques is a frame structure of the OFDM symbols that allows a coarse time synchronization of several symbols at once. In [17], [30], [52], [56], and [72], the authors present an excellent review of the majority of the synchronization techniques. We will see in the literature that the authors usually address only a subset of the synchronization offsets in a paper and assume the other offsets are zero. However, in a real system, all offsets are non-zero and they must all be compensated. One of the contributions of this dissertation is to show how synchronization of one type of offset is impacted by all the others.

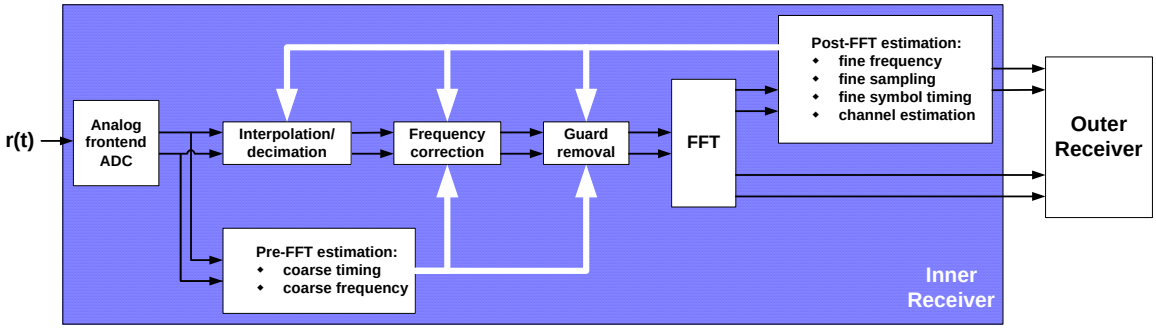

Figure 13: Common synchronization structure [78].

2.4.1 Frame or Symbol Acquisition

The algorithms presented in the literature all rely on additional redundancy inserted in the transmitted data stream. Some systems use a so-called null symbol as the first OFDM symbol in the time frame. No energy is transmitted during the null symbol and it is detected by monitoring the received baseband power in the time domain, without invoking FFT processing.

In [17], Classen and Meyr propose an OFDM synchronization burst of at least three OFDM symbols per time frame. Two of the OFDM symbols in the burst contain synchronization subcarriers bearing known information symbols along with normal data transmission carriers, but one of the OFDM symbols is the exact copy of one of the other two, thus it results in more than one OFDM symbol synchronization overhead per synchronization burst. This method jointly finds both the symbol timing and carrier frequency offset.

In [89], Warner proposes the employment of a power detector and subsequent correlation-based detection of a set of received synchronization subcarriers embedded in the data symbols. The received synchronization tones are extracted from the received

time domain signal using an iterative algorithm for updating the synchronization tone values once per sampling interval.

In [59], Nogami and Nagashima present algorithms to find the carrier frequency offset and sampling rate offset. They use a null symbol for one symbol period so that the drop in received power can be detected to find the beginning of the frame. In [10], Van de Beek *et al*. describe a method of using a correlation with the cyclic prefix to find the symbol timing, but they do not solve the problem of finding the start of the frame to know where the training symbols are located.

Finally, in [72], Schmidl and Cox introduce some modifications of Classen's method, which greatly simplify the computation necessary for synchronization. The method avoids the extra overhead of using a null symbol by using one unique symbol, which has a repetition within half a symbol period. This method can be used for bursts of data to find whether a burst is present and to find the start of the burst. Acquisition is achieved in two separate steps through the use of a two-symbol training sequence, which will usually be placed at the start of the frame. First the symbol/frame timing is found by searching for a symbol in which the first half is identical to the second half in the time domain. Then the carrier frequency offset is partially corrected, and a correlation with a second symbol is performed to find the carrier frequency offset.

2.4.2 Frame or Symbol Tracking

Symbol tracking algorithms are generally based on correlation operations either in the time or in the frequency domain. The basic operation is shown in Figure 14. The frequency domain approach is indicated by Warner [89] and Bingham [12]. They employ a DA frequency domain correlation of the received synchronization pilot tones with

known synchronization sequences. A time domain NDA correlation can be performed as de Couasnon [18] and Sandell's [70] groups suggest. The former utilizes the redundancy of the cyclic prefix by integrating over the magnitude of the difference between the data and the cyclic extension samples. The latter proposes exploiting the autocorrelation properties of the received time domain samples imposed by the cyclic extension for fine time domain tracking.

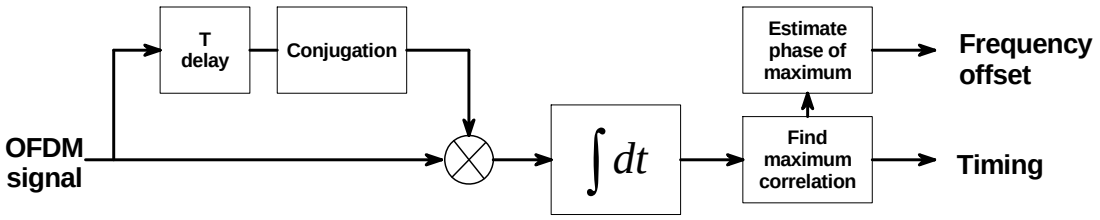

Figure 14: Basic correlation process.

2.4.3 Frequency Offset Acquisition

The frequency offset acquisition algorithm has to provide an initial frequency error estimate, which is sufficiently accurate for the subsequent frequency-tracking algorithm to operate reliably. Generally, the initial estimate must be accurate to half a subcarrier spacing. For the acquisition process, most of the techniques use DA algorithms.

In [71], Sari proposes the use of a pilot tone embedded into the data symbol, surrounded by zero-valued virtual subcarriers, so that the receiver can locate the frequency-shifted pilot easily.

In [54], Moose gives the ML estimator for the carrier frequency offset that is calculated in the frequency domain after taking the FFT. He assumes that the symbol timing is known, so he just has to find the carrier frequency offset. The limit of the acquisition

range for the carrier frequency offset is $\pm 1/2$ the subcarrier spacing. He also describes how to increase this range by using shorter training symbols to find the carrier frequency offset. For example, shortening the training symbols by a factor of two would double the range of carrier frequency acquisition. This approach will work to a point, but the estimates get worse as the symbols get shorter because there are fewer samples over which to average, and the training symbols need to be kept longer than the guard interval so that the channel impulse response does not cause distortion when estimating the frequency offset.

In [17], Classen and Meyr propose to use binary PN or so-called constant amplitude, zero autocorrelation (CAZAC) training sequences carried by synchronization subcarriers, which are also employed for the frequency tracking. The frequency acquisition, however, is performed by a search for the training sequence in the frequency domain. This is achieved by means of frequency domain correlation of the received symbol with the training sequence. The method is very computationally complex because it uses a trial and error method where the carrier frequency is incremented in small steps over the entire acquisition range until the correct carrier frequency is found. It is impractical to do the exhaustive search and go through a large amount of computation at each possible carrier frequency offset.

Lastly in [72], Schmidl and Cox employ different OFDM blocks. The first one has two identical halves and serves to measure the frequency offset with an ambiguity of multiples of the sub-carrier spacing. The second block contains a pseudo-noise sequence and serves to resolve the frequency ambiguity.

2.4.4 Frequency Offset Tracking

The frequency offset tracking method generally relies on an already established coarse frequency estimation having a frequency error of less than half a subcarrier spacing. In [54], Moose suggests the use of the phase difference between subcarriers of repeated OFDM symbols in order to estimate frequency deviations of up to one-half of the subcarrier spacing.

In [17], Classen and Meyr employ frequency domain synchronization subcarriers embedded into the data symbols, for which the phase shift between consecutive OFDM symbols can be measured. Also in [23] and [70], and Daffara and Sandell respectively, use the phase of the received signal's autocorrelation function, which represents a phase shift between the received data samples and their repeated copies in the cyclic extension of the OFDM symbols.

2.4.5 Sampling Frequency Offset Acquisition

Simoens *et al* [73] propose a joint ML algorithm to estimate the frequency offset and the sampling frequency offset. Under certain assumptions a linearization can be applied, leading to an analytical expression of the estimator. Sliskovic [76], [77] estimates the sampling frequency offset using the repetition of data symbols and comparison of the phases between successive repeated symbols on all subcarriers. The phase difference between successive symbols has two mains causes: either frequency offset or sampling frequency offset. Sliskovic assumes that there is no frequency offset.

One major conclusion from the OFDM synchronization literature survey is that ML estimation of the OFDM synchronization offsets provides high accuracy [19], [20], [24]. Several authors have considered ML for one or two offsets [10], [73], [76], [77]. We need

to estimate all of them; however, joint estimation of all them has too much complexity. In the next chapter, we discuss our adopted approach for OFDM synchronization.

CHAPTER 3

OFDM SYNCHRONIZATION

OFDM systems have become widely popular since the beginning of the 1990s. We can find them as the preferred physical layer (PHY) in many transmission standards such as: DAB, IBOC, DVB, DSRC, IEEE 802.11a, IEEE 802.11g, IEEE 802.11p, IEEE 802.16. OFDM importance will continue to grow along with the wideband requirements of future communication systems; therefore, in this chapter, we present an analysis of one of its weaknesses: synchronization offsets. In the first part of the chapter, we offer a detailed analysis of the degradation produced by these offsets. We will extend the analysis to a static channel. In the second part, we propose a technique to detect and compensate for them that will be useful in a situation where we need to develop a transceiver test bed with fixed parameter components. By fixed parameters, we mean for example an ADC board with a fixed clock. This proposed technique is by no means intended for a real-time communication system. Its main purpose is to provide a tool that will help in the development or calibration of a prototype system.

3.1 OFDM Synchronization Offsets

Previous works in the literature have focused only on subsets of these offsets, and most of these works are referenced to [65]. In particular, we find in [80] one of the few that includes an analysis of all the offsets; however, they are treated singly. In these few, we also have [50], but in this work, Mody made approximations to reduce the expression complexity. We derived most of this work from the experiences and problems encountered in our experimental test-bed. In our test-bed, we had only one clock for all the

transmitter system and only one clock for all the receiver system. Because of these single clocks, we encountered combined synchronization effects in the output signal; therefore, we needed to detect and compensate for each particular offset. We are also extending the analysis of synchronization offsets to generate a degradation function that includes all of them. This analysis will allow us to individually identify the degradation effects produced by each of the synchronization offsets. With this offsets' classification, we will better comprehend or analyze the performance of OFDM synchronization algorithms.

To start, we need to present a reference framework for our nomenclature. For it, we have chosen the DAB parameters (which can easily be referenced to any other standard) as follows:

T	Elementary period
N	FFT/IFFT size or number of OFDM subcarriers
K	Number of transmitted subcarriers
$T_U = N \cdot T$	Useful OFDM symbol period
G	Number of OFDM subcarriers in guard band
$\Delta = G \cdot T$	Guard band period
$T_S = T_U + \Delta$	OFDM symbol period
T_{NULL}	Null symbol period
L	Number of OFDM symbols in a frame
$T_F = LT_S + T_{NULL}$	Frame duration.

With the above parameters, we define one OFDM symbol transmitted at $t = t_s$ as follows:

$$s(t) = \Re\left\{\left(\sum_{k=-K/2}^{K/2} c_{m,l,k} e^{j\frac{2\pi k}{T_U}(t-t_s)}\right) e^{j\pi f_c (t-t_s)}\right\},\ t_s \le t \le (t_s + T_U)$$
$$s(t) = 0,\ t < t_s \wedge t > (t_s + T_U) \qquad (3.1)$$

where f_c is the RF carrier frequency, m is the frame number, l is the OFDM symbol number, and k is the subcarrier number.

3.1.1 Frequency Offset Analysis

The OFDM subcarriers can loose their orthogonality if the transmitter and receiver do not use exactly the same carrier frequencies. We define frequency offset as the difference between transmitter and receiver carrier frequencies. This offset produces inter-carrier interference (ICI). To analyze this effect, we start by looking at the complex envelope of a received baseband OFDM symbol with frequency offset again at $t = t_s$

$$r(t) = \left(\sum_{k=-K/2}^{K/2} c_{m,l,k} e^{j\frac{2\pi k}{T_U}(t-t_s)} \right) e^{j\vartheta(t-t_s)} \tag{3.2}$$

where $\vartheta(t) = 2\pi \frac{\Delta F}{T_U} t$ describes the deterministic effect of a frequency offset $\Delta F = \left(f_{ct} - f_{cr}\right) T_U$ that is expressed as a multiplier of the subcarrier bandwidth $1/T_U$. We can separate $\Delta F = \Delta F_I + \Delta F_F$ into an integer part ΔF_I and a fractional part ΔF_F. Considering for now a perfect channel, the received sampled signal is

$$r(n) = \left(\sum_{k=0}^{N-1} c_{m,l,k} e^{j\frac{2\pi nk}{N}} \right) e^{j\frac{2\pi \Delta F}{N}(n+\alpha)} \tag{3.3}$$

where the discrete version of $t = t_s$ is represented by

$$\alpha = \frac{(m-1)T_F + T_{NULL} + (l-1)T_S + \Delta}{T} \tag{3.4}$$

Using this received signal as the input of the fast Fourier transform (FFT) operator we obtain

$$
\begin{aligned}
R_{m,l,k} &= \sum_{i=0}^{N-1} c_{m,l,i} e^{j\frac{2\pi\Delta F}{N}\alpha} \frac{1}{N} \sum_{n=0}^{N-1} e^{j\frac{2\pi n}{N}(i+\Delta F)} e^{-j\frac{2\pi n}{N}k} \\
&= e^{j\frac{2\pi\Delta F}{N}\alpha} \sum_{i=0}^{N-1} c_{m,l,i} e^{j\pi(i-k+\Delta F)\left(\frac{N-1}{N}\right)} \frac{\sin\left(\pi\left(i-k+\Delta F\right)\right)}{N\sin\left(\frac{\pi}{N}\left(i-k+\Delta F\right)\right)}.
\end{aligned} \tag{3.5}
$$

We can express the received complex symbol as follows:

$$
\begin{aligned}
R_{m,l,k} &= c_{m,l,k} \frac{\sin\left(\pi\Delta F\right)}{N\sin\left(\frac{\pi}{N}\Delta F\right)} e^{j\frac{\pi\Delta F}{N}(2\alpha+N-1)} \\
&\quad + e^{j\frac{2\pi\Delta F}{N}\alpha} \sum_{\substack{i=0 \\ i\neq k}}^{N-1} c_{m,l,i} e^{j\pi(i-k+\Delta F)\left(\frac{N-1}{N}\right)} \frac{\sin\left(\pi\left(i-k+\Delta F\right)\right)}{N\sin\left(\frac{\pi}{N}\left(i-k+\Delta F\right)\right)} \qquad \text{(ICI)} .
\end{aligned} \tag{3.6}
$$

The first term corresponds to an amplitude distortion and phase rotation. The second term expresses the inter-carrier interference (ICI) produced.

3.1.2 Sampling Frequency Offset Analysis

We define sampling frequency offset as the difference in sampling instants between the transmitter and receiver clocks. We use (3.2) with $\vartheta(t) = 0$ (since we can ignore the frequency offset for now) for the analysis. We define a sampling clock offset $\beta = (T' - T)/T$ where T' is the receiver system time, T is the transmitter system time. We usually express β in parts per million (ppm). The sampled time for the received signal is nT' where $T' = (1+\beta)T$. The discrete received baseband signal becomes

$$
\begin{aligned}
r\left(nT'\right) &= \sum_{k=-K/2}^{K/2} \mathrm{c}_{m,l,k} e^{j\frac{2\pi k}{\mathrm{T_U}}(1+\beta)nT} \\
&= \sum_{k=-K/2}^{K/2} \mathrm{c}_{m,l,k} e^{j\frac{2\pi k}{\mathrm{N}}n} e^{j\frac{2\pi k}{\mathrm{N}}\beta n}
\end{aligned} \tag{3.7}
$$

The effect of β is a function of subcarrier k, *i.e.*, creates ICI. The signal at the output of the FFT is

$$\begin{aligned} R_{m,l,k} &= \sum_{i=0}^{N-1} c_{m,l,i} \frac{1}{N} \sum_{n=0}^{N-1} e^{j\frac{2\pi n}{N}(i(1+\beta)-k)} \\ &= \sum_{i=0}^{N-1} c_{m,l,i} e^{j\pi\left(i(1+\beta)-k\right)\left(\frac{N-1}{N}\right)} \frac{\sin(\pi\left(i(1+\beta)-k\right))}{N\sin(\frac{\pi}{N}\left(i(1+\beta)-k\right))} \\ &= c_{m,l,k} e^{j\pi(k\beta)\left(\frac{N-1}{N}\right)} \frac{\sin(\pi k\beta)}{N\sin(\frac{\pi}{N}k\beta)} \\ &+ \sum_{\substack{i=0 \\ i\neq k}}^{N-1} c_{m,l,i} e^{-j\frac{\pi}{N}(i-k)} e^{j\pi i\beta\left(\frac{N-1}{N}\right)} \frac{\sin(\pi i\beta)}{N\sin(\frac{\pi}{N}\left(i(1+\beta)-k\right))} \qquad \text{(ICI)} \end{aligned} \tag{3.8}$$

We need to consider the phase shift that the sampling offset creates through time. For expression (3.8), we applied the FFT at time $n = 0$. We need to include the time delay that the difference in sampling frequencies produces. The time difference between the sampling periods is βT; therefore, the cumulative time delay at the beginning of an OFDM symbol is $\alpha\beta T$. β produces a double effect. One effect is similar to the frequency offset effect, and the other one is a result of the cumulative time shift expressed as an integer multiple, δ, of the sampling period. This time shift produces an error in the FFT window position. We now include the cumulative time delays as follows:

$$\begin{aligned} R_{m,l,k} &= \frac{1}{N} \sum_{n=0}^{N-1} \sum_{i=0}^{N-1} c_{m,l,i} e^{j\frac{2\pi ni}{N}(1+\beta)} e^{-j\frac{2\pi k}{N}(n-(\alpha+\delta)\beta)} \\ &= \sum_{i=0}^{N-1} c_{m,l,i} \frac{1}{N} \sum_{n=0}^{N-1} e^{j\frac{2\pi n}{N}(i(1+\beta)-k)} e^{j\frac{2\pi k(\alpha+\delta)\beta}{N}} \\ &= c_{m,l,k} e^{j\frac{\pi k\beta}{N}(2(\alpha+\delta)+N-1)} \frac{\sin(\pi k\beta)}{N\sin(\frac{\pi}{N}\beta k)} \\ &+ e^{j\frac{2\pi k(\alpha+\delta)\beta}{N}} \sum_{\substack{i=0 \\ i\neq k}}^{N-1} c_{m,l,i} e^{-j\frac{\pi}{N}(i-k)} e^{j\frac{\pi i\beta}{N}(N-1)} \frac{\sin(\pi i\beta)}{N\sin(\frac{\pi}{N}\left(i(1+\beta)-k\right))} \qquad \text{(ICI).} \end{aligned} \tag{3.9}$$

Once again, the first term corresponds to an amplitude distortion and phase rotation. The second term expresses the inter-carrier interference (ICI) produced.

3.1.3 Symbol Timing Offsets Analysis

Symbol timing for an OFDM signal is significantly different than for a single carrier signal since there is not an “eye opening” where a best starting time sample can be found. Rather there are hundreds or thousands of samples per OFDM symbol since the number of samples necessary is proportional to the number of subcarriers. Finding the symbol timing for OFDM means finding an estimate of where the symbol starts. OFDM also requires timing synchronization to preserve orthogonality. The receiver must obtain the timing information from the received OFDM signal, but the information obtained includes offsets, estimation errors, and jitter. OFDM is relatively more robust to these time effects than to the frequency ones produced by the inclusion of a cyclic prefix or guard band, but a trade-off between timing error sensibility and multipath tolerance is produced. We define timing offset as the propagation time from transmission to reception. We denote the time offset with a propagation delay $D = \iota + \varepsilon$ with ι an integer and ε a fraction, and we reference both to the transmitter system time $T = T_U / N$. We can show the overall effect of only the time offset D in the received baseband signal as follows:

$$\begin{aligned} r(t) &= s(t) * \delta(t - DT) \\ &= \sum_{k=-K/2}^{K/2} c_{m,l,k} e^{j\frac{2\pi k}{T_U}(t-DT)}. \end{aligned} \tag{3.10}$$

If we consider just the fractional delay ε, we have the output of the FFT as follows:

$$
\begin{aligned}
R_{m,l,k} &= \sum_{i=0}^{N-1} c_{m,l,i} \frac{1}{N} \sum_{n=0}^{N-1} e^{j\frac{2\pi ni}{N}} e^{-j\frac{2\pi k}{N}(n-\varepsilon)} \\
&= e^{j\frac{2\pi k\varepsilon}{N}} \sum_{i=0}^{N-1} c_{m,l,i} e^{j\frac{\pi}{N}(i-k)(N-1)} \frac{\sin\left(\pi\left(i-k\right)\right)}{N\sin\left(\frac{\pi}{N}\left(i-k\right)\right)} \\
&= e^{j\frac{2\pi k\varepsilon}{N}} c_{m,l,k}
\end{aligned}
\tag{3.11}
$$

An important issue is that the phase shift produced is different for each subcarrier since (3.11) is a function of k. The phase difference between the first and last subcarrier is $2\pi\varepsilon(N-1)/N$.

For the fixed time offset derivation, we assumed a perfect knowledge of ι. We now describe its effect. To start, we assume a non-dispersive Gaussian channel and no guard band. The received sampled signal during the time of a complete OFDM symbol is

$$
r_{m,l} = \left\{r_{m,l,\iota}, r_{m,l,\iota+1}, ..., r_{m,l,N-1}, r_{m,l+1,0}, r_{m,l+1,1}, ..., r_{m,l+1,\iota-1}\right\}. \tag{3.12}
$$

Performing the FFT on this vector yields

$$
R_{m,l,k} = \sum_{i=0}^{N-1} \left\{ \left(c_{m,l,i} \frac{1}{N} \sum_{n=\iota}^{N-1} e^{j\frac{2\pi ni}{N}} \cdot e^{-j\frac{2\pi k}{N}(n-\iota)} \right) + \left(c_{m,l+1,i} \frac{1}{N} \sum_{n=0}^{\iota-1} e^{j\frac{2\pi ni}{N}} \cdot e^{-j\frac{2\pi k}{N}(n+N-\iota)} \right) \right\} \tag{3.13}
$$

$$
\begin{aligned}
R_{m,l,k} &= e^{j\frac{2\pi k\iota}{N}} c_{m,l,k} \frac{N-\iota}{N} \\
&+ e^{j\frac{2\pi k\iota}{N}} \sum_{\substack{i=0; \\ i\neq k}}^{\text{N-1}} c_{m,l,i} e^{j\frac{\pi}{N}(i-k)(N-1+\iota)} \frac{\sin\left(\pi\left(i-k\right)\left(1-\frac{\iota}{N}\right)\right)}{N\sin\left(\frac{\pi}{N}\left(i-k\right)\right)} \qquad \text{(ICI)} \\
&+ e^{j\frac{2\pi k\iota}{N}} \sum_{i=0}^{N-1} c_{m,l+1,i} e^{j\frac{\pi}{N}(i-k)(\iota-1)} \frac{\sin\left(\frac{\pi}{N}\left(i-k\right)(\iota)\right)}{N\sin\left(\frac{\pi}{N}\left(i-k\right)\right)} \qquad \text{(ISI).}
\end{aligned}
\tag{3.14}
$$

The signal now consists of disturbances caused by ICI and inter-symbol interference (ISI) and a useful portion attenuated and rotated by a phasor whose phase is a function of subcarrier k and a fixed ι. If we include the cyclic prefix or guard band of length G where we copy the last G samples of the OFDM symbol to the beginning, the received sampled signal after the guard band extraction and during the time of a complete OFDM symbol now becomes

$$r_{m,l} = \left\{ r_{m,l,\iota}, r_{m,l,\iota+1}, \ldots, r_{m,l,N-1}, r_{m,l+1,0}, r_{m,l+1,(N-G)}, \ldots, r_{m,l+1,(N-G+\iota-1)} \right\}. \tag{3.15}$$

That is, we consider the samples after the cyclic prefix. Performing the FFT on this new vector yields

$$R_{m,l,k} = \sum_{i=0}^{N-1} \left\{ \left(c_{m,l,i} \frac{1}{N} \sum_{n=\iota}^{N-1} e^{j\frac{2\pi ni}{N}} \cdot e^{-j\frac{2\pi k}{N}(n-\iota)} \right) + \left(c_{m,l+1,i} \frac{1}{N} \sum_{n=0}^{\iota-1} e^{j\frac{2\pi ni}{N}} \cdot e^{-j\frac{2\pi k}{N}(n+G-\iota)} \right) \right\} \tag{3.16}$$

$$\begin{aligned} R_{m,l,k} &= e^{j\frac{2\pi k\iota}{N}} c_{m,l,k} \frac{N-\iota}{N} \\ &\quad + e^{j\frac{2\pi k\iota}{N}} \sum_{\substack{i=0; \\ i\neq k}}^{\text{N-1}} c_{m,l,i} e^{j\frac{\pi}{N}(i-k)(N-1-\iota)} \frac{\sin\left(\pi(i-k)\left(1-\frac{\iota}{N}\right)\right)}{N\sin\left(\frac{\pi}{N}(i-k)\right)} \qquad \text{(ICI)} \\ &\quad + e^{-j\frac{2\pi kG}{N}} e^{j\frac{2\pi k\iota}{N}} \sum_{i=0}^{N-1} c_{m,l+1,i} e^{j\frac{\pi}{N}(i-k)(\iota-1)} \frac{\sin\left(\frac{\pi}{N}(i-k)(\iota)\right)}{N\sin\left(\frac{\pi}{N}(i-k)\right)} \qquad \text{(ISI).} \end{aligned} \tag{3.17}$$

We now have an extra phase rotation in the ISI part of (3.17).

The guard band or cyclic prefix can help us to eliminate the ISI that the integer delay produces, but the price to pay is a reduction of multipath tolerance provided by the guard band, *i.e.*, there is a reduction in the guard band length. We can provide integer delay

protection if we start the guard band extraction at the last p samples of the guard band as the first samples of the OFDM symbol as follows:

$$r_{m,l} = \left\{ r_{m,l,N-p}, r_{m,l,N-p+1}, \ldots, r_{m,l,N-1}, r_{m,l,0}, r_{m,l,1}, \ldots, r_{m,l,(N-1-p)} \right\}. \tag{3.18}$$

We can clearly see that we are only using samples of the same OFDM symbol, hence, we are eliminating the ISI, but we are shortening the guard band length to $G - p$ samples. We have now protection against ISI up to $\iota = p$ since the input to the FFT is

$$r_{m,l} = \left\{ r_{m,l,N-p+\iota}, r_{m,l,N-p+\iota+1}, \ldots, r_{m,l,N-1}, r_{m,l,0}, r_{m,l,1}, \ldots, r_{m,l,(N-1-p+\iota)} \right\}, \tag{3.19}$$

and the output of the FFT becomes

$$\begin{aligned} R_{m,l,k} &= \sum_{i=0}^{N-1} c_{m,l,i} \frac{1}{N} \sum_{n=\iota}^{N-1} e^{j\frac{2\pi ni}{N}} \cdot e^{-j\frac{2\pi k}{N}(n+p-\iota)} \\ &= e^{-j\frac{2\pi k}{N}(p-\iota)} \sum_{i=0}^{N-1} c_{m,l,i} e^{j\frac{\pi}{N}(i-k)(N-1)} \frac{\sin\left(\pi\left(i-k\right)\right)}{N \sin\left(\frac{\pi}{N}\left(i-k\right)\right)} \\ &= e^{-j\frac{2\pi k}{N}(p-\iota)} c_{m,l,k} \end{aligned} \tag{3.20}$$

which is just a phase rotation as in (3.11).

3.1.4 Combined Effects of Synchronization Offsets

To summarize the previous sections, we have individually analyzed the offsets that result from the different oscillators involved in the transmission and reception of an OFDM signal. Until now, we have assumed a perfect channel and perfect transmission and reception amplifiers, *i.e.*, no PAR distortions. In this section, we shall present an analysis of the three previous offsets combined. We can start by deriving an analytical expression that includes the three offsets: frequency offset, sampling frequency offset, and synchronization offset. The received sampled signal becomes

$$r(n) = \left(\sum_{k=0}^{N-1} c_{m,l,i} e^{j\frac{2\pi kn}{N}(1+\beta)} \right) e^{j\frac{2\pi\Delta F}{N}(n+\alpha)} \quad \text{for} \quad 0 \le n \le (N-1). \tag{3.21}$$

For (3.21), we are referencing the sampling process to the receiver's clock. We have included the sampling clocks' difference for the IFFT window created at the receiver. We have also included the frequency offset as an external oscillator multiplying the base-band continuous-time received signal. This generator operates for all time; therefore, we must include the α term to account for it. This sampled signal, (3.21), is input to the FFT processor after the cyclic-prefix removal. Two errors can occur in the positioning of the FFT window. Not finding the exact starting point produces the time offset D, and the length difference between the IFFT window at the transmitter and the FFT window at the receiver produces an extra time offset $\alpha\beta$. If we include both errors, we have the following expression for the FFT process at the receiver:

$$R_{m,l,k} = \frac{1}{N} \sum_{n=0}^{N-1} \sum_{i=0}^{N-1} c_{m,l,i} e^{j\frac{2\pi ni}{N}(1+\beta)} e^{j\frac{2\pi\Delta F}{N}(n+\alpha)} e^{-j\frac{2\pi k}{N}(n-\alpha\Delta S-D)}. \tag{3.22}$$

Since the effect of the integer part, ι, of D covers contiguous IFFT windows, we just consider the fractional part, ε, for now. We now modify (3.22) as follows:

$$\begin{aligned} R_{m,l,k} &= \frac{1}{N} \sum_{n=0}^{N-1} \sum_{i=0}^{N-1} c_{m,l,i} e^{j\frac{2\pi ni}{N}(1+\beta)} e^{j\frac{2\pi\Delta F}{N}(n+\alpha)} e^{-j\frac{2\pi k}{N}(n-\alpha\beta-\varepsilon)} \\ &= e^{j\frac{2\pi\Delta F\alpha}{N}} e^{j\frac{2\pi k\alpha\beta}{N}} e^{j\frac{2\pi k\varepsilon}{N}} \sum_{i=0}^{N-1} c_{m,l,i} \frac{1}{N} \sum_{n=0}^{N-1} e^{j\frac{2\pi n}{N}(i(1+\beta)-k+\Delta F)} \\ &= e^{j\frac{2\pi\Delta F\alpha}{N}} e^{j\frac{2\pi k\alpha\beta}{N}} e^{j\frac{2\pi k\varepsilon}{N}} \sum_{i=0}^{N-1} c_{m,l,i} e^{j\frac{\pi}{N}(i(1+\beta)-k+\Delta F)(N-1)} \frac{\sin(\pi\left(i(1+\beta)-k+\Delta F\right))}{N\sin(\frac{\pi}{N}\left(i(1+\beta)-k+\Delta F\right))}. \end{aligned} \tag{3.23}$$

If we separate the ICI effect, we obtain the following:

$$R_{m,l,k} = e^{j\frac{2\pi\Delta F\alpha}{N}} e^{j\frac{2\pi k\alpha\beta}{N}} e^{j\frac{2\pi k\varepsilon}{N}} c_{m,l,k} e^{j\frac{\pi}{N}(k\beta+\Delta F)(N-1)} \frac{\sin(\pi(k\beta+\Delta F))}{\pi(k\beta+\Delta F)}$$
$$+ e^{j\frac{2\pi\Delta F\alpha}{N}} e^{j\frac{2\pi k\alpha\beta}{N}} e^{j\frac{2\pi k\varepsilon}{N}} \sum_{\substack{i=0,\\ i\neq k}}^{N-1} c_{m,l,i} e^{j\frac{\pi}{N}(i(1+\beta)-k+\Delta F)(N-1)} \frac{(-1)^{(i-k)}\sin(\pi(i\beta+\Delta F))}{N\sin(\frac{\pi}{N}(i(1+\beta)-k+\Delta F))} \quad \text{(ICI)}. \tag{3.24}$$

We can include the effect of the integer time offset to a signal with cyclic prefix to obtain a complete description of the synchronization offsets as follows:

$$R_{m,l,k} = e^{j\frac{2\pi\Delta F}{N}(\alpha+\delta+\iota)} e^{j\frac{2\pi k\beta}{N}(\alpha+\delta+\iota)} e^{j\frac{2\pi k\varepsilon}{N}} c_{m,l,k} e^{j2\pi k(1+\beta)\left(\frac{\delta+\iota}{N}\right)} e^{j\pi(k\beta+\Delta F)\left(\frac{N-1-\delta-\iota}{N}\right)} \frac{\sin\left(\pi(k\beta+\Delta F)\left(1-\frac{\delta+\iota}{N}\right)\right)}{N\sin\left(\frac{\pi}{N}(k\beta+\Delta F)\right)}$$
$$+ \underbrace{e^{j\frac{2\pi\Delta F}{N}(\alpha+\delta+\iota)} e^{j\frac{2\pi k\beta}{N}(\alpha+\delta+\iota)} e^{j\frac{2\pi k\varepsilon}{N}} \sum_{\substack{i=0;\\ i\neq k}}^{N-1} c_{m,l,i} e^{j2\pi i(1+\beta)\left(\frac{\delta+\iota}{N}\right)} \frac{e^{j\pi(i(1+\beta)-k+\Delta F)\left(\frac{N-1-\delta-\iota}{N}\right)} \sin\left(\pi(i(1+\beta)-k+\Delta F)\left(1-\frac{\delta+\iota}{N}\right)\right)}{N\sin\left(\frac{\pi}{N}(i(1+\beta)-k+\Delta F)\right)}}_{\text{ICI}} \tag{3.25}$$
$$+ \underbrace{e^{j\frac{2\pi\Delta F}{N}(\alpha+\delta+\iota)} e^{j\frac{2\pi k\beta}{N}(\alpha+\delta+\iota)} e^{j\frac{2\pi k\varepsilon}{N}} \sum_{i=0}^{N-1} c_{m,l+1,i} e^{j2\pi i(1+\beta)\left(\frac{\delta+\iota-G}{N}\right)} \frac{e^{j\pi(i(1+\beta)-k+\Delta F)\left(\frac{2N-\delta-\iota-1}{N}\right)} \sin\left(\frac{\pi\iota}{N}(i(1+\beta)-k+\Delta F)\right)}{N\sin\left(\frac{\pi}{N}(i(1+\beta)-k+\Delta F)\right)}}_{\text{ISI}}.$$

We can organize (3.25) as follows:

$$R_{m,l,k} = \underbrace{e^{j\Phi_{m,l,k}(\Delta F,\beta,\varepsilon,\alpha_{m,l},\delta,\iota,\theta)}}_{\text{General Rotation}} \left[c_{m,l,k} \underbrace{e^{j\Theta_{m,l,k}(\Delta F,\beta,\delta,\iota)}}_{\text{Symbol Rotation}} \underbrace{A_{m,l,k}(\Delta F,\beta,\delta,\iota)}_{\text{Amplitude Distortion}} + I_{ICI} + I_{ISI} \right]. \tag{3.26}$$

The harmful effects of rotation depend on the type of modulation. The amplitude distortion, ICI, and ISI degrade the signal-to-noise (SNR) ratio. We can obtain an expression for this SNR degradation by first analyzing the energy exchange for each received symbol per subcarrier as follows:

$$E_{ST}(k) = E_{SM}(k) + E_{SICI}(k) + E_{SISI}(k)$$
$$= \frac{E_S}{N^2} \frac{\sin^2\left(\pi(k\beta+\Delta F)\left(1-\frac{\delta+\iota}{N}\right)\right)}{\sin^2\left(\frac{\pi}{N}(k\beta+\Delta F)\right)} + \frac{E_S}{N^2} \sum_{\substack{i=0\\ i\neq k}}^{N-1} \frac{\sin^2\left(\pi(i(1+\beta)-k+\Delta F)\left(1-\frac{\delta+\iota}{N}\right)\right)}{\sin^2\left(\frac{\pi}{N}(i(1+\beta)-k+\Delta F)\right)} + \frac{E_S}{N^2} \sum_{i=0}^{N-1} \frac{\sin^2\left(\frac{\pi}{N}(i(1+\beta)-k+\Delta F)(\delta+\iota)\right)}{\sin^2\left(\frac{\pi}{N}(i(1+\beta)-k+\Delta F)\right)} \tag{3.27}$$

Energy that is lost by the amplitude distortion is spread or transformed into interference. The SNR of a subcarrier should be $SNR(k) = E_S(k)/N_O$, but since we lost energy in ICI and ISI, we should modify the SNR per carrier as follows:

$$\begin{aligned} SNR_M(k) &= \frac{E_{SM}(k)}{N_O + E_{SICI}(k) + E_{SISI}(k)} \\ &= \frac{E_S}{N_O} \frac{\frac{1}{N^2}\frac{\sin^2\left(\pi(k\beta+\Delta F)\left(1-\frac{\delta+\iota}{N}\right)\right)}{\sin^2\left(\frac{\pi}{N}(k\beta+\Delta F)\right)}}{1+\frac{E_S}{N_O N^2}\sum_{\substack{i=0\\ i\neq k}}^{N-1}\frac{\sin^2\left(\pi(i(1+\beta)-k+\Delta F)\left(1-\frac{\delta+\iota}{N}\right)\right)}{\sin^2\left(\frac{\pi}{N}(i(1+\beta)-k+\Delta F)\right)}+\frac{E_S}{N_O N^2}\sum_{\substack{i=0\\ i\neq k}}^{N-1}\frac{\sin^2\left(\frac{\pi}{N}(i(1+\beta)-k+\Delta F)(\delta+\iota)\right)}{\sin^2\left(\frac{\pi}{N}(i(1+\beta)-k+\Delta F)\right)}} \\ &= SNR(k)\frac{1}{D(k)} \end{aligned} \tag{3.28}$$

We define $D(k)$ as the degradation of the SNR produced by synchronization offsets. We can express the degradation in dB

$$\begin{aligned} D(k)_{dB} = 10\log&\left(1+\frac{E_S}{N_O N^2}\sum_{\substack{i=0\\ i\neq k}}^{N-1}\frac{\sin^2\left(\pi(i(1+\beta)-k+\Delta F)\left(1-\frac{\delta+\iota}{N}\right)\right)}{\sin^2\left(\frac{\pi}{N}(i(1+\beta)-k+\Delta F)\right)}+\frac{E_S}{N_O N^2}\sum_{\substack{i=0\\ i\neq k}}^{N-1}\frac{\sin^2\left(\frac{\pi}{N}(i(1+\beta)-k+\Delta F)(\delta+\iota)\right)}{\sin^2\left(\frac{\pi}{N}(i(1+\beta)-k+\Delta F)\right)}\right) \\ &-10\log\left(\frac{1}{N^2}\frac{\sin^2\left(\pi(k\beta+\Delta F)\left(1-\frac{\delta+\iota}{N}\right)\right)}{\sin^2\left(\frac{\pi}{N}(k\beta+\Delta F)\right)}\right) \end{aligned} \tag{3.29}$$

The expression for the SNR in dB becomes

$$SNR_M(k)_{dB} = 10\log\left(\frac{E_S}{N_O}\right) - D(k)_{dB} \quad [72] \tag{3.30}$$

3.2 OFDM Offsets Estimation and Compensation

As we have summarized in (3.29), synchronization will be one of the biggest challenges of any OFDM communication system. In Section 4.1.2.1, we will describe that even for precision laboratory grade instruments, we will have clock offsets. For example,

in our particular setup, we derive the up/down conversion oscillator frequency from the ADC clock, which we know has an offset compared to the transmitter clock that creates a sampling frequency offset; therefore, there is also frequency offset. In this case, which can easily be the case for many systems, we have no means of adjusting the clock frequency in real time; therefore, we propose an off-line algorithm to detect ΔF, ι, ε, and β to compensate via software.

As we described in Section 2.4, we can find a vast amount of information about OFDM synchronization in the literature. Out of this information, we can propose two categories for the detection algorithms: pre-FFT and post-FFT. In the former, the signal is the sampled baseband signal where we can use some form of correlation of the guard-band to detect ΔF and ι, and we have the frame separation signal to also detect ι. In the latter, we can use the symbol rotation information to detect ΔF, β and ε. Since our objective is a calibration procedure, our interest is in accuracy; therefore, we propose using a combination of DA and NDA maximum-likelihood (ML) techniques. Out of all the techniques in the literature, we have chosen the pre-FFT technique in [10], [70] to detect ΔF and ι. This is a NDA technique since it uses the guard-band or cyclic prefix interval. We now present a brief summary. The log-likelihood function is

$$\Lambda\left(\iota,\Delta F\right)=\left|\gamma\left(m\right)\right|-\rho\Phi\left(m\right) \tag{3.31}$$

where the correlation is

$$\gamma\left(m\right)=\sum_{k=m}^{m+N-1}r\left(k\right)r^{*}\left(k+N\right), \tag{3.32}$$

the energy is

$$\Phi(m) = \frac{1}{2}\sum_{k=m}^{m+N-1} \left|r(k)\right|^2 + \left|r(k+N)\right|^2, \tag{3.33}$$

and

$$\rho = \frac{SNR}{SNR+1}. \tag{3.34}$$

From this log-likelihood function, the estimates are

$$\begin{aligned} \hat{\imath}_{ML} &= \arg\min\left\{\Lambda\left(\Delta F, \imath\right)\right\} \\ \hat{\Delta F}_{ML} &= angle\left\{\gamma\left(\hat{\imath}_{ML}\right)\right\}. \end{aligned} \tag{3.35}$$

Since all the post-FFT techniques rely on the measurement of the rotation angle of the symbol at the output of the FFT, every parameter to detect adds a dimension to the ML function; therefore, we should try to detect and correct as many parameters as possible before the FFT. So far, we have detected two of the four parameters that appear in the symbol rotation. To detect the other two, we must compensate for the ones that we have found. First, we multiply the baseband signal as follows:

$$r'(n) = r(n)e^{-j\frac{2\pi\hat{\Delta F}}{N}(n+\alpha)}, \tag{3.36}$$

and then, we use $\hat{\imath}$ to correctly start the FFT window. We have reduced the synchronization distortion to:

$$\begin{aligned} R_{m,l,k} &= e^{j\frac{2\pi}{N}k\alpha\beta} e^{j\frac{2\pi}{N}k\varepsilon} c_{m,l,k} e^{j\pi k\beta\left(\frac{N-1}{N}\right)} \frac{\sin(\pi k\beta)}{\pi k\beta} \\ &\quad \underbrace{+ e^{j\frac{2\pi}{N}k\alpha\beta} e^{j\frac{2\pi}{N}k\varepsilon} \sum_{\substack{i=0,\\ i\neq k}}^{N-1} c_{m,l,i} \frac{e^{j\pi\left(i(1+\beta)-k\right)\left(\frac{N-1}{N}\right)}}{N} \frac{(-1)^{(i-k)}\sin(\pi i\beta)}{\sin\left(\frac{\pi}{N}\left(i(1+\beta)-k\right)\right)}}_{ICI} + W_{m,l,k}. \end{aligned} \tag{3.37}$$

We now present a post-FFT DA technique to detect the last two parameters. We suggest using a frame of L OFDM symbols for this purpose. The technique is a modification of [24], [41], [73], [76], [77]. The log-likelihood function given a set of parameters $\{c_{1,l,k}, \varepsilon, \beta\}$, with non-random offsets, for an AWGN channel is

$$\Lambda = \frac{2}{N_0} \int_{T_0} \Re\{r(t)s^*(t)\}dt \tag{3.38}$$

From (3.38), the ML estimates are

$$(\hat{\varepsilon}, \hat{\beta}) = \underset{(x,y)}{\arg\min} \left\{ \ln \left[p\left(R_{1,l,k} \middle| (\varepsilon = x, \beta = y), c_{1,l,k}\right)_{\substack{l=1,\mathrm{K},L \\ k=0,\mathrm{K},N-1}} \right] \right\} \tag{3.39}$$

(3.39) implies that we have to minimize the expression $\sum_{l=1}^{L} \left\| \mathbf{R}_{1,l} - \mathbf{T}_{1,l} \right\|^2$ where we define the components of the vector $\mathbf{T}_{1,l}$ as $T_{1,l,k} = c_{1,l,k} e^{-j\frac{2\pi}{N}k\left(x+\left(\alpha_{1,l}+\frac{N-1}{2}\right)y\right)}$. We expand the square norm to obtain

$$\sum_{l=1}^{L} \sum_{k=0}^{N-1} \left[\underbrace{\left|R_{1,l,k}\right|^2}_{\text{independent of } (x,y)} + \left|T_{1,l,k}\right|^2 - 2\Re\left(R_{1,l,k} c_{1,l,k}^* e^{-j\frac{2\pi}{N}k\left(x+\left(\alpha_{1,l}+\frac{N-1}{2}\right)y\right)} \right) \right]. \tag{3.40}$$

The ML estimates expression becomes

$$(\hat{\varepsilon}, \hat{\beta}) = \underset{(x,y)}{\arg\min} \left\{ -\sum_{l=1}^{L} \sum_{k=-K}^{K} \left[\Re\left(R_{1,l,k} c_{1,l,k}^* e^{-j\frac{2\pi}{N}k\left(x+\left(\alpha+\frac{N-1}{2}\right)y\right)} \right) \right] \right\} \tag{3.41}$$

from which we define a function to minimize as

$$F(x,y)=\sum_{l=1}^{L}\sum_{k=-K}^{K}\left[\Re\left(R_{1,l,k}c_{1,l,k}^{*}e^{-j\frac{2\pi}{N}k\left(x+\left(\alpha+\frac{N-1}{2}\right)y\right)}\right)\right]. \tag{3.42}$$

There are many computer programs available for this classical two-dimensional minimization problem, but we will present a differential procedure that transforms the problem into a one-dimensional case. We can start by using a simplified expression for (3.36) as follows:

$$R_{1,l,k}\cong c_{1,l,k}e^{jA}+(\mathrm{ICI})+(noise) \tag{3.43}$$

Now, let us multiply this symbol by the conjugate of the previous symbol as shown:

$$\begin{aligned}R_{1,l,k}R_{1,l-1,k}^{*}&\cong\left[c_{1,l,k}e^{jA}+(\mathrm{ICI}_1)+(noise_1)\right]\left[c_{1,l-1,k}^{*}e^{-jB}+(\mathrm{ICI}_2)+(noise_2)\right]\\&=c_{1,l,k}c_{1,l-1,k}^{*}e^{j(A-B)}+NOISE.\end{aligned} \tag{3.44}$$

If we look only at the exponent

$$\begin{aligned}A-B&=\frac{2\pi k}{N}\left(\varepsilon+\left(\alpha_{1,l}+\frac{N-1}{2}\right)\beta\right)-\frac{2\pi k}{N}\left(\varepsilon+\left(\alpha_{1,l-1}+\frac{N-1}{2}\right)\beta\right)\\&=\frac{2\pi k\beta}{N}\left(\alpha_{1,l}-\alpha_{1,l-1}\right),\end{aligned} \tag{3.45}$$

we can see that we have gotten rid of the time-offset term ε. We have now to estimate just one parameter. We define $Q_{m,l,k}=R_{m,l,k}R_{m,l-1,k}^{*}$, $S_{m,l,k}=c_{m,l,k}c_{m,l-1,k}^{*}$, and $Z_{m,l,k}=Q_{m,l,k}S_{m,l,k}^{*}$, and the ML expression becomes

$$F(y)=-\sum_{l=2}^{L}\sum_{k=-K}^{K}\Re\left(Z_{m,l,k}e^{-j\frac{2\pi ky}{N}\left(\alpha_{m,l}-\alpha_{m,l-1}\right)}\right) \tag{3.46}$$

(3.46) is not limited to any particular constellation. We now proceed to find an expression for the minimum argument of (3.46). If we differentiate, equate to zero, and use a first order Taylor series expansion approximation of the exponent, we obtain:

$$\hat{y} \approx \frac{\sum_{l=2}^{L}\sum_{k=-K}^{K} \frac{2\pi k}{N}\left(\alpha_{m,l}-\alpha_{m,l-1}\right)\Im\left(Z_{m,l,k}\right)}{\sum_{l=2}^{L}\sum_{k=-K}^{K}\left(\frac{2\pi k}{N}\left(\alpha_{m,l}-\alpha_{m,l-1}\right)\right)^{2}\Re\left(Z_{m,l,k}\right)} \tag{3.47}$$

As we can see in Figure 15 and Figure 16, this approximation is good enough for values of β below 100 ppm. A second order Taylor series approximation works for values close to 200 ppm, but we must solve the following second order equation

$$\begin{aligned}&\frac{\hat{y}^2}{2}\sum_{l=2}^{L}\sum_{k=-K}^{K}\left(\frac{2\pi k}{N}\left(\alpha_{m,l}-\alpha_{m,l-1}\right)\right)^{3}\Im\left(Z_{m,l,k}\right)\\&+\hat{y}\sum_{l=2}^{L}\sum_{k=-K}^{K}\left(\frac{2\pi k}{N}\left(\alpha_{m,l}-\alpha_{m,l-1}\right)\right)^{2}\Re\left(Z_{m,l,k}\right)-\sum_{l=2}^{L}\sum_{k=-K}^{K}\frac{2\pi k}{N}\left(\alpha_{m,l}-\alpha_{m,l-1}\right)\Im\left(Z_{m,l,k}\right)=0\end{aligned} \tag{3.48}$$

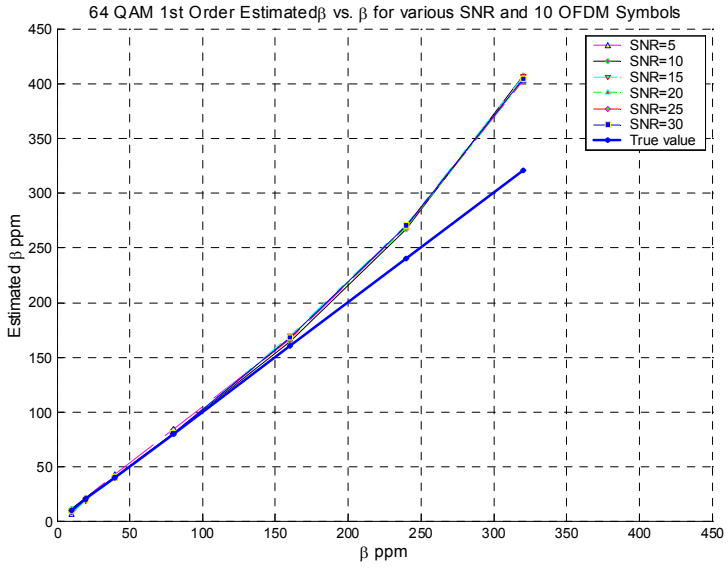

Figure 15: First order approximation behavior for L=10.

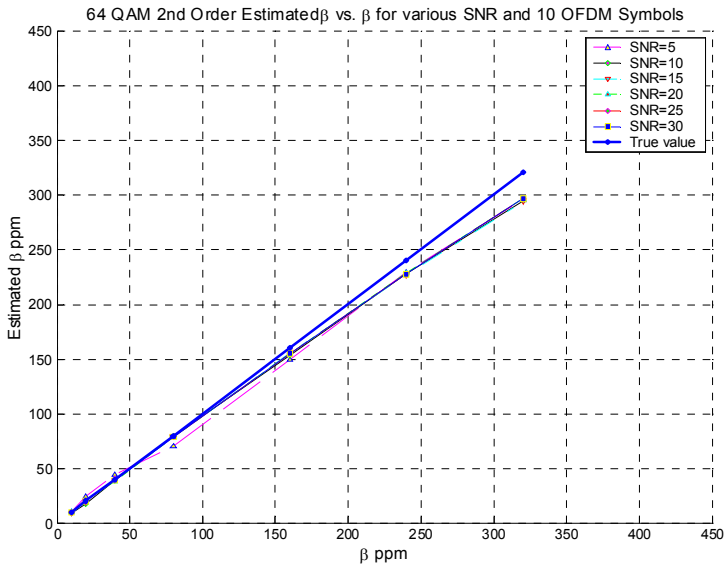

Figure 16: Second order approximation behavior for L=10.

Since the effects of sampling frequency offset affect the symbol rotation and create ICI, it is not that simple to compensate for it. The best solution is to adjust the sampling clock. This way we can compensate for both distortions. If we do not have access to the sampling clock, we can compensate the rotation by multiplying the baseband signal by $e^{-j\frac{2\pi\alpha_{m,l}\hat{\beta}}{N}}$, and to compensate for the ICI is quite complicated since the only way to eliminate it is to generate a modified Fourier matrix and multiply each OFDM symbol by it; therefore, we lose the advantages of the FFT. In [76] and [77], we can find a mid-way solution since the modified FFT reduces without eliminating the ICI, but we still have the advantages of an FFT.

Finally, we detect the time offset ε. We follow the same procedure, and we have the last function to minimize as follows:

$$F(x) = \sum_{l=1}^{L} \sum_{k=-K}^{K} \left[\Re \left(R_{m,l,k} c^*_{m,l,k} e^{-j\frac{2\pi}{N}kx} \right) \right]. \tag{3.49}$$

Once again, we can obtain approximations using Taylor series expansions. A first order approximation is

$$\hat{x} \approx \frac{\sum_{l=1}^{L} \sum_{k=-K}^{K} \frac{2\pi k}{N} \Im \left(R_{m,l,k} c^*_{m,l,k} \right)}{\sum_{l=1}^{L} \sum_{k=-K}^{K} \left(\frac{2\pi k}{N} \right)^2 \Re \left(R_{m,l,k} c^*_{m,l,k} \right)} \tag{3.50}$$

We performed a series of experiments by using different types of communication links: IF wired, RF wired, and RF wireless (static); and with induced offsets and free running uncontrolled offsets. We used 64-QAM data symbols, N=256-FFT, G=64, and L=16. We summarize the results of nine different experiments and close to 70 frames per experiment in Figure 17. In this figure, we present the empirical cumulative distribution functions (CDF) of the errors in the synchronization offsets remaining after compensation for all of the frames of all of the experiments. The small values of the errors indicate the effectiveness of our synchronization technique.

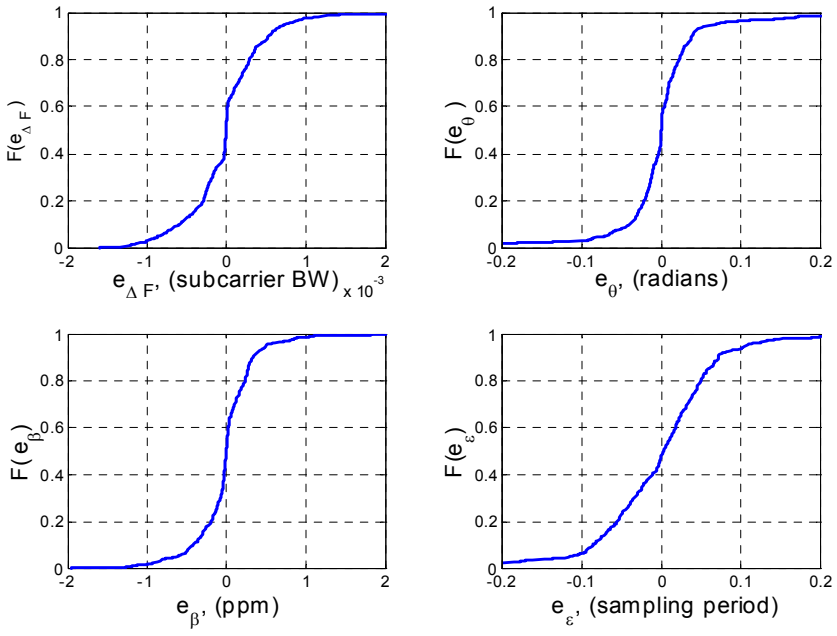

Figure 17: Normalized empirical cumulative distribution functions (CDF) for the measurement error of the four synchronization offsets. Each CDF represents approximately 600 data points.

CHAPTER 4

CHANNEL MEASUREMENT SYSTEMS

The complete channel measurement campaign was performed at two different frequency bands: 2.4 and 5.9 GHz. In each of this chapter's sections, we will describe the channel sounding system developed for a particular frequency band. We will indicate the system's specifications and limitations. We will also include a description and analysis of the sounding waveform. We developed both systems by integrating available general purpose equipment. As with any new system design, ours had some mistakes and errors; therefore, we present an analysis of their effects, and how we managed to overcome them.

4.1 2.4 GHz Channel Sounding System Development

In this section, we present a detailed description of the design and performance of our channel sounding system developed for the 2.4 GHz frequency band. For this purpose, we also present a detailed analysis of the sounding waveform.

As shown on the right in Figure 18, an Agilent™ ESG E4438C RF signal generator was used to create the MLS waveform of 511 chips, with the chip period of 50 ns, and a 3 dB bandwidth of approximately 20 MHz, centered at 2.445 GHz. The 511-chip burst was repeated back-to-back, corresponding to a repetition period of 25.5 μs, which further corresponds to a maximum unambiguous excess path length of 7.65 km and a maximum unambiguous Doppler shift of ±19.5 kHz. Following amplification and transmission from a 8 dBi omnidirectional antenna mounted on the middle of the roof of a compact

car, the signal power was 2.1 W (ERP), which enabled measurements over ranges of up to 300m.

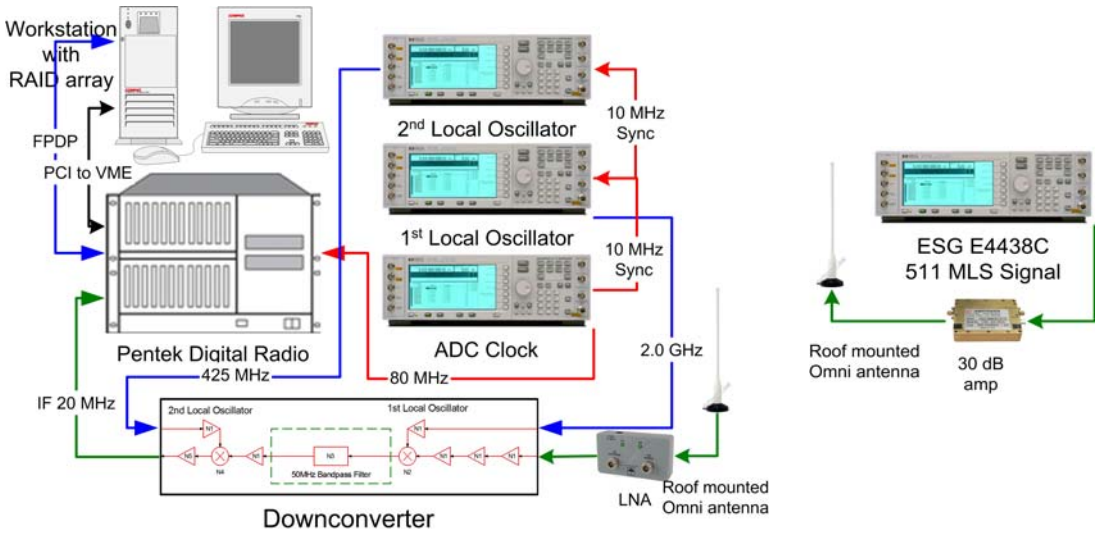

Figure 18: Receiver system in van to the left and transmitter system in compact car to the right.

The receiver front end, shown on the left in Figure 18, consisted of another 8 dBi omnidirectional antenna, mounted on the middle of the roof of a van, followed by a HyperAmp™ HA2401DX-AGC100 and a custom down-conversion to a first IF of 445 MHz, and then to a second IF of 20 MHz. The first IF filter 3 dB bandwidth was approximately 46 MHz. The backend of the receiver begins with the A-to-D converter in the Pentek™ 6235, sampling with 12 bits at 80 MHz. The samples are fed to the Digital Downconverter also in the Pentek™ 6235, which included a 10 MHz output lowpass filter. The complex baseband samples were transferred via an FPDP link at a rate of 20 Msamples/s, and recorded directly into a hard disk array at 80 MBytes/s.

4.1.1 Sounding Waveform Analysis and Processing

In this next section, we analyze all parts of our channel sounding system. This is necessary to validate our design and to perform trouble shooting. First, we focus on just

the transmitter and the receiver up to the IF output. Later, we continue with the analysis of the sampling process and signal processing.

In the first part of the section, we present a complete analysis of the spectrum of our sounding waveform. This analysis will enable us to detect irregularities or problems in the system in real time using a spectrum analyzer. We analyze the spectrum three ways: theoretically, through simulation and through measurement in a hardware implementation. The theoretical treatment derives the autocorrelation function of our probe waveform, and the transform of this to get the PSD of the waveform. We next compare the theoretical PSD with that obtained from a SIMULINK™ simulation of the transmitter. Finally, we obtain measurements of the PSD at several points in the hardware implementation of the transmitter and receiver, for example one is from the RF output of the transmitter and another is from the IF output of the receiver. We show that all of these PSDs agree.

In the last part, we address the nonlinearities of the power amplifier and the receiver low noise amplifier. It confirms that at the power levels of measurement, there should be no intermodulation distortion in the recorded signal.

Since we are working with wideband signals modulated at 2.445 GHz, a spectrum analyzer is the only available measurement equipment for passband signals; therefore, we need a thorough understanding of the spectrum of our sounding waveform since this way we will know the expected spectrum shape beforehand. This understanding will also allow us to detect irregularities or problems in the system. In addition, we make extensive use of simulations; therefore, we require a close link among theory, simulation, and measurements. Finally, we need an analytical description of the processing performed by the Pentek™ digital radio.

4.1.1.1 Autocorrelation

To obtain the power spectral density (PSD) of the sounding signal, we need to obtain the autocorrelation. This section describes in detail the autocorrelation of the 511 MLS used. The analysis is as follows: The ideal intermediate frequency (IF) signal is given by

$$\begin{aligned} s(t) &= \Re\left[\sum_{k=-\infty}^{\infty} g\left(t-kT_c\right)e^{j\pi\bar{d}_{k \bmod 511}}e^{j2\pi f_l t}\right] \\ &= \sum_{k=-\infty}^{\infty} g\left(t-kT_c\right)\cos\left(2\pi f_l t+\pi\bar{d}_{k \bmod 511}\right) \end{aligned} \tag{4.1}$$

where

$$g(t) = U(t) - U(t-T_c) \tag{4.2}$$

and $d_{k \bmod 511}$ represents the binary pseudo-random (PN) sequence vector, $U(t)$ the unit step function, f_l the IF carrier, and T_c the chip period. We can obtain the baseband or complex envelope signal from (4.1) as follows:

$$\begin{aligned} x(t) &= \sum_{k=-\infty}^{\infty} g\left(t-kT_c\right)e^{j\pi\bar{d}_{k \bmod 511}} \\ &= \sum_{k=-\infty}^{\infty} g\left(t-kT_c\right)\cos\left(\pi\bar{d}_{k \bmod 511}\right) \end{aligned} \tag{4.3}$$

with autocorrelation function

$$R_{xx}\left(\tau\right) = \frac{1}{T}\int_0^T x\left(t\right)x^*\left(t+\tau\right)dt \tag{4.4}$$

since we are using a full period of the spreading sequence $T = NT_c$ where $N = 511$ is the length of the sequence. Since the delay τ can assume any value, we can define [82] $\tau = lT_c + \delta$ where $l = \lfloor \tau / T_c \rfloor$ is an integer and $0 \le \delta \le T_c$ to obtain

$$\begin{aligned} R_{xx}(\tau) &= \frac{1}{NT_c}\int_0^{NT_c} x(t)x^*(t + lT_c + \delta)dt \\ &= \frac{1}{NT_c}\int_0^{NT_c} \sum_{k=-\infty}^{\infty} g(t - kT_c)e^{j\pi\bar{d}_{k \bmod 511}} \sum_{j=-\infty}^{\infty} g(t + lT_c + \delta - jT_c)e^{-j\pi\bar{d}_{j \bmod 511}}dt \\ &= \frac{1}{N}\sum_{k=-\infty}^{\infty}\sum_{j=-\infty}^{\infty} e^{j\pi\bar{d}_{k \bmod 511}}e^{-j\pi\bar{d}_{j \bmod 511}} \frac{1}{T_c}\int_0^{NT_c} g(t - kT_c)g(t + (l-j)T_c + \delta)dt \end{aligned} \quad (4.5)$$

Let us analyze the integrand in (4.5). In Figure 1 and for any time k, we sketch two possible overlapping regions for which the integrand is not zero. Both regions are referenced to the sum in k. These regions can only occur for one chip period from kT_c to $(k+1)T_c$. From these two regions, we obtain the integrand region as follows:

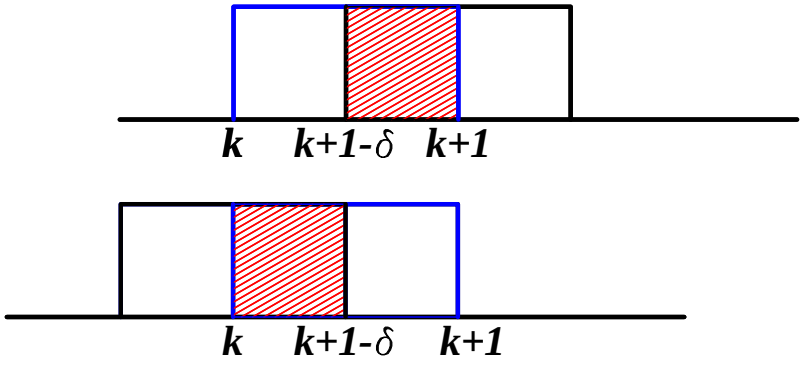

Figure 19: Possible overlapping regions.

$$\begin{aligned} \frac{1}{T_c}\int_{kT_c}^{(k+1)T_c} g(t - kT_c)g(t + (l-j)T_c + \delta)dt &= \frac{1}{T_c}\int_{kT_c}^{(k+1)T_c-\delta} g(t - kT_c)g(t - (kT_c - \delta))dt \\ &+ \frac{1}{T_c}\int_{(k+1)T_c-\delta}^{(k+1)T_c} g(t - kT_c)g(t - ((k+1)T_c - \delta))dt \end{aligned} \quad (4.6)$$

The first region indicates

$$\begin{aligned}&(l-j)T_c+\delta=-(kT_c-\delta)\\&\Rightarrow j=k+l\end{aligned}\tag{4.7}$$

and the second region indicates

$$\begin{aligned}&(l-j)T_c+\delta=-((k+1)T_c-\delta)\\&\Rightarrow j=k+l+1\end{aligned}\tag{4.8}$$

(4.5) now becomes

$$\begin{aligned}R_{xx}(\tau)=&\frac{1}{N}\sum_{k=-\infty}^{\infty}\sum_{j=-\infty}^{\infty}e^{j\pi\bar{d}_{k\bmod 511}}e^{-j\pi\bar{d}_{(k+l)\bmod 511}}\frac{1}{T_c}\int_{kT_c}^{(k+1)T_c-\delta}g(t-kT_c)\,g(t-(kT_c-\delta))dt\\&+\frac{1}{N}\sum_{k=-\infty}^{\infty}\sum_{j=-\infty}^{\infty}e^{j\pi\bar{d}_{k\bmod 511}}e^{-j\pi\bar{d}_{(k+l+1)\bmod 511}}\frac{1}{T_c}\int_{(k+1)T_c-\delta}^{(k+1)T_c}g(t-kT_c)\,g(t-((k+1)T_c-\delta))dt\end{aligned}\tag{4.9}$$

for which there is not a dependency in j anymore, $0\le k\le N-1$, and defining $t'=t-kT_c$; therefore, we can simplify to

$$\begin{aligned}R_{xx}(\tau)=&\frac{1}{N}\sum_{k=0}^{N-1}e^{j\pi\bar{d}_{k\bmod 511}}e^{-j\pi\bar{d}_{(k+l)\bmod 511}}\frac{1}{T_c}\int_{0}^{T_c-\delta}g(t')\,g(t'+\delta)dt'\\&+\frac{1}{N}\sum_{k=0}^{N-1}e^{j\pi\bar{d}_{k\bmod 511}}e^{-j\pi\bar{d}_{(k+l+1)\bmod 511}}\frac{1}{T_c}\int_{T_c-\delta}^{T_c}g(t')\,g(t'-T_c+\delta)dt'\end{aligned}\tag{4.10}$$

Substituting for $g(t)$

$$\begin{aligned}R_{xx}(\tau)&=\frac{1}{N}\sum_{k=0}^{N-1}e^{j\pi\bar{d}_{k\bmod 511}}e^{-j\pi\bar{d}_{(k+l)\bmod 511}}\left(1-\frac{\delta}{T_c}\right)+\frac{1}{N}\sum_{k=0}^{N-1}e^{j\pi\bar{d}_{k\bmod 511}}e^{-j\pi\bar{d}_{(k+l+1)\bmod 511}}\\&=\phi_{xx}(l)\left(1-\frac{\delta}{T_c}\right)+\phi_{xx}(l+1)\frac{\delta}{T_c}\end{aligned}\tag{4.11}$$

where

$$\phi_{xx}(n) = \frac{1}{N}\sum_{k=0}^{N-1} e^{j\pi \bar{d}_{k \bmod 511}} e^{-j\pi \bar{d}_{(k+n) \bmod 511}} \tag{4.12}$$

We present the behavior of (4.11) in Figure 20. Notice the periodic behavior with period equal to the length of the PN sequence.

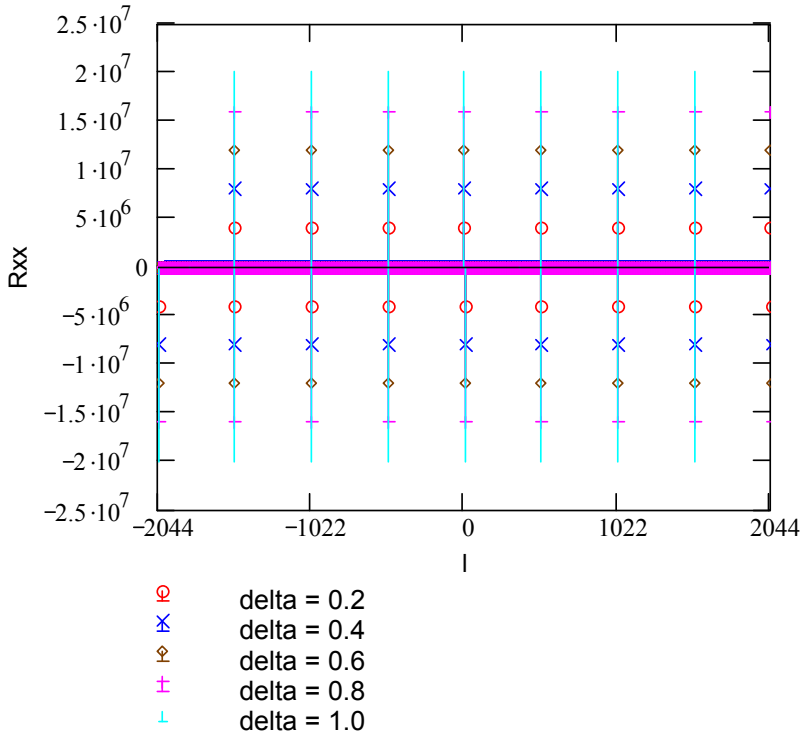

Figure 20: Simulation of (4.11) for different values of δ and $T_c = 50$ ns.

4.1.1.2 Spectral Estimation

In this section, we present the analytical expression for the PSD of the sounding waveform. We compare this expression with the simulated spectra, the generated spectra, and the recorded spectra. This comparison will allow us to evaluate the system's performance.

We can use (4.12) to obtain the power spectrum of $s(t)$. For a linearly modulated signal [66], we can express the base-band power spectrum by

$$S_{xx}(f) = \frac{1}{T_c}\left|G(f)\right|^2 \left|X(f)\right|^2 \tag{4.13}$$

where for a rectangular pulse the square of its Fourier transform is

$$\left|G(f)\right|^2 = T_c^2 \left(\frac{\sin(\pi f T_c)}{\pi f T_c}\right)^2 \tag{4.14}$$

and

$$\left|X(f)\right|^2 = \phi_{xx}(0) + 2\sum_{k=1}^{N-1} \phi_{xx}(k)\cos(2\pi f k T_c) \tag{4.15}$$

We present a direct Mathcad™ plot of (4.13) in Figure 21. We can notice the overall spectrum of the rectangular pulse function with the periodic behavior of the complex envelope spectrum. To visualize the periodic complex envelope part, we present a magnified view of the direct Mathcad™ plot in Figure 22. We can see a periodic behavior, but not quite the frequency of the MLS sequence period, which is ±19.57 kHz.

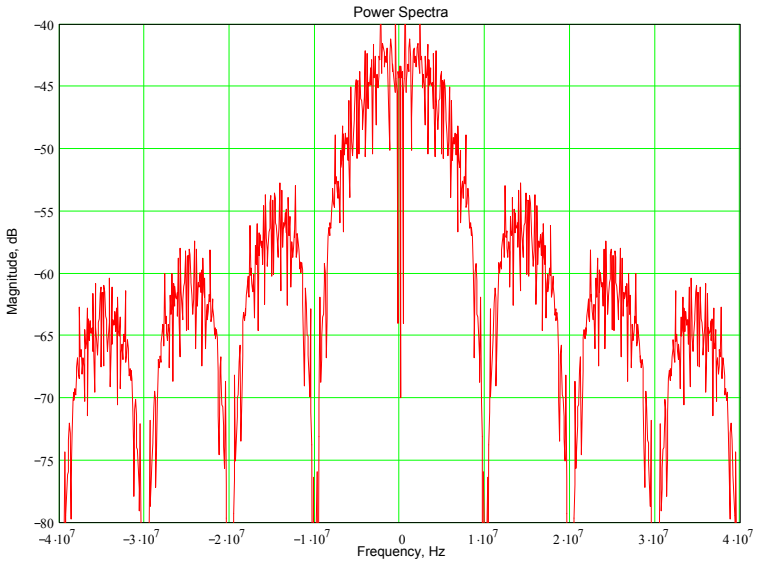

Figure 21: Direct plot of (4.13) for $T_c = 100$ ns .

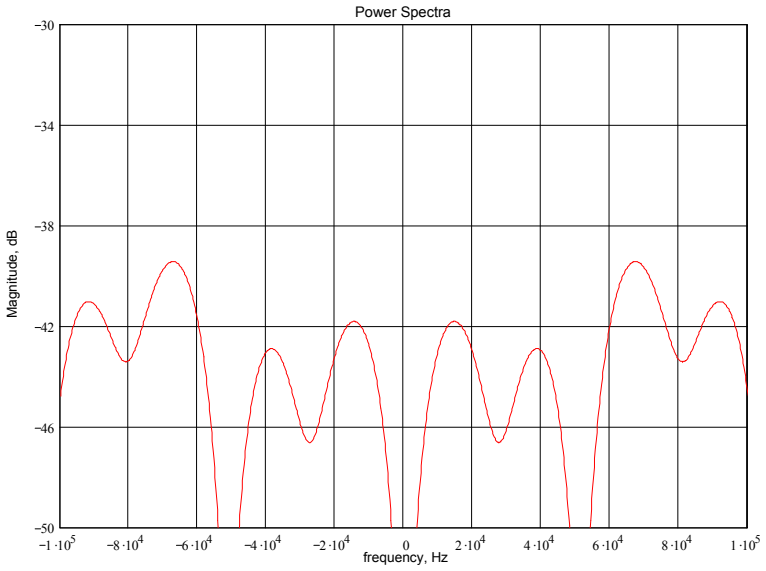

Figure 22: Detailed view of the center peak of direct plot of (4.13).

We proceed to present the results of the Simulink™ simulation shown in Figure 23. In Figure 24, we start with non-averaged (or snapshot) response of the Spectrum Scope3 (the system does not allow editing; therefore, we apologize for the small font). We can see a great resemblance to the direct plot of Figure 21. To obtain a detailed

view of the center lobe, we processed the SPEC signal in Matlab™ using the Pwelch command. To obtain Figure 25, we adjusted the Pwelch command parameters to perform as similar to the Spectrum Scope parameters as possible. We can see that we obtained a very similar response to that of Figure 22. For Figure 26, we set the average option of the Spectrum Scope to 20. As we would expect because of the pseudo-random characteristic of the MLS sequence, the response resembles that of a rectangular pulse. This time, we used the same parameters in the Pwelch command that we have been using for the project's spectra's results to process the SPEC signal. These parameters are "pwelch(SPEC,[],[], 1024*128,1/(511*50e-9),'twosided')" (in Matlab™ syntax) The result is Figure 27 where we now can clearly identify the ±19.57 kHz sequence period.

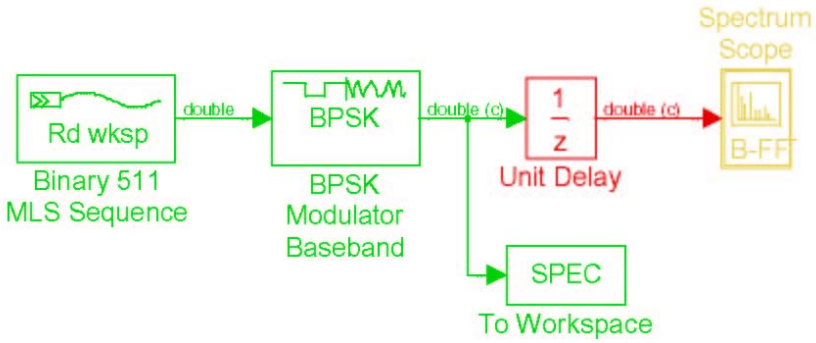

Figure 23: 511-MLS waveform simulation.

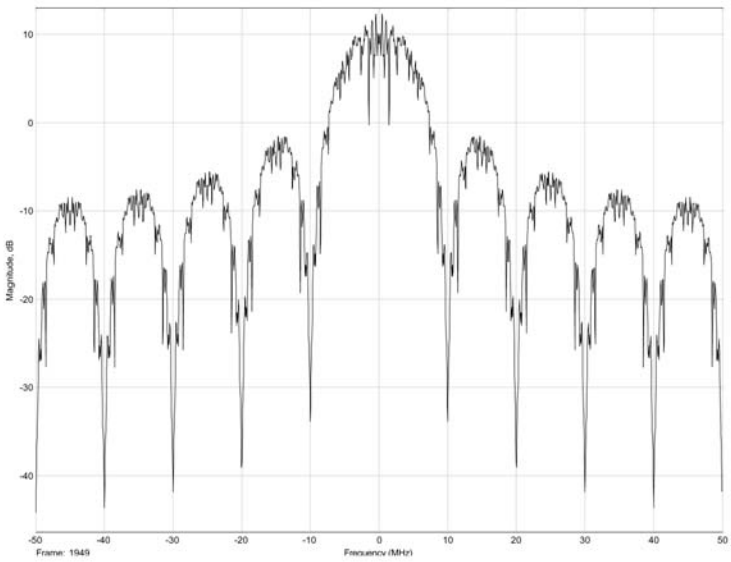

Figure 24: Non-averaged Power Spectrum estimation of simulated waveform for $T_c = 100$ ns .

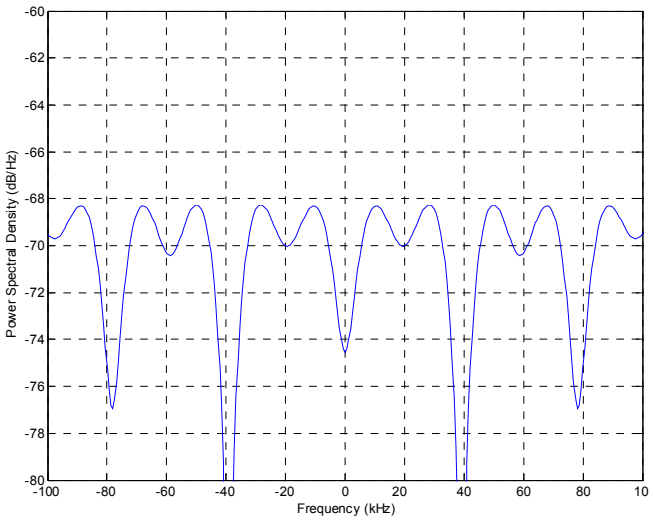

Figure 25: Detailed view of the center peak of Figure 24.

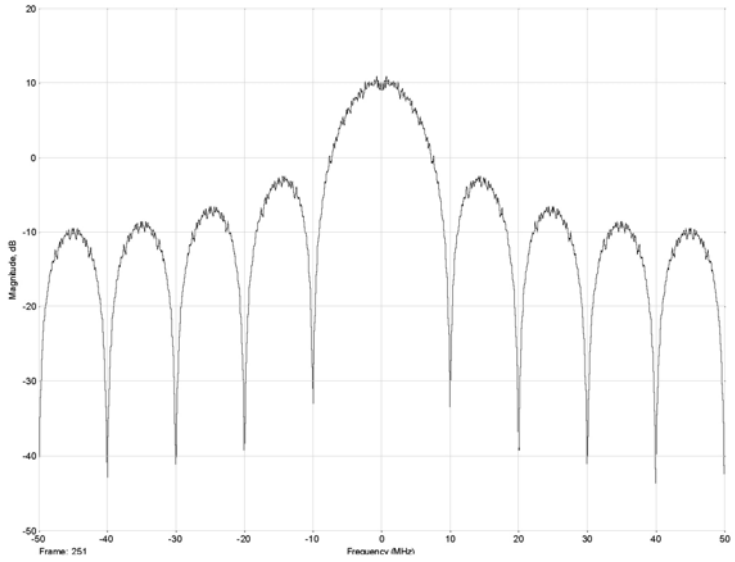

Figure 26: Averaged (20 periodogram) Power Spectrum estimation of simulated waveform for $T_c = 100$ ns .

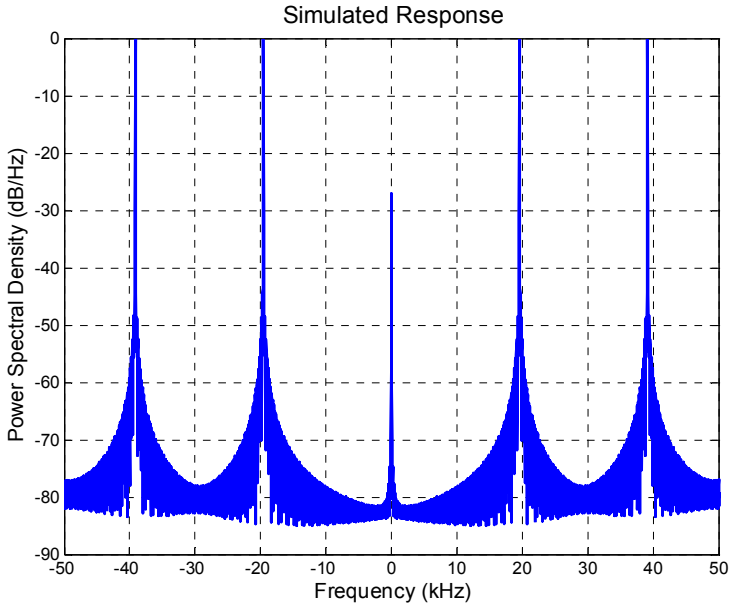

Figure 27: Detailed view of the center peak of Figure 26.

In Figure 28, we have a picture of the power spectra measured with a spectrum analyzer. There is a trade-off between the sweeping rate and the resolution and video bandwidths; therefore, it is hard to detect the periodic behavior of the complex envelope

with the span required to display the overall spectra of the shaping function. We set the spectrum analyzer span to 100 kHz, and we can clearly identify the complex envelope period as shown in Figure 29 for which we used the video average function (100 sweeps). We can see that the measured waveforms resemble the simulated waveforms of Figure 26 and Figure 27.

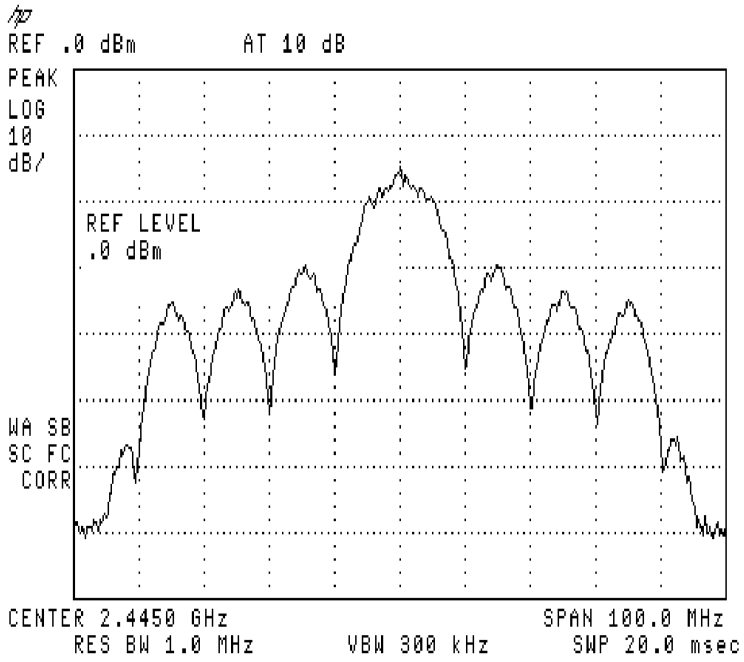

Figure 28: Measured Power Spectrum for $T_c = 100$ ns .

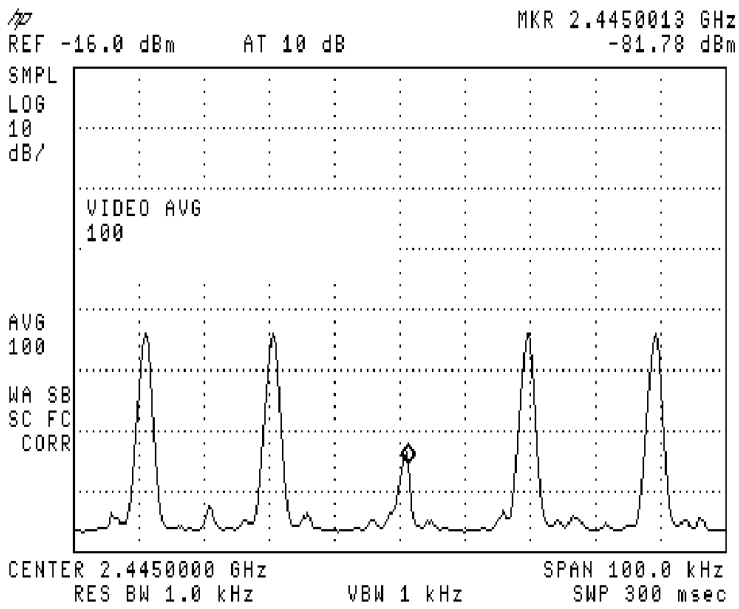

Figure 29: Measured detailed view .

Finally, we present the results for a set of recorded data. These data correspond to a signal fed through the TAS 4500 channel emulator set for bypass or LOS response. We first obtain the overall spectrum shape using the system shown in Figure 30. We followed the same procedure used with the simulated waveform to obtain Figure 31 for a snapshot and Figure 32 for an average response. Lastly, we obtained Figure 33 using the Pwelch command with the project's parameters previously described.

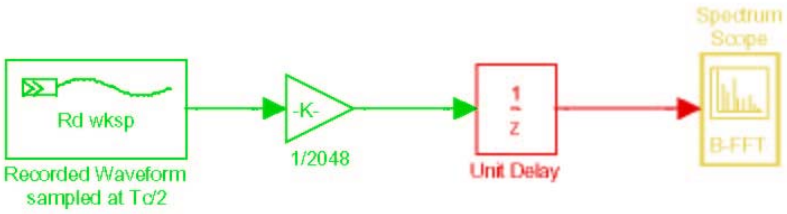

Figure 30: Recorded signal processing.

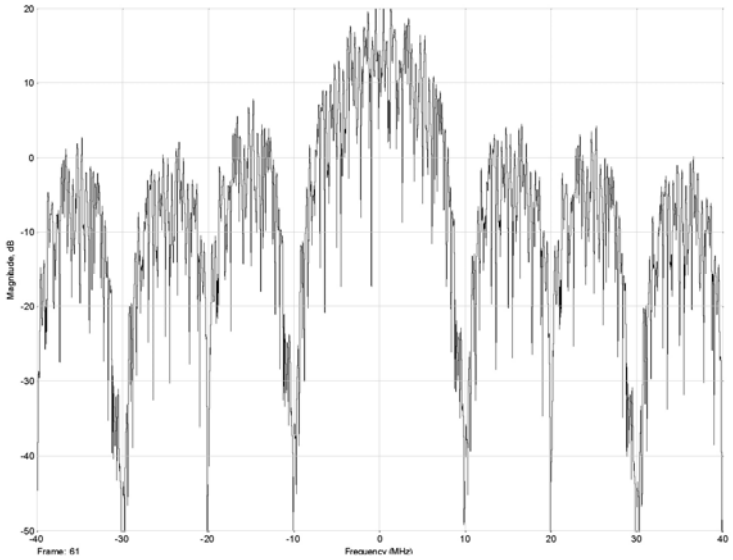

Figure 31: Non-averaged Power Spectrum estimation of the recorded response at the output of the channel emulator with just LOS.

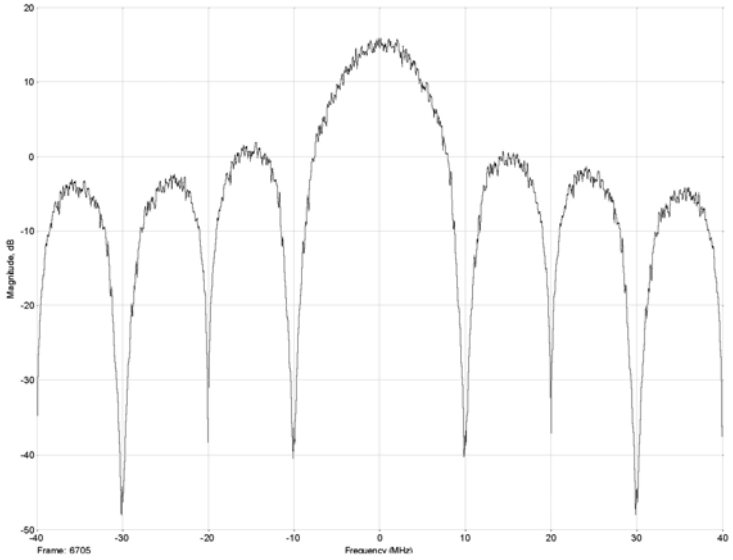

Figure 32: Averaged Power Spectrum estimation of the recorded response at the output of the channel emulator with just LOS.

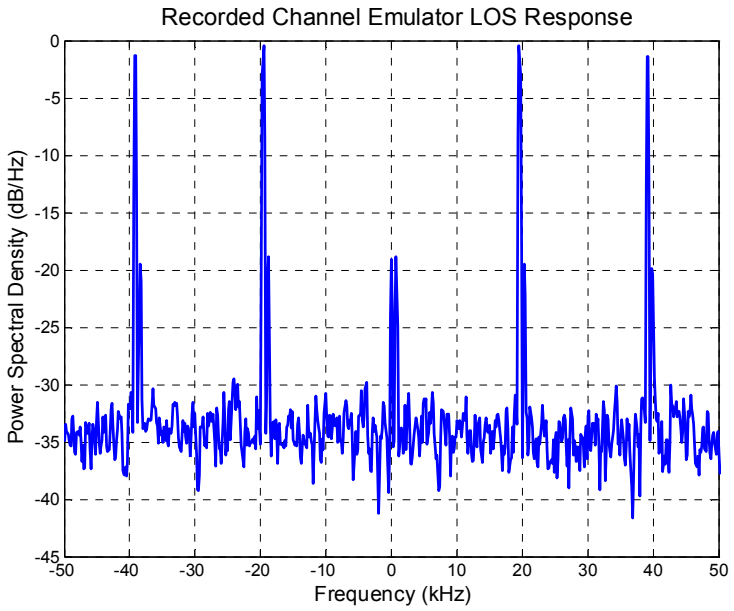

Figure 33: Detailed view of the center peak of Figure 32.

From Figure 27, Figure 29, and Figure 33, we can conclude that we have a tight relation from simulation, implementation, and measurement. In particular, the last two figures tell us that the system records what is input.

4.1.1.3 Sampling Process

This final section describes the internal processing of the digital radio receiver and the off-line processing of the recorded samples. We also describe the timing parameters. We begin by sampling the received signal $s(t)$ at a frequency $f_s = \frac{1}{T_s}$ as follows:

$$s(nT_s) = \Re\left[\sum_{k=-\infty}^{\infty} g\left(nT_s - kT_c\right) e^{j\pi \bar{d}_{k \bmod 511}} e^{j2\pi f_l n T_s}\right] \tag{4.16}$$

Using the identity

$$\Re[\xi] = \frac{1}{2}\left(\xi + \xi^*\right) \tag{4.17}$$

we represent the sampled signal as

$$s(nT_s) = \frac{1}{2}\sum_{k=-\infty}^{\infty} g\left(nT_s - kT_c\right)\left(e^{j\left(2\pi f_l nT_s + \pi \bar{d}_{k \bmod 511}\right)} + e^{-j\left(2\pi f_l nT_s + \pi \bar{d}_{k \bmod 511}\right)}\right) \tag{4.18}$$

We now proceed to down-convert to base-band

$$\begin{aligned} r\left(nT_s\right) &= s\left(nT_s\right)e^{-j2\pi f_l nT_s} \\ &= \frac{1}{2}\sum_{k=-\infty}^{\infty} g\left(nT_s - kT_c\right)\left(e^{j\pi \bar{d}_{k \bmod 511}} + e^{-j\left(4\pi f_l nT_s + \pi \bar{d}_{k \bmod 511}\right)}\right). \end{aligned} \tag{4.19}$$

The digital down-converter system in the Pentek digital radio receiver provides a low-pass filter with a response close to 90 percent of half the Nyquist rate after decimation. For example, a $f_s = 80\,\text{MHz}$ corresponds to an 8x over-sampling for a $T_c = 100\,\text{ns}$ or $T_s = \frac{T_c}{8}$. If we band-limit the signal to its first 10 MHz null, we can decimate by four to obtain a Nyquist frequency of $f_N = \frac{2}{T_c}$ giving two samples per baud. The corresponding filter for these specifications is shown in Figure 34.

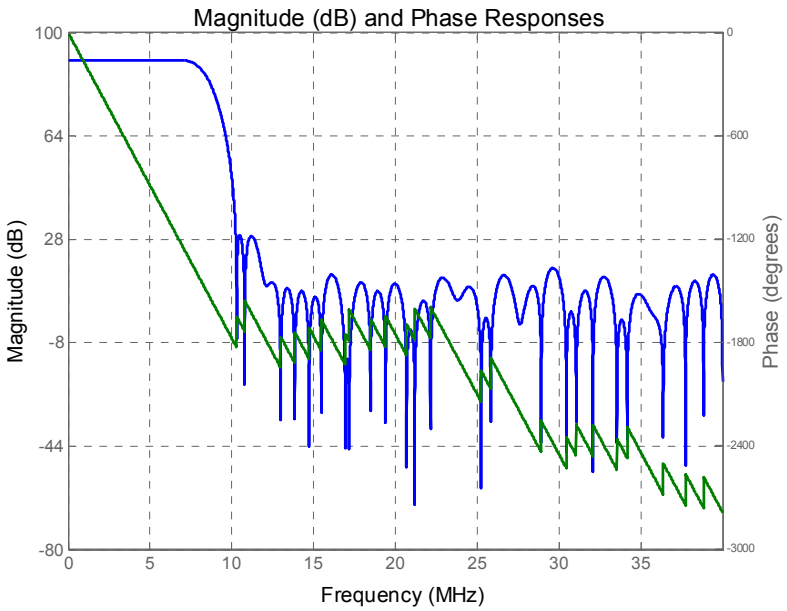

Figure 34: Digital down-converter lowpass filter response for a decimation of four.

Assuming an ideal low-pass filter response, we can describe the sampled base-band signal as follows:

$$y\left(n\frac{T_c}{8}\right)=\frac{1}{2}\sum_{k=-\infty}^{\infty}g\left(\left(\frac{n}{8}-k\right)T_c\right)e^{j\pi\bar{d}_{k\bmod 511}}. \tag{4.20}$$

Finally, we decimate by four $n=4m$ to obtain

$$\begin{aligned} y\left(n\frac{T_c}{8}\right) &= y\left(m\frac{T_c}{2}\right) \\ &= \frac{1}{2}\sum_{k=-\infty}^{\infty}g\left((m-2k)\frac{T_c}{2}\right)e^{j\pi\bar{d}_{k\bmod 511}} \\ &= y[m]. \end{aligned} \tag{4.21}$$

Since we are using the straightforward method described in the above equations, we must account for the possible distortions during the reception process. We can start with the carrier phase offset

$$s(t) = \Re\left[\sum_{k=-\infty}^{\infty} g\left(t - kT_c\right) e^{j\pi \bar{d}_{k \bmod 511}} e^{j2\pi f_l t} e^{j\theta} \right], \tag{4.22}$$

which produces a constellation rotation

$$y[m] = \frac{1}{2} \sum_{k=-\infty}^{\infty} g\left(\left(m - 2k\right) \frac{T_c}{2} \right) e^{j\pi \bar{d}_{k \bmod 511}} e^{j\theta}. \tag{4.23}$$

We are mostly concerned with carrier frequency offset produced by the Doppler characteristics of the channel. We can represent this carrier frequency offset as $f_D(t)$ and ignoring any other distortions, we have a received signal

$$\begin{aligned} s(t) &= \Re\left[\sum_{k=-\infty}^{\infty} g\left(t - kT_c\right) e^{j\pi \bar{d}_{k \bmod 511}} e^{j2\pi f_l t} e^{j2\pi f_D(t) t} \right] \\ &= \sum_{k=-\infty}^{\infty} g\left(t - kT_c\right) \cos\left(2\pi \left(f_l + f_D\left(t\right) \right) t + \pi \bar{d}_{k \bmod 511} \right), \end{aligned} \tag{4.24}$$

which produces a time dependant constellation rotation

$$y[m] = \frac{1}{2} \sum_{k=-\infty}^{\infty} g\left(\left(m - 2k\right) \frac{T_c}{2} \right) e^{j\pi \bar{d}_{k \bmod 511}} e^{j2\pi f_D\left(m\frac{T_c}{2} \right)}. \tag{4.25}$$

The next step in the processing, which is done off-line in Matlab™, is the periodic correlation. The operation is

$$z\left[k\right] = \sum_{j=0}^{N-1} y\left[k - j\right] a\left[N - j\right] \tag{4.26}$$

where $y\left[k\right]$ is the input real signal, *N* is the length of the MLS with coefficients $a\left[j\right]$. Since this is a real operator, we first need to obtain the quadrature components of (4.25).

Considering that we are using a BPSK signal, $e^{j\pi\bar{d}_{k \bmod 511}}$ generates the real sequence a_j of ± 1's, *i.e.*, the PN sequence coefficients. The real and imaginary components are

$$\begin{aligned} y_I[m] &= \frac{1}{2}\sum_{k=-\infty}^{\infty} g\left(\left(m-2k\right)\frac{T_c}{2}\right) a_{k \bmod 511} \cos\left(2\pi f_D\left(m\frac{T_c}{2}\right)\right) \\ &= \hat{a}_m \cos\left(2\pi f_D\left(m\frac{T_c}{2}\right)\right) \\ y_Q[m] &= \frac{1}{2}\sum_{k=-\infty}^{\infty} g\left(\left(m-2k\right)\frac{T_c}{2}\right) a_{k \bmod 511} \sin\left(2\pi f_D\left(m\frac{T_c}{2}\right)\right) \\ &= \hat{a}_m \sin\left(2\pi f_D\left(m\frac{T_c}{2}\right)\right). \end{aligned} \tag{4.27}$$

From the sampling process just described, the main conclusion is that the recorded samples will always have two samples per baud. As we will describe in Section 4.1.2.3, this is one of the major restrictions of our system.

4.1.2 Post-Collection System Testing

This is one of the most important sections of this dissertation since it is here where we assess the validity of the measurements.

4.1.2.1 Clock Synchronization

Since one of the main purposes of channel sounding is to measure small fade metrics, it is vital to have an adequate synchronization between the transmitting and receiving systems. Most communication systems must synchronize to a time or frequency standard, *i.e*. an internal or external oscillator. Today's technology provides four different levels in frequency standards: cesium beam, hydrogen maser, rubidium, and quartz [83]. They are listed in descending order according to their accuracy and stability. The top commercially available technology is the cesium beam standard. It is capable of providing an accuracy of a few parts in 10^{12} and a stability of a few parts in 10^{13}/year. In many

channel sounding systems, it is common to use rubidium reference generators for synchronization. Rubidium generators are much cheaper than the first two technologies, but their stability reduces to approximately one part in 10^{11}/month. The rubidium is generally selected for applications in which the quartz crystal oscillator does not provide adequate long-term stability, and cost and size considerations restrict the use of cesium beam standards. The rubidium has excellent retrace characteristics (return to the frequency of interest after a cold start) and warms up to its nominal frequency in a matter of minutes. On the other hand, the quartz crystal oscillator has a number of qualities that make its use as a reliable frequency standard desirable. It has mechanical stability and is relatively immune to external environmental conditions. When connected into a closed loop electric circuit in such a manner as to sustain oscillations and control the frequency of oscillation, the quartz oscillator provides a convenient and reliable frequency source. To improve the performance of the quartz oscillator, temperature compensation circuitry is used to limit the variations in output frequency that result from variations in the operating temperature. Crystal oscillators with such compensation are referred to as temperature compensated crystal oscillators (TCXO). Another alternative to improve the stability is to place the quartz in an oven controlled environment. This environment maintains a constant temperature and provides shielding from the affects of line voltage.

For our measurement campaign, we used Agilent ESG series signal generators as shown in Figure 18 where we display the complete system. For the receiver system, we used the ESG E443xB series. This series has TCXO internal generators. For the transmitter system, we used the ESG E4438C. This series has an improved internal oscillator. The specifications for the two signal generators are shown in Table 1, where we also show the specifications for a commercially available rubidium generator for comparison.

Since, according to specifications, the accuracy of the generators is the same as that of the internal or external reference generator, we tried to reference all of them to the transmitter generator. For this purpose, we calibrated the ADC clock internal generator frequency to match the ESG E4438C internal generator frequency as close as possible, and then we used the ADC clock as the master generator in the receiver system.

The measured Doppler would be offset from the true Doppler if the transmitter and receiver clocks are not synchronized. Prior to testing, we performed the aforementioned clocks' calibration. Throughout the data collection, we relied on the precision and stability of the equipment to keep the adjustment. After the collections, we compared the clocks again, at different stages of system warm-up. We found that the clocks differed very little, and should cause errors in the measured Doppler no larger than 3.5 Hz in magnitude. In the rest of this section, we describe the procedure and the results of the post-collection comparison of the clocks.

Table 1: Reference generators specifications

Stability	TCXO	Improved Oscillator	Rubidium
Aging rate	< ± 1 ppm/yr	< ± 0.1 ppm/yr or < ± 0.0005 ppm/day after 45 days	< 0.00005 ppm/month
Frequency	NA	NA	± 0.0005 ppm @ 25° C
Temperature [0 to 55° C]	< ± 1 ppm	< ± 0.05 ppm	NA
Line voltage	< ± 0.1 ppm	< ± 0.002 ppm	NA
Line voltage range	+5% to -10%	+5% to -10%	NA

The initial setup for the clocks' offset measurement is shown in Figure 35. The probing signal is injected directly into the Pentek™ digital radio. For this setup, both Agilent generators use their internal references. It is the difference between these internal reference frequencies that we measured.

We started with the equipment cold. We took a measurement as soon as we turned on the equipment. In Figure 36, we show the first measured offset of -3.5 Hz, taken immediately after turning on the equipment. The 3.5 Hz offset corresponds to a clock difference of approximately 14 Hz in an 80 MHz signal after decimation.

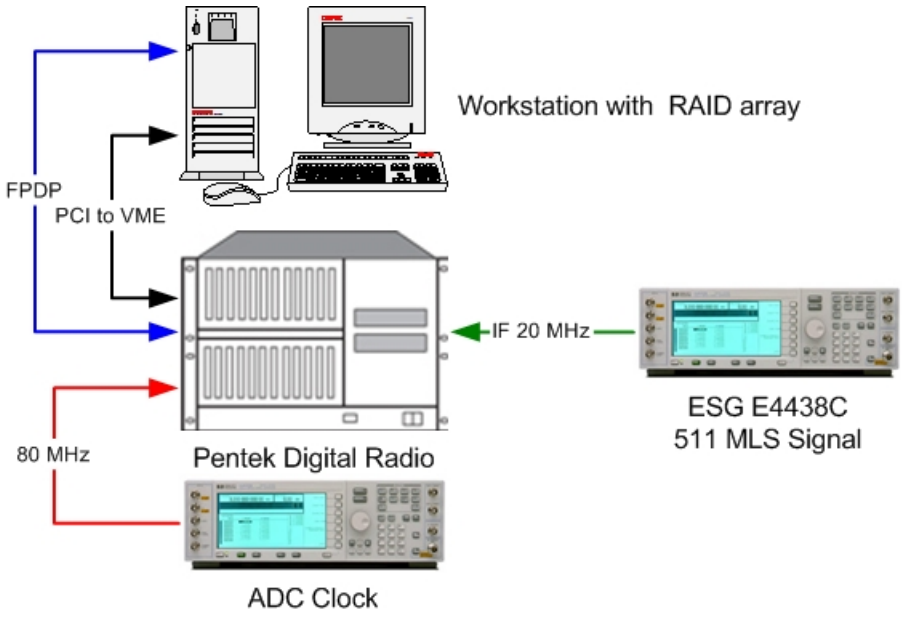

Figure 35: Unsynchronized IF Wired Setup.

A half hour later, the offset decreased to approximately 1.8 Hz. Finally, the measured the offset after a couple hours of operation showed no change from the half-hour offset. Therefore, a half hour is enough time for warming the equipment up.

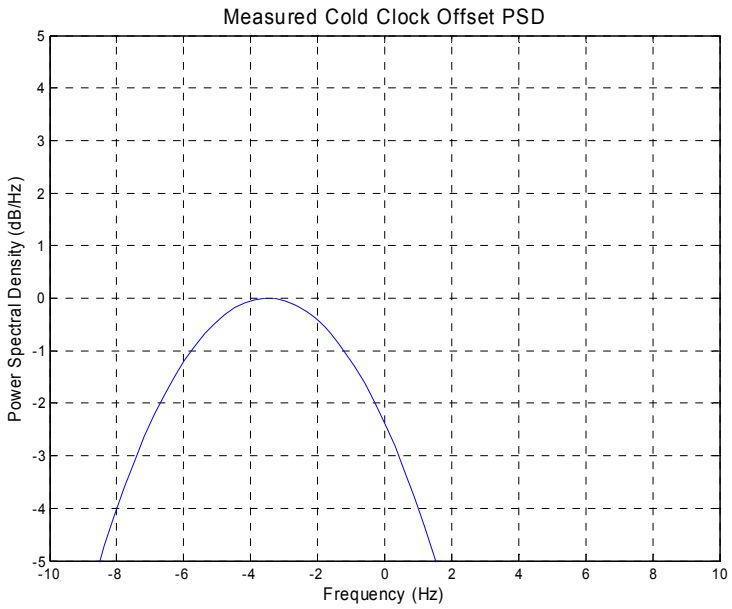

Figure 36: Measured free running IF response with the equipment cold.

4.1.2.2 Harmonic Distortion Test

Since some of the Doppler spectra we measured had features resembling harmonic distortion, we suspected that there might be some sort of inter-modulation (IM) distortion in the system. To test this hypothesis, we performed a series of tests. We tried different configurations, and we also tested individual elements. After a significant amount of measurements, we concluded that the following test represents the worst case scenario. In this test, we used the complete system shown in Figure 18 to have all the elements working together. Next, we located the antennas next to each other surrounded with absorbing foam. This configuration, we believe, will produce the highest amount of harmonic distortion if any. First, we measured the response between the LNA and the downconverter using a traditional two-tone test with 2 MHz separation. We present the results in Figure 37 to Figure 40. We started with an output level of -35 dBm in the TX generator and increased it to 0 dBm, which was the TX output level we used in the

measurements. We can see that there is a significant amount of harmonic distortion starting at -30 dBm.

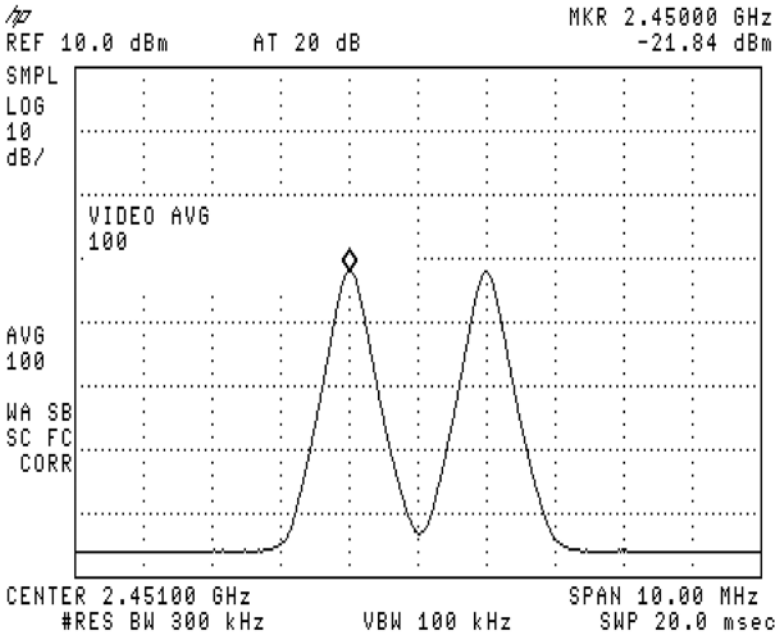

Figure 37: Two-tone LNA output with a -35 dBm TX generator output. This is the maximum level for a clean signal.

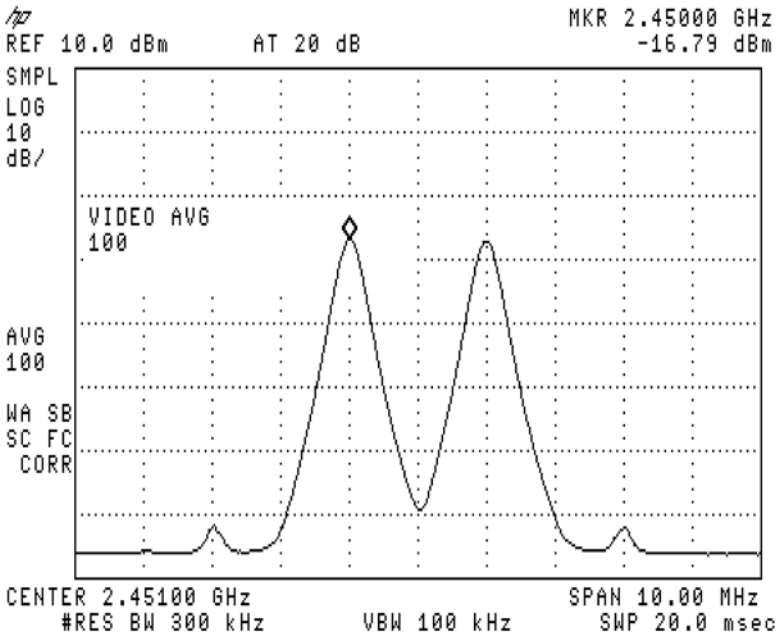

Figure 38: Two-tone LNA output with a -30 dBm TX generator output. Harmonic distortion begins.

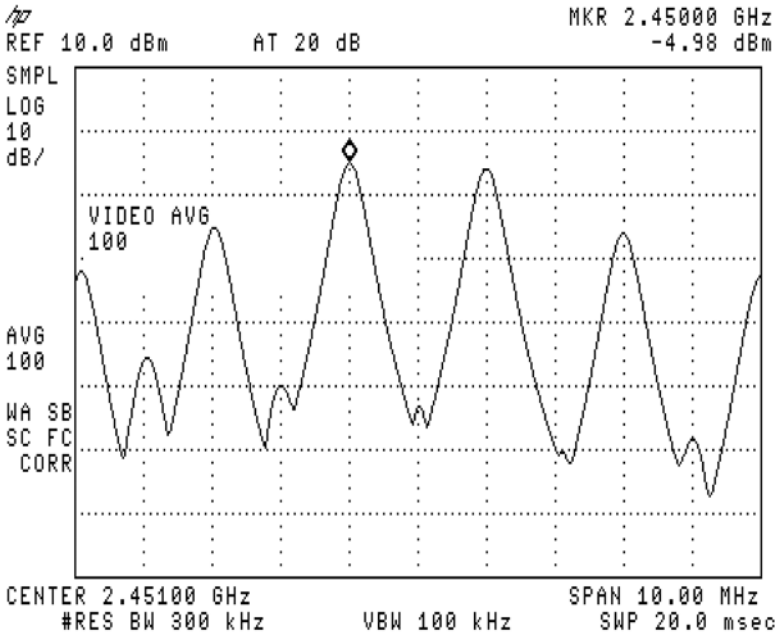

Figure 39: Two-tone LNA output with a -5 dBm TX generator output. LNA output is saturated.

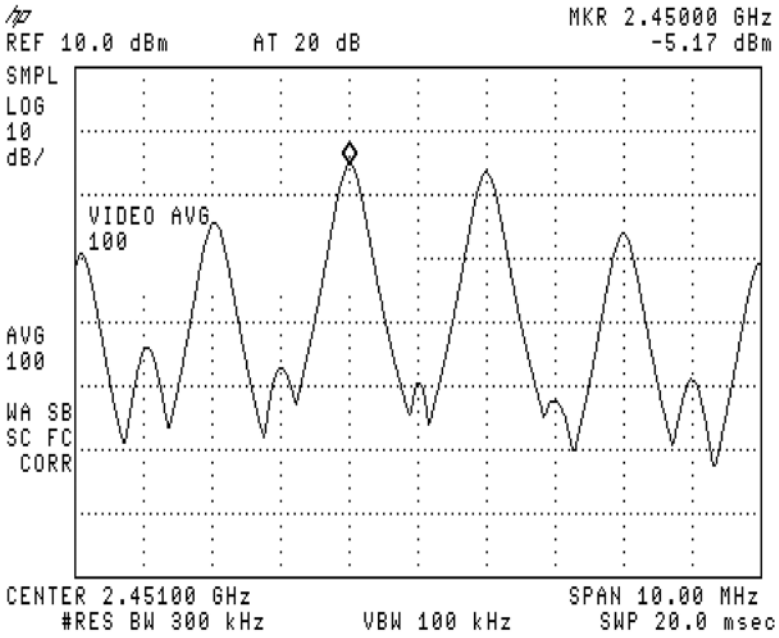

Figure 40: Two-tone LNA output with a 0 dBm TX generator output. Harmonics level almost equals original signal.

Although the previous results look discouraging, we have to recall that the probing signal is a spread spectrum signal with a low PAR; therefore, we repeated the meas-

urement with the probing signal. To analyze the results, we need to keep in mind the spectrum details shown in Figure 27 and in Figure 29. These figures represent the expected response for a correct autocorrelation. Any harmonic distortion will appear between the sequence period peaks. We present the results from Figure 41 to Figure 44. We can see a clean response even for an output level of +5 dBm. In Figure 44, we expand the view to 1 KHz, which is approximately the size of the window we have used to present the short-time Doppler profiles, and again, we cannot see any indication of harmonic problems.

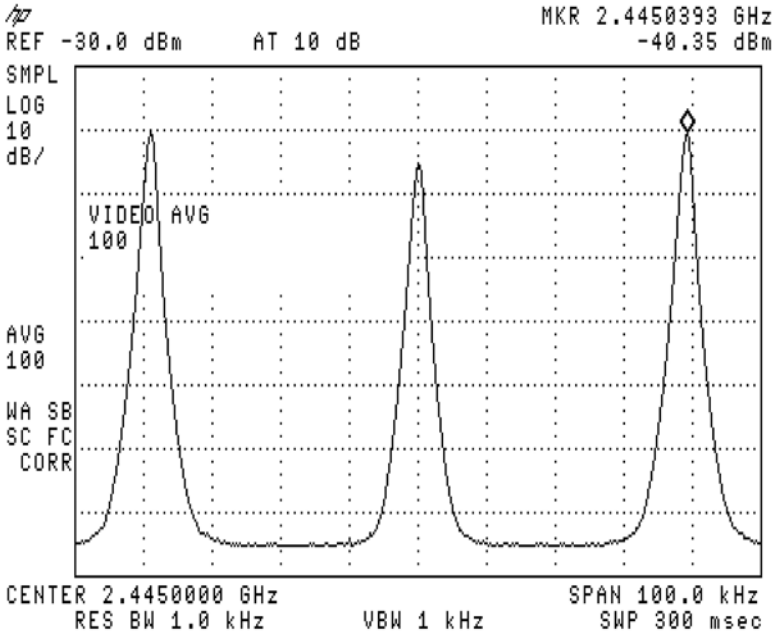

Figure 41: Probing signal LNA output with a -30 dBm TX generator output.

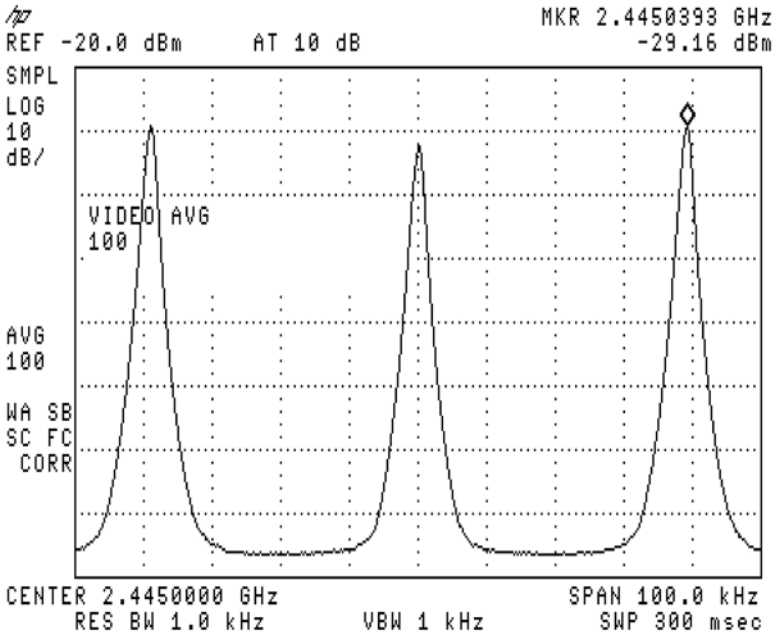

Figure 42: Probing signal LNA output with a 0 dBm TX generator output.

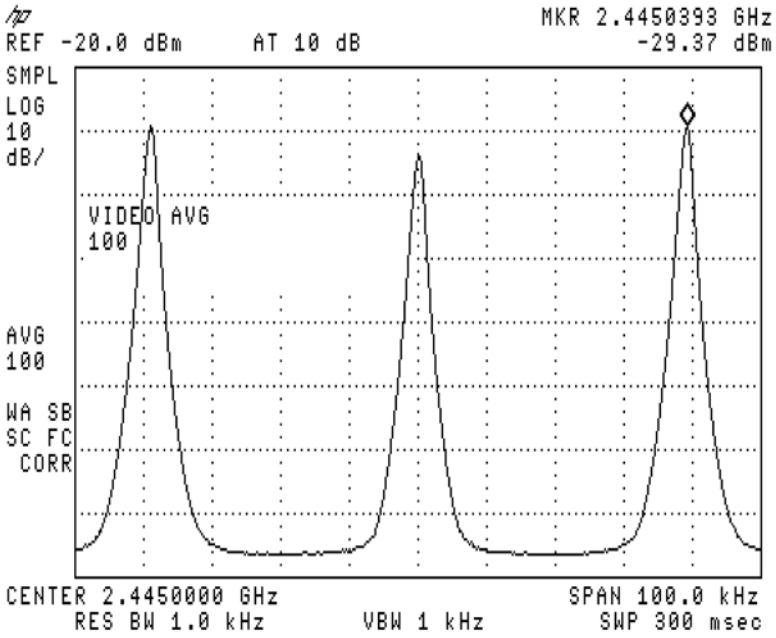

Figure 43: Probing signal LNA output with a +5 dBm TX generator output. Even for this output level, there are no harmonics present.

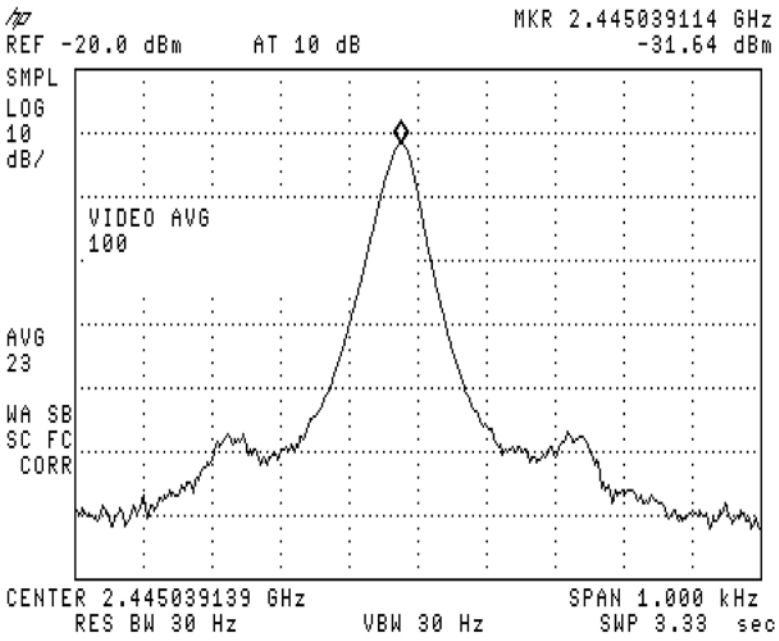

Figure 44: Probing signal LNA output with a +5 dBm TX generator output. Notice that the span is now 1000 Hz.

Finally, we repeated the measurement for a more realistic situation. This time we separated the antennas by about 10 meters, which we can consider the closest the two vehicles can get. This time we present the measurements between the downconverter and the Pentek™ system. First we have a one KHz span in Figure 45, and then a two KHz span in Figure **46**. Both responses for an output power of +5 dBm in the transmitter generator. From Figure **46**, we can conclude that there is enough dynamic range to measure Doppler responses since we have almost 50 dB from peak to noise level and no harmonic or spurious signal inside the long-time Doppler profile window.

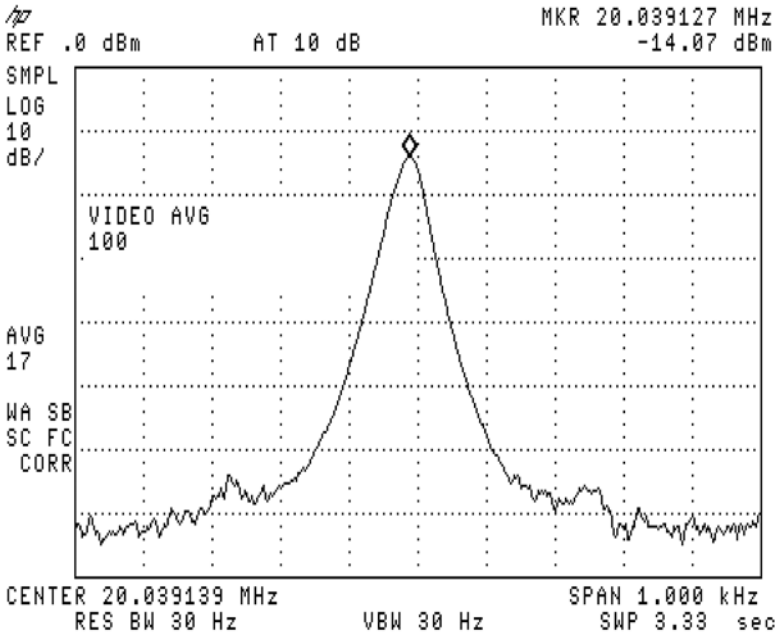

Figure 45: Probing signal downconverter IF output with a +5 dBm TX generator output. This window size is similar to the short-time Doppler profile.

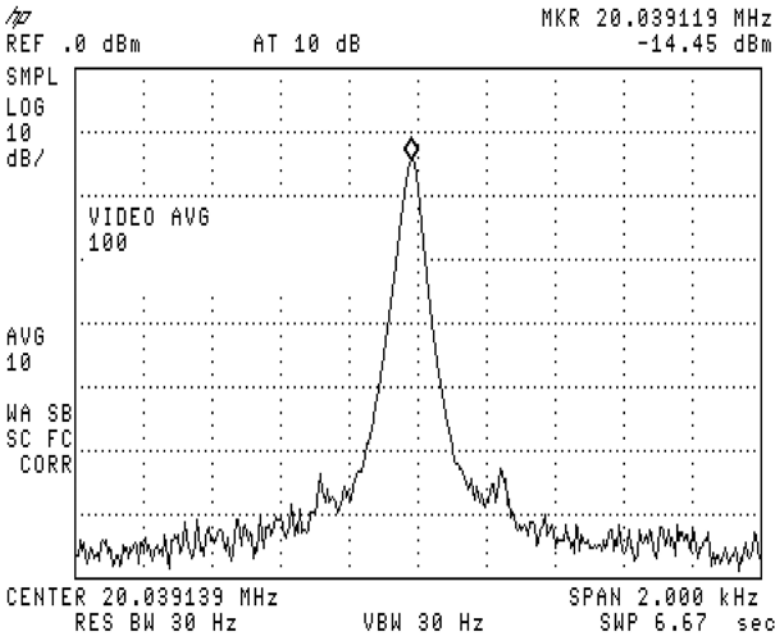

Figure **46**: Probing signal downconverter IF output with a +5 dBm TX generator output. This window size is equal to the long-time Doppler profile.

4.1.2.3 System's Performance

As we have described in Section 4.1.13, the Pentek™ system was designed in such a way that the baseband could be fed directly into a DAC. That is why the digital low-pass filter outputs at least two samples per symbol, which is the minimum Nyquist rate. Unfortunately, we acknowledged this performance specification after the measuring campaign when we started to process the recorded data. This section examines the impact of this filtering on the measured scattering function and demonstrates the validity of the results.

Originally, we thought that the decimation process would deliver symbols. We were counting on having the recording capability of 20 Megasymbols per second, which allows a 50 ns delay spread resolution. Therefore, all of the data have been filtered to half the baseband bandwidth. Our original idea was to obtain a response as close as possible to the simulated response shown in Figure 47. Here we show the PDP of a two path channel with LOS and a second path with a delay of 650 ns, half the power, and a classical Doppler spectrum with $f_D = 500$ Hz. We can notice that since the delay is exactly at a 50 ns multiple, we can measure the correct delay position. We can also see that we are very close to the theoretical dynamic range of 54 dB. We performed a similar simulation for a 100 ns resolution. The result is very similar except that we will have a 50 ns offset in the delay position and the peak base is twice as wide.

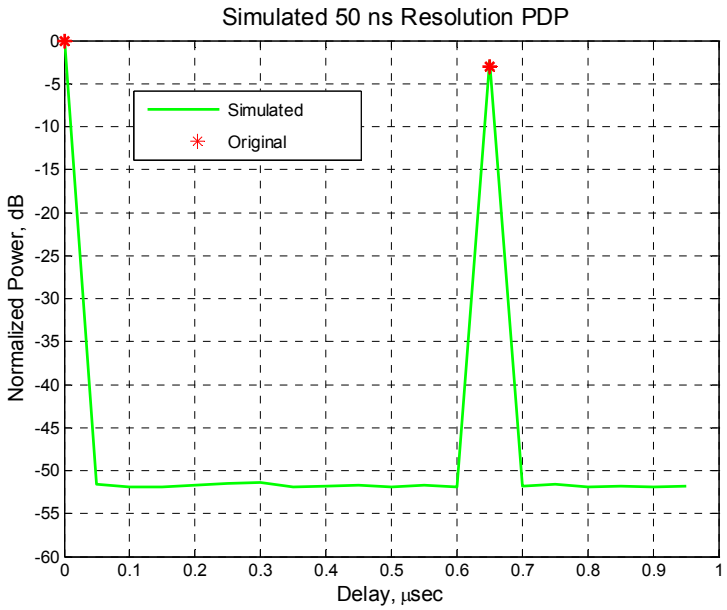

Figure 47: Simulated two path 50 ns resolution PDP.

To analyze the distortion produced by the low-pass filter in the recorded data, we need to define the specifications of the undistorted system. As we can deduce, the best achievable delay spread resolution is 100 ns since the system is limited to the maximum data transfer between the Pentek™ system and the workstation through the FPDP interface, which is 20 Megasamples (complex) per second. Since we have a sampled signal, we face symbol timing problems and sampling frequency offsets. So far, we have two samples for each symbol. Which one should we use? Before answering the question, let us look into the timing recovery problem. The first issue at hand is that we are dealing with recorded data. Our goal is to obtain a sequence of symbols with period $T_c = 100\,\text{ns}$ out of an originally sampled signal at supposedly $T_c/8$ and decimated by four. We say supposedly because we must recall that there will always exists an offset between the clock frequencies of the two separate and free running clocks at the transmitter and receiver. The slightest offset would cause (in the long run) cycle slips. The entire operation of digital timing recovery is best understood by emphasizing that the only time scale

available at the receiver is defined by units of T_s; therefore, the transmitter time scale defined by units of T_c must be expressed in terms of units of T_s [49]. The situation is illustrated in Figure 48 where the transmitter time scale, defined by multiples of T_c, is shifted by a constant amount ε_0 that indicates the symbol starting point difference, and the time scale at the receiver is defined by multiples of T_s. Since we will always have this starting point difference, the receiver symbol timing is $\left(nT_c + \varepsilon_0 T_c\right)$, which we can rewrite as follows:

$$nT_c + \varepsilon_0 T_c = T_s \left\lceil n\frac{T_c}{T_s} + \varepsilon_0 \frac{T_c}{T_s} \right\rceil. \tag{4.28}$$

The key step is to rewrite the expression in brackets in the form

$$\begin{aligned} \left\lceil n\frac{T_c}{T_s} + \varepsilon_0 \frac{T_c}{T_s} \right\rceil &= \left\lceil n\frac{T_c}{T_s} + \varepsilon_0 \frac{T_c}{T_s} \right\rceil + \mu_n \\ &= m_n + \mu_n \end{aligned} \tag{4.29}$$

where $\lceil \bullet \rceil$ is the ceiling operator and μ_n is a fractional difference.

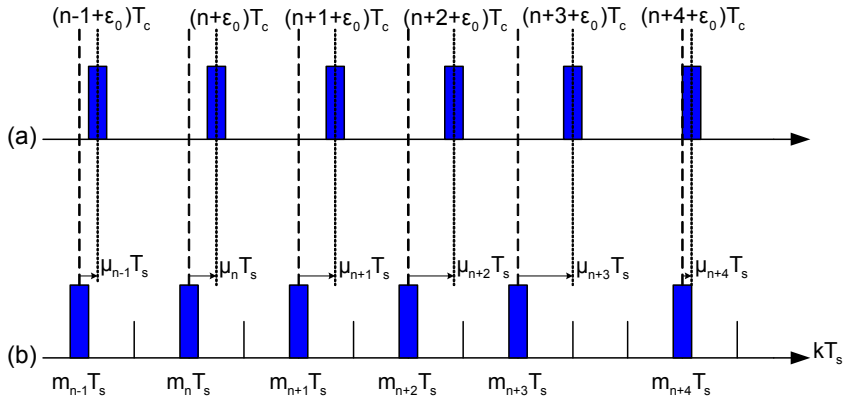

Figure 48: (a) Transmitter time scale (nTc), and (b) Receiver time scale (kTs) [49].

We can observe that the relative time shift $\mu_n T_s$ is time-variable despite the fact that ε_0 is constant. Also, we can observe that the time instances $m_n T_s$ form a completely irregular (though deterministic) pattern on the time axis. This irregular pattern is required in order to obtain an average of exactly T_c between the received symbols, given a time quantization of T_s. Notice that the timing parameters (m_n, μ_n) are uniquely defined given $\{\varepsilon_0, T_c, T_s\}$. Summarizing, digital timing recovery requires the estimation of ε_0, the interpolation from the samples $\{r(kT_s)\}$ to compute a set of samples $\{r(kT_s + \hat{\mu}_n T_s)\}$, and finally the decimation $\{y(m_n T_s)\} = \{z(nT_c + \hat{\varepsilon} T_c)\}$. We selected the Mueller-Muller Simulink™ blockset [49], [55] to perform the timing recovery.

At any given instant, the timing algorithm generates only one value; therefore, we can define

$$\hat{a}_m = \frac{1}{2} \sum_{k=-\infty}^{\infty} g\left((m - 2k) \frac{T_c}{2} \right) a_{k \bmod 511}. \tag{4.30}$$

The periodic correlation requires two correlators in parallel. For each quadrature component we obtain

$$\begin{aligned} z_I[m] &= \sum_{j=0}^{N-1} \hat{a}_{m-j} \cos\left(2\pi f_D \left((m - j) \frac{T_c}{2} \right) \right) a_{N-j} \\ z_Q[m] &= \sum_{j=0}^{N-1} \hat{a}_{m-j} \sin\left(2\pi f_D \left((m - j) \frac{T_c}{2} \right) \right) a_{N-j} \end{aligned} \tag{4.31}$$

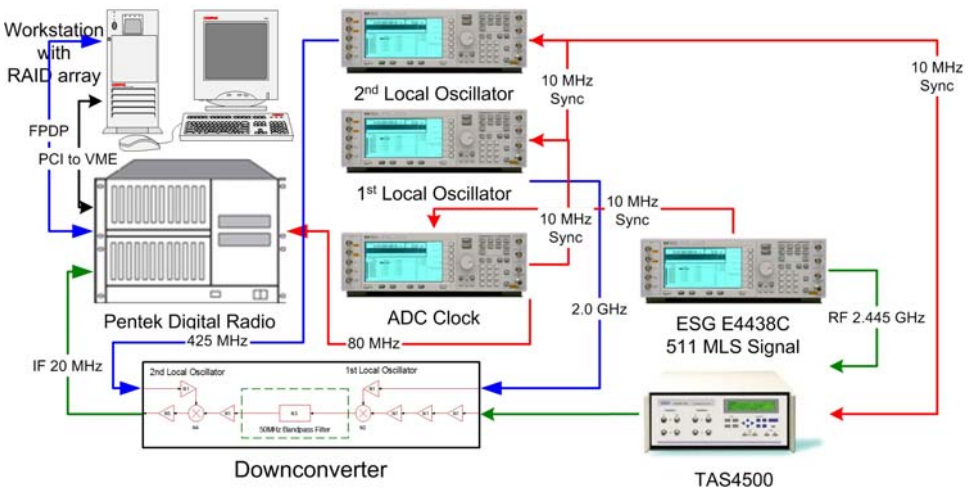

Figure 49: Channel emulator setup.

In Figure 49, we present the setup to test the system using the TAS4500 channel emulator. First, we will show the results for a $T_c = 100\,\text{ns}$ resolution setup. As we have discussed so far, this setup would provide the best possible system's specifications. We used the same two-path channel parameters that produced the simulation results in Figure 47 for the channel emulator. We then repeat the experiment with a $T_c = 50\,\text{ns}$, which is what we used in the channel sounding campaign. This way we will be able to define the limitations and distortions of the recorded data. We start by showing the PDP's for the first setup considering the response for each of the two samples in the symbol and for the synchronized or time aligned symbol. We can see in Figure 50 that the synchronized response provides the best dynamic range and that its up and down-ward slopes are an average of the two samples.

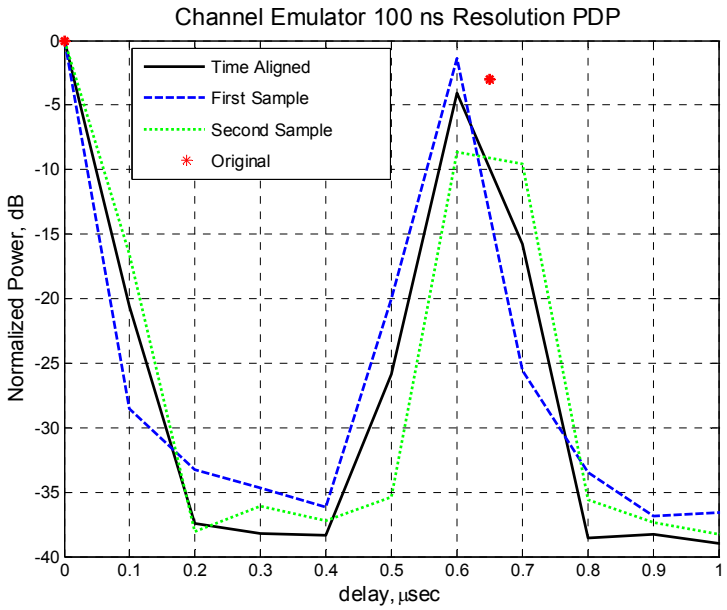

Figure 50: Channel emulator $T_c = 100\,ns$ PDP for first and second baud sample and time aligned response.

In Figure 51, we have the PDP comparison between the best possible system's response and the response that we obtained from the recorded data. The first thing to notice is the loss of dynamic range. With the 50 ns resolution, we can correctly detect the power of the second path. The most critical distortion in the filtered 50 ns resolution system is the correlation or spreading that we can observe after and before the peaks. The best example is the second power value after the LOS peak at 0.5 μs. This power level is just 2 dB below the maximum peak, which should be at -54 dB according to the simulation. This distortion is better exemplified in Figure 52 where we show the scattering function for each response. In particular, the delay vs. amplitude views, (c) & (d), depict a better picture of the correlation between samples. One alternative to compensate for this correlation can be to process only every other sample of the recorded data.

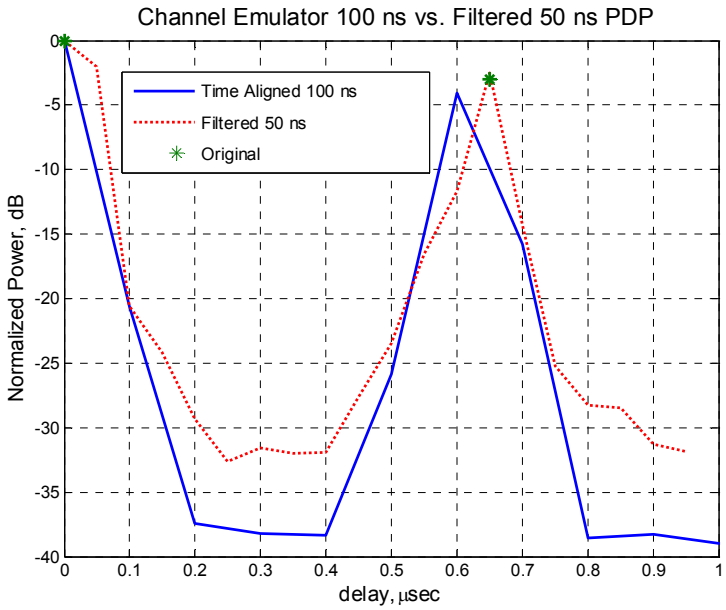

Figure 51: Channel emulator $T_c = 100$ ns vs. $T_c = 50$ ns PDP's.

We have learned in this section that even though we have a loss of dynamic range in our recorded data, it does provide the correct power level for the detected paths within a 50 ns resolution. We can also observe that the available dynamic range should be enough for a 30 dB threshold. The main disadvantage appears to be in the power level of a bin following the detection of a strong direct path. We can detect a direct path through its Doppler spectrum; therefore, we might be able to analyze the immediate path to make an educated decision about its inclusion in the final model.

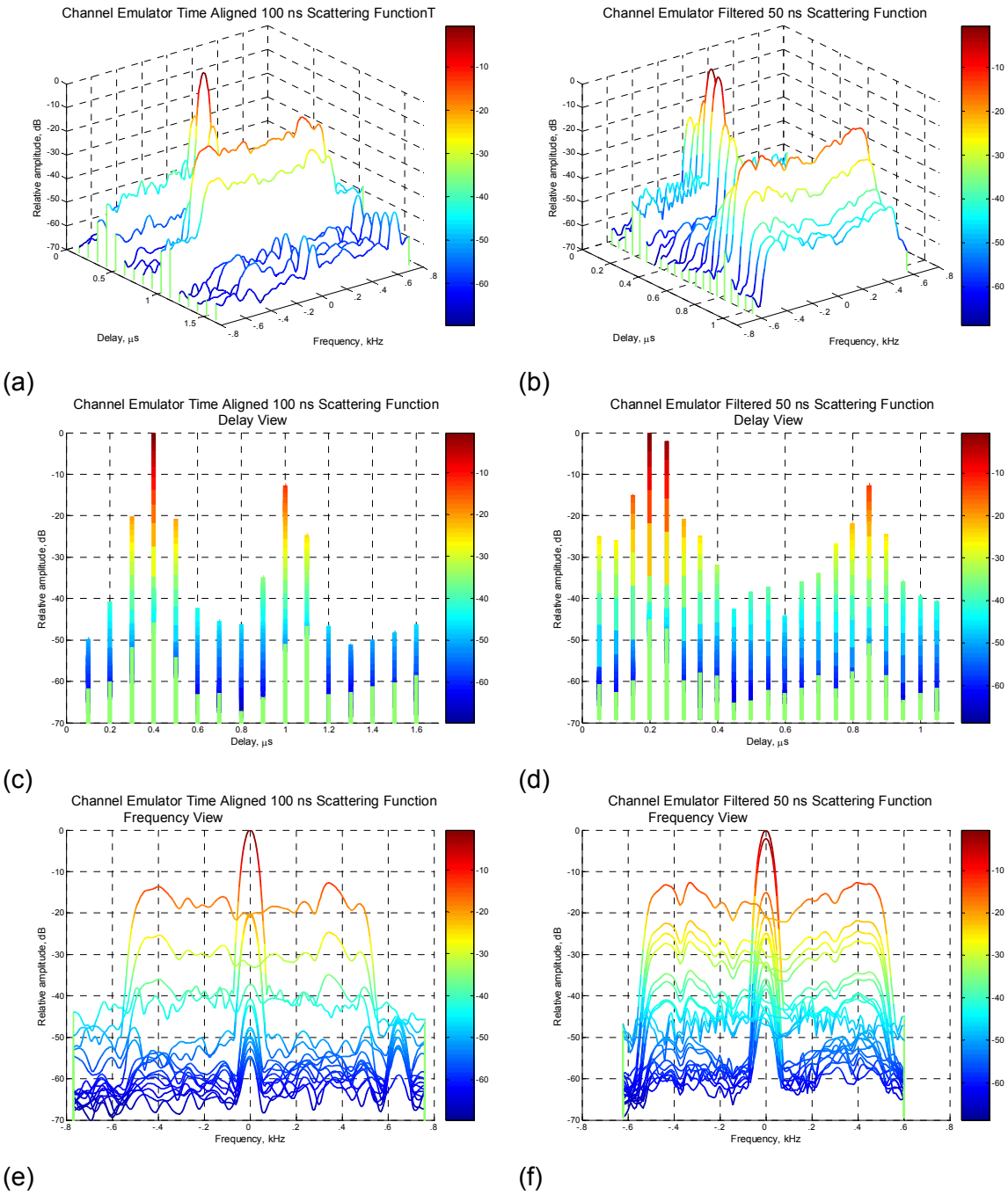

Figure 52: Channel emulator $T_c = 100$ ns vs. $T_c = 50$ ns scattering functions: (a) & (b) Isometric views, (c) & (d) delay vs. amplitude views, and (e) & (f) frequency vs. amplitude views.

4.2 5.9 GHz Channel Sounding System Development

For the 5.9 GHz measurement campaign, we had the opportunity to correct or upgrade many of the limitations and deficiencies we faced in the previous measurement campaign. In this section, we first present the description of the transmitter and receiver systems where we indicate the improvements with respect to the previous system. We then proceed to describe the sounding waveform. For 5.9 GHz, we combined two sounding techniques: STDCC and OFDM. Finally, we present the consequences of an unfortunate error detected in the STDCC waveform after the measurement campaign.

4.2.1 System Description

In Figure 53, we show the 5.9 GHz transmitter system. As we have described in Section 4.1.2.1, we had to rely on the internal clock references of the signal generators. This time, we have the opportunity to use Rubidium reference clocks. For this new campaign, we are required to measure channels up to one kilometer of separation between vehicles. For this purpose, we are using a 25 Watt amplifier.

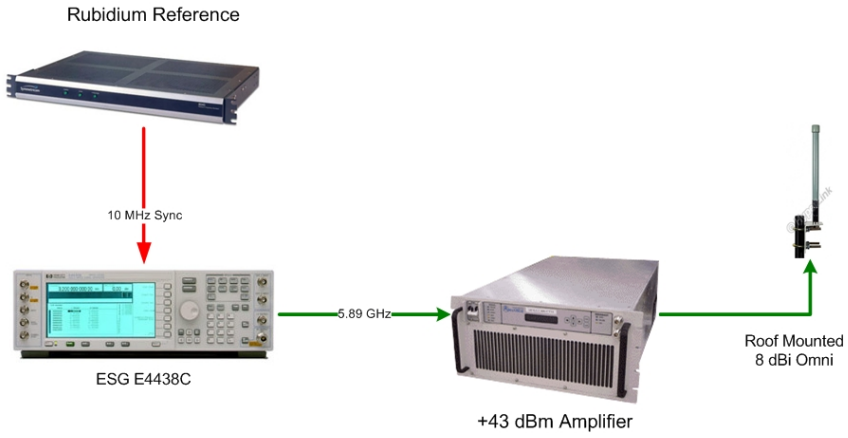

Figure 53: 5.9 GHz transmitter system.

In Figure 54, we have the receiver system. Of all the improvements or differences, the use of a Rubidium reference generator and the availability of the Mercury Computer

Systems ADV 3000T RF tuner are the most important. These radios provide excellent baseband downcovertion because of their superior linearity, stability, and dynamic range. Unfortunately, the frequency range of the radio goes only up to 3 GHz; therefore, we require a second downcovertion. We achieve the first downconvertion with the shown mixer, but this time we include directional couplers to monitor the received signal and a 60 dB variable attenuator. Although this time we use two computers and one buffer board, the net effect is similar to the previous system, *i.e*., we are capable of recording 20 Megasymbols per second from a $f_s = 80\,\text{MHz}$ with a decimation of four.

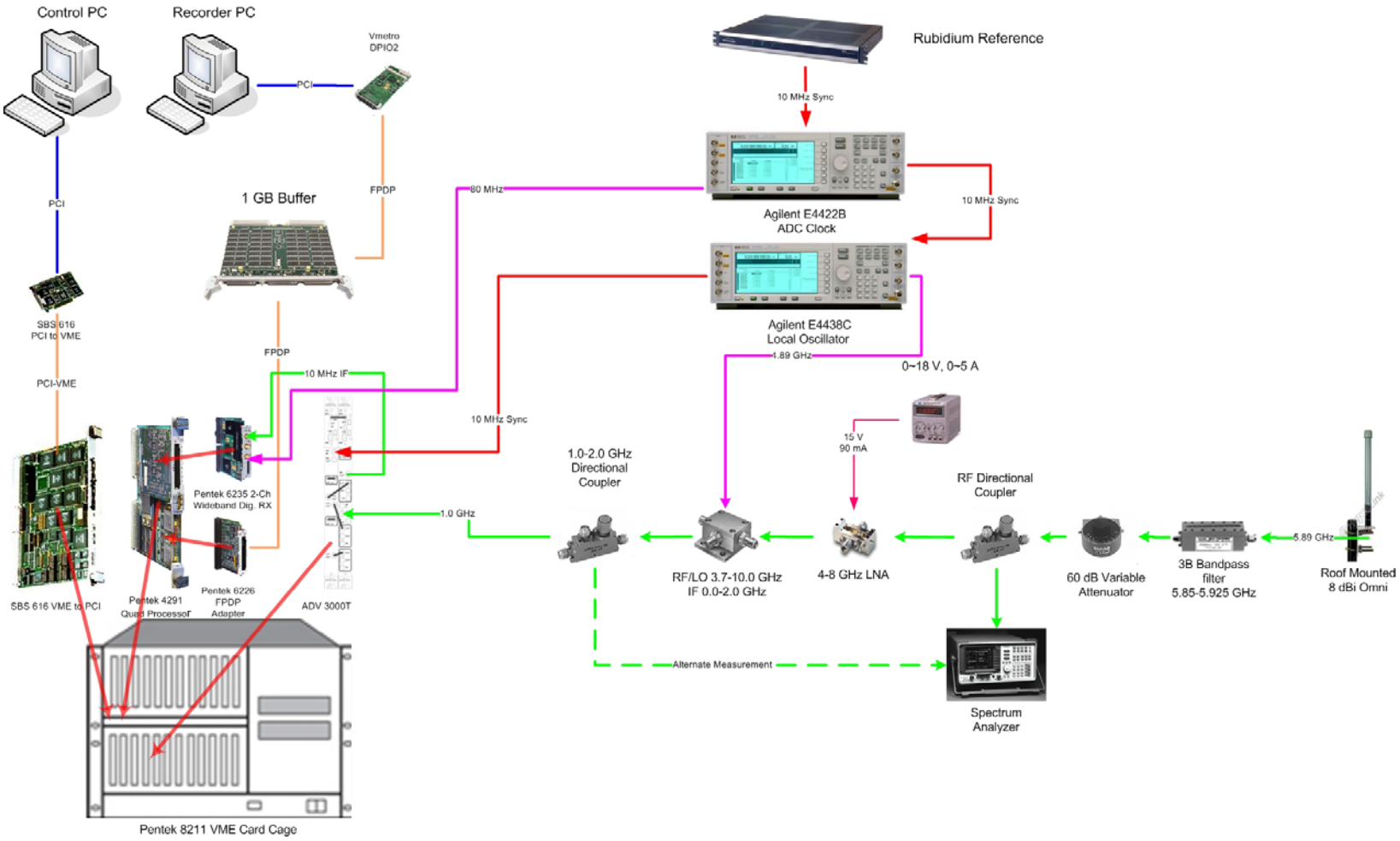

Figure 54: 5.9 GHz receiver system.

4.2.2 Sounding Waveform

As we described in Section 4.1.2.3, the maximum multipath resolution attainable with an MLS sounding signal is 100 ns. We also mentioned in Section **Error! Reference source not found.** that it is possible to double this maximum resolution using an OFDM sounding waveform. For this campaign, we used a combined, MLS and OFDM, sounding waveform. As we have indicated in previous sections, a 511 MLS sequence with a 100 ns chip period provides a Doppler measuring range of ±9.78 kHz. This is more than enough since we are not required to measure Doppler shifts greater than ±2,100 Hz [6]. In other words, we can have a sequence length of up to 450 μs.

This time, the sounding waveform contains four sections. The first section is a 511 MLS sequence with a 100 ns chip period. The second and fourth sections are 320 zeros with a 50 ns period. The third section is an OFDM signal with a 512 FFT size with a guard band of size 128 for a total length of 640 samples with also a 50 ns period. Therefore, the total length of the combined sequence is (511x2)+(320x2)+(512+128)=2,302 for a time of 115.1 μs and a Doppler range of ±4,345 Hz.

In Figure 55 and Figure 56, we show the PDPs obtained when we tested our combined signal through a channel emulator set for a three-tap static channel. The delays were 0, 100, and 250 nanoseconds, and the power settings were 0, -4, and -7 dB respectively. In particular, we can see the improved time resolution by comparing their responses at 250 ns.

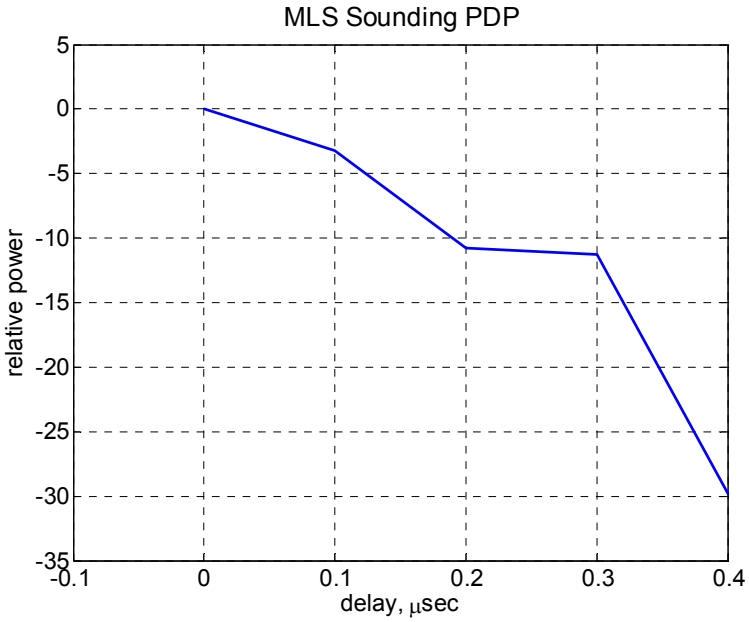

Figure 55: PDP obtained using the MLS signal through a channel emulator.

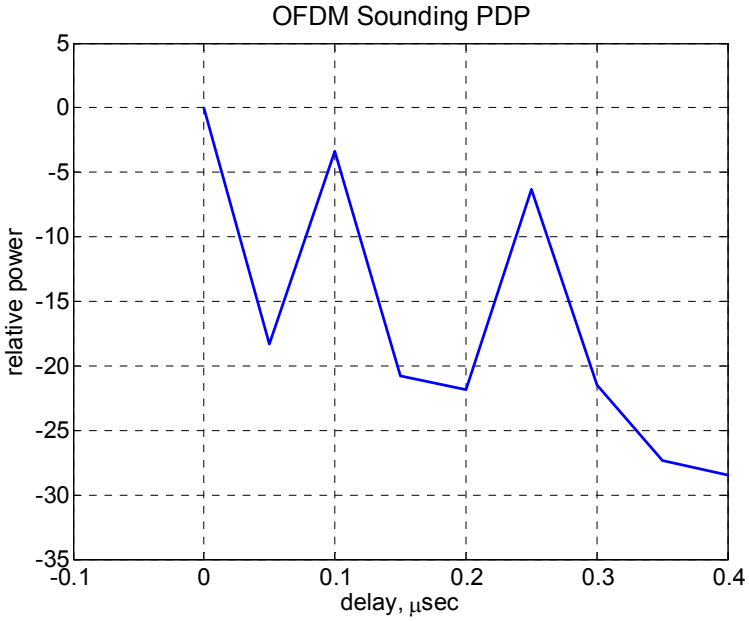

Figure 56: PDP obtained using the OFDM signal through the same setting in a channel emulator. We can clearly see the improvement in time resolution.

4.2.3 OFDM Sounding

If we follow the description of the RUSK™ system as specified in Section 2.2.2.2, we can notice that we can reproduce such a system using an OFDM signal. We start by looking at just one OFDM symbol transmitted at $t = t_s$

$$s(t) = \Re\left\{\left(\sum_{k=\mathrm{K_{min}}}^{\mathrm{K_{max}}} \mathrm{c}_{m,l,k} e^{j2\pi \frac{(k-(\mathrm{K_{max}}+\mathrm{K_{min}})/2)}{\mathrm{T_U}}(t-t_s)}\right) e^{j\pi f_c}\right\},\ t_s \le t \le \left(t_s + T_U\right)$$
$$s(t) = 0,\ t < t_s \wedge t > \left(t_s + T_U\right) \tag{4.32}$$

where m is the frame number, l is the OFDM symbol number, and k is the subcarrier number. From the system's specifications, we see that the first relationship is $t_p \Leftrightarrow T_U$. Using for example the $25.6\mu s$ repetition rate, we have a 39.062 kHz separation for each single tone or in this case, each subcarrier. If we use an 8192 size IFFT to generate the probing signal, we have a total bandwidth of 320 MHz and the time resolution of 3.12 ns. Using the following data vector

$$c_{m,l,k} = \begin{cases} 0, 0 \le k \le 1023 \\ 1, 1024 \le k \le 7167 \\ 0, 7168 \le k \le 8192 \end{cases}, \tag{4.33}$$

we occupied only a 240 MHz bandwidth with 6,144 single tones of amplitude one. This zero padding also eases the anti-alias filter specifications. In this case, there is a $1\frac{1}{3}$ oversampling that might be enough to use a 320 MHz frequency in the DAC depending on the generator parameters (*e.g.*, reconstruction filter characteristics, bandwidth, etc.). Since the transmitted signal represents a band-limited flat spectrum, we can expect some sort of impulse signal in time domain; therefore, before we continue with a system

description, let us analyze this signal. Let us start with an all ones signal at the input of the DAC as follows:

$$\begin{aligned} s(n) &= \frac{1}{N}\sum_{k=0}^{N-1}(1)e^{-j\frac{k2\pi n}{N}} \quad \text{for } n = 0..N-1 \\ &= \begin{cases} 1, & n = 0 \\ 0, & n = 1..N-1 \end{cases}. \end{aligned} \tag{4.34}$$

We have a discrete impulse, but when we pad the signal with zeros as in (4.33), the value of *s(0)* reduces proportionally to $(1-\#0's/N)$ with a ripple effect near it for $s(n \neq 0)$ as shown in Figure 57. This will diminish the dynamic range of the signal. To validate this idea, we passed the signal through simulated multipath non-separable channel. As we can see in Figure 58, we could obtain a scattering function that describes the non-separable multipath channel; therefore, we can conclude that this OFDM signal is a valid sounding signal.

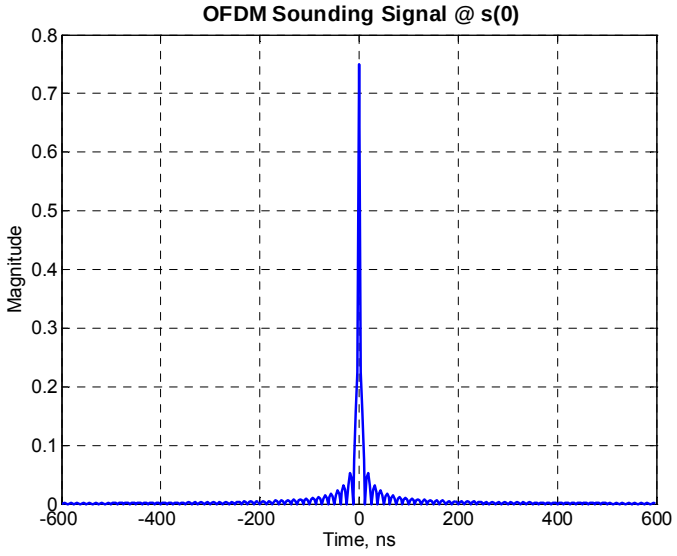

Figure 57: Zero padded OFDM sounding signal. We can notice the impulse magnitude reduction and the ripples surrounding it.

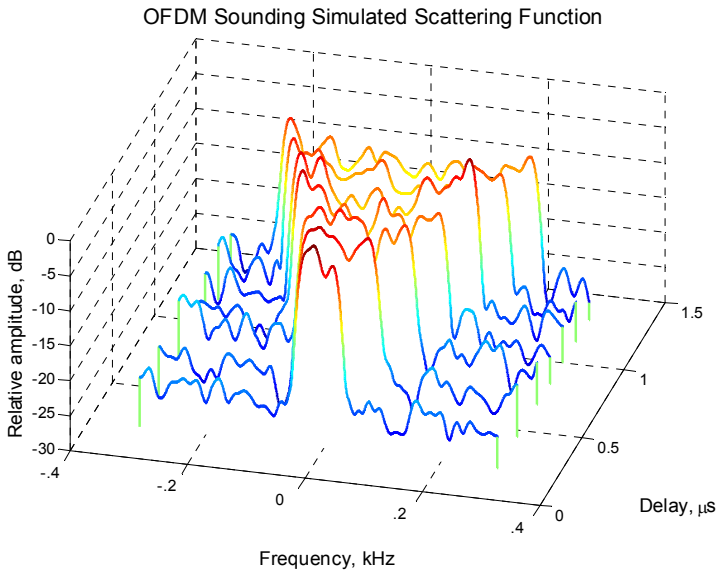

Figure 58: Scattering function using an OFDM sounding signal through a seven path channel with different maximum Doppler frequencies.

If we take a closer look at (4.34), we can notice that it is just a pulse. Although this signal works in simulation, its implementation will have most of the deficiencies described in Section 2.2.2.3. The main difference between this OFDM signal and a periodic pulse is in their spectra. The OFDM spectra is flat, and it is not double-sided; therefore, it provides twice the time resolution, *i.e.*, its multipath resolution is $1/BW$. In order to take advantage of this bandwidth efficiency, we need to use something other than a single pulse signal. One way to do this is to use a chirp signal such as:

$$s(n) = \cos\left(\frac{\pi}{N}n^2\right) + j\sin\left(\frac{\pi}{N}n^2\right) \quad \text{for } n = 0..N-1. \tag{4.35}$$

This way we have the pulse compression advantage described in Section 2.2.2.5 but without its processing complexity or maximum Doppler frequency reduction.

For the OFDM section, we use a chirp signal as specified in (4.35). If we recall, this signal has a flat spectrum in the available bandwidth. For an ideal sytem, the sounding process is as follows: first, we have a received symbol

$$r(t_m,\tau) = h(t_m,\tau) * s(t_m,\tau) \tag{4.36}$$

where t_m indicates the sounding instant and $h(t_m,\tau)$ is the channel impulse response. The next step is to perform a Fourier transform with respect to τ to obtain

$$R(t_m,\nu) = H(t_m,\nu)S(t_m,\nu). \tag{4.37}$$

Since we can easily generate $S(t_m,\nu)$ at the receiver end, we can just divide the Fourier transformed received symbol to obtain the frequency response of the channel at time t_m. The channel impulse response will be its inverse Fourier transform.

In a real system, we will have two main problems to solve: exact time synchronization and system calibration. The first problem is not a hard problem since in our combined waveform; we can use the other three segments for synchronization. The second problem is much more difficult since it depends on the frequency response of all the elements in the communication chain. To better explain this problem, we have to modify (4.37) as follows:

$$R(t_m,\nu) = H(t_m,\nu)Sys(\nu)S(t_m,\nu) \tag{4.38}$$

where $Sys(\nu)$ represents the cumulative or combined frequency response of all the elements in the communication system. For example, we know that the recording system has a response given by the filter shown in Figure 34. This filter response can be $Sys(\nu)$ for the minimum complexity system, which is the ESG generator connected di-

rectly into the recorder at IF. To obtain this system response, it is necessary to somehow delete the channel from the received signal. The best option is to transmit the signal through the best possible cable and to include all the elements of the transmission chain. We did this, and in Figure 59, we show the calibrated system impulse response, which is the inverse Fourier transform of $R(t_m,\nu)/\hat{S}ys(\nu)S(t_m,\nu)$, where $\hat{S}ys(\nu)$ is the measured system response. We compare this to uncalibrated system impulse response, which is the inverse Fourier transform of $R(t_m,\nu)/S(t_m,\nu)$. The effect of the system response is a spreading of the PDP. We can see how in the calibrated system the value at 50 ns is less than -30 dB, which should be the case of a direct connection.

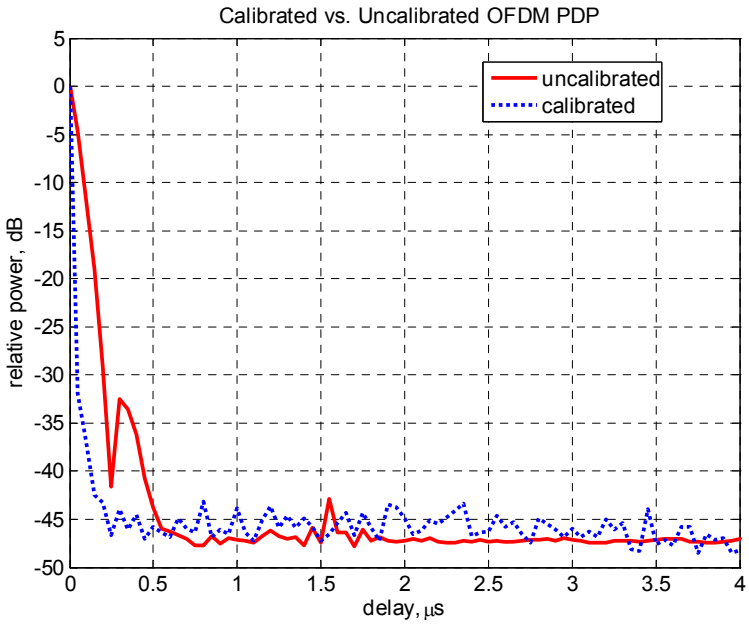

Figure 59: Example of OFDM PDPs with and without calibration.

4.2.4 Alias Problem

When we proceeded to analyze the data at 5.9 GHz after the measurement campaign, we detected aliasing in the Doppler spectra of the MLS section. This aliasing was most notable in the spectra for the oncoming-vehicle scenario, where the LOS had a

non-zero Doppler shift. In Figure 60 and Figure 61, we show tap-one spectra obtained from the OFDM and MLS sections, respectively. We can observe that the approaching vehicle created a frequency shift of approximately 1,000 Hz. In Figure 61, we can clearly see that the MLS section has an alias since there are additional frequency shifts at integer multiples of 1,000 Hz.

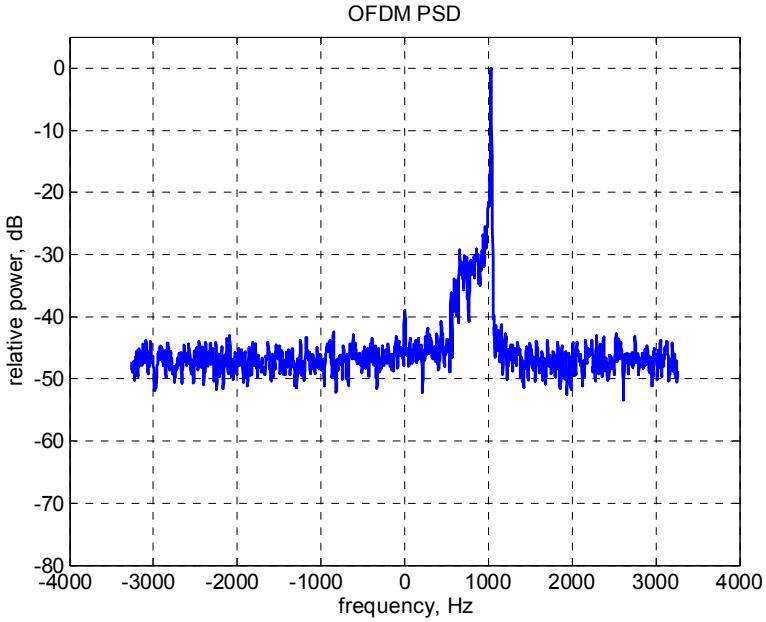

Figure 60: First tap Doppler spectrum from the same segment used in Figure 61 obtained using the OFDM section of the sounding waveform.

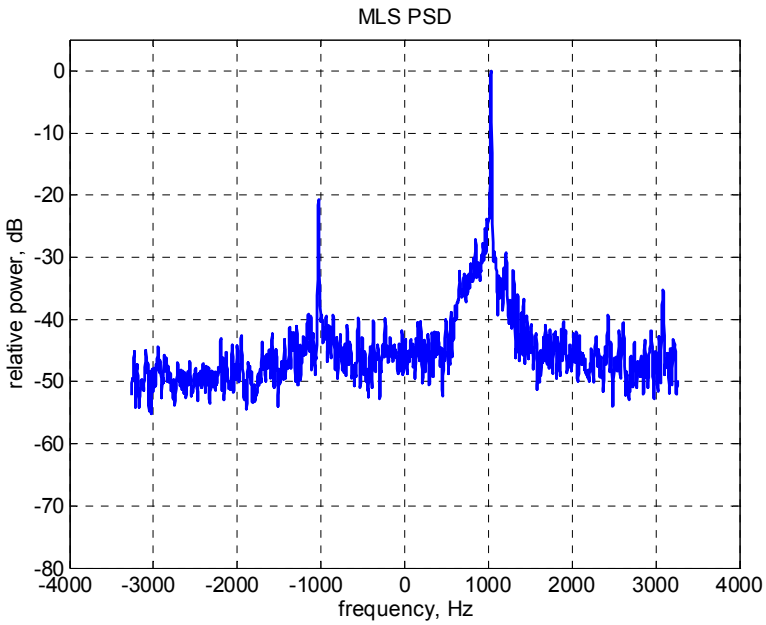

Figure 61: First tap Doppler spectrum from an oncoming scenario segment obtained using the MLS section of the sounding waveform.

This happened because the IF of 10 MHz, while adequate for the OFDM section, was not adequate for the MLS section. To see this, we first need to look at Figure 62, where we show the measured spectrum of the OFDM section at the output of the ADV-3000T. To show clearly that it only occupies 20 MHz, we used a 20 MHz IF. Therefore, the optimum setting for the OFDM section was to use a 4x oversampling with the available $f_s = 80\,\text{MHz}$ sampling frequency and a 10 MHz IF frequency. The ADV-3000T radios have a 40 MHz bandwidth passband filter at the baseband output. This is the main anti-aliasing filter in the system. The combined waveform spectrum produced by the ESG E4438C is shown in Figure 63. We can clearly observe the resulting sinc square shape produced by the 100 ns rectangular pulse used for the MLS section. The MLS section spectrum of the combined measured spectrum shown in Figure 63 is the same as the one we showed in Figure 28 as expected. We could have avoided the problem if we were able to filter the transmitter signal generator output with 20 MHz passband filter

to just have the main lobe of the $sinc^2$. This way we could have used all the advantages given by the 4x oversampling that we wanted for the OFDM section. We could have opted for a Nyquist pulse instead of the rectangular, but that would have substantially complicated the data processing. Either option would have affected significally the time and budget constraints of the project.

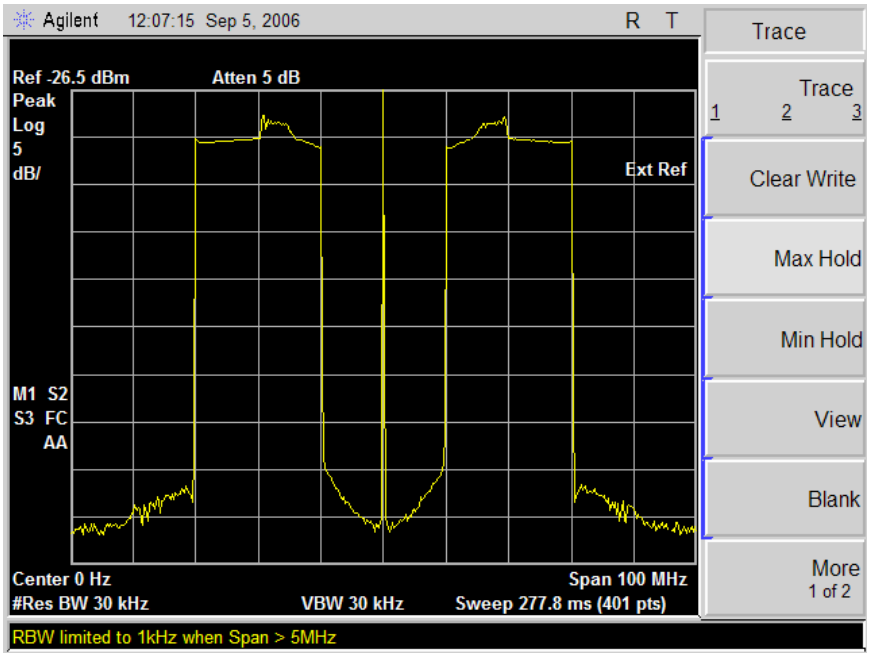

Figure 62: Measured OFDM section spectrum.

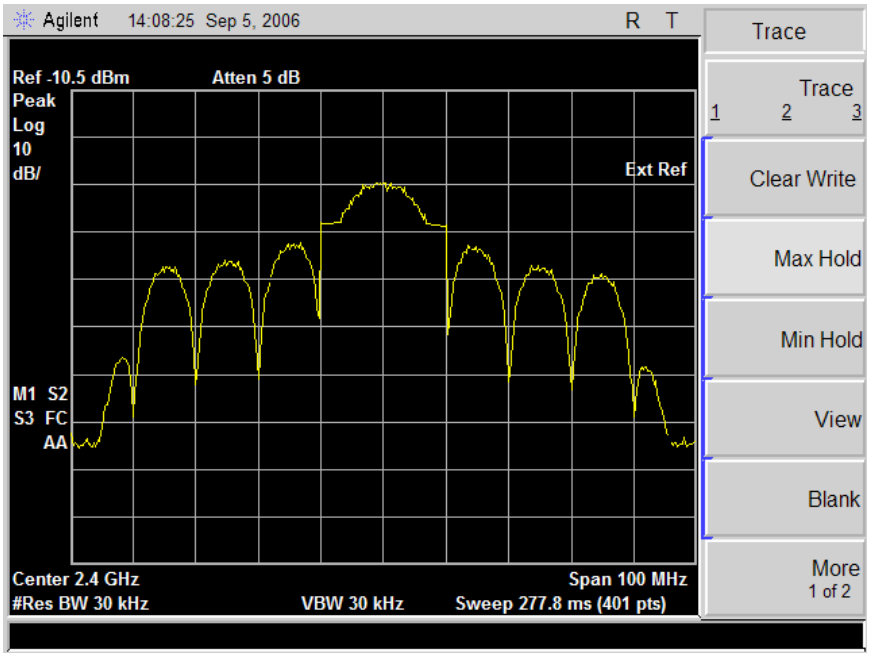

Figure 63: Combined waveform spectrum produced by the ESG E4438C signal generator.

In Figure 64, we show the MLS section spectrum at the output of the ADV-3000T radio. The effect of the 40 MHz filter is very clear. To avoid aliasing, this spectrum should be sampled at a minimum of 80 MHz. For this to happen in our system, we should have used a 20 MHz IF to produce the spectrum shown in Figure 65. Instead, we sampled the MLS section spectrum shown in Figure 66. We immediately notice that the left sidelobe will combine with the mirror image of the main lobe. If we notice the magnitude difference of around 15 dB between the main lobe and the sidelobes, this magnitude is similar to the magnitude difference observed in Figure 61 between the real spectral line and the phantom or aliased ones.

The good news is that thanks to our combined sounding waveform, we had redundancy, and the project was saved. Also, the MLS waveform, while not useful for sounding, was useful for time-shynchronization for the OFDM part. However, we found that the dynamic range of the PDPs derived from the OFDM signal had high sensitivity to imper-

fect calibration of the recording system. The calibration example shown in Figure 59 was obtained in the laboratory with a minimal complexity system. Once we had to include all the elements of the complete system (*i.e.*, all the different type of cables, connectors, equipment, etc.), we could not achieve such a clean response. Therefore, we used the PDP of the MLS signal. In spite of the aliasing of the MLS waveform in the receiver, the MLS waveform still provides a better PDP estimate than the OFDM waveform.

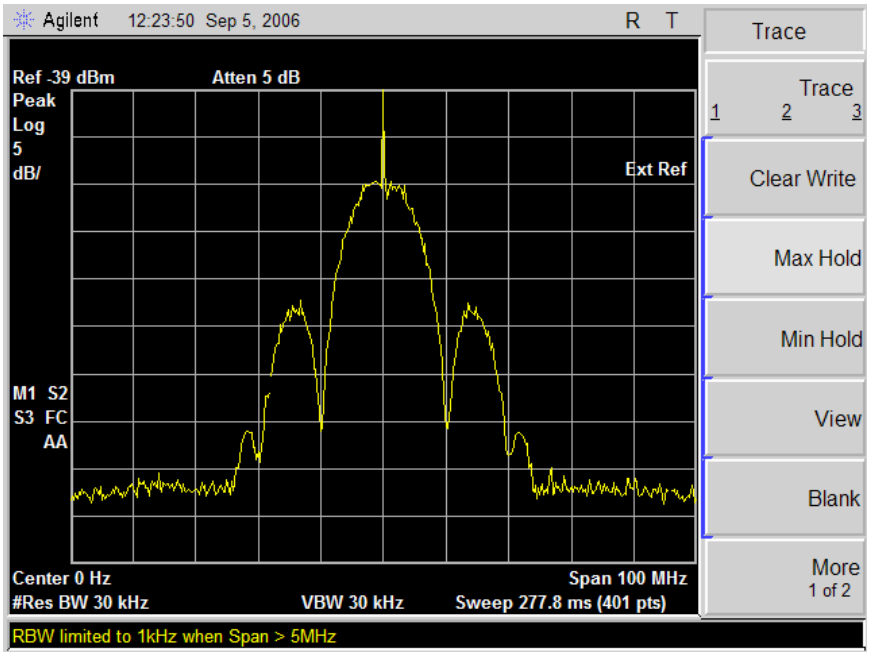

Figure 64: MLS section spectrum at the output of the ADV-3000T downconverter.

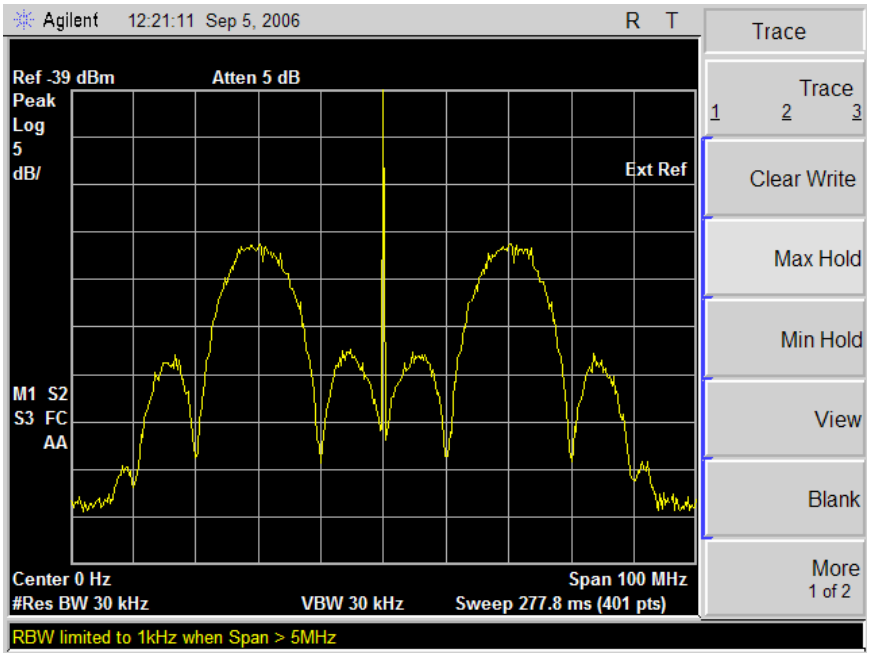

Figure 65: Correct MLS section spectrum for a 2x sampling.

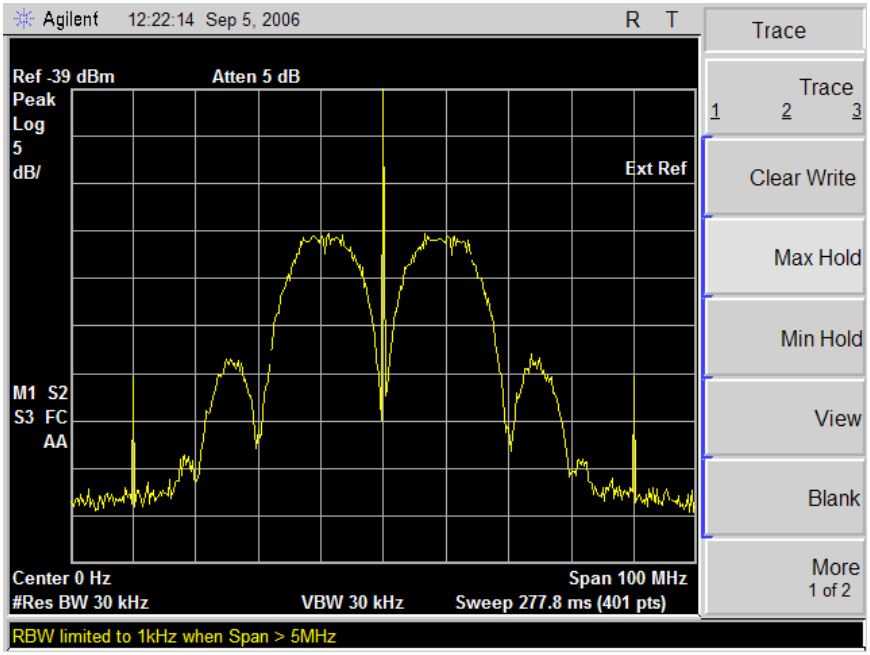

Figure 66: MLS section spectrum used in the measurement campaign.

CHAPTER 5

MEASUREMENT CAMPAIGNS

In this chapter, we present an overview of the two measurement campaigns we performed. The first campaign that we shall refer to as Phase One, started in June of 2003, and concluded in December of 2004. The objective of Phase One was to identify the worst case MTM channel. This campaign was performed at 2.4 GHz. The second campaign or Phase Two was performed at 5.9 GHz during 2006. The objective of Phase Two was to identify nominal channels at various specified ranges in specified environments.

5.1 Phase One: 2.4 GHz Measurement Campaign

The most challenging environment for MTM communications is the doubly selective channel that has large spreads in both delay and Doppler. We divided Phase One campaign into two periods. In Period One, we measured only delay spreads. In Period Two, we measured the doubly selective channel at only those sites found in Period One with long delay spreads.

5.1.1 Period One: Finding Worst-Case Delay

This first period was simple and economical. The second period required a considerable investment and logistics; therefore, it was very important to concentrate the resources in sites that would provide adequate data to develop a “worst-case scenario” model for future equipment testing. Using off-the-shelf 802.11b “sniffing” equipment, we measured power delay profiles along several streets and freeways in the area surround-

ing Georgia Tech for inter-vehicle distances ranging from roughly 30 m to 1000 m. While most of the delay spreads measured along our routes were small and consistent with previous inter-vehicle measurements [22], [25], occasionally, they increased temporarily and dramatically (by factors of six or more). We present aerial photographs of the locations where the spikes in delay spread occurred, and in most cases, we can see terrain features that may explain these increases in delay spread.

The Berkeley-Varitronics™ Locust system provides an affordable and simple STDCC implementation. The measurement system relies on a commercial access point with a transmit frequency of 2.4 GHz, to generate a channel-probing signal based on the 802.11b length-11 Barker code. The Locust system "listens" for the specified channel-probing signal. The chip period of this signal is 90 nS; therefore, the system can detect up to 990 nS delays. The system also includes a GPS recorder. The Locust system creates and records a length-22 delay (apparently a $2\times$ sampling) profile "snapshot" every time the access point starts a frame. Since the IEEE 802.11b frame rate depends on the receiver response and since the Locust just listens or "sniffs," there is no way of knowing the repetition rate of each correlation output.

We conducted a series of measurement sessions to cover as many distinct scenarios as possible within the Atlanta metropolitan area. During the experiments, we used two vehicles: a compact sedan for reception and a cargo van for transmission. We used the same antennas shown in Figure 18, and we had two antenna positions: (1) an antenna on the roof of each vehicle and (2) the transmission antenna on the van's hood and reception antenna on the car's trunk. The latter configuration is shown in Figure 68.

Figure 67: Berkeley-Varitronics Locust system to the left and the chosen Linksys access point to the right.

Figure 68: Vehicles used with transmission antenna on van's hood and reception antenna on car's trunk.

During each session, we varied the relative position and distance between the vehicles, and we allowed traffic to obstruct the line-of-sight. The vehicles' speeds typically matched that of traffic flow. Each session contained from 34,000 to 65,000 sounding snapshots, corresponding to approximately 30 minutes to 1 hour in duration. A power-level reading, a set of GPS coordinates, time, and vehicle speed were recorded with each delay profile snapshot as shown in Figure 69.

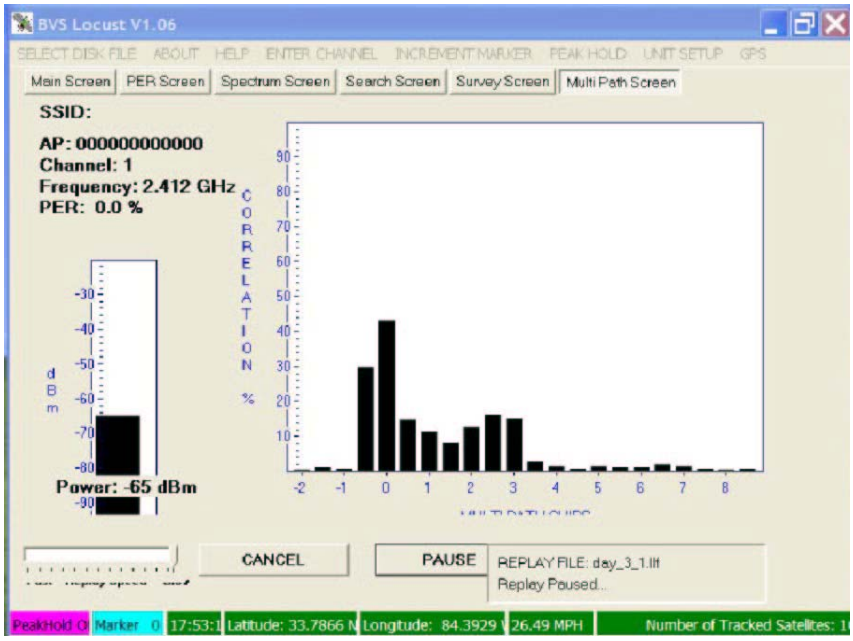

Figure 69: Berkeley-Varitronics Locust multipath screen.

To enable us to see trends in delay spread, we performed the following data processing. We first defined four power-level thresholds: -90, -80, -70, and -60 dBm. For each threshold, we deleted all of the snapshots below it. Not all snapshot sets allowed the four threshold levels. We then obtained the RMS delay spread for each surviving snapshot according to [67]:

$$\sigma_\tau = \sqrt{\overline{\tau^2} + \left(\overline{\tau}\right)^2} \tag{5.1}$$

where

$$\overline{\tau} = \frac{\sum_k P(\tau_k)\tau_k}{\sum_k P(\tau_k)} \tag{5.2}$$

and

$$\overline{\tau^2} = \frac{\sum_k P(\tau_k)\tau_k^2}{\sum_k P(\tau_k)} \tag{5.3}$$

for which $P(\tau_k) = \left(a_k / 100\right)^2$ is the power of the k^{th} *(k=1,…,22)* multipath in a snapshot and a_k is the percent correlation for the kth multipath measured with the Locust system. We then performed a moving average (MA) of length L=10 for these RMS values, where we ignored the *L* averaged values following a deletion, to avoid edge effects. For each set of averaged RMS delay spreads, we obtained a histogram of the 100 highest values. We obtained a total of 20 sets. We then selected the locations where the histograms indicated a significant cluster of high values independent of the threshold level, *i.e*., where the cluster repeated for different power thresholds. Since each snapshot has GPS information, we could locate these clusters. With the clusters' geographical coordinates, we were able to obtain aerial photos of the locations.

We present the results for four sessions of measurements. In Figure 70 and Figure 71, we show the received power, the averaged RMS delay spreads and the histogram of highest averaged RMS delays spreads, respectively, for the first session. This session was the only one where the antennas were on the roofs of the vehicles. We observed substantial power variation through the vehicles' trajectory. The delay spread record and the histogram show four clusters of high spreads. Other than these clusters, the delay spreads were similar to platooning-type spreads (~ 40 ns) [22], [25]. The three highest histogram clusters are labeled A, B, and C. Often, as indicated by comparing Figure 70 and Figure 71, the lowest power corresponds to the largest delay spreads, because of loss or obstruction of the line-of-sight. The narrow clusters are about 1 to 2 minutes wide. The aerial photographs corresponding to clusters A, B, and C are shown in Figure 72 through Figure 74. All photos have the same scale and are oriented with North to-

wards the top of the page. The center of each photograph corresponds to the GPS coordinates of the corresponding cluster. Referring to Figure 72, the vehicle was traveling southwest on the freeway. Cluster A corresponds to the gently curving exit ramp. This exit has a high wall adjacent to the vehicle, distant reflectors including the opposite freeway wall, and buildings in view further along the exit ramp. Similar combinations of nearby reflectors and clear sight to faraway reflectors were often associated with clusters representing large delay spreads, as indicated in subsequent examples.

For Site B, shown in Figure 73, the vehicle was traveling north, and was passing a city park within an urban canyon in downtown Atlanta. Again, we have the combination of buildings nearby (on the left) and distant reflectors flanking the other three sides of the park. Similarly, in Figure 74, for Site C in midtown Atlanta, we have flat land surrounded by very tall buildings, including the two tallest buildings in the city.

The other six sites in the remaining figures show various combinations of parking lots, construction sites, and extremely large parking structures. Site D (Figure 75 to Figure 77) deserves special mention because its cluster is quite isolated and corresponds to an easily identifiable three-way intersection flanked by large buildings and open space.

With the exception of the third session (Figure 78 to Figure 80), each session included averaged RMS delay spreads on the order of 300 nS. All sessions reported here included averaged RMS delay spreads that are significantly higher than previous reports [22], [25] that used small transmitter-receiver separations (< 30 m). Noting that the transmitter-receiver separations used here were larger, ranging from 30 m to 1000 m, this observation is consistent with a trend observed in micro-cellular scenarios: delay spreads increase with transmitter-receiver separation [44].

Although the largest delay spreads often correspond to large power dips, as indicated previously, large delay spreads can occur without significant power dips, as documented in the fourth session, Figure 81 to Figure 86.

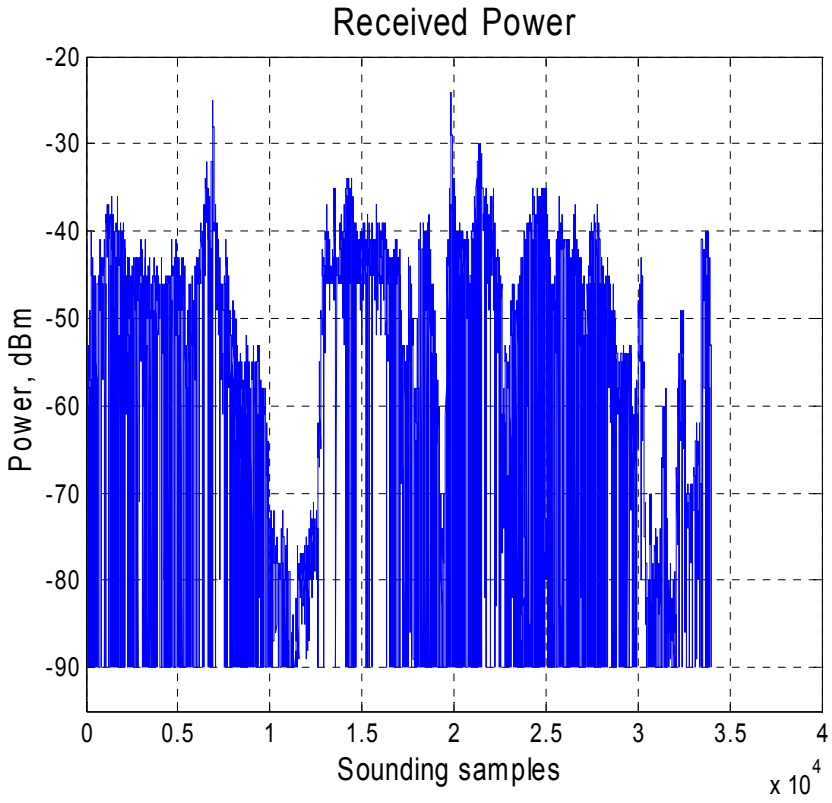

Figure 70: Received power for the first session.

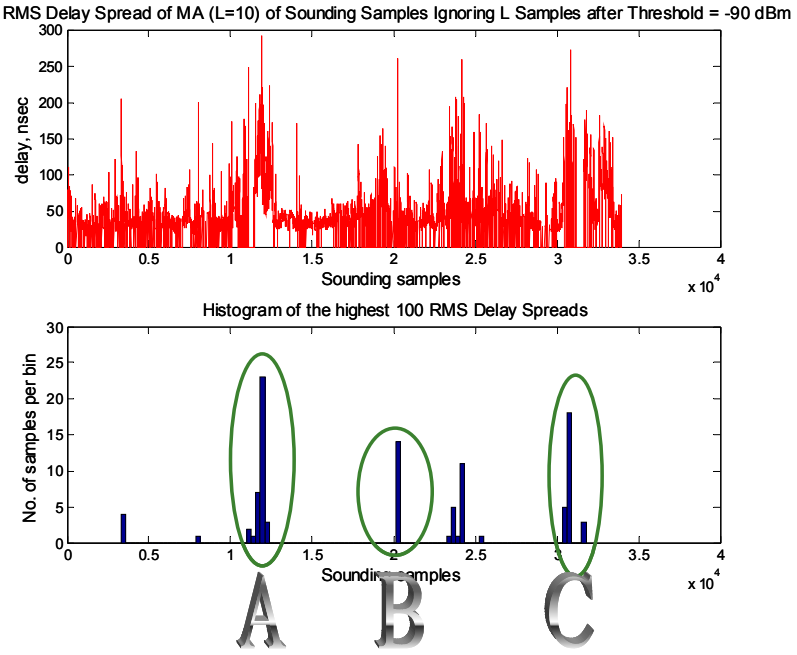

Figure 71: Above threshold RMS delay spread MA with corresponding histogram for the first session.

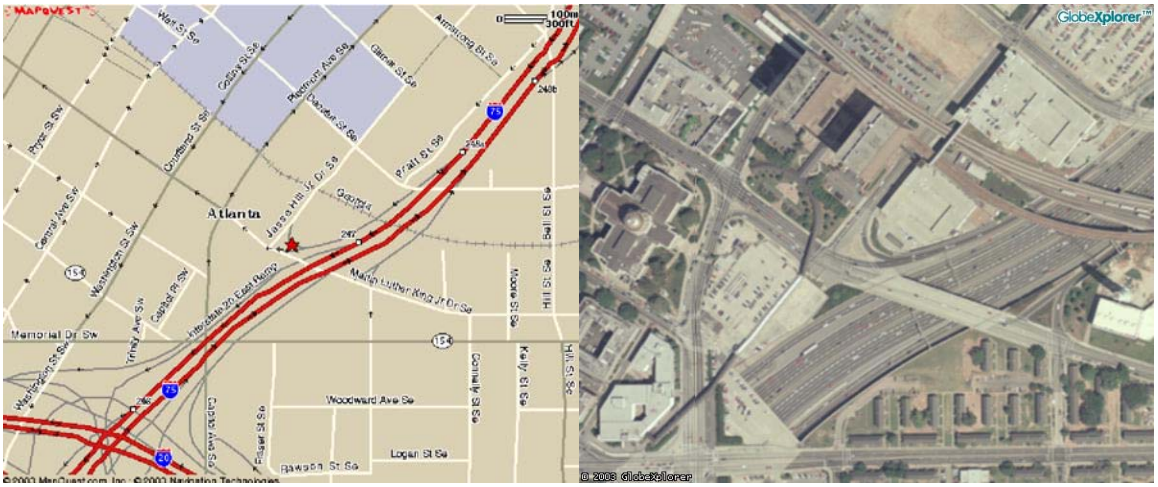

Figure 72: Location A @ (33.7487, -84.3857) I-285 exit ramp with distant office buildings.

Figure 73: Location B @ (33.7552, -84.389) Downtown Atlanta involving a park inside an urban canyon.

Figure 74: Location C @ (33.7723, -84.3872) Midtown Atlanta near the two tallest buildings in the city. We have flat land surrounded by very tall buildings.

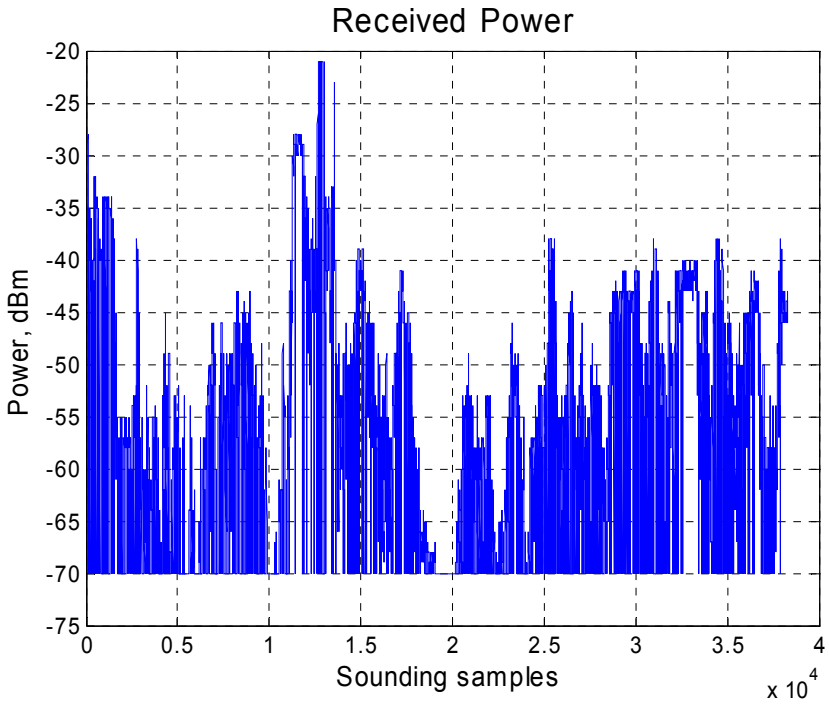

Figure 75: Received power for the second session.

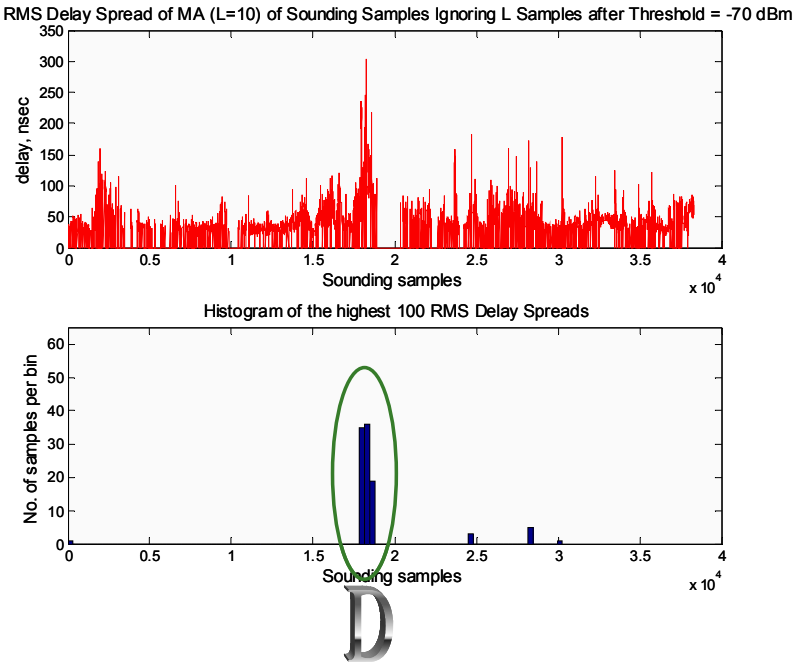

Figure 76: Above threshold RMS delay spread MA with corresponding histogram.

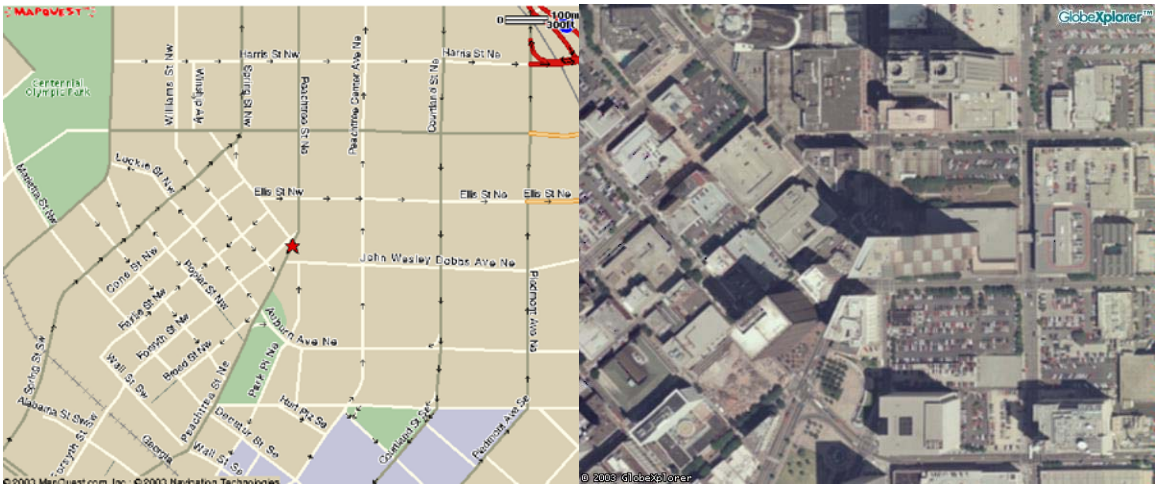

Figure 77: Location D @ (33.7575, -84.3877) Three-way intersection in downtown Atlanta.

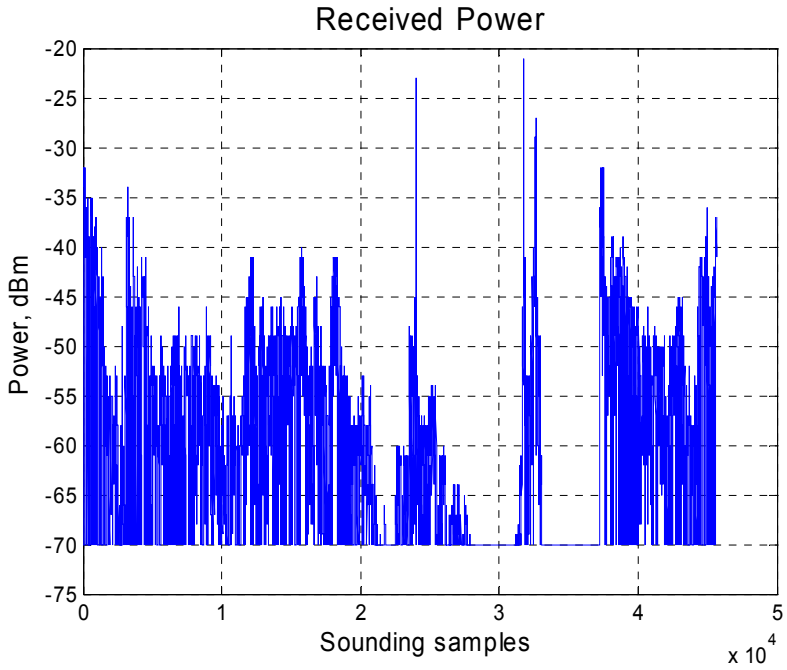

Figure 78: Received power for the third session.

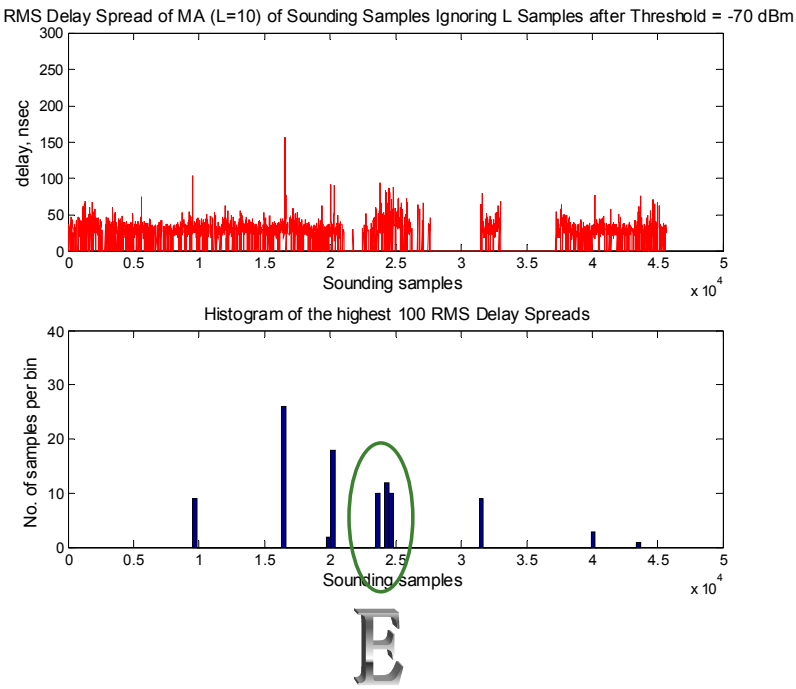

Figure 79: Above threshold RMS delay spread MA with corresponding histogram for the third session.

Figure 80: Location E @ (33.9179, -84.3392) Another I-285 exit ramp located close to office buildings.

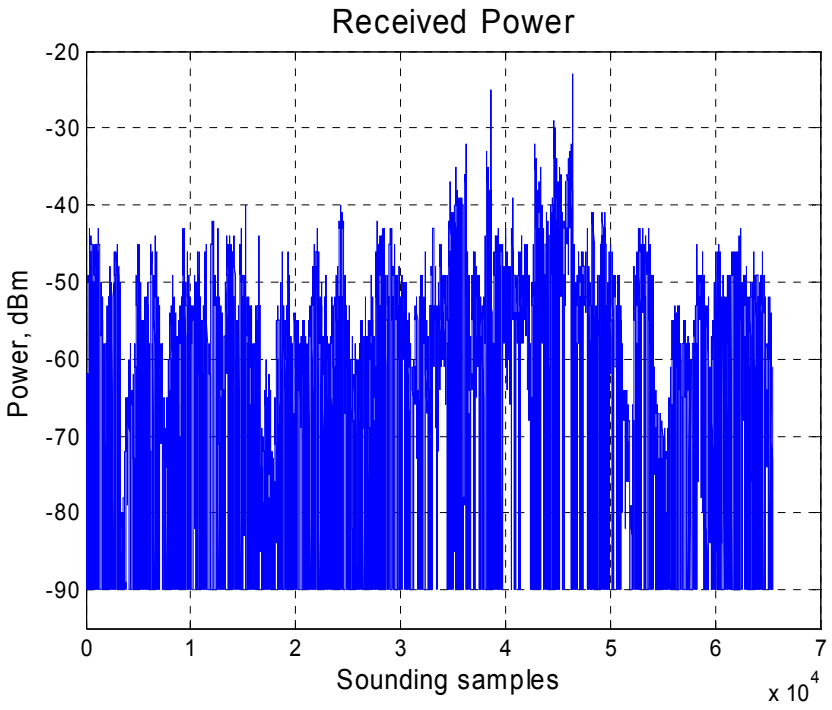

Figure 81: Received power for the fourth session.

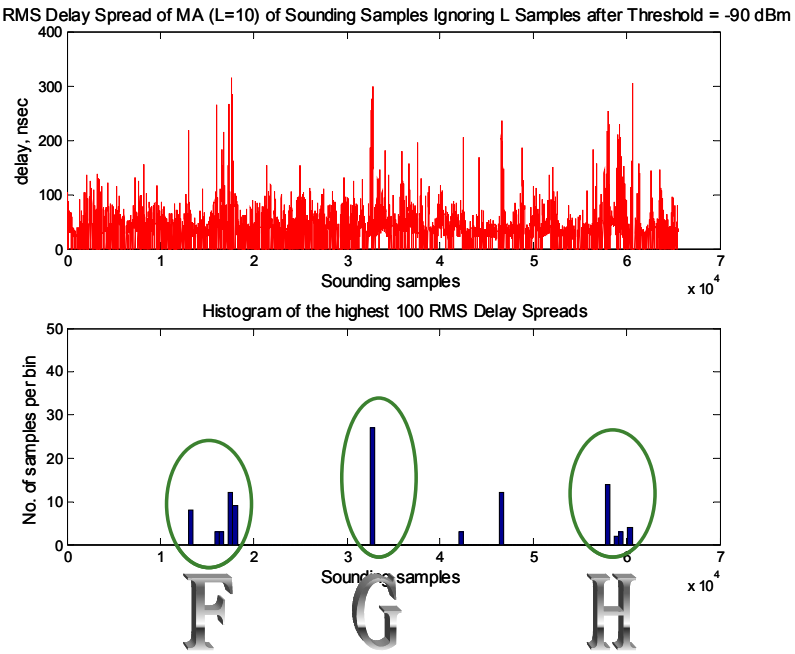

Figure 82: Above threshold RMS delay spread MA with corresponding histogram for the fourth session.

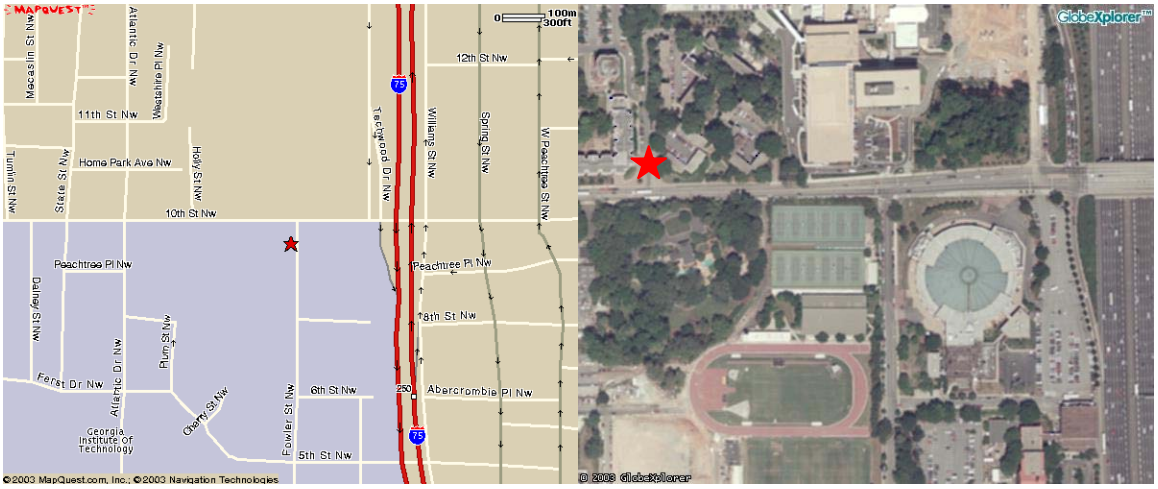

Figure 83: Location F @ (33.7810, -84.3937) Georgia Tech campus next to the Alexander Memorial Coliseum and Turner Television studios with a T-intersection with flat land near long buildings.

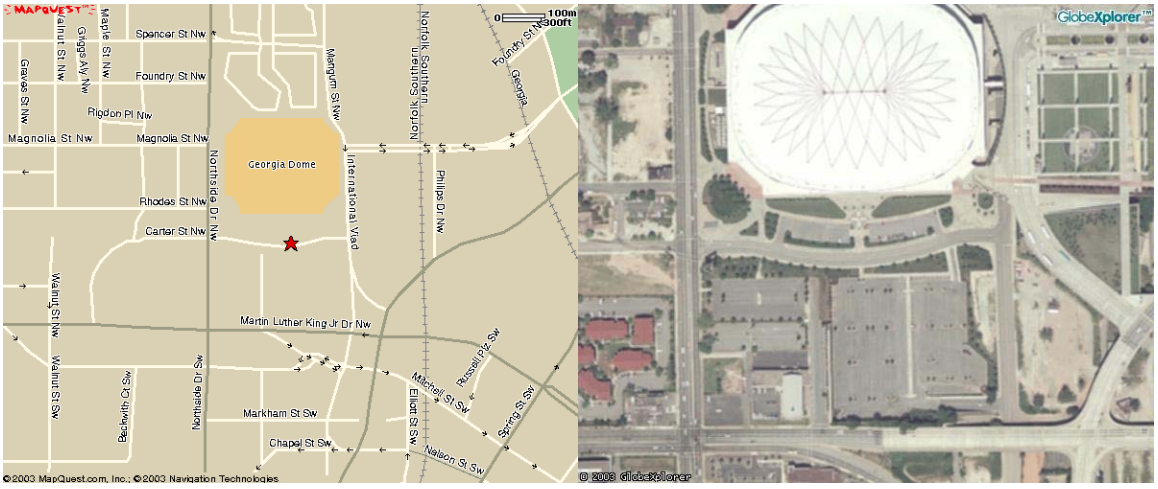

Figure 84: Location G @ (33.7562, -84.3008) Georgia Dome parking lot.

Figure 85: Location G is a very complex steel structure with many tunnels and ramps.

Figure 86: Location H @ (33.7756, -84.3873) Georgia Tech Centergy construction site. It is an urban canyon with parking lots.

5.1.2 Period Two

For Period Two [2], we measured the joint delay-Doppler characteristics using the system described in Section 4.1, at most of the sites described in Period One. Precise position of the vehicles was not available since the Locust GPS did not have enough resolution. We mostly traveled with the traffic flow trying to maintain the distance between vehicles less than 300 meters. We had LOS for most of the recordings, but sometimes intervening vehicles blocked it. At each site, we recorded 12 to 14 non-contiguous ten-second "Takes." Each of these "Takes" produced close to one gigabyte of data; therefore, by the end of the measurement campaign we had more than 100 gigabytes of data to process. Because of the memory limitations of Matlab™, we had to break each of the recordings into 0.7 second segments. The final data structure is shown in Figure 87.

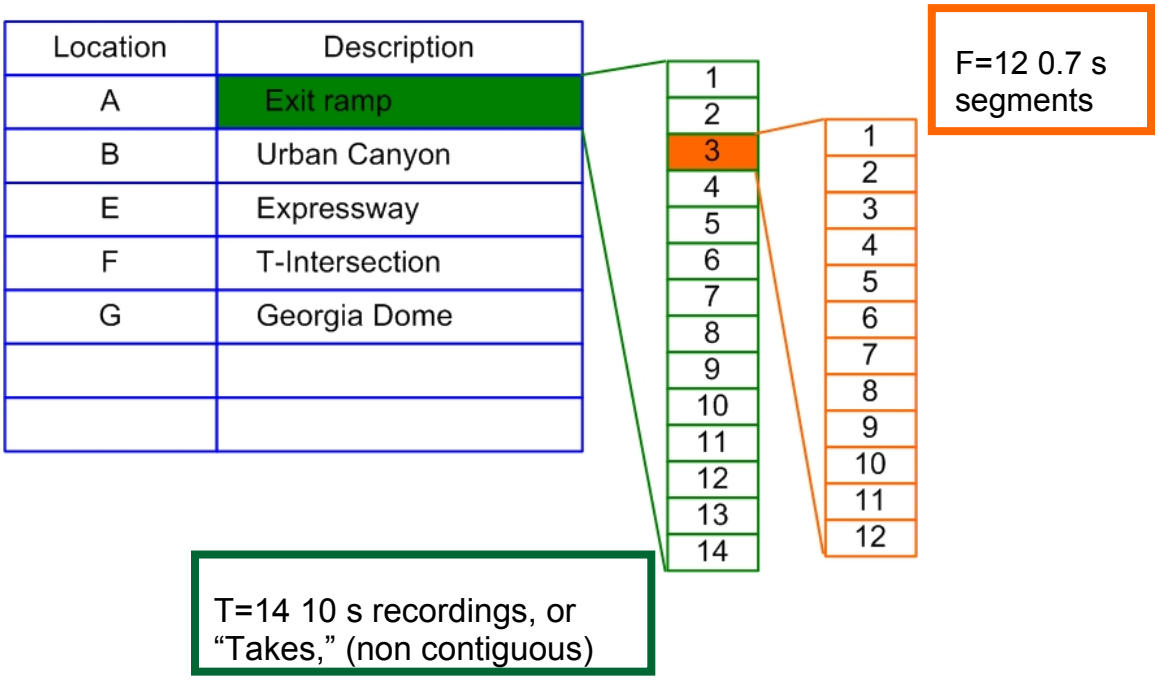

Figure 87: Phase One Period Two recorded data format.

Each segment was correlated with the original 511-chip sequence, and each one produced close to 27,500 IRs. The complex correlator outputs were read into a matrix,

row by row, so that the matrix dimensions were $27{,}500 \times 511$. Therefore, the columns of this matrix correspond to 50 ns "delay bins." Because there was no absolute time reference, there was no way to determine the absolute excess delay of the bins. However, the relative excess delays of the bins were known. Furthermore, because of the long length of the sequence (25.5 μs) and the usually small delay spreads of the MTM channel (on the order of 300 ns), it was easy to locate the consecutive bins with energy because the vast majority of bins were empty. By averaging the squared magnitudes of the correlator outputs down each column of the matrix, we could obtain power delay profiles for each 0.7 seconds segment.

5.2 Phase Two: 5.9 GHz Measurement Campaign

For Phase Two, we measured three main environments: Urban Canyon, Suburban Expressway, and Suburban Surface Street, and for each one, we had two types of links: MTM and roadside-to-mobile (RTM). Each combination of link type and environment defined a "scenario" from which we could develop a particular model.

For each scenario, we recorded several "Takes." Each "Take" was 9.6 seconds long, and we divided each one into 16 0.6 second segments. Each recorded segment was split into its MLS and OFDM parts. Similarly to Phase One, the MLS part was correlated to the chip sequence, and the output of the correlator was arranged into an impulse response matrix such that each row was a channel IR taken at a certain time (i.e. certain position of the cars) and each column represented a particular delay in the impulse response. For the Phase Two MLS part, the matrix dimensions for each 0.6 second segment were approximately $5{,}500 \times 511$, and they corresponded to 100 ns "delay bins." For the OFDM section, the number of columns was 512, and they corresponded to 50 ns "delay bins."

In Figure 88, we show the complete structure and organization of the measurement campaign. Each lower block indicates a particular scenario where we recorded at least a couple of “Takes.” From all these 138 “Takes,” we were required to develop specific models for particular scenarios in support of the IEEE 802.11p wireless access in vehicular environments (WAVE) / DSRC Standard. The specific task to support the aforementioned standard is to choose a particular scenario model to use in the motion-related standard’s equipment cerification test. The required models for particular scenarios are shown in Table 2. We selected the “Takes” for each model after obtaining the MLS part PDP and scattering function for all the segments. We based our selection criteria on SNR and stationarity of LOS Doppler shifts. The chosen segments had at least 25 dB of dynamic range. The vehicle speeds during measurement were approximately 105 km/h (65 mph) for the expressway and 32 km/h to 48 km/h (20 mph to 30 mph) for the surface streets. The biggest challenge in selecting locations for the measurements was finding straight roads to enable LOS conditions. Unless otherwise noted, magnetically mounted monopole antennas were used for the measurements.

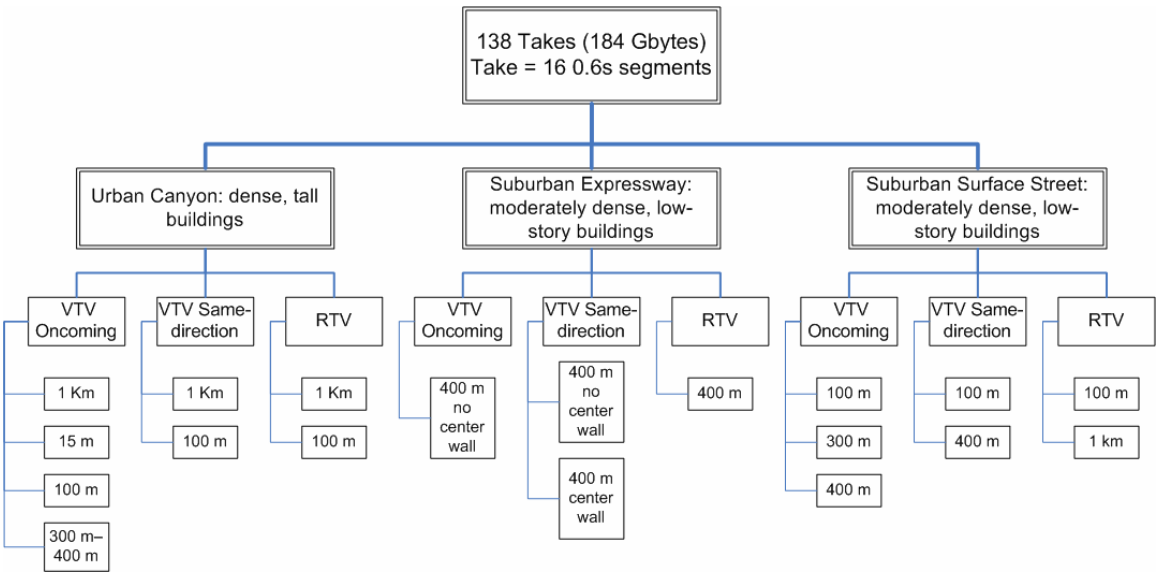

Figure 88: Phase Two recorded data structure.

Table 2: Description of the locations for each scenario

Scenario	Date	Location	Takes
MTM - Expressway Oncoming, 300-400 m	04/19/2006	GA 675 between exits 5 and 7	4
RTM - Urban Canyon 100 m	04/24/2006	Approach Peachtree Street at Colony Square from the North	4
RTM - Expressway 300-400 m	04/25/2006	Westbound GA 78	4
		Eastbound GA 78	4
MTM - Urban Canyon Oncoming 100 m	04/12/2006	Along Edgewood Avenue	2
	04/25/2006	Along Edgewood Avenue	2
RTM - Suburban Street 100 m	04/25/2006	Four different approaches to Memorial Drive and Candler Road	10
MTM - Expressway Same Direction With Wall, 300-400 m	04/19/2006	Along North I-285	7
		West on I-20	6
	04/17/2006	I-285 @ Ashford Dunwoody	4
		GA 400 North, just north of I-285	4

In the rest of this section, we present a brief description of each of the scenarios chosen for Phase Two. In each one, we show a representative photo of the scenario, the particularities encountered, and any other specific information necessary.

- **MTM - Expressway Oncoming, 300-400 m Scenario**

For this scenario, we found a stretch of highway without a middle wall at GA 675 between exits 5 and 7. For the measurement, we synchronized each of the vehicles so that they entered the highway at the same time. We then accelerated each one to 65 mph, and it was at that instance that we began recording. The recording or "Take" period sometimes allowed for the vehicles to cross or pass each other. We were able to obtain four good "Takes," *i.e*., good SNR, vehicle speeds, etc. From the total 64 0.6 second segments, we only chose the ones that represented a vehicle separation of 300-400 m for processing. We found these segments either by looking at their Doppler spectrum or by using the notes taken. These particular segments showed a fixed LOS Doppler shift in the first tap spectrum. In Figure 89, we show an instance when we had the required

separation between the vehicles. The traffic conditions shown in the picture were typical for all the “Takes.’

Figure 89: Approaching or oncoming vehicle is the white van seen on the left..

- **RTM - Urban Canyon, 100 m Scenario**

For this scenario, the transmitting antenna was mounted on a pole near the urban intersection of Peachtree Street with Peachtree Circle, as shown in Figure 90. The antenna was 6.1 m (20 feet) high. The target range was 100 m. For the measurement, we had to wait for the traffic lights and traffic conditions to allow us to initiate a “Take” when the receiver vehicle attained the required 20-30 mph speed. We obtained four “Takes” with the required specifications. Once again, from the 64 0.6 second segments that we collected, we only chose the ones with the 100 m separation as indicated by the notes taken.

Figure 90: Roadside antenna at the intersection of Peachtree Street and Peachtree Circle.

To avoid deleterious effects from very deep fades, from all the remaining segments, we did not include the segments with an envelope level less than a threshold in the analysis. The envelope of the signal for all the measured data in this scenario is shown in the top of Figure 91. The threshold, which was arbitrarily set, is shown in blue. The stem plot in the lower part of Figure 91 indicates the deleted segments. As we can notice from the figure, we only had 30 segments to process.

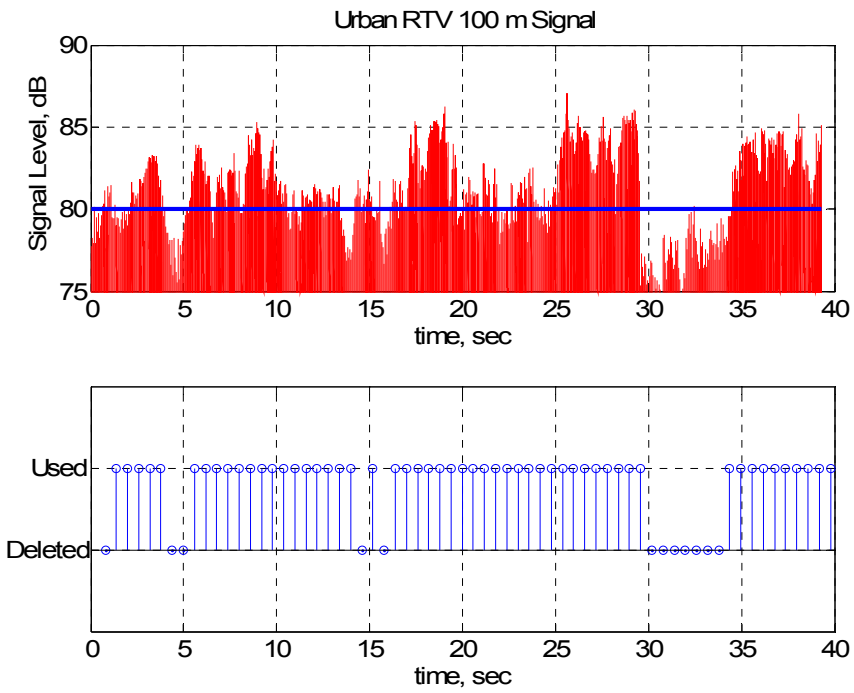

Figure 91: Signal envelope and deleted segments for the RTM – Urban Canyon 100m scenario. The signal level corresponds to relative power, i.e., relative to the minimum signal recorded. It **does not** represent RF signal power.

- **RTM – Expressway, 300-400 m Scenario**

For this scenario, the transmitting antenna was mounted on a pole off the side of the GA 78 expressway, as shown in Figure 92. The antenna was 6.1 m (20 feet) high. A half-dome antenna was used for these measurements. Measurements were taken as the vehicle approached from both directions on the expressway. We coordinated the start of the recordings to initiate when the receiver vehicle reached 65 mph. We could obtain four “Takes” for each direction for a total of eight. Of the collected 128 0.6 second segments that we collected, only 91 complied with our specifications as described in previous scenarios.

Figure 92: Roadside antenna on GA 78.

- **MTM – Urban Canyon Oncoming, 100 m Scenario**

For this scenario, it was very difficult to find a location with the urban canyon characteristics that allowed the required 20-30 mph speed. The best location we could find was Edgewood Avenue in Downtown Atlanta. In Figure 93, we show the starting point of the receiver vehicle. From the figure, we can notice that to reach the required speed, we had to synchronize the vehicles' movement to the traffic lights. Because of the dense traffic, we required a considerable time to set up the vehicles for a "Take." We were only able to obtain two good "Takes" in each of the two days we dedicated to this scenario. Of the 64 0.6 second segments that we collected, we could only used 56 because the others did not present a Doppler spectrum indicating a 100 m separation.

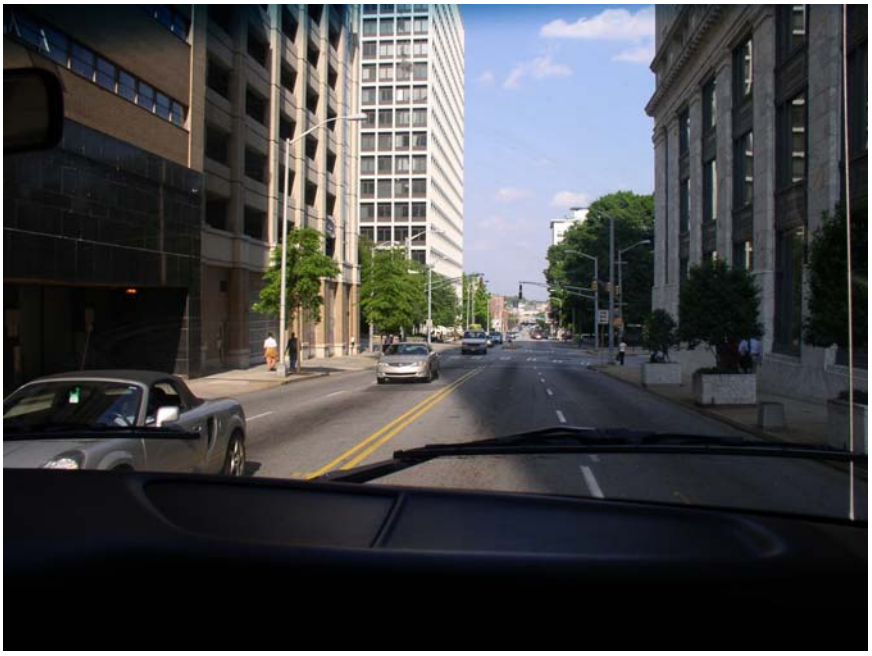

Figure 93: Starting point of receiver vehicle on Edgewood Avenue.

- **RTM - Suburban Street, 100 m Scenario**

For these measurements, the transmitting antenna was mounted on a pole near the intersection of Memorial Drive and Columbia Drive, as shown in Figure 94. The antenna was 6.1 m (20 feet) high. The target range was 100m. The receiver vehicle approached the intersection from the four possible directions. We started each “Take” when the receiver vehicle reached the required 20-30 mph speed. We obtained a total of ten good “Takes.” Of the 160 0.6 second segments that we collected, we were able to use only 97 because of the same reasons previously explained.

Figure 94: Roadside antenna at the intersection of Memorial Drive and Candler Road.

To avoid possible very deep fades, of the remaining 97 segments, the ones with less than a threshold were not included in the analysis. The envelope of the signal for the available measured data is shown in the top of Figure 95. The threshold is shown in blue. The stem plot in the lower part of Figure 95 indicates which segments were used and which were deleted.

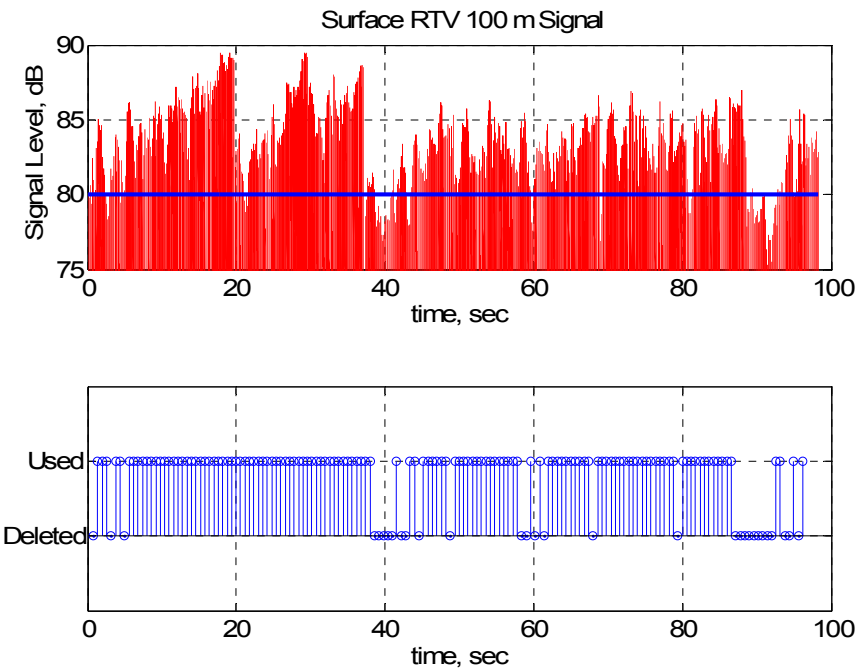

Figure 95: Signal envelope and deleted segments for the RTM – Suburban Street 100m scenario. The signal level corresponds to relative power, i.e., relative to the minimum signal recorded. It **does not** represent RF signal power.

- **MTM - Expressway Same Direction with Wall, 300–400 m Scenario**

This scenario contains data measured at many different locations along various expressways in Atlanta, Georgia. However, all locations had a center wall between oncoming lanes as shown in Figure 96. Of all the scenarios, this was the easiest to record. For each "Take," we only had to verify the 300-400 m separation since most of the time we were able to maintain the required 65 mph speed. We obtained 21 good "Takes." We used 334 0.6 second segments out of the available 336.

Figure 96: Typical conditions for the Expressway Same Direction with Wall scenario. The transmitter vehicle kept a 400 m separation to the front of the receiver vehicle.

CHAPTER 6

MEASUREMENT RESULTS AND CHANNEL MODELING

In this chapter, we used one common scenario from each of the two measurement campaigns to describe how we develop the final product of this investigation, which is a reliable channel model to use either in simulation or a channel emulator. The most similar scenarios that we found were the Location E Expressway from Phase One and the Suburban Expressway MTM Same Direction Wall from Phase Two. We have to clarify at this point that the modeling process presented in this chapter has been progressive, *i.e.*, for the second phase, we started the modeling process including all the previous experience gained in the first phase. For Phase One, we concentrated our efforts in matching the BER behavior between the recorded channel and our proposed synthesized channels. For the channel synthesis, we used the random noise filtering technique. From the recorded channel, we obtained the number of taps, their delay, their power, and a filter template. As we will describe in Section 6.1.2.4, we have learned two main lessons from Phase One channel modeling. First, we have learned that even when a spectral template clearly indicates a narrow frequency peak, as you would expect from a strong LOS component, it does not produce a significant K-factor. Second, the BER performance over the recorded channel clearly indicates that there is a strong relationship between BER and the existence of a LOS component. For Phase Two, we developed a technique to separate the random and deterministic parts of the recorded channel. Once we had this separation, we used the random part to obtain the per-tap spectra. This time, instead of using the obtained spectra as filter templates, we develop a spectrum fitting

procedure to use a combination of the four possible spectrum shapes we can find in either a simulation system or a channel emulator. We used the deterministic part to produce the K-factor. For this second phase, instead of using a simulation system, we tested our proposed models with hardware prototypes developed for the DSRC standard. Once again, we empirically noticed a strong relationship between the K-factor and, for this phase, the packet error rate (PER) of the prototype sytem. This relationship suggests that in order to have a more precise model, it is necessary to model the dynamics of the K-factor.

6.1 Phase One Channel Modeling

In the first of two parts of this section, we developed a channel model, which we will call a statistical model, following the procedure of Section 2.3. In the second part, we propose a new channel modeling method, which we named Partitioned Model, to compensate the limitations encountered in the Statistical Model.

6.1.1 Statistical Model Develpment

We considered Mohr's method [51] as our first approach for our model development. This method considers direct averaging of the extracted model parameters to obtain the overall model parameters. As we shall demonstrate, this approach is far from satisfactory to comply with the performance extremes encountered in the real or recorded channel. To justify this claim, we developed a system simulation tool capable of measuring the performance of a real or synthesized channel.

6.1.1.1 Resulting Tap Characteristics

For the expressway location, we recorded 14 ten-second "Takes." We divided each take into 12 0.7-second segments for their analysis. Please note that each "Take" corre-

sponds to a physically different time and location, *i.e.*, each "Take" could be minutes and kilometers apart from another. In Figure 97, we show the PDPs computed according to (2.37) for all the 0.7 s segments of the 14 "Takes." We observe that most of the PDPs die out before 1 μs because of the generally confined nature of the channel.

Assuming that most commercial channel emulators are six or 12 taps per channel, we decided to generate 6- and 12-tap channel models using the methodology described in the previous section. First, we generated a model for each of the 168 0.7 s segments, and then, we generated overall models by averaging the 168 segment models as follows:

$$\begin{aligned} \tau o_m &= \frac{1}{N}\sum_{i=1}^{N}\tau_{mi} \\ Po_m &= \frac{1}{N}\sum_{i=1}^{N}P_{mi} \qquad \text{for } m = 1,\mathrm{K}\ M \\ PSDo(f)_m &= \frac{1}{N}\sum_{i=1}^{N}PSD(f_i)_m \end{aligned} \tag{6.1}$$

where o indicates an overall or averaged model, PSD indicates power spectral density, f indicates frequency, and N is the number of segments corresponding to non-zero powers in the mth group.

We present the 6 and 12-tap scattering functions for the overall models in Figure 98 and Figure 99 respectively. The corresponding statistical parameters are given in Table 3. The first thing we notice in the Doppler spectra is the "LOS-like" or Ricean behavior for each of the first several paths. We show in Table 3 that the first five paths in both models have a significant K_{Rice} factor. This suggests that there are many reflectors traveling at a similar speed inside a 45 m locus of an ellipse defined by the reflecting path length. We also notice a widening of the Doppler spectra for the later taps. We will later

show that the spectra can widen up to ±400 Hz, which corresponds to path-length rates of change of ±110 mph. Since the vehicles were traveling in the right lane at speeds of approximately 55 mph, 110 mph suggests a single-bounce path that is either approximately in front of or behind the vehicle, and could be attributed to stationary scatterers on the side of the road. In several of these later spectra, we can notice some small spikes on the sides of the spectra. These spikes were likely caused by transient paths reflecting from highway overpasses.

Table 3: 6- and 12-tap model results

Tap	Delay, ns τ_m from (2.38)		Magnitude, dB P_m from (2.39)		K_{Rice} from (2.40)	
1	0	0	0.0	0.0	93.4	100.9
2	115	64	-12.0	-7.6	1.1	5.7
3	226	125	-18.3	-14.9	1.3	4.3
4	377	189	-22.5	-18.6	1.7	3.5
5	608	251	-23.3	-21.0	1.1	1.9
6	991	340	-25.3	-23.8	0.4	0.7
7		477		-25.8		0.3
8		547		-25.4		0.4
9		666		-24.4		0.0
10		789		-24.3		0.1
11		1115		-25.8		0.1
12		1499		-27.6		0.1

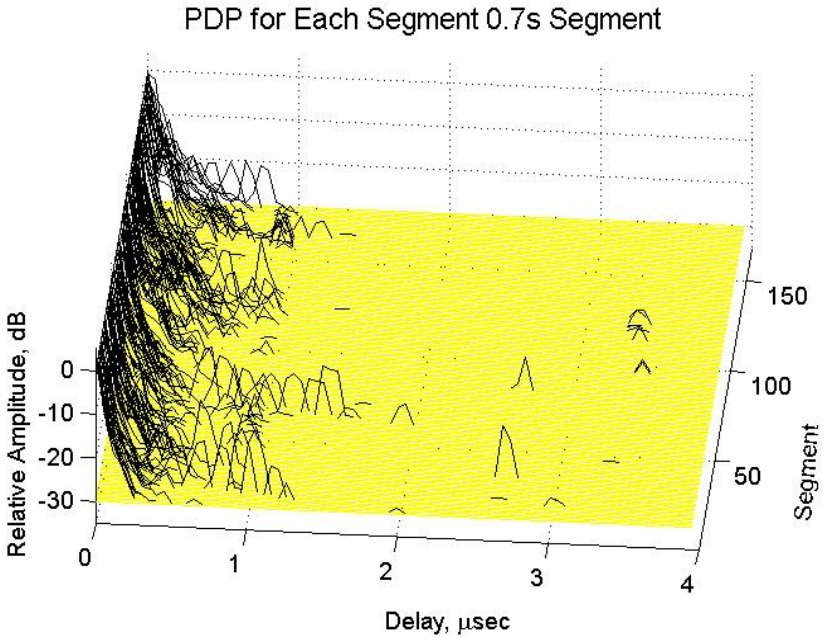

Figure 97: Expressway PDPs obtained using (2.37).

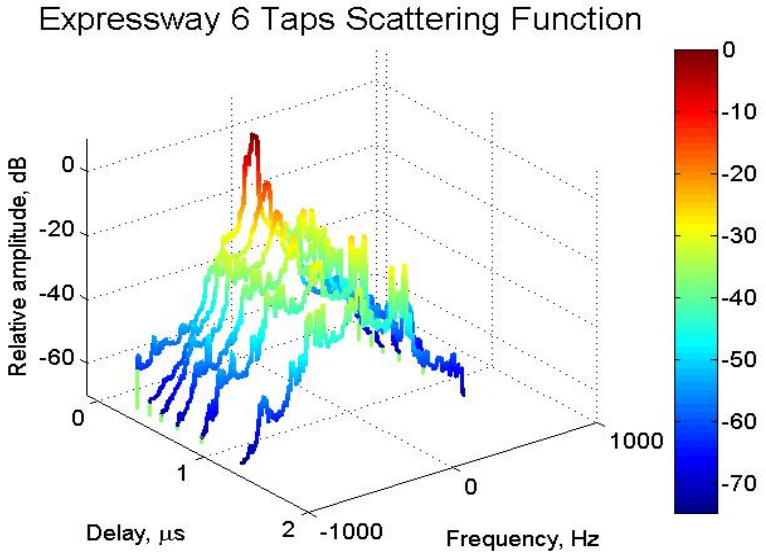

Figure 98: 6-tap model scattering function.

We can synthesize the channel using filtered noise on each tap, where the filter characteristics match the spectra of the statistical model [37]. As an example, the estimated scattering function of the synthesized 12 tap model is shown in Fig. 5, which represents a long-time (*i.e.* 0.7 s) estimation. To confirm the short-time behavior, we estimated the long-term and short-term Doppler spectra of similar taps of the recorded and

synthesized channel. For the long-time spectrum, we used the approximately 27,000 IRs in 0.7 s for the estimate, and for the short-time spectra, we obtained the estimate every 2,048 IRs or approximately every 50 ns. In Figure 101, we show the resulting Doppler spectra for the third tap of the synthesized model. In Figure 102, we present the results of a latter tap of one 0.7-second segment of one of the “Takes” of the recorded channel. As we can see in these figures, the short-time spectra of the synthesized channel have transient behavior similar to that of the real channel. We can also notice a spectra widening up to 400 Hz.

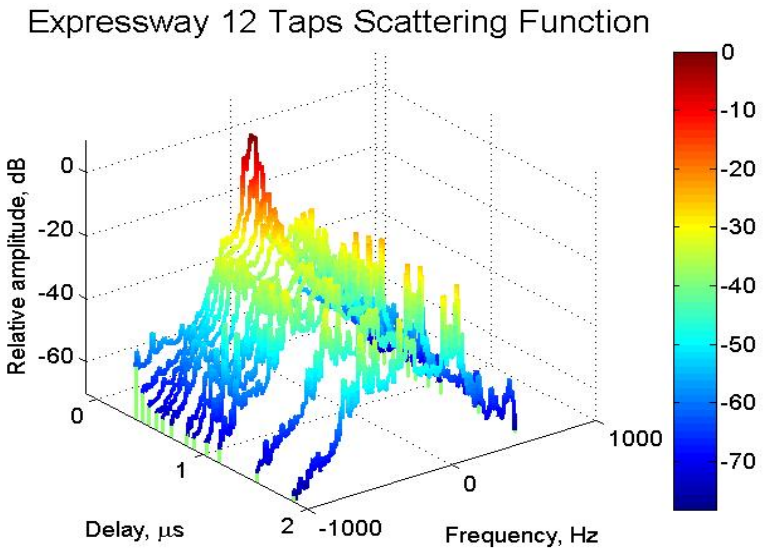

Figure 99: 12-tap model scattering function.

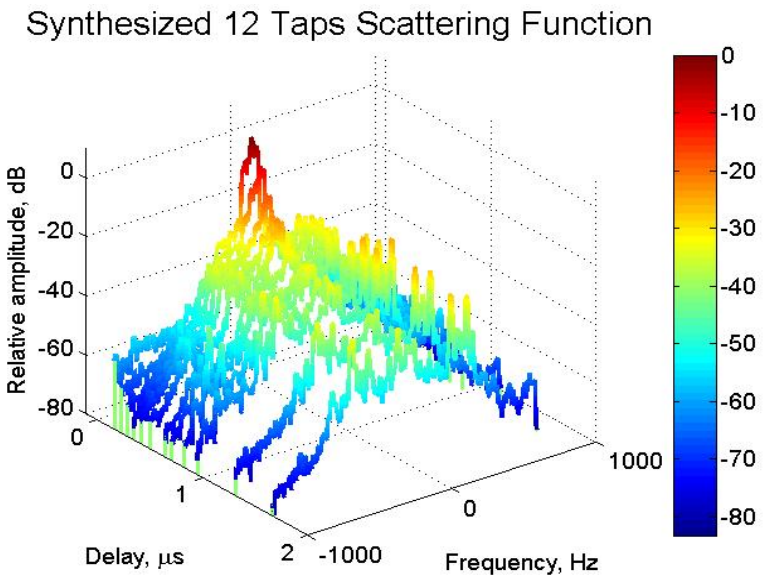

Figure 100: Synthesized 12-tap model scattering function.

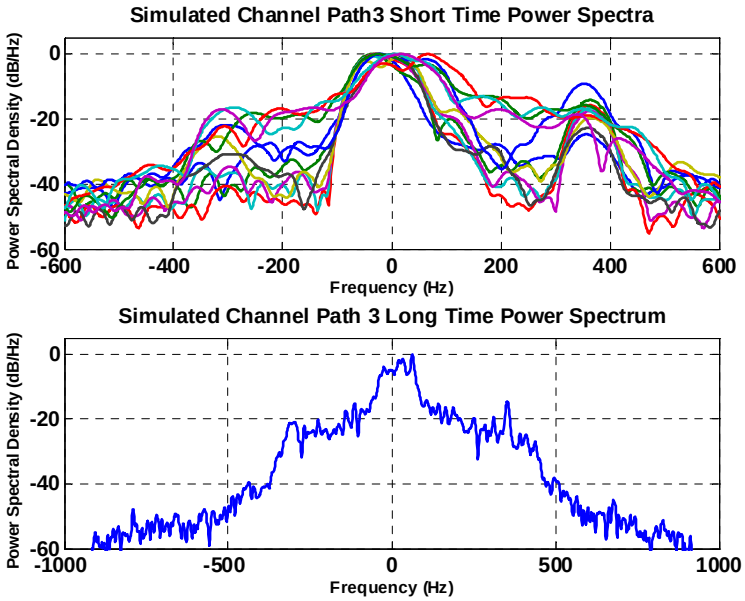

Figure 101: Simulated short time Doppler spectra and long time Doppler spectrum for the third tap of the 12-tap model scattering function.

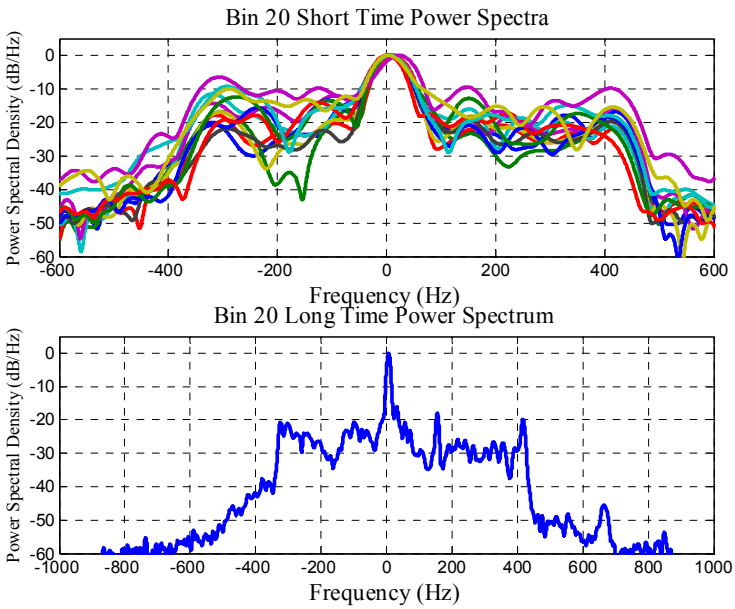

Figure 102: Measured short time Doppler spectra and long time Doppler spectrum of a latter tap of one of the resulting scattering functions.

6.1.1.2 Testing Using a DSRC Simulink™ Model

To validate the statistical channel model, we compared the bit error rate (BER) performance of a DSRC link over the recorded channel and over the synthesized channel. We normalized all the channels so that their PDPs had unit area; this includes separate normalization for each measured segment. We developed a Simulink™ model that follows faithfully the specifications of the DSRC standard [6] shown in Table 4. The DSRC standard is a half bandwidth version of the 802.11a standard; therefore, all the coding, training symbol structure, framing, etc. are identical [35]. The model includes an adaptive modulation system to select among the eight transmission modes. This adaptive modulation relies on a SNR threshold detector that works on a frame by frame basis. The noise is defined as the mean square of the difference between the received complex symbol and its corresponding constellation point. The receiver also contains a two- step channel equalization process. The first step uses the long training symbol to obtain an initial channel estimate for each frame. The second is a per-symbol adaptive channel

equalizer that uses the pilot tones following the specifications in [33]. The OFDM symbol is modulated in only 52 subcarriers (48 data and four pilot tones) out of 64, has a central null, and has 8.0 μs duration with a 1.6 μs guard band interval. The total occupied bandwidth is 8.3 MHz. No thermal noise was added in our simulations

The length of a frame is set in the medium access control (MAC) layer. The total number of symbols per frame is set by two parameters: LENGTH and DATARATE. The LENGTH parameter value has a range of 1 to 4095 octets or bytes. This range is for un-coded data bits. The DATARATE parameter value is specified by the range covered in the first column of Table 4 [6]. For example, the longest frame for the fastest 27 Mbps modulation will contain 156 OFDM symbols, or the longest frame for the slowest 3 Mbps modulation will contain 1369 symbols. For the simulation, and since we used adaptive modulation, we used 68 OFDM symbols per frame, from which the first four symbols are the short and long training symbols. We chose this frame length as a compromise for the frame length vs. modulation mode trade-off and as a compromise between the frame length and equalizer performance.

Table 4: DSRC standard specifications

Data Rate, Mbps	Modulation	Coding Rate	Coded Bits per OFDM Symbol	SNR Threshold dB
3	BPSK	1/2	48	<10
4.5	BPSK	3/4	48	10
6	QPSK	1/2	96	11
9	QPSK	3/4	96	14
12	16-QAM	1/2	192	18
18	16-QAM	3/4	192	22
24	64-QAM	2/3	288	26
27	64-QAM	3/4	288	28

6.1.1.3 Model Validation Process

We were interested in exploring channel dynamics and how those dynamics impact BER statistics. Therefore, we considered two types of models: “overall” and “per-segment.” The overall model is based on the entire data set of 168 0.7 s segments, whereas a per-segment model is based on only a 0.7 s segment. For each type of model, 6 and 12 Tap versions were produced. We collected BER statistics for the overall models and compared them to the BER statistics collected for the set of per-segment models. Additionally, we compared these statistics to those of the recorded channel.

We collected BER statistics as follows. For all models and the recorded channel, we calculated a different BER value for every 0.7 s segment. For the recorded channel, this was just a matter of dividing the record into 168 0.7s segments, simulating the DSRC link over each segment, and for each segment, dividing the number of information bit errors (after decoding) by the total number of information bits transmitted in that segment. This procedure yielded 168 trials or samples of the BER.

For each overall model, 168 0.7 s segments of channel impulse responses were synthesized, each with different random seeds. The BER was computed for each segment to create 168 samples of BER for each overall model. To synthesize the overall 6 and 12 tap model processes, we used the scattering functions of Figure 98 and Figure 99 as the filter templates for 168 0.7 s different random sequences that produced 4,603,200 different IRs for each process.

For each per-segment model, we obtained a different scattering function and therefore a different “per-segment” model for each 0.7 s segment. Thus, we had 168 models for the 6-Tap case and 168 models for the 12-tap case. We then used each per-segment model to synthesize a 0.7 s segment of channel IRs. We calculate a BER for each 0.7 s

segment. Because of changes in the types of distortion in the channel as we drove along and in different “Takes,” we expect these per-segment models to be different from one another, and as a collection, to produce a wider range of BER variation.

Each 0.7 s segment, and therefore, each BER sample, corresponded to 1,286 frames and 64 OFDM data symbols per frame. At the lowest data rate, this corresponded to 24 bits per symbol, or about 1.98e6 bits per segment. Since adaptive modulation was used, 1.98e6 bits is just a lower bound. The BER was also averaged over the 168 segments, which implies that the average was taken over a minimum of 3.32e8 information bits.

We also collected the statistics of BER when each BER sample is calculated over a frame period. Although the BER calculated this way, when viewed as a sample mean, is not statistically significant, it is useful to view these BER statistics, since protocol performance is impacted by the frame error rate.

6.1.1.4 Model Results

In Figure 103, we show the CDFs of BER calculated over 0.7 s segments, for each of the four models and the recorded channel. From this figure, we see that none of the synthesized channels produced zero errors for this long time period. We also observe that CDFs of the per-segment channel models match the CDF of the recorded channel better than the overall models, with the 6-tap model having the closest match. This mismatch between the overall model CDFs and the others suggests that this stretch of expressway produces a quite dynamic channel that cannot be captured adequately by a single tapped delay line model. In Figure 104, we present the CDF when the BER is calculated for each frame. For this shorter time, 544 μs, the synthesized models do produce a significant number of frames with zero errors. Once again, the per segment models

produce the best match, and from the two figures, we can conclude that the 6 taps per segment model is the closest match to the real channel under our experiment conditions.

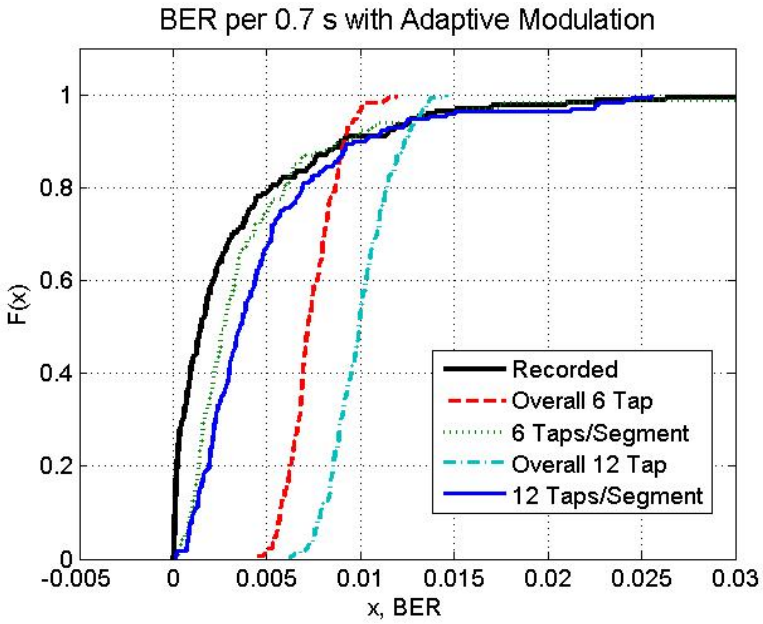

Figure 103: Recorded channel and models CDFs using the BER per 0.7 s segment, a 64 OFDM symbol frame, and adaptive modulation.

Table 5: Total transmitted bits, received errors, and BER for each process

	Data bits	Errors	BER
Recorded	1.18e9	2.48e6	2.10e-3
6 Taps	1.23e9	9.07e6	7.37e-3
6 Taps/Segment	1.66e9	5.33e6	3.22e-3
12 Taps	0.85e9	8.45e6	9.93e-3
12 Taps/Segment	1.28e9	4.94e6	3.84e-3

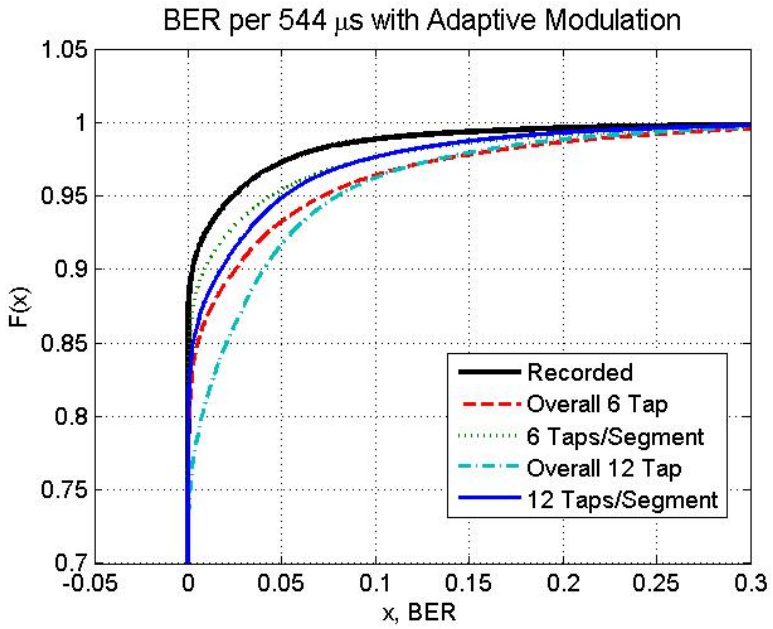

Figure 104: Recorded channel and models CDFs using the BER measured for each 64 OFDM symbol frame and adaptive modulation.

To further quantify the performance of the overall or averaged statistical channels, we present the average BER for each case in Table 5. We observe the adaptive modulation effect in the total number of data bits per process. From this information, we deduce that the per-segment models allow higher modulation modes or are “easier” channels.

6.1.1.5 Statistical Model Extraction Defficiencies

When we first averaged the segment models, we encountered a problem in the averaged tap delay values since they were not monotonically increasing. As we can see in Figure 97**,** many of the significant bins of each segment PDP will not be consecutive. In particular for the latter taps, the average will include many zeros and decrease the final delay value, which will create shorter delay values than the previous taps hence non-monotonically increasing; therefore, for the averaged models, we ignored the zero elements in the average, *i.e.*, the value of *N* in (6.1) was not 168 for these cases. The value was the number of nonzero elements. Another problem was that the averaged spectra

included contributions from quite different delays. These diverse contributions created excessively wide spectra. Because of the OFDM sensitivity to frequency offsets, the wider spectrum causes a higher BER.

In Figure 98 and Figure 99**,** we can notice that for such a high K_{Rice} factor, the peak of the first tap spectrum looks “wide.” The shape for this tap spectrum in any given segment is a high, very narrow peak with a lower wide base. The frequency position of this narrow peak varies from segment to segment since the vehicles speeds are different. When we average the contributing spectra, the different peak positions will show as a broad central peak as seen in Figure 105.

Averaging also increases base width. This effect is also shown for the last tap of the model in Figure 106. As indicated by the thick line, the averages tend toward the wider section of the spectra set.

For an RF channel emulator, the spectrum for a tap is specified in part by its K_{Rice} factor, the frequency offset of the deterministic part (a spectral line), and shape of the spectrum of the random part. If the model of this paper is to be further modified to be suitable for an RF channel emulator, then spectral lines must be assigned, and shapes, such as “rounded” or “classic 6 dB” [79], must be fit to the tap spectra. We observe that the broad peak of the averaged spectrum in Figure 105 should not be fit to some shape, but rather should be concentrated in a single spectral line in an RF channel emulator model, since it is the average of many spectral lines.

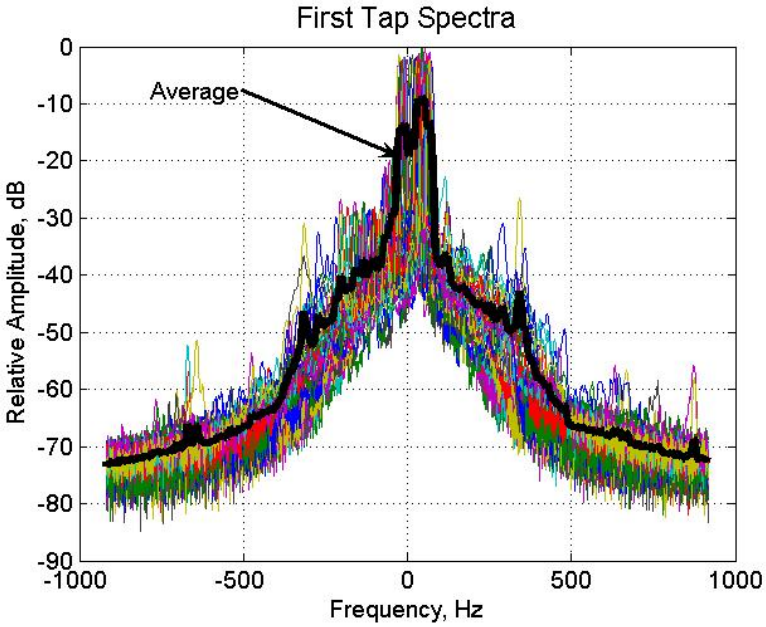

Figure 105: All spectra contribution for the first tap of an averaged statistical model. The thick line represents the tap spectrum.

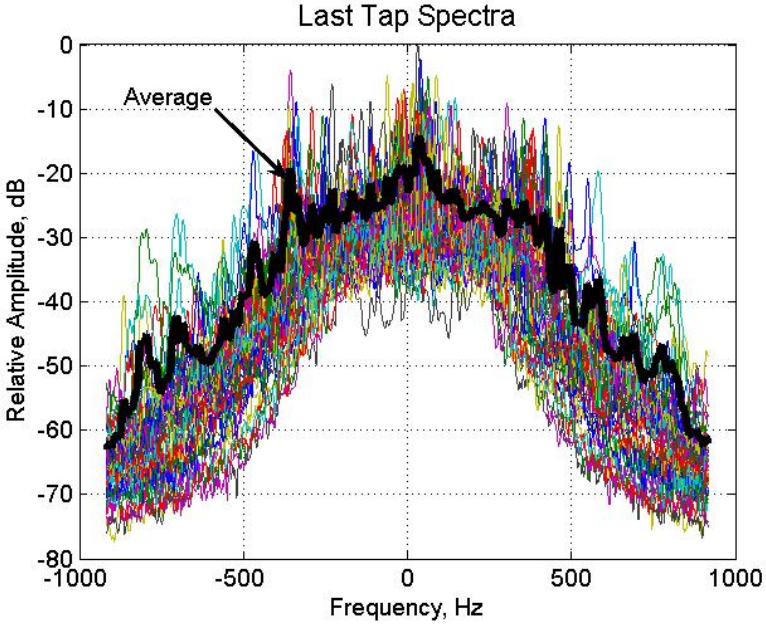

Figure 106: All spectra contribution for the last tap of an averaged statistical model. The thick line represents the tap spectrum.

To solve the delay position inconsistencies, we decided to regenerate the overall model considering just one PDP for the complete data set. We achieved the latter by setting Q=(14x12x27400) in (2.37). This complete PDP contained only 10 consecutive

significant bins. We then followed the previously described methodology to generate the model described in Table 6. In this table, we specified the number of taps, the tap delay, the tap power magnitude, and the K-factor. We will further discuss this K-factor in a later section. From these statistical parameters we obtain the model whose scattering function we present in Figure 107.

Table 6: Overall 10-Tap model parameters

Tap	Delay, ns	Relative Power, dB	K_{Rice}
1	0	0.0	102.0
2	50	-6.5	7.3
3	100	-14.4	4.7
4	150	-17.5	3.6
5	200	-19.7	1.8
6	250	-22.0	0.5
7	300	-24.4	0.2
8	350	-25.3	0.2
9	400	-27.1	0.0
10	450	-28.1	0.0

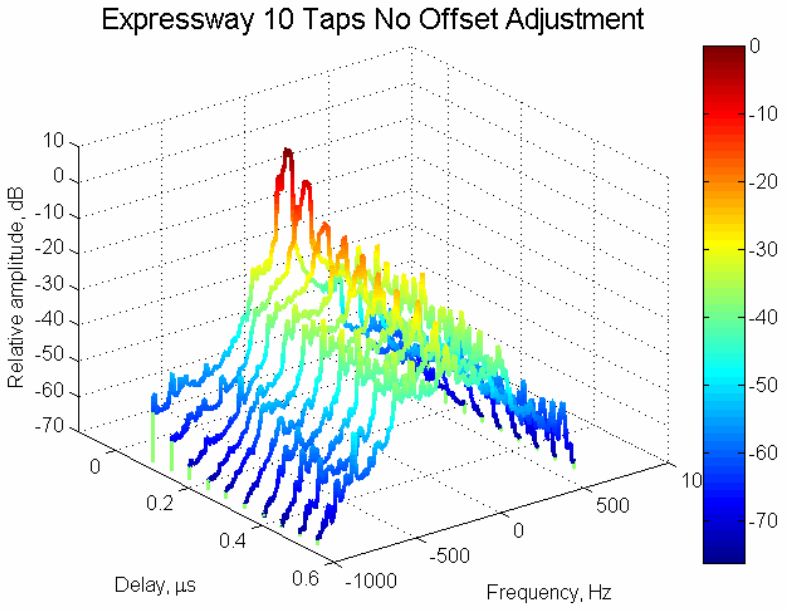

Figure 107: Overall 10-tap model without frequency adjustment scattering function.

We can reduce the widening caused by the different frequency offsets by centering each of the spectra before averaging. To do so, we need to estimate the offset separately for each of the bins and shift each of them independently. We obtained the offset value by treating the spectra as a probability distribution and obtaining its first moment after normalization. In Table 7, we have the correlation coefficients of the frequency offsets where we can corroborate that there is no one single frequency shift measure that can be applied to all the taps.

In the next two figures, Figure 108 and Figure 109, we show the improvement obtained after the frequency offset adjustment. We now have a narrow peak in the first tap as wanted. We still have the widening effect of the averaging, but it is reduced. In Figure 110, we have the corresponding scattering function for the frequency adjusted model.

Table 7: Spectra offset correlation coefficient matrix

1.00	0.83	0.59	0.52	0.45	0.39	0.30	0.21	0.25	0.31
0.83	1.00	0.82	0.58	0.50	0.37	0.24	0.12	0.18	0.24
0.59	0.82	1.00	0.66	0.46	0.29	0.10	-0.01	0.07	0.15
0.52	0.58	0.66	1.00	0.71	0.42	0.22	0.08	0.12	0.24
0.45	0.50	0.46	0.71	1.00	0.73	0.41	0.18	0.20	0.12
0.39	0.37	0.29	0.42	0.73	1.00	0.75	0.44	0.39	0.14
0.30	0.24	0.10	0.22	0.41	0.75	1.00	0.75	0.53	0.28
0.21	0.12	-0.01	0.08	0.18	0.44	0.75	1.00	0.71	0.34
0.25	0.18	0.07	0.12	0.20	0.39	0.53	0.71	1.00	0.66
0.31	0.24	0.15	0.24	0.12	0.14	0.28	0.34	0.66	1.00

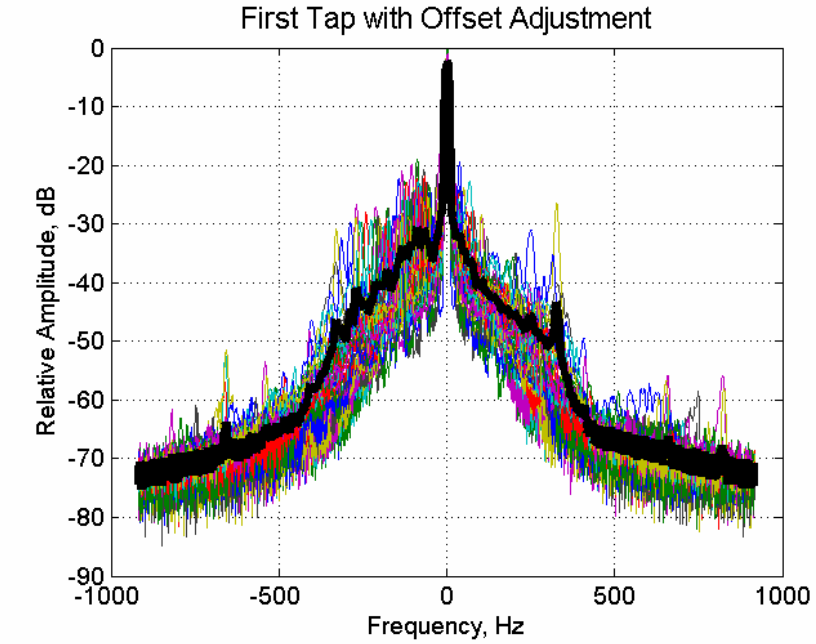

Figure 108: Frequency aligned spectra contribution for the last tap of the overall model. The thick line represents the tap spectrum.

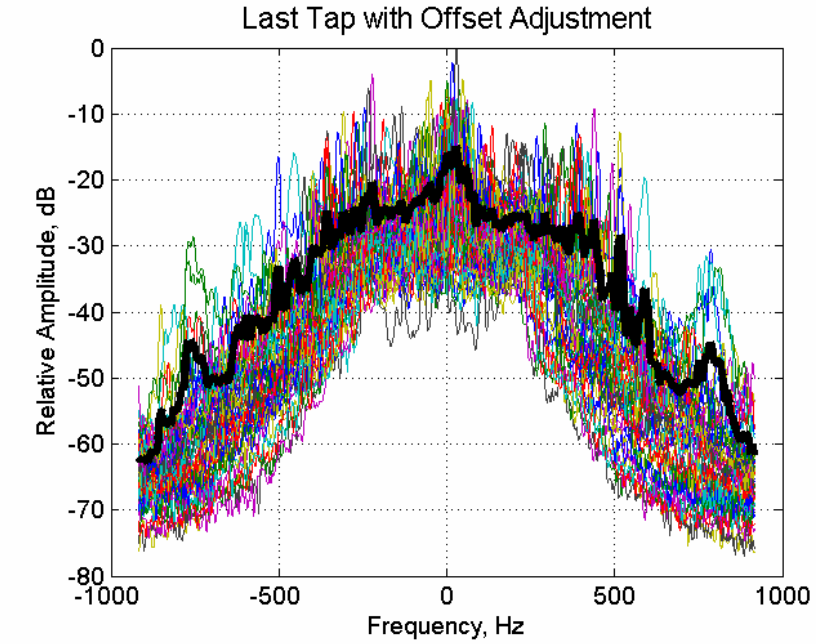

Figure 109: Frequency aligned spectra contribution for the last tap of the overall model. The thick line represents the tap spectrum.

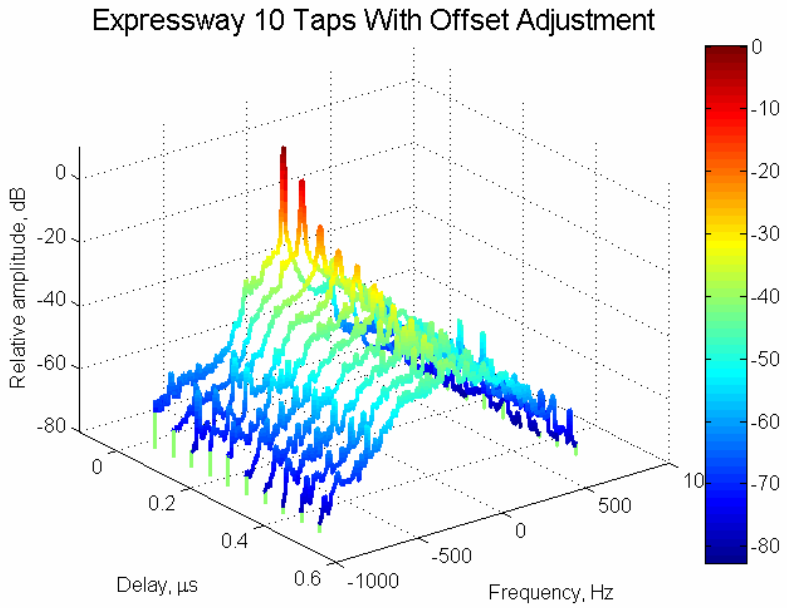

Figure 110: Overall 10-tap model with frequency adjustment scattering function.

6.1.1.6 Statistical Model Conclusions

A statistical model extraction method has been applied to the MTM frequency selective highway channel when both vehicles travel in the same direction. This channel has the feature of a significant Ricean component in more than just the first tap. The models and the recorded channel were compared in terms of the BER they produced in a simulation of the DSRC link. All the models produced a higher BER than the recorded channel. The overall models failed to capture the extremes of performance of the recorded channel. We require further investigations of model dynamic to better emulate such performance extremes.

6.1.2 Partitioned Model Development

In this section, we present two other approaches for modeling the MTM channel. As we will show in Section 6.1.2.3, the two overall channels do not provide the same extremes of performance that the recorded channel provides. After analyzing the behavior of the recorded channel, we observed that there are two correlated parameters with a

wide range of variation: BER and maximum delay (MD). We decided to use these parameters to partition the recorded channel data into sets with similar BER performance or similar delay profile characteristics. We need to emphasize that we performed frequency offset alignment in both models.

6.1.2.1 BER Partitions

For the partition with respect to BER performance, we divided the recorded 0.7 segments according to their BER after simulation with a 64 symbol frame and adaptive modulation. We define four partitions for each order of magnitude of the BER starting at 10^{-4} as shown in Table 8. In this table, we indicate the number of segments belonging to each partition along with the number of taps used in the partition's statistical model. We also show the average BER for each partition for the corresponding recorded channel segments and for the synthesized channel derived from each partition model. It is interesting to notice that the synthesized channel BER stays in the same order of magnitude, which makes it higher for two partitions and lower for two. We do not have a concrete explanation for this behavior, but we think that the fixed number of taps for every synthesized IR reduces the BER variability from segment to segment.

Table 8: Partition by BER Criterion Results

BER Partition	Selection Criterion: BER per 0.7 s Segment	Number of 0.7 s Segments	Partition Recorded Channel Average BER	Number of Taps in Partition Statistical Model	Partition Synthesized Channel Average BER
1	$BER \leq 10^{-4}$	11	7.407×10^{-5}	4	1.668×10^{-3}
2	$10^{-4} < BER \leq 10^{-3}$	55	4.066×10^{-4}	4	2.419×10^{-3}
3	$10^{-3} < BER \leq 10^{-2}$	87	3.862×10^{-3}	5	2.881×10^{-3}
4	$10^{-2} < BER \leq 10^{-1}$	15	1.656×10^{-2}	7	8.344×10^{-3}

We show the scattering functions for the first and fourth partitions in Figure 111 and Figure 112 respectively. From these figures, we can observe that the higher BER partition has longer delays and wider spectra.

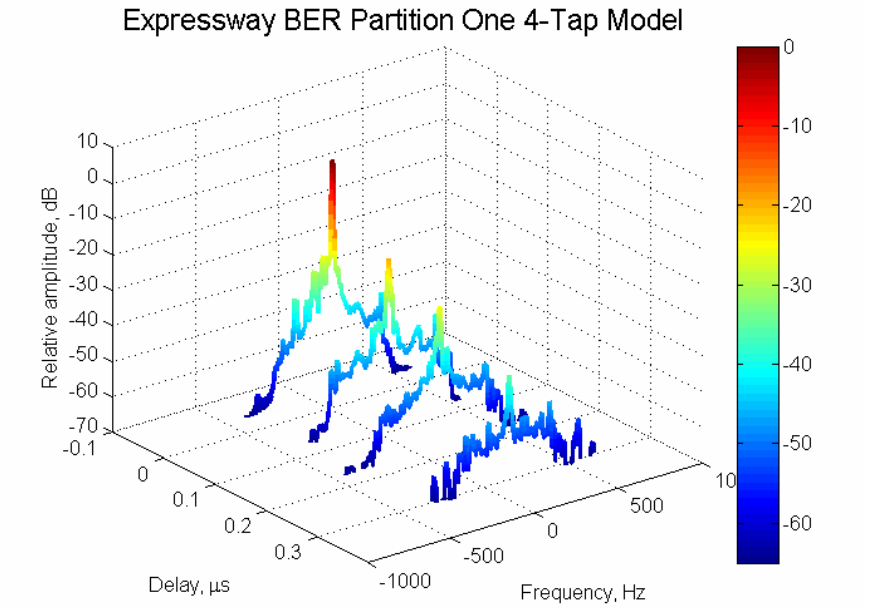

Figure 111: BER partition one scattering function.

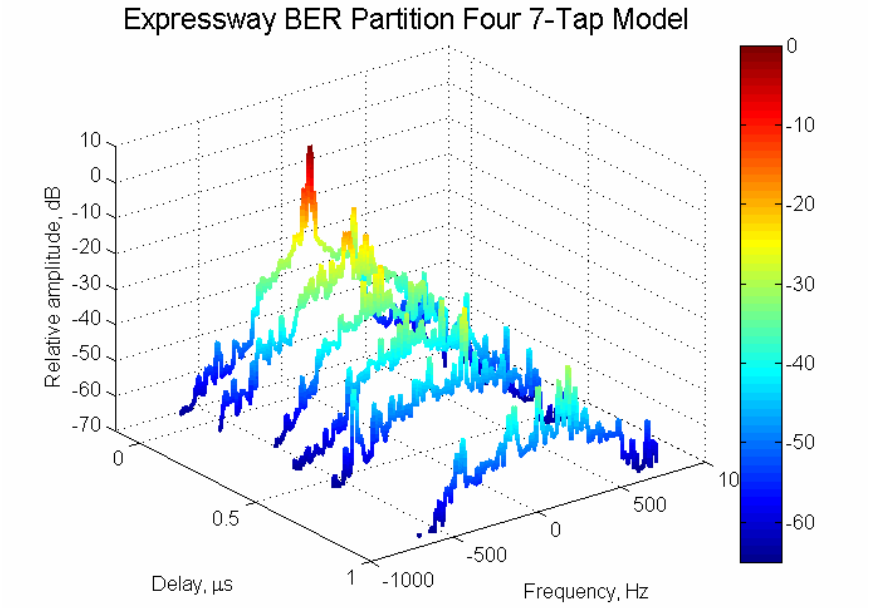

Figure 112: BER partition four scattering function.

6.1.2.2 MD Partitions

For the MD partition model, we create the partitions according to the number and position of the significant bins of each 0.7 s PDP. First we identified the PDPs with consecutive significant bins. We found from five and up to 12 consecutive significant bins

after the first. From this set, we created four partitions so that each partition model would contain two consecutive bins per tap. For the non-consecutive significant bins, we created two partitions: one for segments with less than 12 significant bins and one for segments with 12 or more significant bins. The number of segments per partitions is shown in Table 9 where we also indicate the number of taps for the partition model. As in the previous table, we also show the BER per partition for recorded and synthesized channels. Once again, we obtained BER of the same order of magnitude for the synthesized channel.

Table 9: Partition by MD Results

Maximum Delay Partition	Selection Criterion: BER per 0.7 s Segment	Number of 0.7 s Segments	Partition Recorded Channel Average BER	Number of Taps in Partition Statistical Model	Partition Synthesized Channel Average BER
1	5 & 6 Consecutive First Significant Bins	24	6.679×10^{-4}	3	2.639×10^{-3}
2	7 & 8 Consecutive First Significant Bins	31	1.060×10^{-3}	4	3.049×10^{-3}
3	9 & 10 Consecutive First Significant Bins	12	1.188×10^{-3}	5	2.622×10^{-3}
4	11 & 12 Consecutive First Significant Bins	12	7.537×10^{-3}	6	6.184×10^{-3}
5	Long (>12) Non-consecutive Significant Bins	65	6.762×10^{-3}	11	4.615×10^{-3}
6	Short (<12) Non-consecutive Significant Bins	24	1.541×10^{-3}	5	2.465×10^{-3}

6.1.2.3 Results for Phase I Techniques

In this section, the models developed in the previous sections are compared in terms of the CDF of the BER. The BER is impacted strongly by the length of the frame, the length of the time period over which the BER is computed, and the choice of fixed or adaptive modulation. Longer frames yield higher BER because the high initial quality of the channel estimates degrades over time, even though there are pilot tones. The shape of the CDF of the BER is impacted by the length of the observation interval because

zero and very low values of BER become less likely as the interval grows. Finally, the type of modulation, fixed or adaptive, makes a difference, because ideally, adaptive modulation makes the BER constant.

The BER will be computed for four cases, two which use adaptive modulation and short frames, and two which use fixed modulation (6 Mbps) and long frames. The latter case was included because it is the basis of the motion-related equipment test in the current DSRC standard [6]. For adaptive modulation, two interval lengths are considered: 0.7 seconds, which corresponds to the “segment” length in the database, and 544 μs, which corresponds to a frame containing 64 symbols. For fixed modulation, the two interval lengths are 0.7 seconds and 1.376 ms. The 1.376 ms frame holds 168 symbols, or 1000 bytes of information at 6 Mbps; this is the “long frame” part of the motion-related equipment test in the DSRC standard.

Figure 113 and Figure 114 contain the adaptive modulation results and Figures 19 and 20 contain the fixed modulation results. The adaptive modulation results include CDFs of BER for the recorded channel and four models: the overall aligned, the overall non-aligned, the BER partition, and the MD partition. Recall that for all models except the overall non-aligned model, the segment spectra are centered prior to averaging. The fixed modulation results include only the recorded channel and the BER partition model.

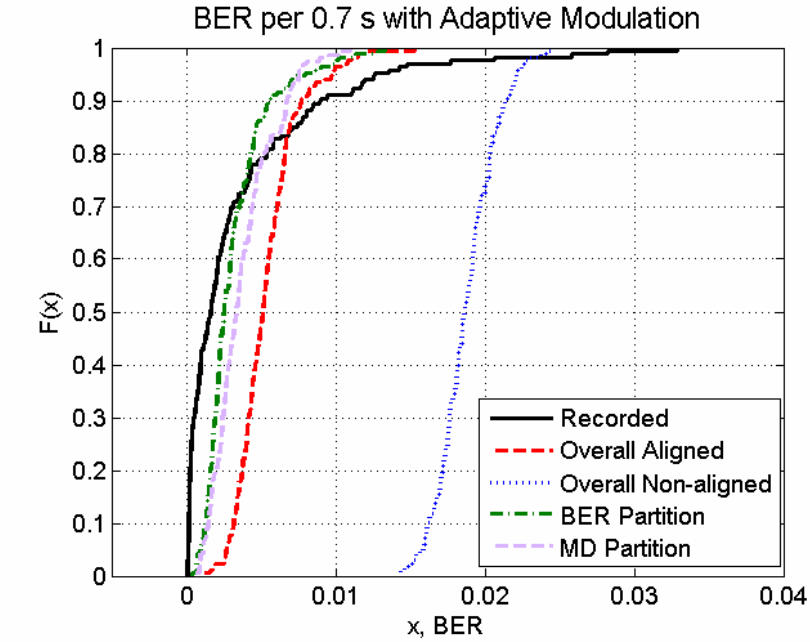

Figure 113: Recorded channel and models CDFs using the BER per 0.7 s segment, a 64 OFDM symbol frame, and adaptive modulation.

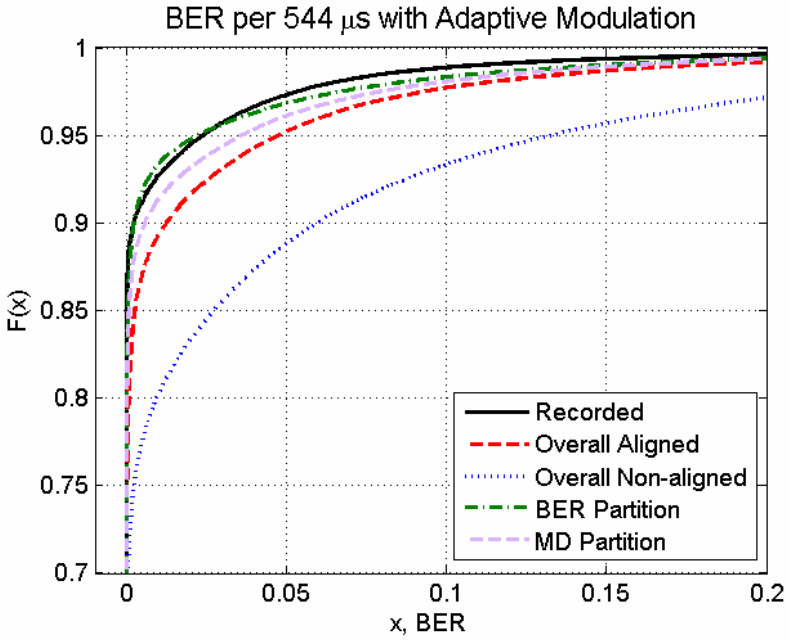

Figure 114: Recorded channel and models CDFs using the BER measured for each 64 OFDM symbol frame and adaptive modulation.

In Figure 113, the recorded channel BER has a larger variance than each of the models. Observations of bit errors versus time (not shown in this document) indicate that

the recorded channel has relatively long periods of time when there are no errors, and then other periods of time with a high density of bit errors. In contrast, the synthesized channels produce a more uniform distribution of errors in time. Because the recorded channel produces a significant percentage of 0.7 segments with zero or very few errors, we may conclude that the low-error periods are often at least 0.7 seconds long.

In Figure 114, the BER partition model produces a very good fit to the recorded channel. The MD partition model is next closest, and the overall aligned model is the worst fit of the aligned models. Evidently, the 64 symbol frame is short enough that the synthesized models produce between 80 and 90 percent error free frames.

As observed in Figure 115 and Figure 116, the long frames and fixed modulation degrade the performance of the recorded channel and all the models. Interestingly, the BER partition model and recorded channel diverge significantly for in the low BER region when BER is computed over the long frame period (1.376 ms). Comparing Figure 114 and Figure 116, we observe that the BER partition model is only slightly degraded by the longer frame and fixed modulation, but the recorded channel degrades significantly for the longer frame. Long frame vs. short frame effects would seem to depend more on small scale phenomena than large scale, and the long frame would suffer more from Doppler spread. One possible reason for the divergence of these curves is that the design of the partition model was based on the short frame and adaptive modulation, yet in Figure 116, the model is being evaluated on a link using a different type of modulation. Had the partition model been based on the modulation assumed in Figure 116, fewer segments would have been assigned to the lowest BER partition. The excessive number of segments in the low BER partition could be the reason that the BER partition model performs so much better than the recorded channel in the low BER regime.

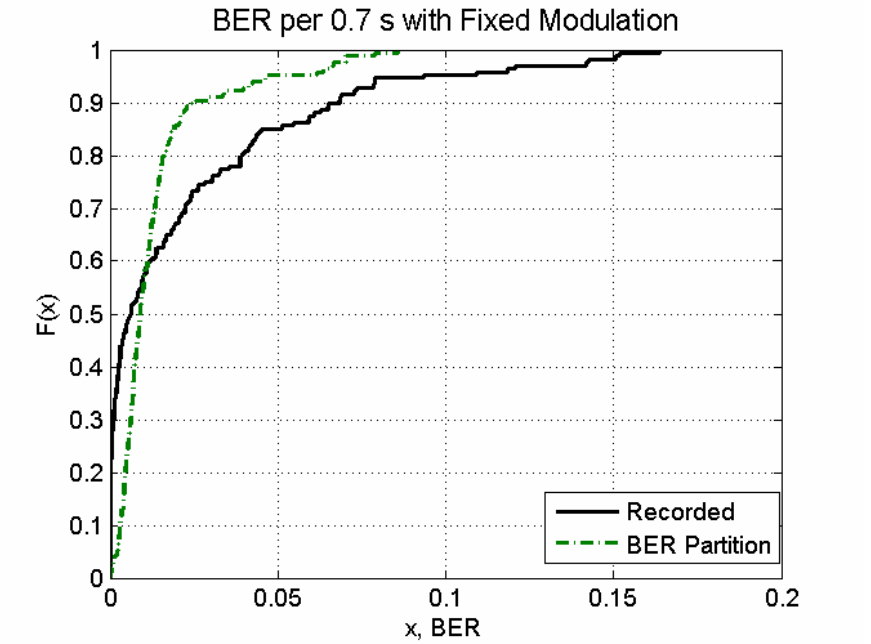

Figure 115: Recorded channel and BER partition model CDFs using the BER per 0.7 s segment, a 168 OFDM symbol frame, and a fixed 6 Mbps modulation.

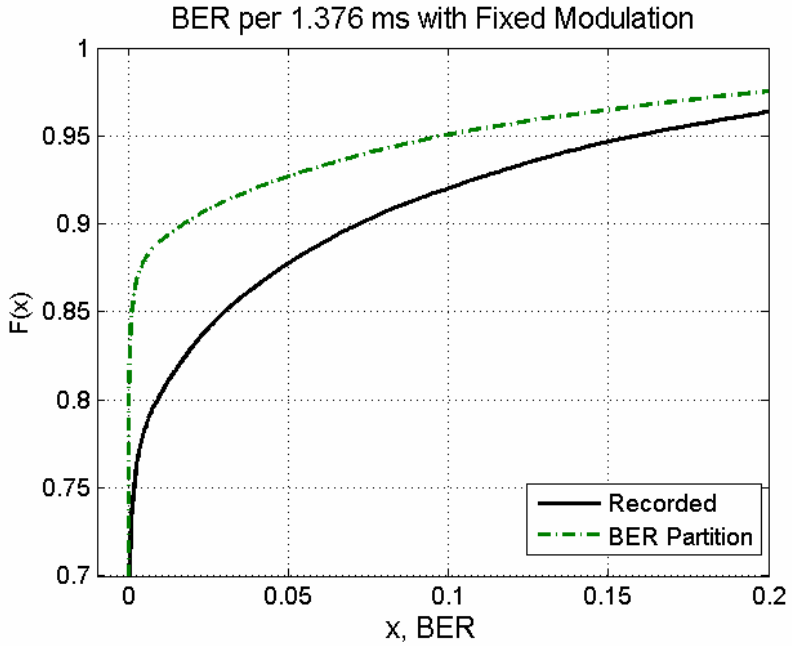

Figure 116: Recorded channel and BER partition model CDFs using the BER measured for each 168 OFDM symbol frame (1000, data bytes) with fixed 6 Mbps modulation.

6.1.2.4 K-Factor

The Rice or K factor has not been part of our Phase One model specification, but it is an important feature of models; therefore, it should be examined. Also, K-factors must be explicitly specified in RF channel emulators. For these reasons, in this section, we compute the K-factors of the taps of our models and compare them to the recorded channel. We determine the Rice or K factor for any bin *m* using the moment-method [1], [29] described in (2.40). Applying this method to each 0.7 s recorded segments, for which Q = 27,400, we obtained a 168 x 511 K-factor matrix. Any complex K-factors were set to zero. The K-factors given for the overall model in Table 10 are the first ten column averages of the K-factor matrix. In Table 10, we present the K-factors for the corresponding rows and columns of the K-factor matrix for each of the sections of the BER partition model. For example, for Partition One; we have 11 0.7 s segments and seven significant bins for the PDP of the partition. To obtain the K-factors for the partition, we choose the corresponding rows and columns, and we perform a column average on the new 11 x 7 matrix. For Table 10, we also calculated the K-factors for the synthesized channel. Continuing with the partition one example, the partition contains four taps; therefore, the K-factor submatrix size is 11 x 4. Each matrix element was obtained from the 27,400 samples per tap of the synthesized channel. The table values are the column averages.

By looking at the scattering function of Figure 111 and by considering the bins K-factor values, we should expect a high K-factor for the first tap of the synthesized channel, but it is surprisingly small. This means that even when we use the recorded spectra, which shows a significant K-factor, as the filter template for the synthesized channel, it is not enough to create a representative K-factor. We have empirically notice that the segments with low BER present very high K-factors in the first bin, but we have also notice a

significant variation in the BER from segment to segment in these cases. We believe that there is a dynamic correlation between BER and K-factor that should be further investigated.

Table 10: K-factors for the BER partition model.

Partition One Bins	Partition One Taps	Partition Two Bins	Partition Two Taps	Partition Three Bins	Partition Three Taps	Partition Four Bins	Partition Four Taps
159.4	0.8	174.8	1.2	61.8	1.1	26.5	1.1
5.1		8.1		7.1		8.0	
13.3	0.4	6.5	0.4	3.1	0.4	1.3	
10.0		6.0		1.8		0.6	0.2
5.9	0.3	3.6	0.2	0.6	0.3	0.7	
1.8		1.1		0.4		0.2	
0.1	0.3	0.4	0.2	0.4	0.2	0.7	0.2
		0.4		0.5		0.1	
				0.1	0.2	0.0	
						0.1	0.2
						0.0	
						0.0	
						0.0	0.2
						0.0	
						0.0	
						0.0	0.3
						0.0	
						0.1	
						0.4	0.3

6.2 Phase Two Channel Modeling

As mentioned before, the Suburban Expressway MTM Same Direction Wall scenario was used to explain the model procedure of this section. This scenario or site data contained 21 total “Takes” from several different expressway locations in the metro Atlanta, Georgia area, all with approximately 400 m separation between the vehicles, with and average vehicle speed of 100.3 km/hr (62.3 mph). Following the procedure outlined in Section 6.1.1.1, we obtained the corresponding PDPs for the site as shown in Figure 117. The first thing we notice is that this time we have almost twice as many PDPs as in Figure 97. We also notice a similar response in the two sites with respect to the number of taps behavior.

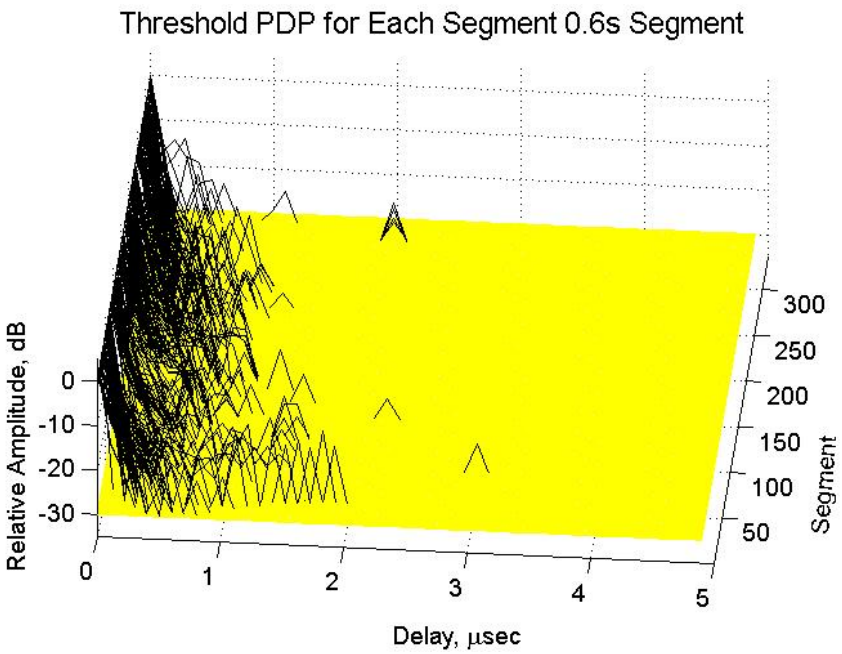

Figure 117: Suburban Expressway MTM Same Direction Wall PDPs obtained using (2.37).

6.2.1 Methodology

The magnitude squared of each element of the MLS-based impulse response matrix was averaged down the columns to provide a PDP for each segment. A threshold of approximately 30 dB relative to the peak of the PDP was applied to eliminate noise effects in the PDP. Samples below the threshold were set to zero. Then the PDPs were averaged across segments and "Takes" to create the "overall PDP." Again, a 30 dB threshold is applied to the overall PDP. The bins with power greater than this threshold are called the significant taps of the overall PDP, and they become the taps of the final model for the site.

Next, the PSD for each significant tap in each segment is found. One way to proceed from here is to average the PSDs for a given tap across the segments and "Takes," yielding an average PSD for that tap for the site. However, the Doppler frequency of the LOS component causes a problem with this approach [4]. The Doppler frequency of the

LOS component varies from segment to segment as the relative velocity of the vehicles changes. Because of the changing Doppler of the LOS, the averaged spectrum ends up having a broad peak which would not correspond to a Rician characteristic if that spectrum were used as a basis for channel simulation. In other words, a significant K factor is indicated in a tap PSD by a spectral line. If a PSD without a narrow line is used as a basis for a filter in the filtered white noise approach to tap process simulation [37], then the measured K factor for that simulated tap would be insignificant.

In Section 6.1.1.5, we dealt with this problem for the expressway same-direction channel by aligning the spectra (i.e. translating them in frequency) before averaging, such that the peaks of the aligned spectra were all at zero Doppler. Then we averaged those spectra and ignored the somewhat less broad peak in our subjective shape-fitting process. Since the same translation should not necessarily apply to all spectral components, we decided to take a different and more objective approach in this modelling procedure.

For the procedure, we estimate the K factor of each bin in each segment using the moment method [29], and we use this as a basis for removing the spectral peak. The K factor is the ratio of the power of the "deterministic" or dominant spectral component over the power of the random or diffuse reflection component. We note that the method of moments approach measures the relative power of any phase or frequency modulated component; it is not necessary that the component have zero Hz Doppler. Using the K factor, we calculate the fraction of power that is attributed to the deterministic component. By incrementally lowering a horizontal line, starting at the spectral peak, we can identify the level such that the PSD area above this line equals the deterministic power and the area below equals the random power. We then store the separated parts of the spectrum and store the frequency of the peak for each segment. Finally, by aver-

aging the random parts across segments and “Takes,” we can arrive at an average random spectral part for the site. We can also produce an average of the deterministic parts, which shows the range of variation of the spectral line frequency and also shows the influence of the segments with a particularly strong LOS. Alternatively, we can produce a histogram of spectral peak locations.

Our approach to identifying the shape of the random part of the spectrum is based on the limitations of the RF channel emulators and by the type of link (OFDM) that is being evaluated. Usually, the identified channel model is intended to be an inherent property of the channel, and applicable to any type of air interface with a similar RF frequency and bandwidth. Therefore, propagation modellers are usually interested in the geometrical properties of the channel, such as the distinct parameters of each path of propagation, such as its power, delay and angle of arrival. However, our objective is only to characterize the tap spectra, within the limited delay resolution of the target system and the limited degrees of freedom of the RF channel emulator. The delay resolution (100ns) of our measurements is large and corresponds to 30 m of excess path distance, which will include many actual paths of propagation with different Doppler shifts. Furthermore, for OFDM, if the excess delay is within the guard interval and if the channel frequency response nulls are not too deep, then the primary channel impairment to the link will be the ICI caused by the Doppler spreads of the tap processes [14]. This impairment can be quantified based on the Doppler spectrum. Therefore, in our modelling approach, we will attempt to optimally fit to the measured tap spectrum.

With such limited degrees of freedom in the fitting process, some parts of the spectrum will not be matched well. Therefore, the question arises, should certain parts of the spectrum be considered as more important than others? For this, we will use a weighting

function that would match the ICI of the measured and modelled channels, if every tap had the same spectrum (i.e. assuming a separable channel).

Assuming also that the Doppler spectra are symmetrical, Cai and Giannakis [14] give the following expression for the average interference power that a signal on subcarrier *k* makes on subcarrier *m*:

$$\psi_q = \pi^{-2} E_s \int_0^1 \varphi_n(f) \sin^2\left(\pi f_d T_s f\right) \left[\frac{1}{\left(f_d T_s f + q\right)^2} + \frac{1}{\left(f_d T_s f - q\right)^2} \right] df \tag{6.2}$$

where $q = m - k$ and $\varphi_n(f)$, $0 \le f \le 1$, is a normalized version of the spectrum, such that $2\int_0^1 \varphi_n(f) df = 1$, and $\varphi_n(f) = f_d \varphi\left(f_d f\right)$, where $\varphi(f)$ is the original Doppler spectrum, except normalized to unit area.

The main observation is that for 802.11p, and vehicle speeds of about 143 km/hr, $f_d T_s \approx 0.01$, which means that (6.2) simplifies to

$$\psi_q \approx \frac{2E_s \left(f_d T_s\right)^2}{q^2} \int_0^1 \varphi_n(f) f^2 df \tag{6.3}$$

This expression tells us that the higher frequencies in the Doppler spectrum contribute more to the ICI, as indicated by the weighting by the square of the frequency. It also tells us that the effect of the distance between subcarriers (*q*) is decoupled from the Doppler spectrum effects. Finally, we note that the square root of twice the integral is the Doppler spread.

Suppose that $\varphi_n'(f)$ and ψ_q' are the proposed RF channel emulator spectrum and its corresponding ICI, respectively. We can consider the difference between the ICI values produced by the two spectra:

$$\left|\psi_q - \psi_q'\right| \approx \frac{2E_s\left(f_d T_s\right)^2}{q^2}\left|\int_0^1 \left[\varphi_n(f) - \varphi_n'(f)\right] f^2 df\right| \tag{6.4}$$

The choices of shape, center frequency, and width of the RF channel emulator spectrum impact only the integral. By the triangle inequality, we have:

$$\left|\psi_q - \psi_q'\right| \le \frac{2E_s\left(f_d T_s\right)^2}{q^2}\int_0^1 \left|\varphi_n(f) - \varphi_n'(f)\right| f^2 df, \tag{6.5}$$

which suggests the cost function:

$$\left(\int_0^1 \left|\varphi_n(f) - \varphi_n'(f)\right| f^2 df\right)^{-1}. \tag{6.6}$$

For each tap, we employed the genetic algorithm [34] to optimize (6.6) over the channel emulator spectrum parameters for one, two, or three paths, under the constraint that the areas of $\varphi_n(f)$ and $\varphi_n'(f)$ are held constant.

Prior to optimization, we set to zero all measured spectrum values for |f| > 1200 Hz, to avoid fitting to noise. We defined the domain of the optimization to be |f| < 1500 Hz to force the spectrum shapes to be within the +/- 1500 Hz window.

The resultant model is of the “tapped delay line” type and normalized so that the first tap power is 0 dB. In most cases, a tap is constructed from several paths of the channel emulator. This is because the choices for the spectral shapes of paths in a channel emulator are limited, and quite insufficient to describe many of the measured tap Doppler

spectra. By superimposing several paths with nearly the same delay, it is possible to create a customized Doppler spectrum that fits better. To avoid problems with the channel emulator, paths comprising a single tap were separated in delay by one nanosecond. The customized Doppler spectrum is constrained to have the same total power (i.e. same area in a non-dB plot) as the measured Doppler spectrum, so that the power delay profile is preserved.

Each tap spectrum fit was optimized by taking the best of five runs of the genetic algorithm. The cost function used in the genetic algorithm and for selecting the best of the five was the integrated weighted difference between the measured spectrum and the customized spectrum as indicated in (6.6). The weighting function was $(f - f_{peak})^2$, where f_{peak} is the frequency of the peak (usually very well defined) of the spectrum of the first (and strongest) tap. It is assumed that f_{peak} is the recovered carrier frequency in the receiver. The cost function ensures that the ICI that would be produced by the customized spectrum in an OFDM receiver is as close as possible to the ICI produced by the measured spectrum [14]. In some cases, it seems that the fit of the customized spectrum to the measured spectrum could be made better by simply widening or shortening a shape, however, this generally violates the equal power constraint.

6.2.2 Results for Phase II Techniques

In Figure 118, we show the overall PDP for the site. There are eight significant bins or taps. In Figure 119, we have one snapshot of the Doppler spectrum for Tap One, illustrating the level method of Rician component removal. There is still a broad peak remaining, which may be there because of shifting of the Doppler frequency of the LOS over the 0.6 s segment. In Figure 120, we present the histogram of Doppler frequencies of the LOS for the 334 segments. The Doppler varies roughly from -100 Hz to +100 Hz.

In Figure 121, we show the averaged deterministic part of the Tap One spectrum. The level and hole methods coincide except for the four small peaks on the left. The frequencies of these small peaks are less than -200 Hz, indicating that the level method clipped more than just one peak in at most four out of 334 segments. The different shapes of the histogram vs. the averaged spectrum in Figure 120 and in Figure 121 indicate that the LOS Doppler was apparently more powerful when it was farther away from zero Hz.

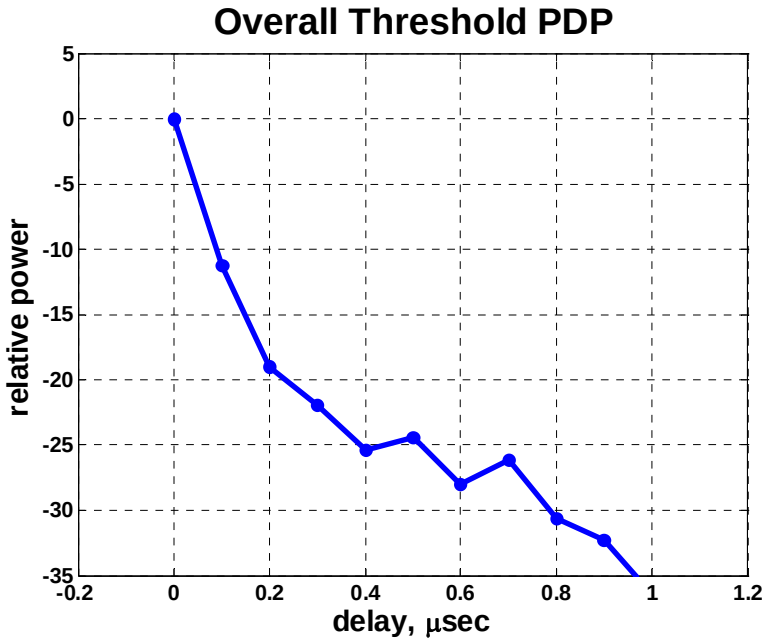

Figure 118: The overall power delay profile (PDP) for the expressway, same-direction travel scenario.

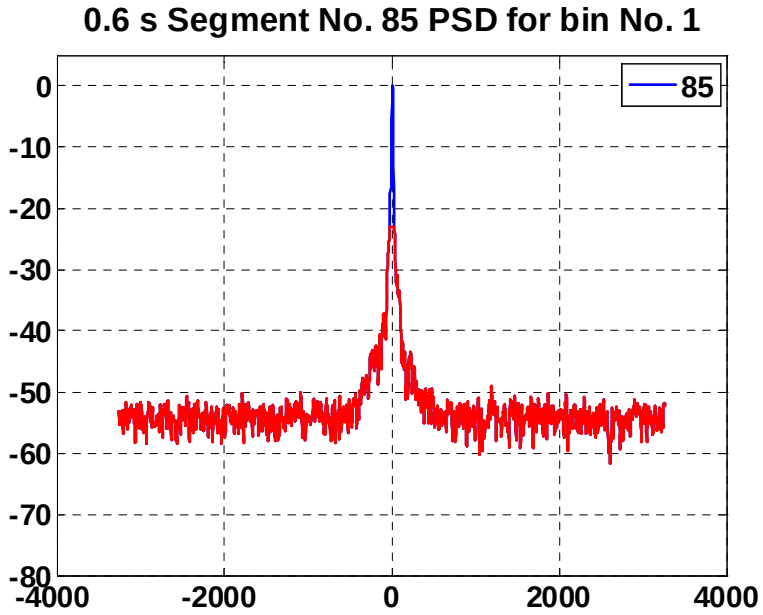

Figure 119: An example spectrum estimate for a 0.6 second segment. The flat part indicates the level corresponding to the K-factor measured for this segment.

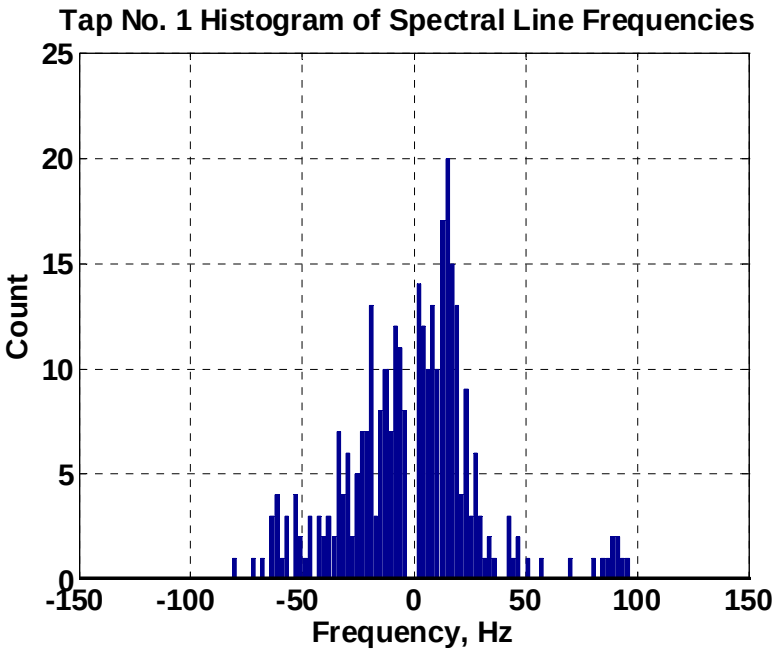

Figure 120: Histogram of Rician component frequencies for Tap. No. 1.

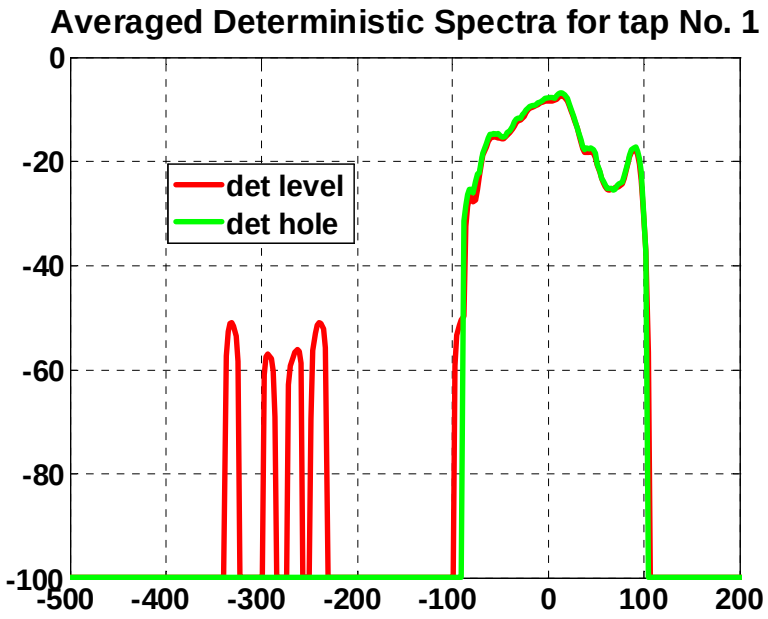

Figure 121: Average of the parts of the spectra that were removed by the level and hole methods for Tap. No. 1.

Figure 122 and Figure 123 are the histogram and averaged deterministic spectrum for Tap Four. We observe Rician components with Doppler frequencies as large as about 1200 Hz in magnitude. This frequency corresponds to twice the vehicle speed, and results from reflections from stationary objects, such as bridges, that are nearly directly in front of or directly behind the two traveling vehicles. The two curves in Figure 123 are very close, indicating little multi-peak clipping by the level method.

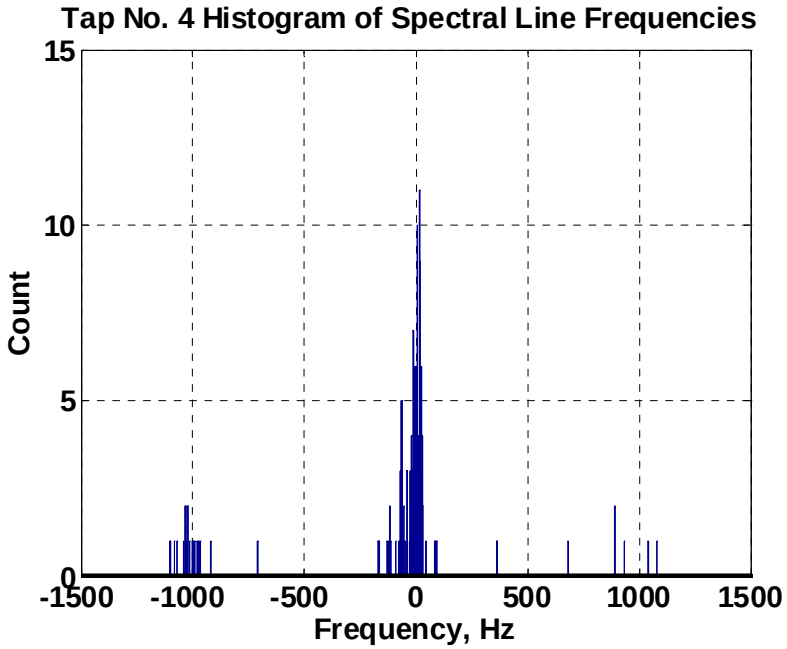

Figure 122: Histogram of Rician component frequencies for Tap No. 4.

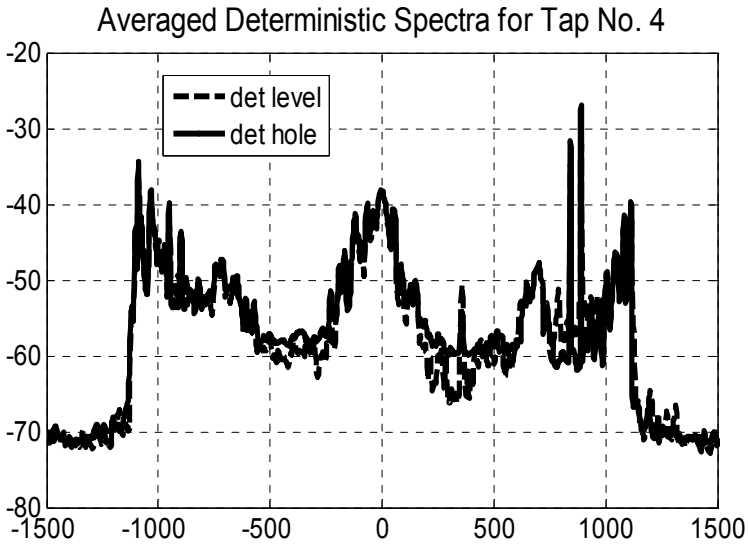

Figure 123: Average of the parts of the spectra that were removed by the level and hole methods for Tap. No. 1.

In Figure 124 and Figure 125, we now have histograms of the K factors for Tap One and Tap Four. We observe an especially wide variation in K factor for Tap One, ranging

from zero to about 95. For Tap Four, the variation is more limited, but clearly indicates that for many segments, the later taps in the model have significant K factors. If the K factors for the segments are simply averaged, as they were in Section 6.1.2.4, the results are 12.0, 2.1, 1.7, 1.3, 0.78, 0.55, 0.22, 0.15, for Taps One through Eight, respectively. On the other hand, if the ratio of averaged areas is used, the values are much lower, yielding for example 2.52 for Tap One; using this method the K factors for many later taps are so small that a Rayleigh fading assumption is appropriate.

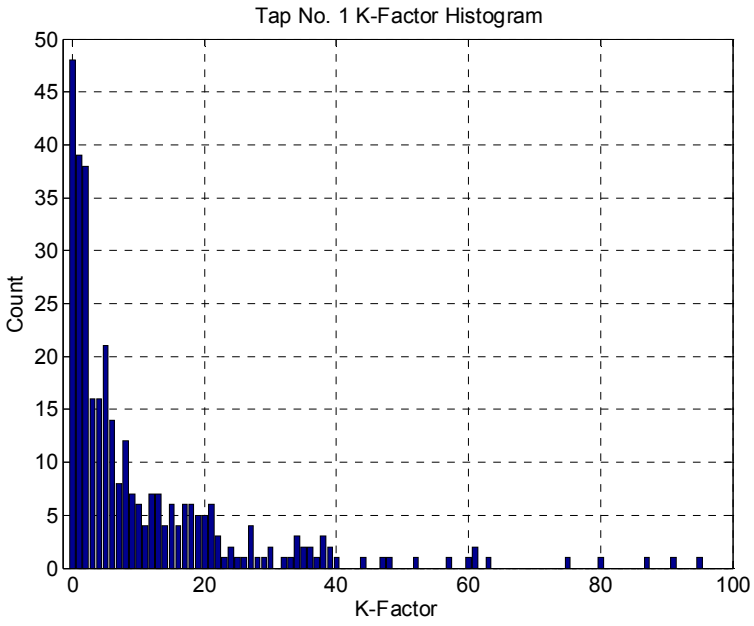

Figure 124: Histogram of K-factor values for Tap. 1.

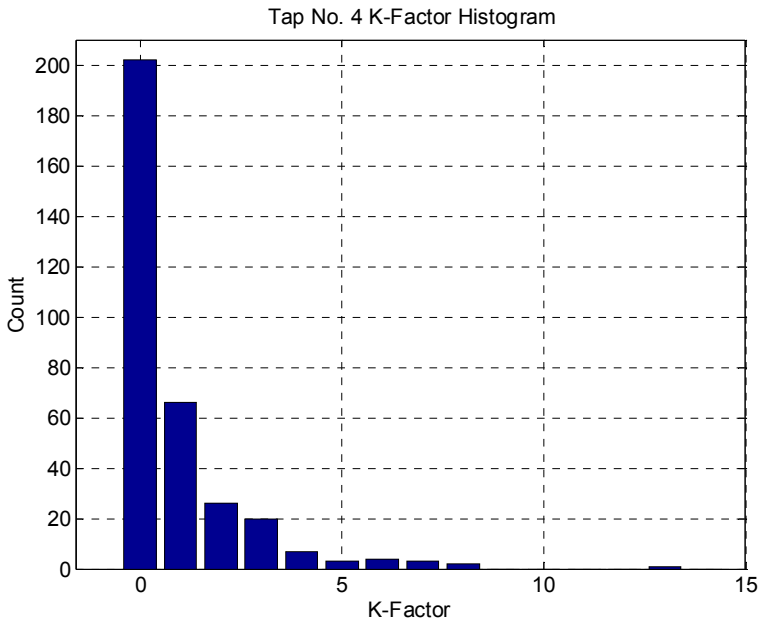

Figure 125: Histogram of K-factor values for Tap 4.

In Figure 126, we show the result of the genetic algorithm fit of two path spectra to the average of the random spectrum parts produced by the level method. These are both “rounded” spectra. The result for the single path spectrum (“one shape”) fit is very similar to just the narrow rounded shape of Figure 126, except it is almost imperceptively (at the scale of this figure) taller and wider. The difference in dB of the ICI power between measured and shape-fitted spectra indicates how important it is to have two shapes when optimizing under a constraint of same PSD area: for Tap One, the difference is 11.52 dB for a one shape fit and 6.23 dB for a two-shape fit.

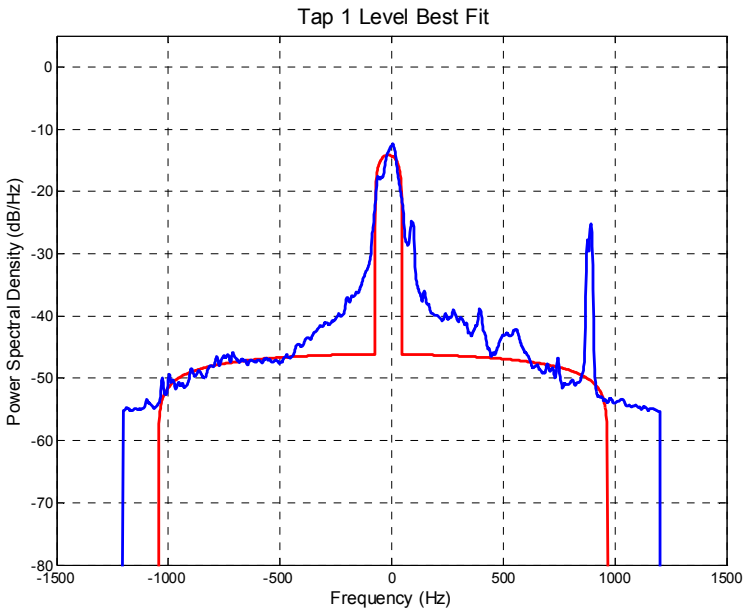

Figure 126: Two-shape fit to the random part spectrum of Tap One.

To complete the model specification, a spectral line needs to be added to the first tap spectrum, with a power according to the K factor 2.52 and with a frequency selected based on the distributions in Figure 120 and Figure 121, for example the mean of Figure 118 could be used. This spectral line should not be added as a pure frequency shift, which is an option for a path with the SPIRENT 5500, because through laboratory testing, we determined that this will not produce the desired Rician characteristic. Rather it should be added by making one of the paths, say the one with the wide spectral shape, be a Rician path. The K factor for that path will be much larger than 2.52, but should be so that the K factor for the whole tap is 2.52. Also one- or two-shape spectra should be determined for the other seven taps.

In the next section, we will describe how we use the developed models to test prototype equipment; therefore, we must at least show that the channel generated by the channel emulator behaves accordingly to the fitted spectra. To show this, we “sound” or

measure the emulated channel produced with the specifications described in this section. Using the same methodology described in previous sections, we obtained the corresponding Doppler spectra. In Figure 127, we show the Tap One spectrum. We can clearly see that it is a very close match to the fitted spectrum. We can also see that we included the corresponding Rician component. The measured K-factor for this emulated tap is 2.58. We can conclude that the proposed spectra combination using several paths to create a tap works.

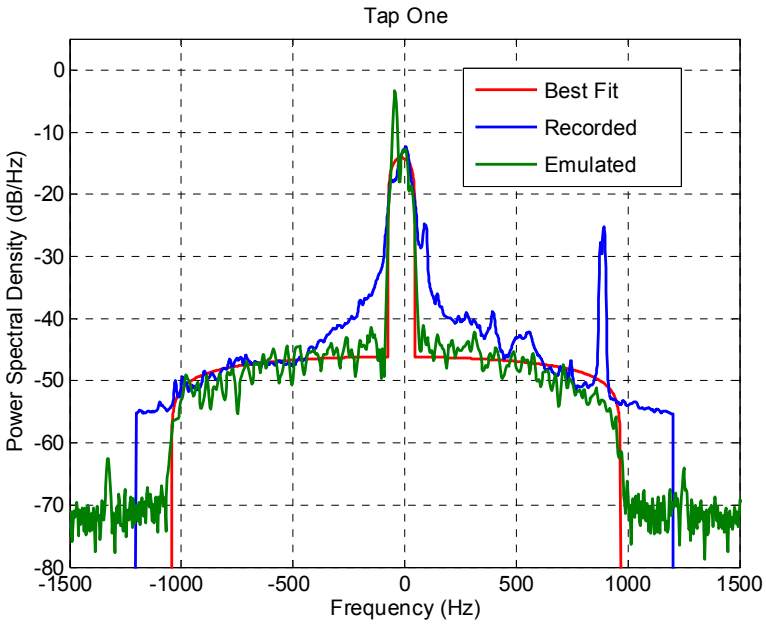

Figure 127: Emulated spectrum comparison.

6.2.3 PER Test Procedure

This section gives a high-level description of the test setup that was used to measure the PER for each model developed. The testing approach was based on the “ping” application of the IPv6 protocol. The test was demonstrated using two prototypes of WAVE/DSRC units (OBU and RSU) supplied by Mark IV and Transcore. Network interface programs were provided by Transcore and C++ Transmitter and receiver PER measurement programs were written at Georgia Tech. The programs enabled the speci-

fication of the PSDU length (200 Bytes or 1000 Bytes) and the fixed data rate of 6 Mbps. The channel models were implemented using a SPIRENT SR5500 RF Channel emulator.

A block diagram of the setup is shown in Figure 128. The RSU was configured as the the transmitter and the OBU was configured as the receiver. The ping application required a bidirectional connection. Because the channel emulator is unidirectional, a feedback path was created using isolators and circulators.

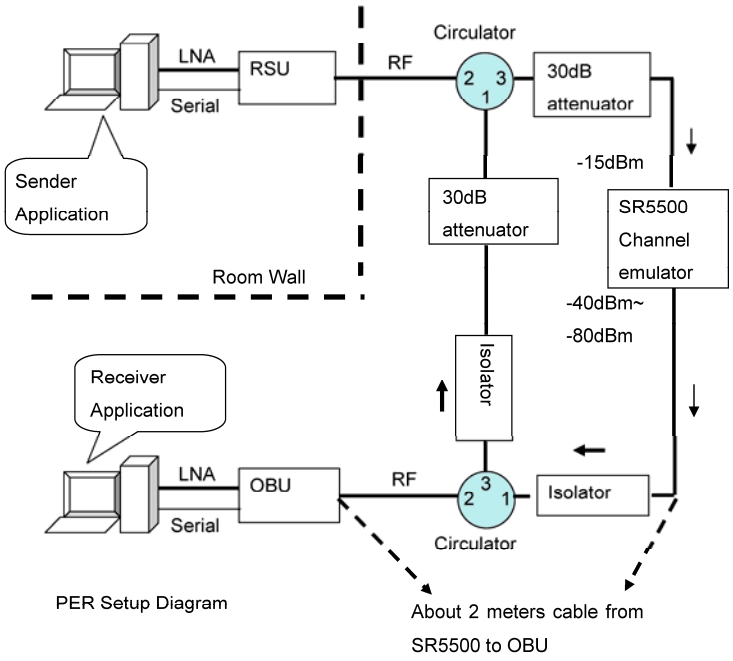

Figure 128: Block diagram of the PER test setup.

Because of this project complexity and because of its time and budget constraints, the PER testing had to be performed by another member of the Smart Antenna Research Laboratory (SARL): Lu Dong.

6.2.4 Phase II Model Conclusions

We have described an approach to channel identification for the purpose of RF channel emulation or Simulink simulation for the MTM channel in the expressway, same-direction travel scenario. Because of limited degrees of freedom in spectrum fitting, we used weighting function to ensure that the ICI for OFDM that is produced by the model tap is as near as possible to that of the measured channel, given a constraint on tap power. With this weighting function, it is clear that at least two shapes per tap are necessary to model the first tap of the model.

The histograms of K factors shown for Phase Two have a wide range of variation, even in later taps. However, since for most of the segments, the K factors are low, then the K factors based on average powers are low, and can be approximated as zero for all taps but the first.

The most important lesson we have learned trough the model development for Phase Two is that the fixed K-factor produced in channel emulation or simulation does not represent the real behavior of the MTM channel; therefore, in order to properly describe this type of communication channel, it is necessary to include the dynamic characteristics of the K-factor.

CHAPTER 7

MODEL SUMMARIES

7.1 Proposed WAVE/DSRC Model

As we mentioned in Section 5.2, the purpose of this investigation has been to define the model to be used in the motion-related equipment certification test for the standard. The model we recommend for the test is the MTM Expressway Oncoming without Wall, because it produces the highest PER among all the channels for the prototype WAVE/DSRC transceivers that were provided to Georgia Tech.

The models represent six of the environments in which the WAVE/DSRC system is expected to operate; three of them are for the MTM link, and the other three are for the RTM link. The models are listed below in order of the PER (from results indicated by Lu Dong) they produced for 1000 Byte packets, from highest (worst channel) to lowest (best channel).

1. MTM – Expressway Oncoming Without Wall, 300m – 400m
2. RTM – Urban Canyon, 100m
3. RTM – Expressway, 300m – 400m
4. MTM – Urban Canyon Oncoming, 100m
5. RTM – Suburban Street, 100m
6. MTM – Expressway Same Direction with Wall, 300m – 400m

The small-scale fading models represent multipath fading effects only and do not include path loss or lognormal shadowing.

7.2 Model Descriptions

In some cases, two models, “long” and “short,” are presented. The short models use a maximum of 12 paths, which is the maximum number of paths on many RF channel emulators. Some channel emulators, such as the model SR5500, have 24 paths, so they can run the “long” model, which has more than 12 paths. When given, the long model has a better fit to the measured spectrum. PER results are presented for both long and short models, so that the user can see how much they differ in terms of PER.

The parameters are named according to the Spirent SR5500 TestKit Instrument Control Software [Section 2.3], [79]. For example, “Fading Spectral Shape” is the Doppler spectrum shape, “Frequency Shift” is the center frequency of the path’s fading spectral shape, and “Fading Doppler” is the half-width of the path’s fading spectral shape. “n/a” means “not applicable.”

7.2.1 MTM - Expressway Oncoming without Wall, 300m – 400m Scenario

Table 11: MTM - Expressway Oncoming without Wall, 300m – 400m Model

Tap No.	Path No.	Tap Power (dB)	Relative Path Loss (dB)	Delay Value (ns)	Rician K (dB)	Freq. Shift (Hz)	Fading Doppler (Hz)	LOS Doppler (Hz)	Modulation	Fad. Spec. Shape
1	1	0.0	0.0	0	-1.6	1451	60	1452	Rician	Round
1	2		-24.9	1	n/a	884	858	n/a	Rayleigh	Round
1	3		-25.5	2	n/a	1005	486	n/a	Rayleigh	Round
2	4	-6.3	-13.1	100	n/a	761	655	n/a	Rayleigh	Classic 3dB
2	5		-7.5	101	n/a	1445	56	n/a	Rayleigh	Round
3	6	-25.1	-28.9	200	n/a	819	823	n/a	Rayleigh	Classic 3dB
3	7		-29.3	201	n/a	1466	75	n/a	Rayleigh	Flat
3	8		-35.6	202	n/a	124	99	n/a	Rayleigh	Round
4	9	-22.7	-25.7	300	n/a	1437	110	n/a	Rayleigh	Flat
4	10		-34.4	301	n/a	552	639	n/a	Rayleigh	Classic 3dB
4	11		-27.4	302	n/a	868	858	n/a	Rayleigh	Classic 6dB

Notes:

1. All Taps have composite spectra. Tap One has a Rician component in the first path, and it has random spectra in the other two paths.
2. This table is consistent with vehicle speeds of 140 km/hr (87 mph) and separation between transmitter and receiver vehicles of approximately 400m.

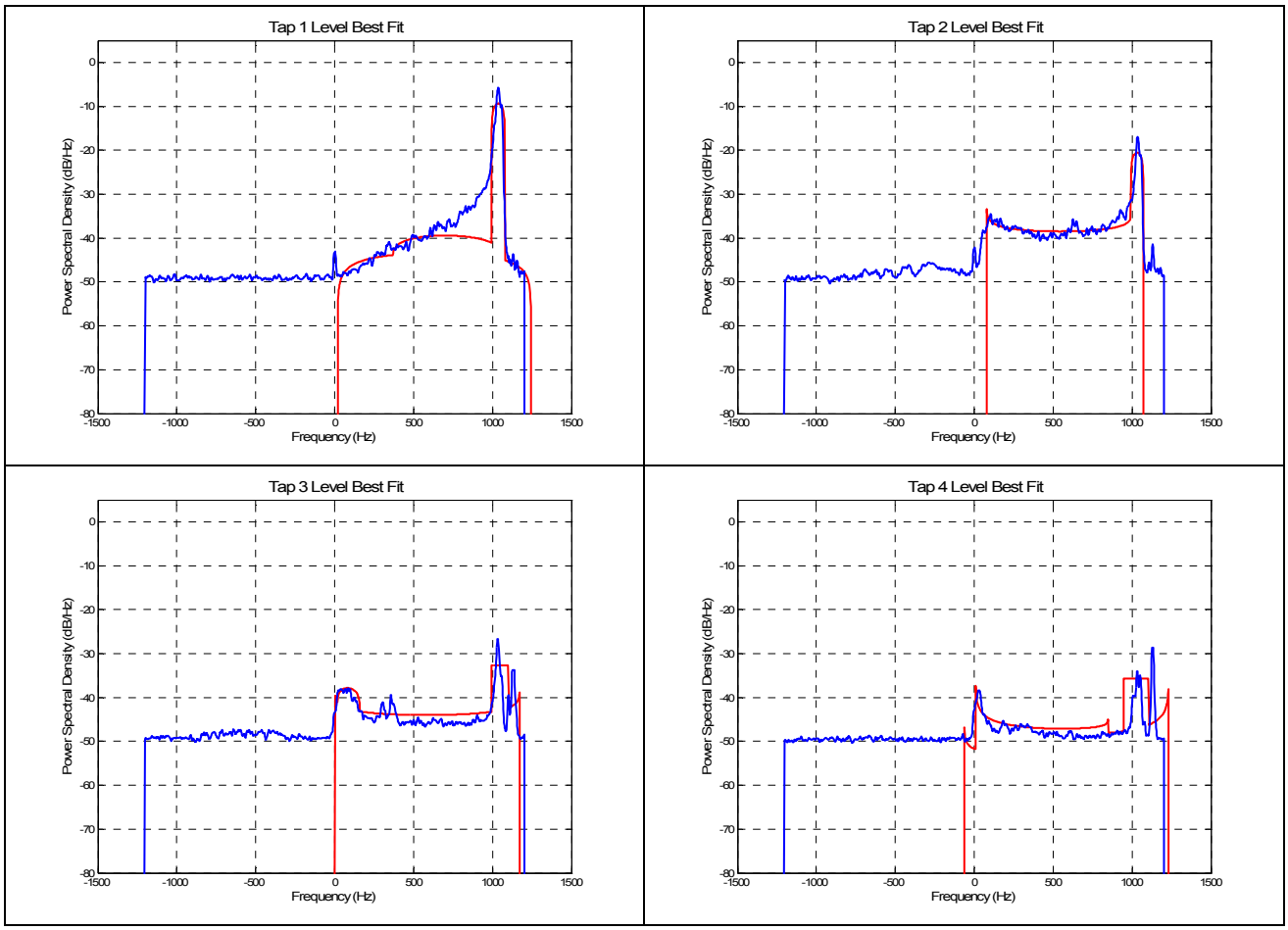

Figure 129: Tap spectra for the MTM Expressway Oncoming scenario. In blue: the measured Doppler spectrum for the random part. In red: the composite or customized spectrum, which corresponds to Table 11.

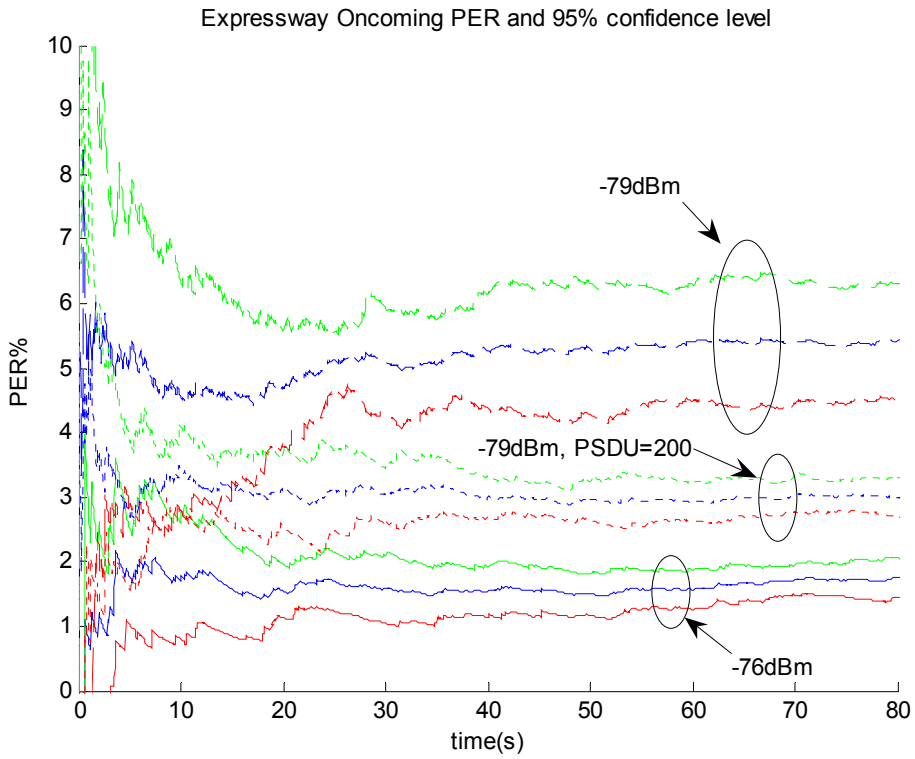

Figure **130**: For the Expressway Oncoming 400m scenario, mean PER and 95% confidence intervals for -79 dBm 1000 Byte PSDU (top curves), -79 dBm, 200 Byte PSDU (middle three curves), and -76 dBm 1000 Byte PSDU (bottom curves).

7.2.2 RTM - Urban Canyon, 100 m Scenario

Both short and long models are presented in Table 12 and Table 13, respectively. As shown in Figure 133, the short model produces a slightly higher PER.

Table 12: RTM – Urban Canyon, 100 m Short Model

Tap No.	Path No.	Tap Power (dB)	Relative Path Loss (dB)	Delay Value (ns)	Rician K (dB)	Freq. Shift (Hz)	Fading Doppler (Hz)	LOS Doppler (Hz)	Modulation	Fad. Spec. Shape
1	1	0.0	-1.8	0	7.5	574	165	654	Rician	Round
1	2		-30.5	1	n/a	-97	543	n/a	Rayleigh	Classic 3dB
1	3		-25.1	2	n/a	-89	478	n/a	Rayleigh	Classic 3dB
2	4	-11.5	-27.1	100	n/a	-549	174	n/a	Rayleigh	Round
2	5		-17.7	101	n/a	559	196	n/a	Rayleigh	Round
2	6		-19.5	102	n/a	115	757	n/a	Rayleigh	Classic 6dB
3	7	-19.0	-17.6	200	n/a	610	258	n/a	Rayleigh	Classic 6dB
3	8		-19.9	201	n/a	72	929	n/a	Rayleigh	Flat
4	9	-25.6	-23.3	300	n/a	183	653	n/a	Rayleigh	Classic 6dB
4	10		-20.6	301	n/a	103	994	n/a	Rayleigh	Round
5	11	-28.1	-29.8	500	n/a	720	220	n/a	Rayleigh	Flat
5	12		-28.0	501	n/a	-20	871	n/a	Rayleigh	Flat

Notes:

1. All Taps have composite spectra. Tap One has a Rician component in the first path, and it has random spectra in the other two paths.
2. Please notice the 200 ns gap between Tap Four and Tap Five.
3. This table is consistent with vehicle speeds of 120 km/hr (75 mph) and separation between transmitter tower and receiver vehicle of approximately 100m.

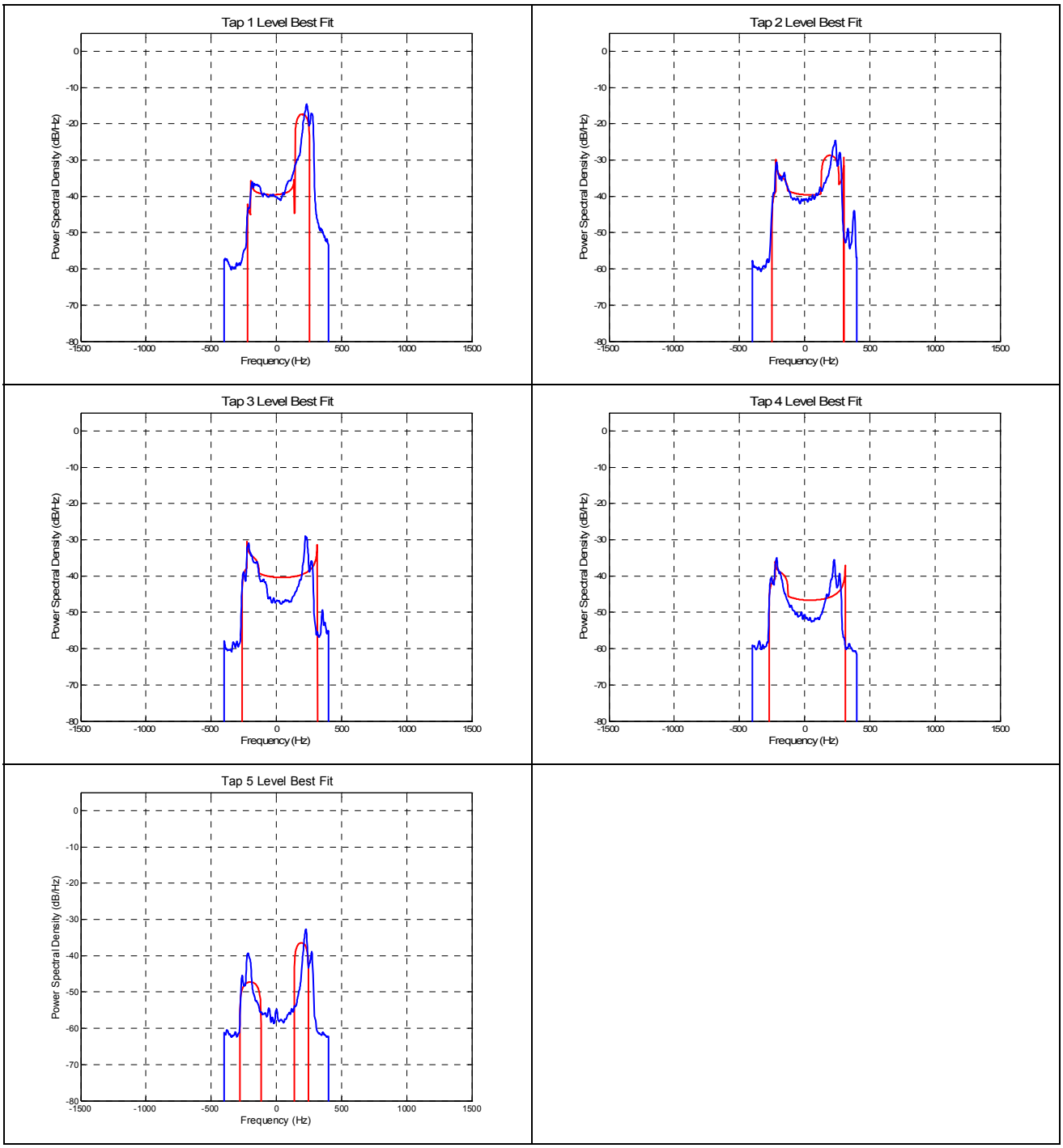

Figure 131: Tap spectra for the RTM Urban Canyon 100m scenario, short model. In blue: the measured Doppler spectrum for the random part. In red: the composite or customized spectrum, which corresponds to Table 12.

Table 13: RTM – Urban Canyon, 100 m Long Model

Tap No.	Path No.	Tap Power (dB)	Relative Path Loss (dB)	Delay Value (ns)	Rician K (dB)	Freq. Shift (Hz)	Fading Doppler (Hz)	LOS Doppler (Hz)	Modulation	Fad. Spec. Shape
1	1	0.0	-1.8	0	7.5	574	165	654	Rician	Round
1	2		-30.5	1	n/a	-97	543	n/a	Rayleigh	Classic 3dB
1	3		-25.1	2	n/a	-89	478	n/a	Rayleigh	Classic 3dB
2	4	-11.5	-27.1	100	n/a	-549	174	n/a	Rayleigh	Round
2	5		-17.7	101	n/a	559	196	n/a	Rayleigh	Round
2	6		-19.5	102	n/a	115	757	n/a	Rayleigh	Classic 6dB
3	7	-19.0	-23.8	200	n/a	43	698	n/a	Rayleigh	Classic 6dB
3	8		-28.1	201	n/a	573	186	n/a	Rayleigh	Flat
3	9		-27.6	202	n/a	-571	193	n/a	Rayleigh	Round
4	10	-25.6	-33.4	300	n/a	-137	494	n/a	Rayleigh	Classic 6dB
4	11		-30.5	301	n/a	-573	211	n/a	Rayleigh	Round
4	12		-31.6	302	n/a	576	250	n/a	Rayleigh	Round
5	13	-28.1	-48.7	500	n/a	-506	644	n/a	Rayleigh	Flat
5	14		-29.9	501	n/a	575	162	n/a	Rayleigh	Flat
5	15		-38.5	502	n/a	-567	241	n/a	Rayleigh	Round

Notes:

1. All Taps have composite spectra. Tap One has a Rician component in the first path, and it has random spectra in the other two paths.
2. Please notice the 200 ns gap between Tap Four and Tap Five.
3. This table is consistent with vehicle speeds of 120 km/hr (75 mph) and separation between transmitter tower and receiver vehicle of approximately 100m.

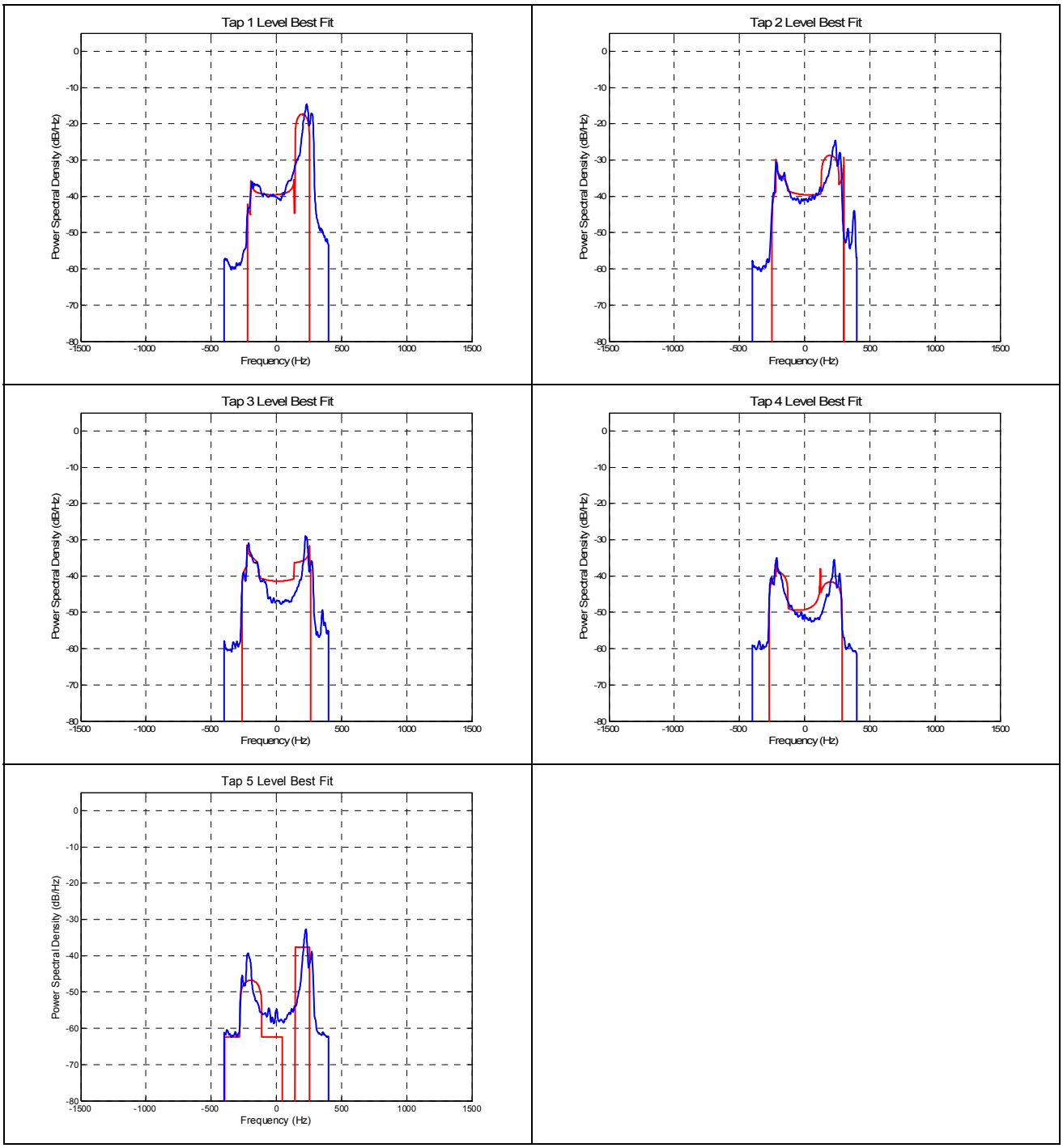

Figure 132: Tap spectra for the RTM Urban Canyon 100m scenario, long model. In blue: the measured Doppler spectrum for the random part. In red: the composite or customized spectrum, which corresponds to Table 13.

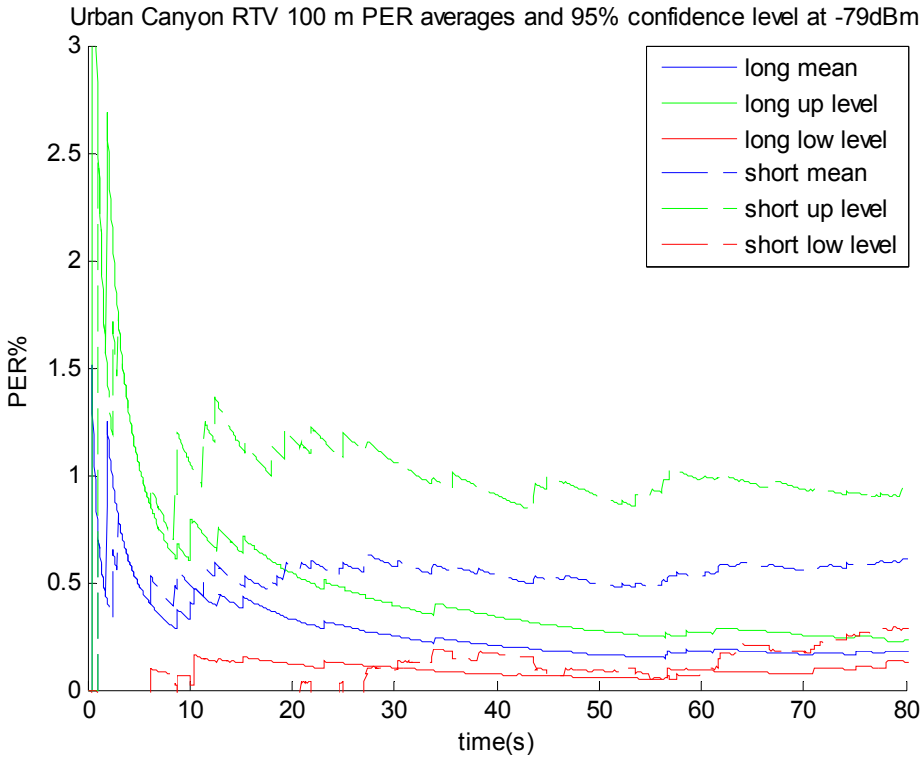

Figure 133: RTM – Urban Canyon 100m scenario: mean PER and 95% confidence intervals for -79 dBm and 1000-Byte PSDU, short and long models.

7.2.3 RTM – Expressway, 300m – 400m Scenario

Table 14: RTM – Expressway, 300m – 400m 140 km/hr Model

Tap No.	Path No.	Tap Power (dB)	Relative Path Loss (dB)	Delay Value (ns)	Rician K (dB)	Freq. Shift (Hz)	Fading Doppler (Hz)	LOS Doppler (Hz)	Modulation	Fad. Spec. Shape
1	1	0.0	0.0	0	-5.3	769	70	770	Rician	Round
1	2		-36.4	1	n/a	-22	600	n/a	Rayleigh	Round
1	3		-30.0	2	n/a	535	376	n/a	Rayleigh	Round
2	4	-9.3	-12.3	100	n/a	754	117	n/a	Rayleigh	Round
2	5		-21.7	101	n/a	548	424	n/a	Rayleigh	Round
2	6		-24.9	102	n/a	-134	530	n/a	Rayleigh	Flat
3	7	-20.3	-24.3	200	n/a	761	104	n/a	Rayleigh	Round
3	8		-25.4	201	n/a	88	813	n/a	Rayleigh	Classic 3dB
4	9	-21.3	-26.8	300	n/a	37	802	n/a	Rayleigh	Classic 6dB
4	10		-28.5	301	n/a	752	91	n/a	Rayleigh	Round
5	11	-28.8	-31.2	400	n/a	16	807	n/a	Rayleigh	Classic 6dB
5	12		-41.8	401	n/a	-755	329	n/a	Rayleigh	Round

Notes:

1. All Taps have composite spectra. Tap One has a Rician component in the first path, and it has random spectra in the other two paths.
2. This table is consistent with vehicle speeds of 140 km/hr (87 mph) and separation between transmitter and receiver vehicle of approximately 400m.

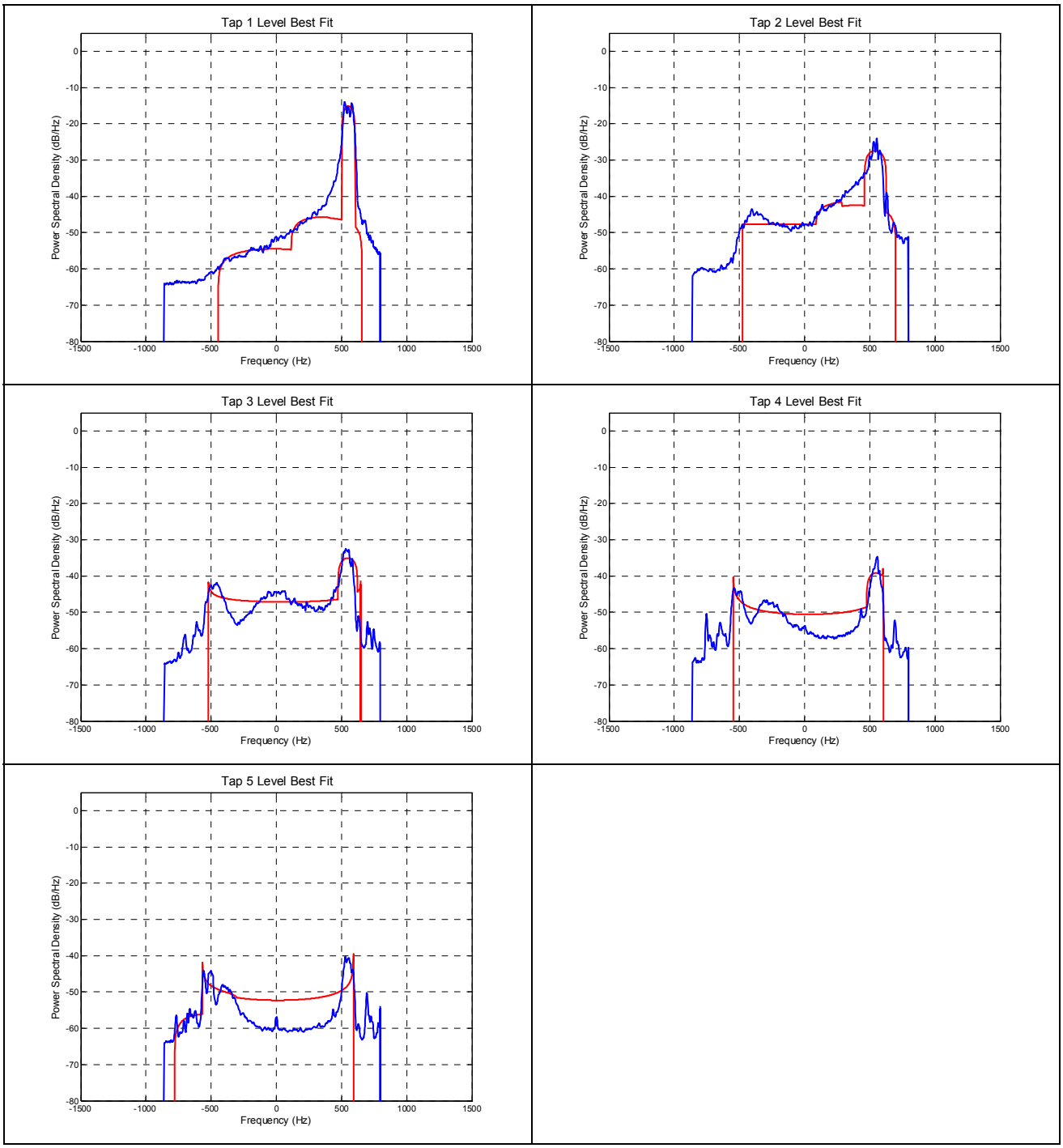

Figure 134: Tap spectra for the RTM Expressway 300-400m scenario. In blue: the measured Doppler spectrum for the random part. In red: the composite or customized spectrum, which corresponds to Table 14.

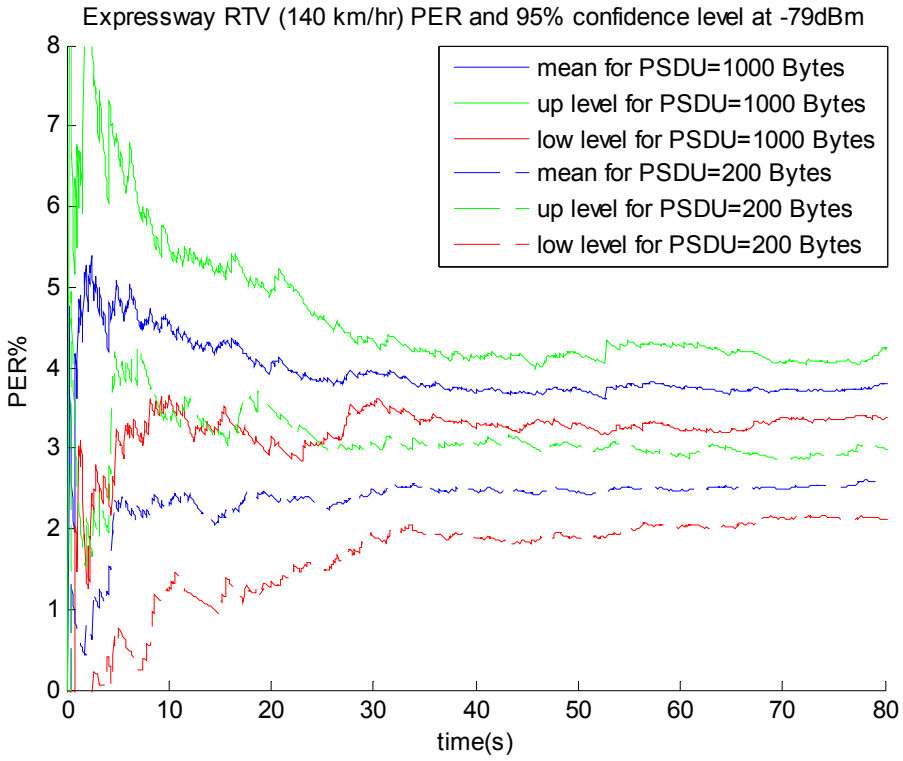

Figure 135: RTM – Expressway 300-400m scenario: mean PER and 95% confidence intervals for -79 dBm, for 200- and 1000-Byte PSDUs and vehicle speed of 140 km/hr.

Table 15: RTM – Expressway, 300m – 400m 200 km/hr Model

Tap No.	Path No.	Tap Power (dB)	Relative Path Loss (dB)	Delay Value (ns)	Rician K (dB)	Freq. Shift (Hz)	Fading Doppler (Hz)	LOS Doppler (Hz)	Modulation	Fad. Spec. Shape
1	1	0.0	0.0	0	-5.3	1101	100	1092	Rician	Round
1	2		-36.4	1	n/a	-32	859	n/a	Rayleigh	Round
1	3		-30.0	2	n/a	766	538	n/a	Rayleigh	Round
2	4	-9.3	-12.3	100	n/a	1080	168	n/a	Rayleigh	Round
2	5		-21.7	101	n/a	784	608	n/a	Rayleigh	Round
2	6		-24.9	102	n/a	-192	759	n/a	Rayleigh	Flat
3	7	-20.3	-24.3	200	n/a	1090	149	n/a	Rayleigh	Round
3	8		-25.4	201	n/a	126	1164	n/a	Rayleigh	Classic 3dB
4	9	-21.3	-26.8	300	n/a	54	1148	n/a	Rayleigh	Classic 6dB
4	10		-28.5	301	n/a	1077	130	n/a	Rayleigh	Round
5	11	-28.8	-31.2	400	n/a	24	1156	n/a	Rayleigh	Classic 6dB
5	12		-41.8	401	n/a	-1081	470	n/a	Rayleigh	Round

Notes:

1. All Taps have composite spectra. Tap One has a Rician component in the first path, and it has random spectra in the other two paths.
2. This table is consistent with vehicle speeds of 200 km/hr (124 mph) and separation between transmitter and receiver vehicle of approximately 400m.

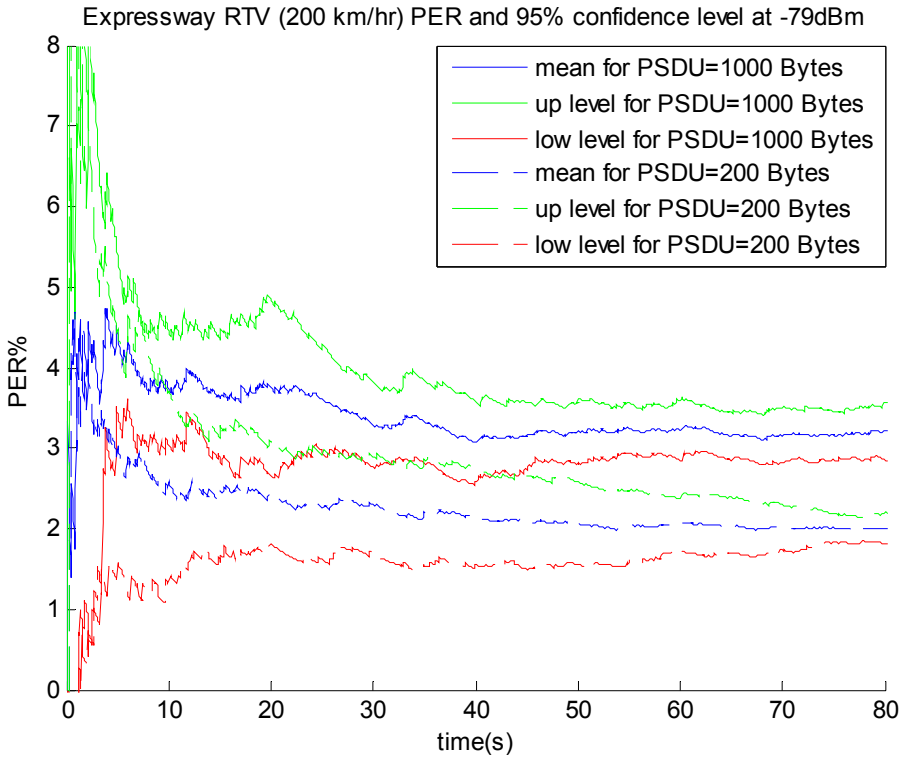

Figure 136: RTM – Expressway 300-400m scenario: mean PER and 95% confidence intervals for -79 dBm, for 200- and 1000-Byte PSDUs and vehicle speed of 200 km/hr.

7.2.4 MTM - Urban Canyon Oncoming, 100m Scenario

There are short and long versions of this model, given in Table 16 and Table 17, respectively. The PER results are shown together in Figure 133.

Table 16: MTM - Urban Canyon Oncoming, 100m Short Model

Tap No.	Path No.	Tap Power (dB)	Relative Path Loss (dB)	Delay Value (ns)	Rician K (dB)	Freq. Shift (Hz)	Fading Doppler (Hz)	LOS Doppler (Hz)	Modulation	Fad. Spec. Shape
1	1	0.0	0.0	0	4.0	1145	284	1263	Rician	Round
1	2		-17.6	1	n/a	833	824	n/a	Rayleigh	Round
2	3	-10.0	-12.9	100	n/a	707	871	n/a	Rayleigh	Round
2	4		-19.0	101	n/a	918	286	n/a	Rayleigh	Classic 6dB
2	5		-36.4	102	n/a	-250	936	n/a	Rayleigh	Flat
3	6	-17.8	-25.8	200	n/a	21	166	n/a	Rayleigh	Round
3	7		-21.2	201	n/a	677	726	n/a	Rayleigh	Flat
3	8		-31.6	202	n/a	-188	538	n/a	Rayleigh	Round
4	9	-21.1	-28.2	300	n/a	538	908	n/a	Rayleigh	Round
4	10		-28.3	301	n/a	41	183	n/a	Rayleigh	Round
5	11	-26.3	-28.5	400	n/a	674	723	n/a	Rayleigh	Classic 6dB
5	12		-35.5	401	n/a	-78	260	n/a	Rayleigh	Round

Notes:

1. All Taps have composite spectra. Tap One has a Rician component in the first path, and it has random spectra in the other two paths.
2. This table is consistent with vehicle speeds of 120 km/hr (75 mph) and separation between transmitter and receiver vehicles of approximately 100m.

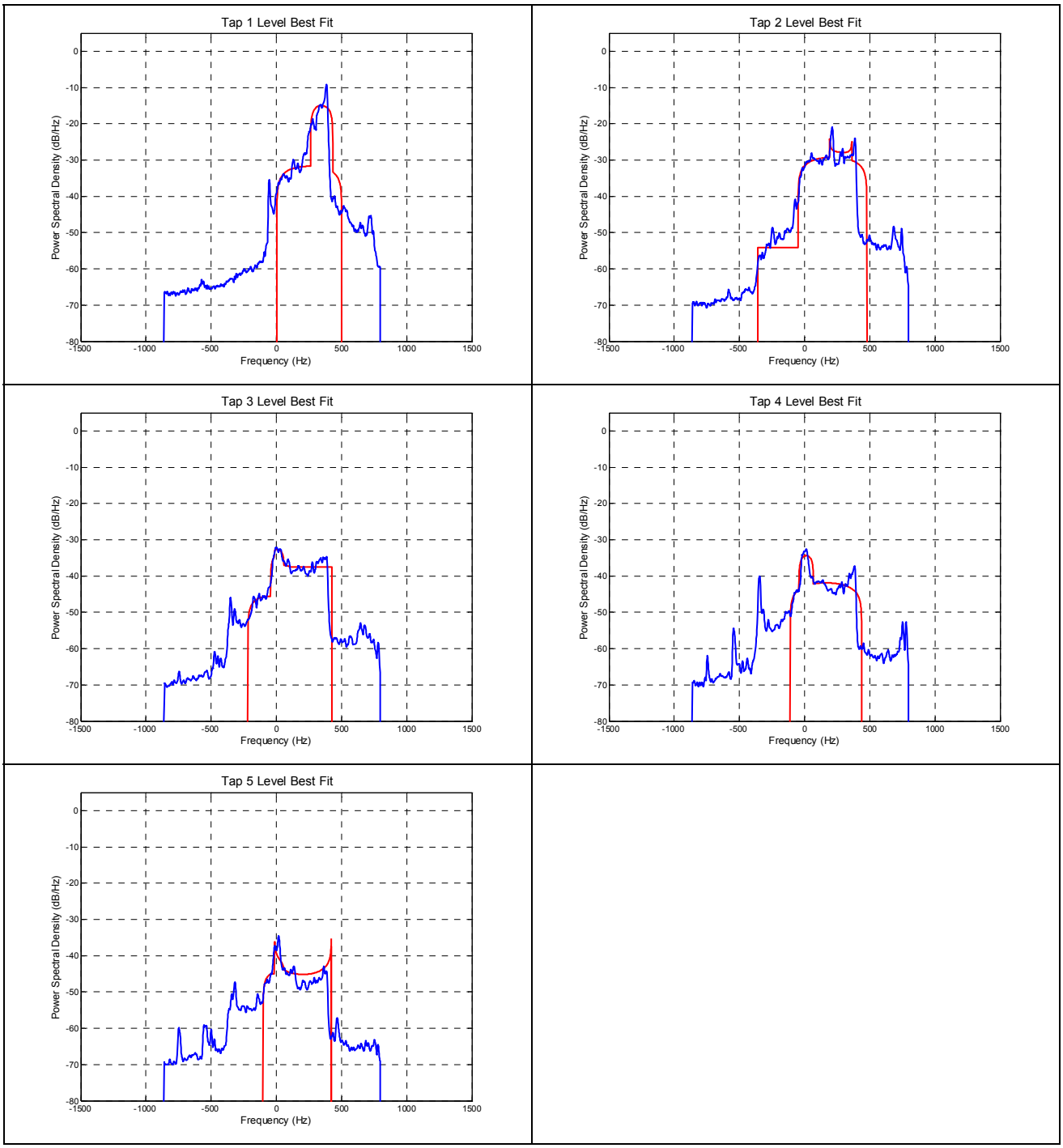

Figure 137: Tap spectra for the MTM Urban Canyon 100m scenario, short model. In blue: the measured Doppler spectrum for the random part. In red: the composite or customized spectrum, which corresponds to Table 16.

Table 17: MTM - Urban Canyon Oncoming, 100m Long Model

Tap No.	Path No.	Tap Power (dB)	Relative Path Loss (dB)	Delay Value (ns)	Rician K (dB)	Freq. Shift (Hz)	Fading Doppler (Hz)	LOS Doppler (Hz)	Modulation	Fad. Spec. Shape
1	1	0.0	0.0	0	4.0	1153	310	1263	Rician	Round
1	2		-18.3	1	n/a	827	449	n/a	Rayleigh	Round
1	3		-26.3	2	n/a	211	236	n/a	Rayleigh	Flat
2	4	-10.0	-12.9	100	n/a	707	871	n/a	Rayleigh	Round
2	5		-19.0	101	n/a	918	286	n/a	Rayleigh	Classic 6dB
2	6		-36.4	102	n/a	-250	936	n/a	Rayleigh	Flat
3	7	-17.8	-25.8	200	n/a	21	166	n/a	Rayleigh	Round
3	8		-21.2	201	n/a	677	726	n/a	Rayleigh	Flat
3	9		-31.6	202	n/a	-188	538	n/a	Rayleigh	Round
4	10	-21.1	-35.6	300	n/a	-68	198	n/a	Rayleigh	Round
4	11		-40.7	301	n/a	-497	484	n/a	Rayleigh	Round
4	12		-25.8	302	n/a	669	751	n/a	Rayleigh	Classic 6dB
5	13	-26.3	-41.9	400	n/a	-759	491	n/a	Rayleigh	Round
5	14		-30.3	401	n/a	451	774	n/a	Rayleigh	Round
5	15		-31.4	402	n/a	24	168	n/a	Rayleigh	Round

Notes:

1. All Taps have composite spectra. Tap One has a Rician component in the first path, and it has random spectra in the two other paths.
2. This table is consistent with vehicle speeds of 120 km/hr (75 mph) and separation between transmitter and receiver vehicles of approximately 100m.

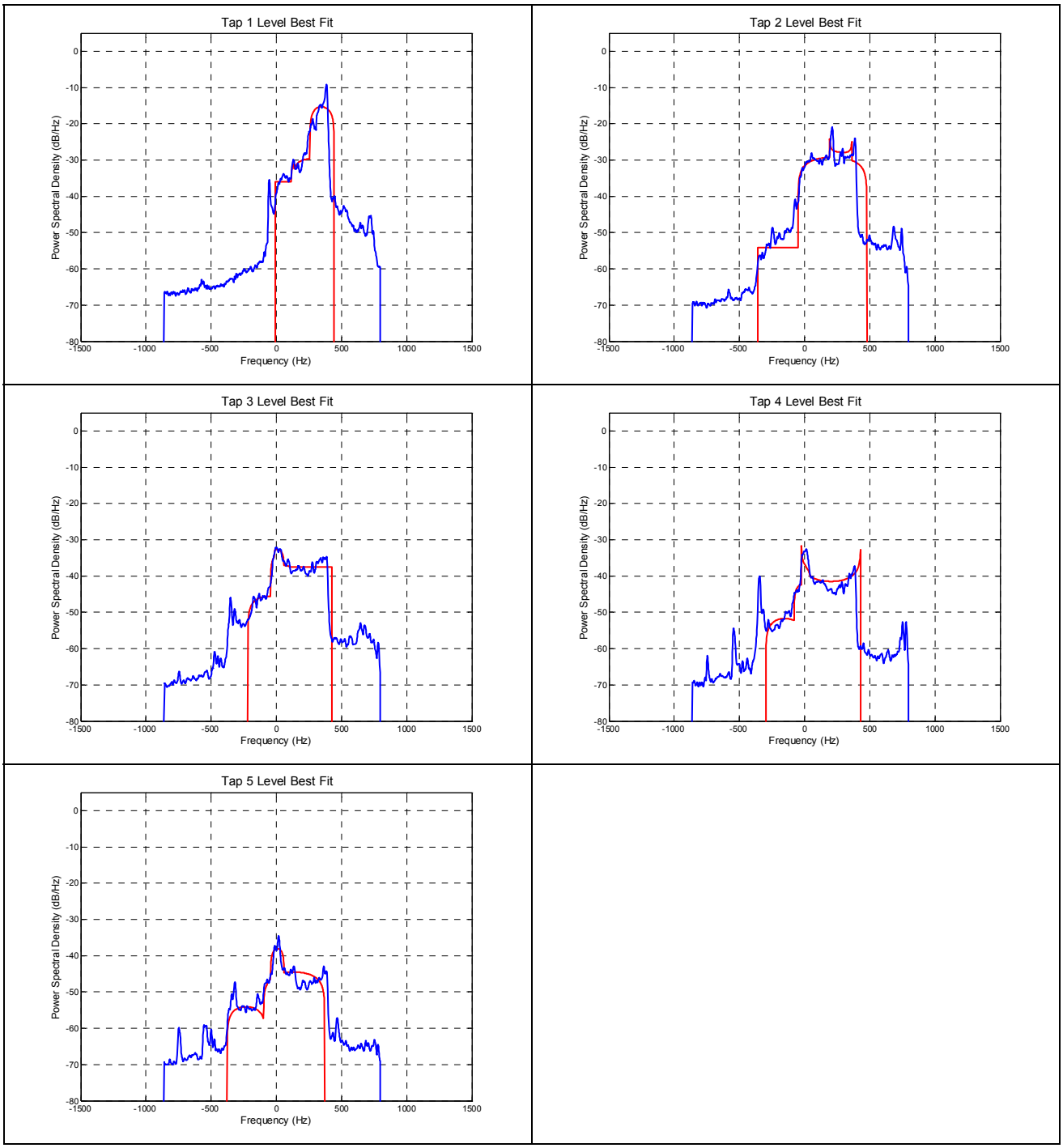

Figure 138: Tap spectra for the MTM Urban Canyon 100m scenario, long model. In blue: the measured Doppler spectrum for the random part. In red: the composite or customized spectrum, which corresponds to Table 17.

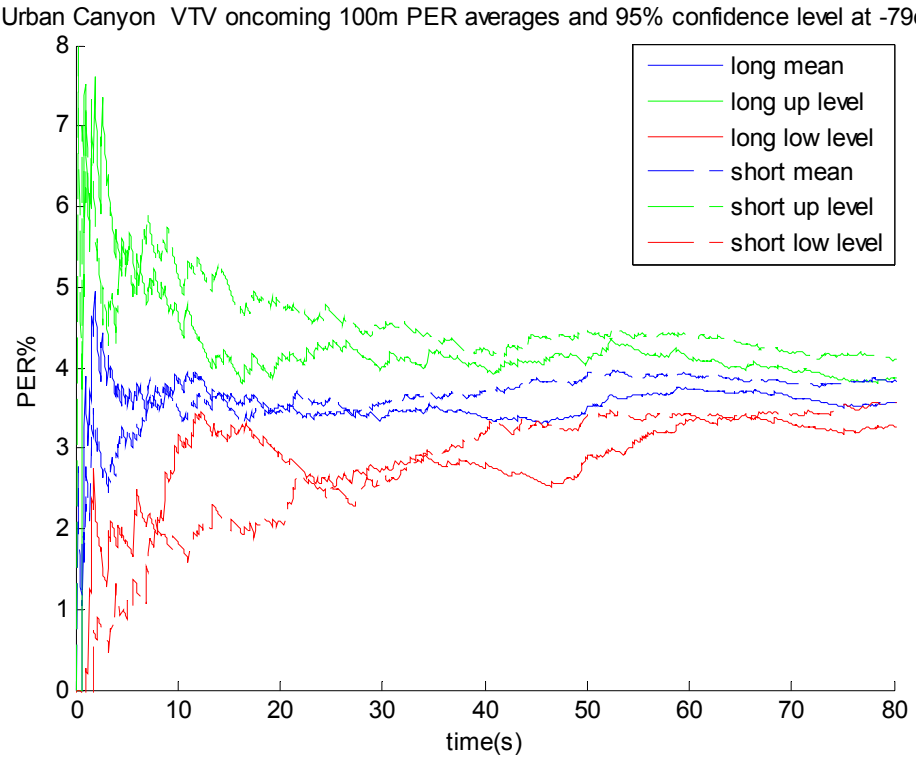

Figure 139: MTM – Urban Canyon 100m scenario: mean PER and 95% confidence intervals for -79 dBm and 1000-Byte PSDU, short and long models.

7.2.5 RTM - Suburban Street, 100m Scenario

This model has both short and long versions specified in Table 18 and Table 19 respectively. The PER results are shown together in Figure 144.

Table 18: RTM - Suburban Street, 100m Short Model

Tap No.	Path No.	Tap Power (dB)	Relative Path Loss (dB)	Delay Value (ns)	Rician K (dB)	Freq. Shift (Hz)	Fading Doppler (Hz)	LOS Doppler (Hz)	Modulation	Fad. Spec. Shape
1	1	0.0	0.0	0	3.3	648	152	635	Rician	Round
1	2		-21.5	1	n/a	171	823	n/a	Rayleigh	Round
2	3	-9.3	-11.8	100	n/a	582	249	n/a	Rayleigh	Round
2	4		-18.8	101	n/a	-119	515	n/a	Rayleigh	Classic 3dB
3	5	-14.0	-17.6	200	n/a	527	223	n/a	Rayleigh	Round
3	6		-19.9	201	n/a	62	802	n/a	Rayleigh	Flat
4	7	-18.0	-23.0	300	n/a	497	396	n/a	Rayleigh	Classic 6dB
4	8		-20.8	301	n/a	87	851	n/a	Rayleigh	Round
5	9	-19.4	-19.4	400	n/a	43	747	n/a	Rayleigh	Round
6	10	-24.9	-24.9	500	n/a	114	742	n/a	Rayleigh	Classic 6dB
7	11	-27.5	-27.5	600	n/a	38	746	n/a	Rayleigh	Classic 3dB
8	12	-29.8	-29.8	700	n/a	8	743	n/a	Rayleigh	Classic 3dB

Notes:

1. Taps 1, 2, 3, and 4 have composite spectra. Tap One has a Rician component in the first path, and it has a random spectrum in the second path. Taps 2, 3, and 8 each comprise two paths.
2. This table is consistent with vehicle speeds of 120 km/hr (75 mph) and separation between transmitter tower and receiver vehicle of approximately 100m.

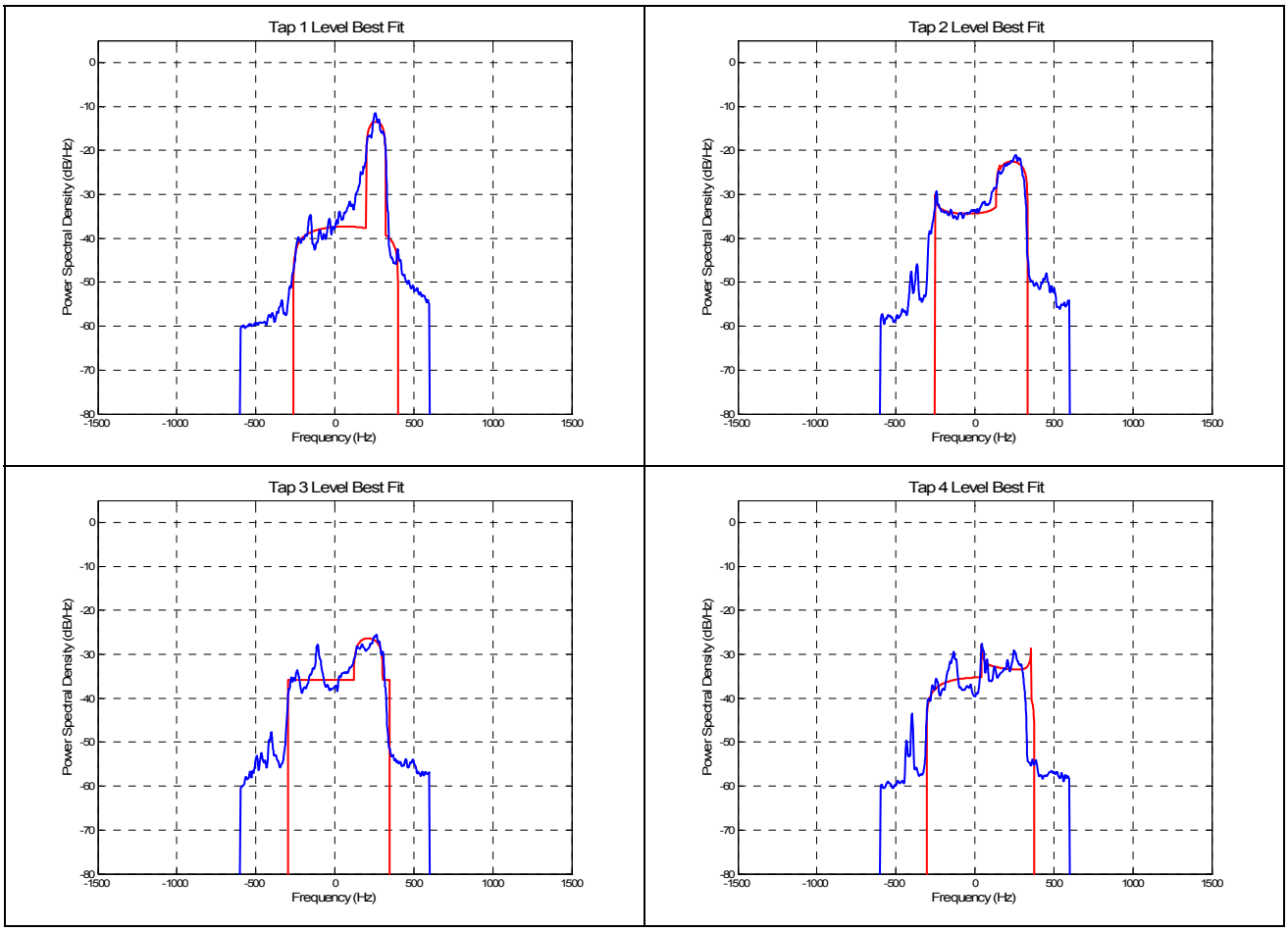

Figure 140: First four tap spectra for the RTM Suburban Street 100m scenario, short model. In blue: the measured Doppler spectrum for the random part. In red: the composite or customized spectrum, which corresponds to Table 18.

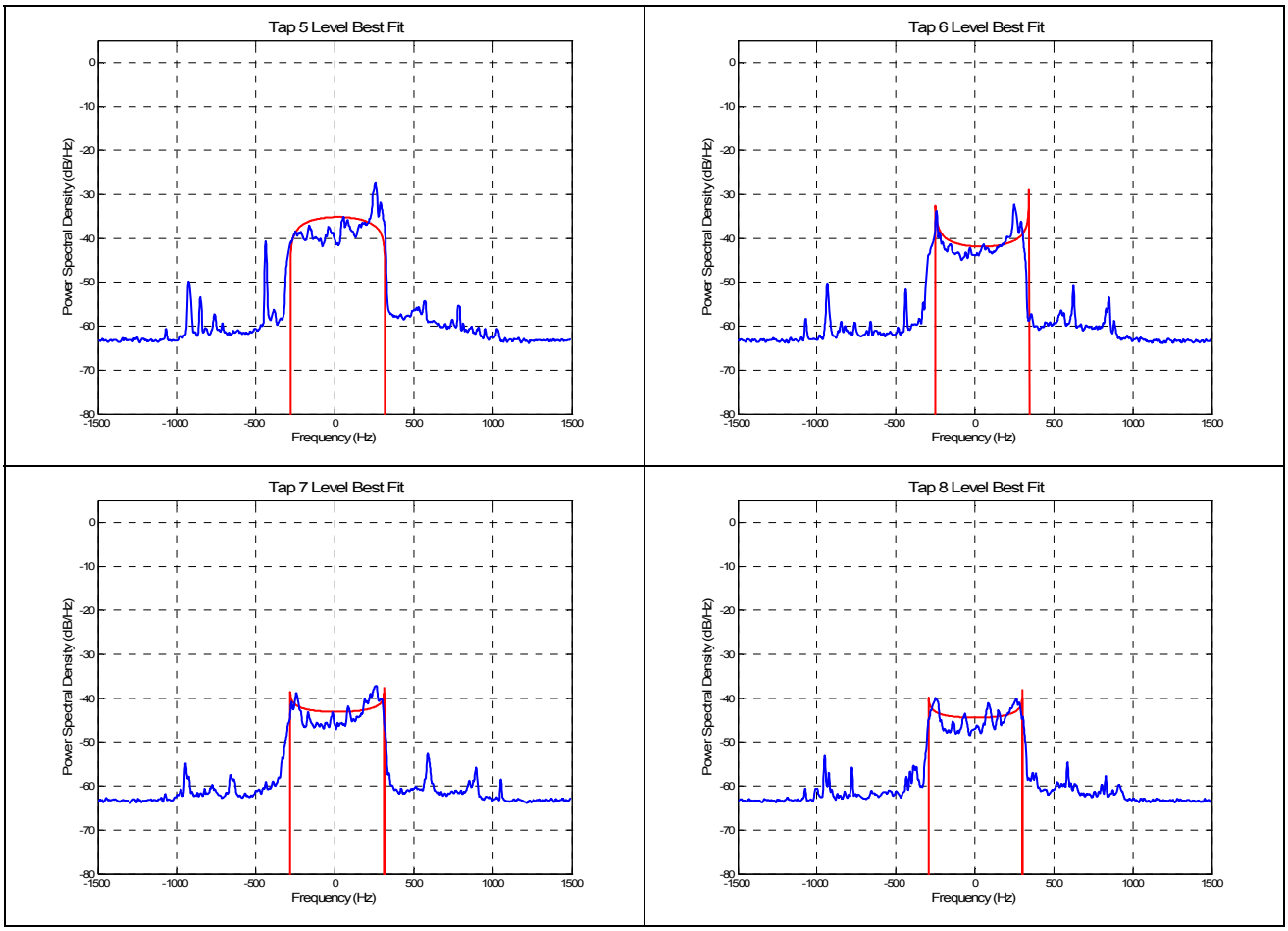

Figure 141: Second four tap spectra for the RTM Suburban Street 100m scenario, short model. In blue: the measured Doppler spectrum for the random part. In red: the composite or customized spectrum, which corresponds to Table 18.

Table 19: RTM - Suburban Street, 100m Long Model

Tap No.	Path No.	Tap Power (dB)	Relative Path Loss (dB)	Delay Value (ns)	Rician K (dB)	Freq. Shift (Hz)	Fading Doppler (Hz)	LOS Doppler (Hz)	Modulation	Fad. Spec. Shape
1	1	0.0	0.0	0	3.3	648	152	635	Rician	Round
1	2		-21.5	1	n/a	171	823	n/a	Rayleigh	Round
2	3	-9.3	-11.8	100	n/a	582	249	n/a	Rayleigh	Round
2	4		-18.8	101	n/a	-119	515	n/a	Rayleigh	Classic 3dB
3	5	-14.0	-17.6	200	n/a	527	223	n/a	Rayleigh	Round
3	6		-19.9	201	n/a	62	802	n/a	Rayleigh	Flat
4	7	-18.0	-23.0	300	n/a	497	396	n/a	Rayleigh	Classic 6dB
4	8		-20.8	301	n/a	87	851	n/a	Rayleigh	Round
5	9	-19.4	-24.5	400	n/a	645	125	n/a	Rayleigh	Round
5	10		25.2	401	n/a	33	753	n/a	Rayleigh	Flat
6	11	-24.9	-29.8	500	n/a	497	128	n/a	Rayleigh	Round
6	12		-27.9	501	n/a	12	634	n/a	Rayleigh	Classic 6dB
7	13	-27.5	-30.8	600	n/a	13	716	n/a	Rayleigh	Classic 6dB
7	14		-32.8	601	n/a	485	315	n/a	Rayleigh	Round
8	15	-29.8	-35.5	700	n/a	473	325	n/a	Rayleigh	Flat
8	16		-32.9	701	n/a	-28	712	n/a	Rayleigh	Classic 3dB

Notes:

1. All Taps have composite spectra. Tap One has a Rician component in the first path, and it has a random spectrum in the second path.
2. This table is consistent with vehicle speeds of 120 km/hr (75 mph) and separation between transmitter tower and receiver vehicle of approximately 100m.

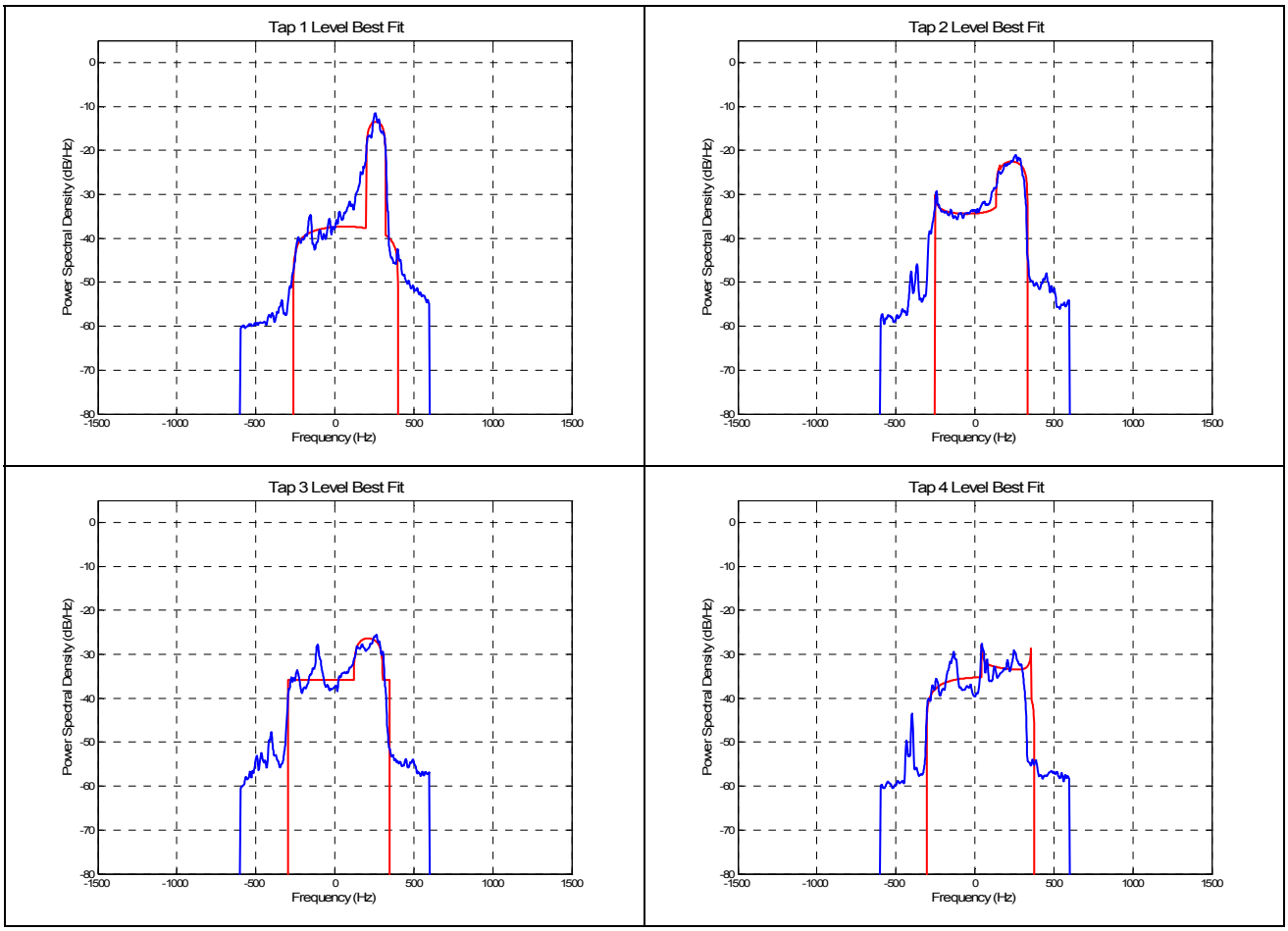

Figure 142: First four tap spectra for the RTM Suburban Street 100m scenario, long model. In blue: the measured Doppler spectrum for the random part. In red: the composite or customized spectrum, which corresponds to Table 19.

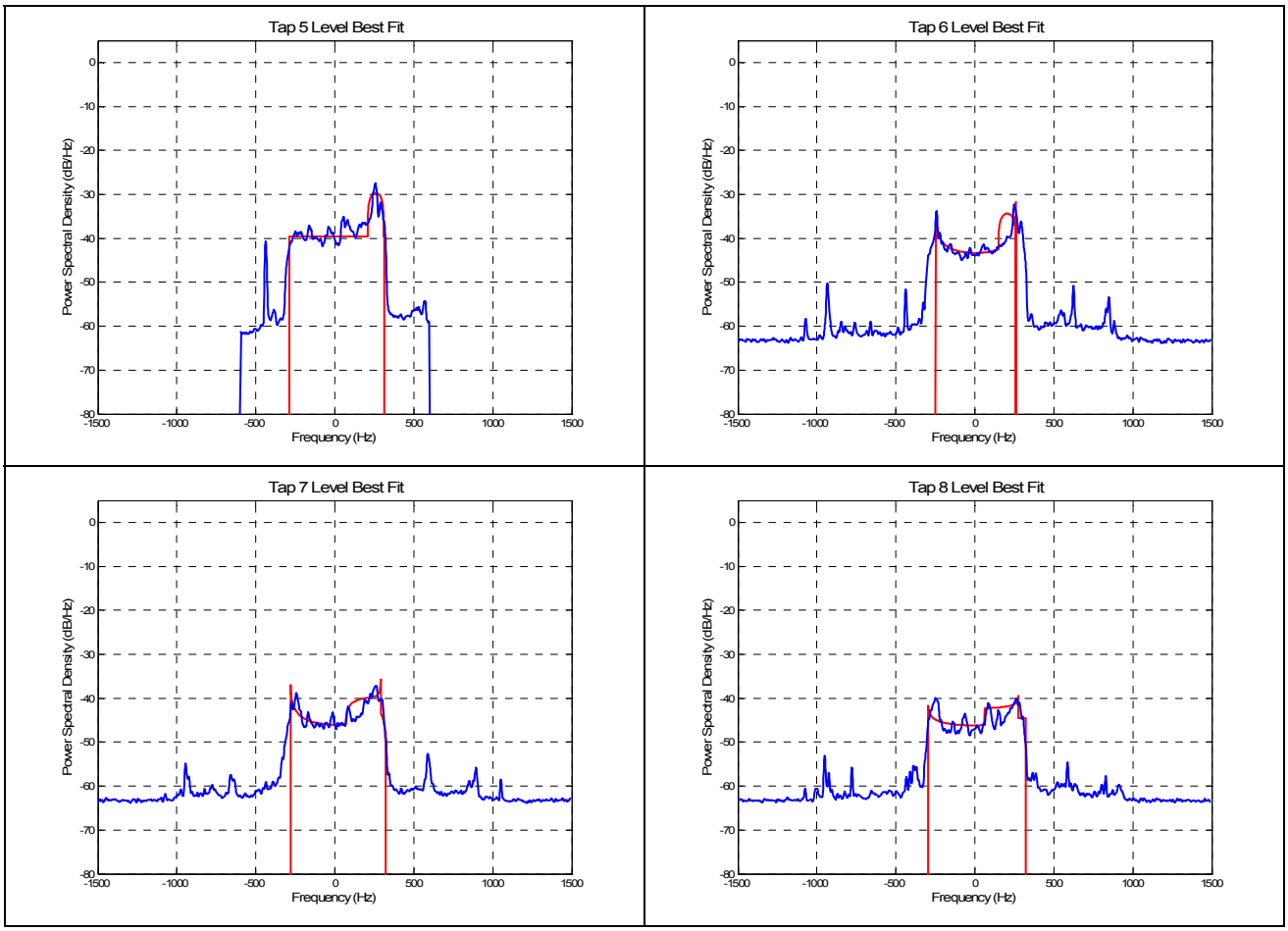

Figure 143: Second four tap spectra for the RTM Suburban Street 100m scenario, long model. In blue: the measured Doppler spectrum for the random part. In red: the composite or customized spectrum, which corresponds to Table 19.

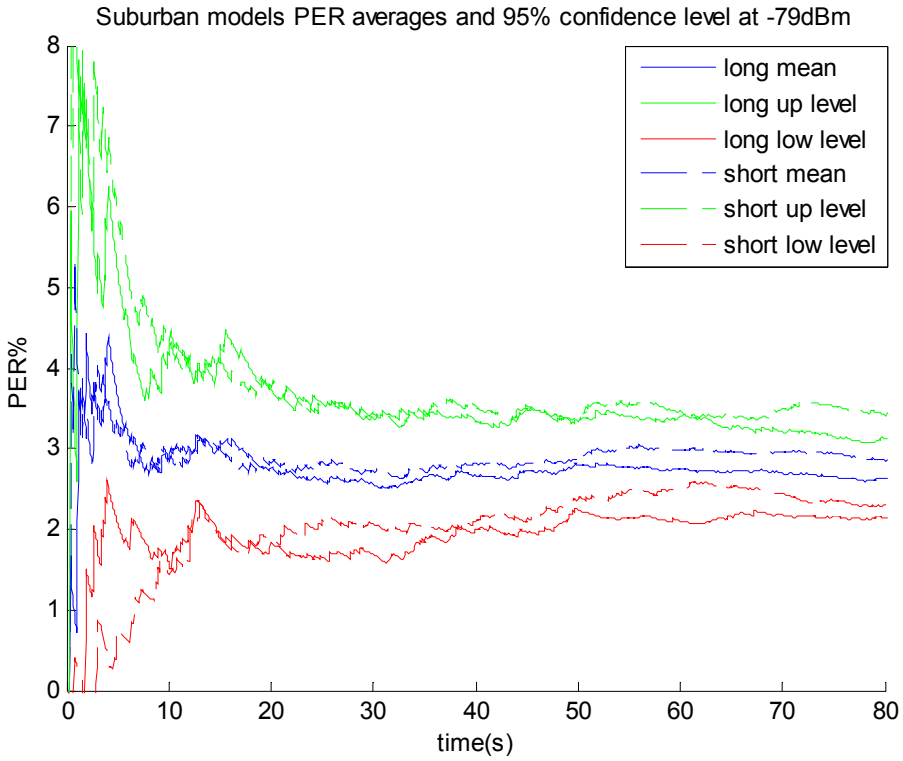

Figure 144: Mean PER and 95% confidence intervals for -79 dBm, 1000-Byte PSDU, for the short and long Suburban Street RTM 100m scenarios.

7.2.6 MTM - Expressway Same Direction with Wall, 300m – 400m Scenario

Because of the large K factor for this model, the PER was 0% for all power levels tested. To induce errors, the deterministic parts of the Rician taps were eliminated, to emulate blocking the LOS component, without changing anything else about the model. This version of the model is called “All Rayleigh Paths.”

Table 20: MTM - Expressway Same Direction with Wall, 300m – 400m Model

Tap No.	Path No.	Tap Power (dB)	Relative Path Loss (dB)	Delay Value (ns)	Rician K (dB)	Freq. Shift (Hz)	Fading Doppler (Hz)	LOS Doppler (Hz)	Modulation	Fad. Spec. Shape
1	1	0.0	-1.4	0	23.8	-55	1407	-60	Rician	Round
1	2		-5.6	1	n/a	-20	84	n/a	Rayleigh	Round
2	3	-11.2	-14.2	100	5.7	-56	1345	+40	Rician	Classic 3 dB
2	4		-14.2	101	n/a	0	70	n/a	Rayleigh	Round
3	5	-19.0	-19.0	200	n/a	-87	1358	n/a	Rayleigh	Classic 6 dB
4	6	-21.9	-21.9	300	n/a	-139	1397	n/a	Rayleigh	Classic 3 dB
5	7	-25.3	-27.9	400	n/a	60	1522	n/a	Rayleigh	Classic 6 dB
5	8		-30.8	401	n/a	-561	997	n/a	Rayleigh	Classic 3 dB
6	9	-24.4	-24.4	500	n/a	50	1529	n/a	Rayleigh	Round
7	10	-28.0	-28.0	600	n/a	13	1572	n/a	Rayleigh	Round
8	11	-26.1	-31.5	700	n/a	-6	1562	n/a	Rayleigh	Classic 6 dB
8	12		-28.1	701	n/a	4	81	n/a	Rayleigh	Round

Notes:

1. Taps 1, 2, 5 and 8 each comprises two paths. The first two taps each have both Rician and Rayleigh paths. The overall K factor is 4.0 dB for Tap 1 and -1.8 dB for Tap 2. Tap 8 comprises two Rayleigh paths.
2. This table is consistent with vehicle speeds of 140 km/hr (87 mph) and separation between transmitter and receiver vehicles of approximately 400m.

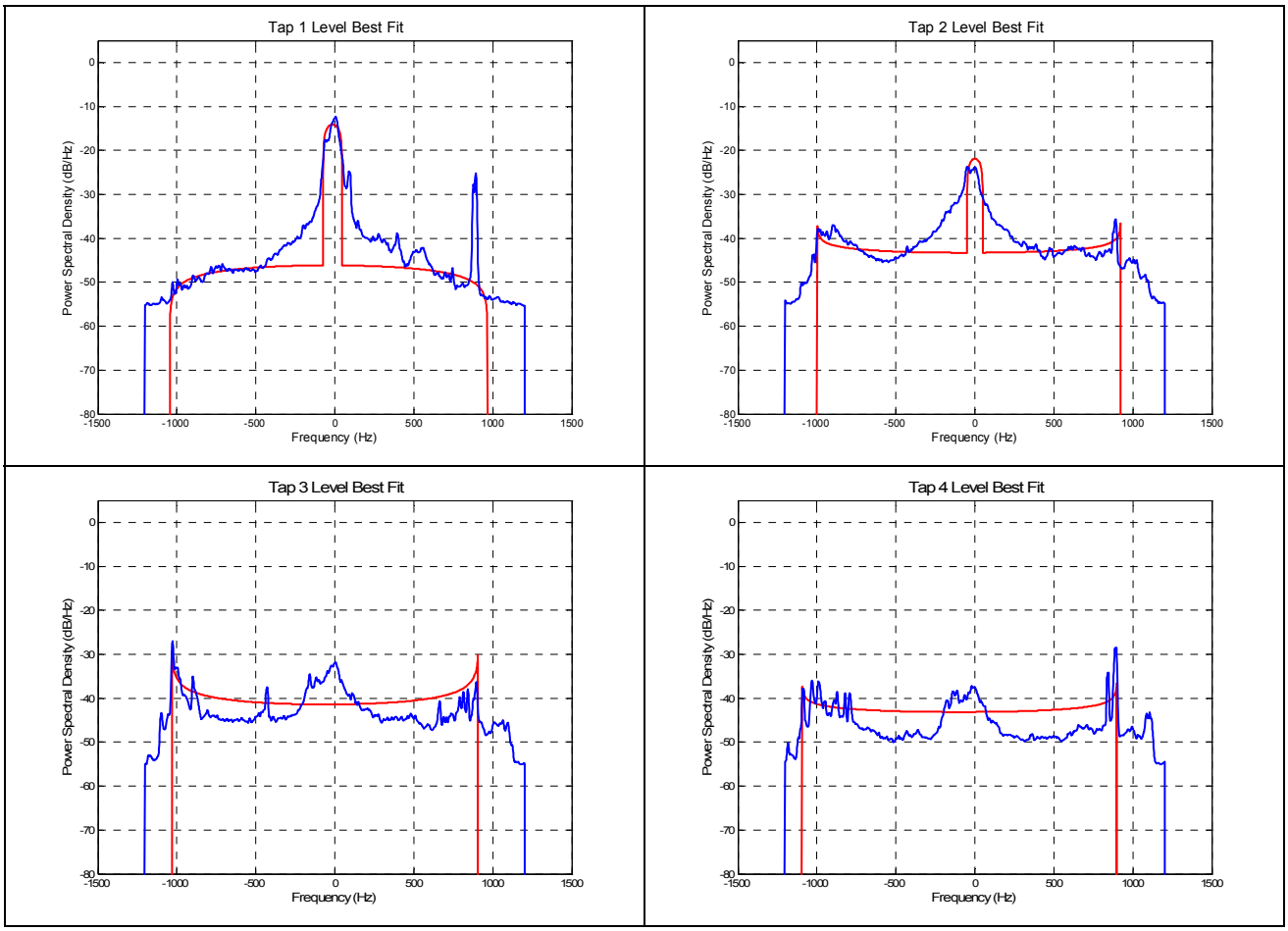

Figure 145: First four tap spectra for the MTM Expressway Same Direction with Wall 300-400m scenario. In blue: the measured Doppler spectrum for the random part. In red: the composite or customized spectrum, which corresponds to Table 20.

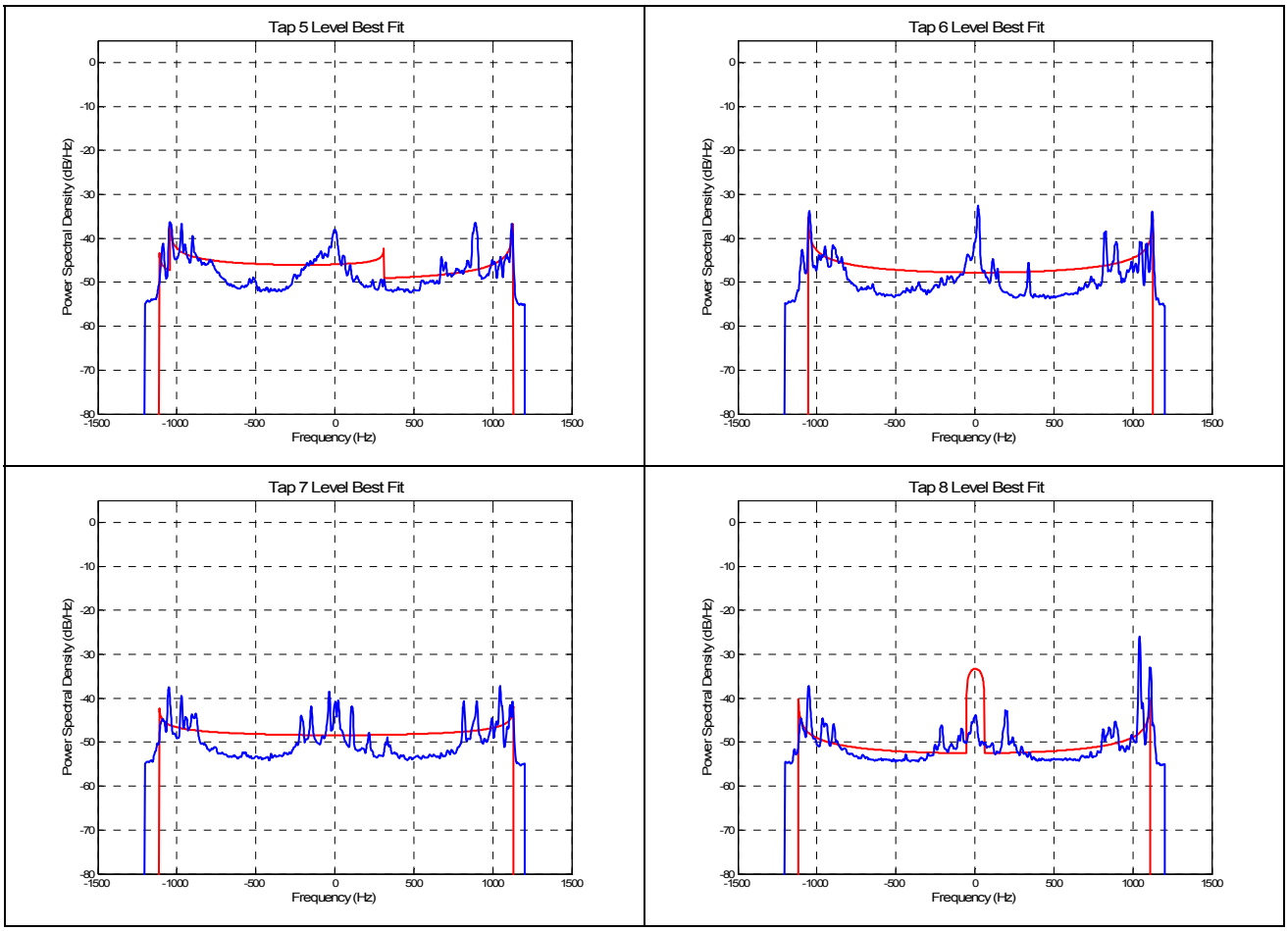

Figure 146: Second four tap spectra for the MTM Expressway Same Direction with Wall 300-400m scenario. In blue: the measured Doppler spectrum for the random part. In red: the composite or customized spectrum, which corresponds to Table 20.

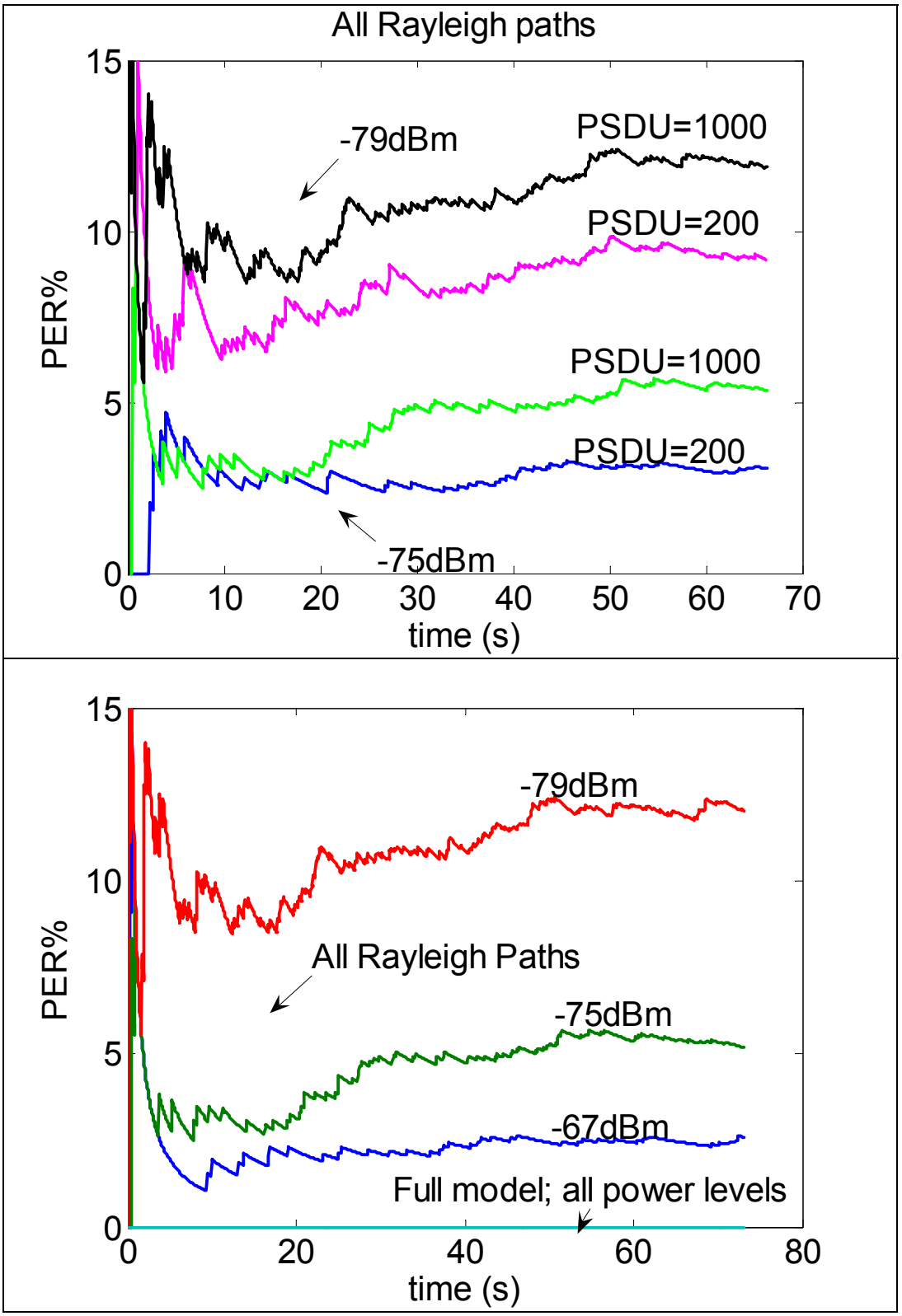

Figure 147: Resulting PER for the Expressway Same Direction scenario.

CHAPTER 8

CONCLUSIONS

In this final chapter, we summarize the contributions of this dissertation. We also present the future work that can result from the extension of the ideas and results presented.

8.1 Contributions

- **Combined sounding waveform:** We were able to combine two pulse compression techniques in our channel sounding waveform. This way, we were able to obtain the maximum dynamic range from our system with the MLS section, and to use the full RF bandwidth available with the OFDM section.

- **OFDM synchronization for design stage:** We have presented an algorithm that allows the identification and compensation of all the static OFDM synchronization offsets. This algorithm is intended for systems where the timing clock is not accessible such as the software radio system that we could develop with the Pentek™ modular system used in this project.

- **Recorded channel in simulation:** We developed a reliable simulated receiver system to compare the behavior of a real recorded channel to the behavior of any proposed synthesized channel. We included all the specifications indicated by the WAVE/DSRC standard and most of the processing required in a similar system.

- **Model methodology**: We have showed the necessity of more comprehensive channel model methodology for the high mobility channels under study. We started with the popular techniques found in the literature, and we grew from them to propose extended methodologies that capture more of the dynamics present in these types of channels. In particular, we were able to show the correlation between the K-factor and the BER using our also developed system to integrate the recorded channel in simulations.

- **Finished Models**: We have presented six models, suitable for simulation on standard RF channel emulators, representing three MTM and three RTM environments measured in the Atlanta, Georgia metropolitan area. The models were ranked in terms of PER measured at -79 dBm with 1000-byte PSDUs, and the MTM Expressway without Wall channel had the highest measured PER. Therefore, this is the model we recommend for the WAVE/DSRC certification test, because if equipment passes the certification test with this channel it is likely that it will pass the other channels as well. Three of the models, RTM Urban Canyon, MTM Urban Canyon, and RTM Suburban Street, had both long and short versions (greater than 12 paths and less than or equal to 12 paths, respectively). Of these, the only long-short pair that produced statistically different mean PERs was the first, and for that one, the mean PERs differed by less than 0.5%. Therefore, the long-short distinction is not very important from a link performance point of view.

8.2 Suggested Future Work

- **Include MTM channel in the combined effects of OFDM synchronization offsets:** In (3.25) and (3.29), we presented the degradation produced by just

fixed or deterministic offsets. To include the effects of a MTM channel, we would have to modify (3.21) as follows:

$$r(n)=\left[\sum_{d=0}^{L-1}h\left(n;\tau_d\right)\delta\left(\tau-\tau_d\right)\right]*\left[\left(\sum_{k=0}^{N-1}c_{m,l,l}e^{j\frac{2\pi kn}{N}(1+\beta)}\right)e^{j\frac{2\pi\Delta F}{N}(n+\alpha)}\right] \quad \text{for} \quad 0\le n\le(N-1). \tag{8.1}$$

where L is the number of paths and

$$h\left(n;\tau_d\right)=\alpha\left(n\right)e^{j2\pi f_m\cos\left(\theta(n)\right)n}e^{-j2\pi f_m\cos\left(\theta(n)\right)\tau_d} \tag{8.2}$$

with the same variable definitions as in (2.2). From this setup, the goal will be to obtain an expression similar to (3.25).

- **More data processing:** There is much more data collected that could not be processed into models for this dissertation. These data contain longer-range or NLOS versions of the scenarios presented. Processing these data is an objective of future research.

- **Dynamic modelling of these channels:** The models presented do not represent the wide range of model variation (i.e. change in delay spreads or Doppler spreads) observed in each given scenario. The models presented give only an average of this behaviour. It is desired to segment the data according to harshness, identify models for different harshness classes, and attempt to identify the dynamics for the classes. In particular, the dynamics of the K-factor are most important.

- **Simulation system extension:** One important characteristic that we were not able to include in our developed simulation system is the correct frame rate. The frame rate is controlled in the MAC layer. The frame rate used by the prototypes

is much lower than the one we used in our simulations. All of our results in comparing real to synthesized or simulated channels assume a continuous frame rate, *i.e*., one frame after another without spaces, and we compare transmitted vs. received data to obtain the BER. We have a significant period between frames in the prototypes, and there is no transmitted vs. received data comparison; therefore, any further comparison between real or recorded channel vs. a proposed model should have a matched frame rate and the same type of error metric.

- **MIMO extension:** The GTRI recording and transmission system used in the measurement campaign has the possibility to grow into a MIMO system. In particular, the system used for Phase Two is ready for a 2x2 MIMO up to 3 GHz. The combined sounding waveform can also be modified for MIMO. We can substitute the MLS section with a Gold sequence, and we can use an odd/even subcarrier separation in the OFDM section.

REFERENCES

[1] A. Abdi, C. Tepedelenlioglu, M. Kaveh, and G. Giannakis, "On the estimation of the *K* parameter for the Rice fading distribution," in *IEEE Communications Letters*, vol. 5, No. 3, pp. 92-94, March 2001.

[2] G. Acosta, K. Tokuda, and M. A. Ingram, "Measured joint Doppler-delay power profiles for vehicle-to-vehicle communications at 2.4 GHz," in Proc. of IEEE Global Telecom. Conf., vol. 6, pp. 3813-3817, 2004.

[3] Guillermo Acosta and Mary Ann Ingram, "Model development for the wideband vehicle-to-vehicle 2.4 GHz channel," Proc. IEEE Wireless Communications & Networking Conference (WCNC 2006), Las Vegas, NV, 3-6 April 2006.

[4] G. Acosta-Marum and M.A. Ingram, "A BER-Based Partitioned Model for a 2.4 GHz Vehicle-to-Vehicle Expressway Channel," in International Journal on Wireless Personal Communication, July 2006.

[5] J. B. Andersen, "Radio channel characterization," in *COST 231 Final Report.*

[6] ASTM E 2213-03, "Standard Specification for Telecommunications and Information Exchange between Roadside and Vehicle Systems— 5.9 GHz Band Dedicated Short Range Communications (DSRC) Medium Access Control (MAC) and Physical Layer (PHY) Specifications," ASTM International, www.astm.org.

[7] A. S. Akki and F. Haber, "A statistical model of mobile-to-mobile land communication channel," in *IEEE Transactions on Vehicular Technology*, pp. 2–7, February 1986.

[8] A. S. Akki, "Statistical properties of mobile-to-mobile land communication channels," in *IEEE Transactions on Vehicular Technology*, vol. 43, No. 4, November 1994.

[9] H. Bantli, E. Ring, and E. Goff, "Requirements for direct short range, vehicle to roadside communications," in *Proceedings of the IEEE Aerospace Conference*, pp. 46-61, Feb. 1997.

[10] J. J. van de Beek, M. Sandell, and P. O. Borjesson, "ML estimation of time and frequency offset in OFDM systems," in *IEEE Transactions on Signal Processing*, vol. 45, pp. 1800-1805, July 1997

[11] P. A. Bello, "Characterization of randomly time-variant linear channels," in *IEEE Transactions on Communication Systems*, vol. 11, pp. 360-393, December 1963.

[12] J. Bingham, "Method and apparatus for correcting for clock and carrier frequency offset, and phase jitter in multicarrier modems." U.S. Patent No. 5206886, April 27, 1993.

[13] W. R. Braun and U. Dersch, "A physical mobile radio channel model," in *IEEE Transactions on Vehicular Technology*, vol. 40, No. 2, pp. 472-482, May 1991.

[14] X. Cai and G.B. Giannakis, "Bounding performance and suppressing intercarrier interference in wireless mobile OFDM," IEEE Trans. Comm. Vol. 51, No. 12, December 2003.

[15] http://www.channelsounder.de (May, 2005).

[16] C-C. Chong, C-M. Tan, D. I. Laurenson, S. McLaughlin, M. A. Beach, and A. R. Nix, "A novel wideband dynamic directional indoor channel model based on a Markov process," in *IEEE Transactions on Wireless Communications*, vol. 4, No. 4, pp. 1539-1552, July 2005.

[17] F. Classen and H. Meyr, "Frequency synchronization algorithms for OFDM systems suitable for communication over frequency selective fading channels," *in Proceedings of IEEE the Global Telecommunications Conference*, vol.3, pp. 1655-1659, 1994.

[18] T. de Couasnon, R. Monnier, and J. Rault, "OFDM for digital TV broadcasting," *Signal Processing*, vol. 39, pp. 1-32, 1994.

[19] A. J. Coulson, "Maximum likelihood synchronization for OFDM using a pilot symbol: Algorithms," in the *IEEE Journal on Selected Areas in Communications,* vol. 19, pp. 2486–2494, December 2001.

[20] A.J. Coulson, "Maximum likelihood synchronization for OFDM using a pilot symbol: Analysis," in the *IEEE Journal on Selected Areas in Communications,* vol. 19, pp. 2495–2502, December 2001.

[21] D. C. Cox, "Delay Doppler characteristics of multipath propagation at 910 MHz in a suburban mobile radio environment," in *IEEE Transactions on Antennas and Propagation*, vol. 20, No. 5, pp. 625-635, September 1972.

[22] A. V. B. Da Silva and M. Nakagawa, "Radio wave propagation measurements in tunnel entrance environment for intelligent transportation systems applications," in *Proceedings of the IEEE Intelligent Transportation Systems Conference*, pp. 883-888, August 2001.

[23] F. Daffara and O. Adami, "A new frequency detector for orthogonal multicarrier transmission techniques," in *Proceedings of the IEEE Vehicular Technology Conference*, vol.2, pp. 804-809, 1995.

[24] F. Daffara and A. Chouly, "Maximum likelihood frequency detectors for orthogonal multicarrier systems," in *Proceedings of the 1993 IEEE International Conference in Communications*, pp. 766-771.

[25] J. S. Davis II and J. P. Linnartz, "Vehicle to vehicle RF propagation measurements," in *Proceedings of the Twenty-Eighth Asilomar Conference on Signals, Systems and Computers*, pp. 470–474, October 1994.

[26] C.R. Dow, P. J. Lin, S. C. Chen, J. H. Lin, and S. F. Hwang, "A study of recent research trends and experimental guidelines in mobile ad-hoc network," in *Proc. of Advanced Information Networking and Applications 19th International Conferen*ce, vol.1, pp. 72-77, March 2005.

[27] P. G. Flikkema and S. G. Johnson, "A comparison of time- and frequency-domain wireless channel sounding techniques," in *Proceedings of the IEEE Southeastcon '96. 'Bringing Together Education, Science and Technology,'* Tampa, FL USA, pp. 488-491, 11-14 April 1996.

[28] H. Gharavi and K. Ban, "Multihop sensor network design for wide-band communications," *IEEE Proceedings*, Vol. 91, No. 8, pp. 1221–1234, August 2003.

[29] L. J. Greenstein, D. G. Michelson, and V. Erceg, “Moment-method estimation of the Ricean *K*-factor,” in *IEEE Communications Letters*, vol. 3, No. 6, pp. 175-176, June 1999.

[30] L. Hanzo, W. Webb, and T. Keller, Single- and Multi-carrier Quadrature Amplitude Modulation Principles and Applications for Personal Communications, WLANs and Broadcasting, Chichester, West Sussex, UK: John Wiley & Sons, Ltd, 2000.

[31] T. J. Harrold, A.R. Nix, and M.A. Beach, “Propagation studies for mobile-to-mobile communications,” in Proc. of IEEE Vehicular Technology Conf., vol. 3, pp. 1251-1255, October 2001.

[32] Y. Higa and H. Furukawa, “One-way relay for wireless multihop networks associated with the intermittent periodic transmit and the spiral mesh routing**,”** in *Proc. of IEEE Vehicular Technology Conf.*, vol. 5, pp. 3202-3206, May 2005.

[33] M. H. Hsieh and C. H. Wei, “Channel estimation for OFDM systems based on comb-type pilot arrangement in frequency selective channels,” in IEEE Transactions on Consumer Electronics, vol. 44, No. 1, pp. 217-225, February 1998.

[34] http://ideas.repec.org/c/cod/matlab/ga.html (February, 2007).

[35] IEEE Std 502.11a-1999. Part 11: Wireless LAN Medium Access Control (MAC) and Physical Layer (PHY) Specifications: High-speed Physical Layer in the 5 GHz Band.

[36] W. C. Jakes, *Microwave Mobile Communications*, IEEE Press, New York, 1993.

[37] M. C. Jeruchim, P. Balaban, and K. S. Shanmugan, *Simulation of Communication Systems: Modeling, Methodology, and Techniques*, Second Edition, Kluwer Academic Press, Boston 2000.

[38] J-S. Jiang and M.A. Ingram, "Enhancing measured MIMO capacity by adapting the locations of the antenna elements," in *Proceedings of the IEEE International Symposium on Personal, Indoor, and Mobile Radio Communications*, vol.3, pp. 1027-1031, 2002.

[39] Zhu Jing and S. Roy, “MAC for dedicated short range communications in intelligent transport system,” in *IEEE Communications Magazine*, Vol. 41, No. 12, pp. 60-67, December 2003.

[40] G. Kadel, “Propagation measurements and their analysis,” in *COST 231 Final Report.*

[41] G. Karam, F. Daffara, and H. Sari, “Simplified versions of the maximum-likelihood frequency detector,” *in Proceedings of the. 1992 IEEE Global Telecommunications Conference*, vol. 1, pp. 345-349.

[42] S. Kato, S. Tsugawa, K. Tokuda, T. Matsui, and H. Fujii, “Vehicle control algorithms for cooperative driving with automated vehicles and intervehicle communications,” in *IEEE Transactions on Intelligent Transportation Systems,* pp. 155-161, September 2002

[43] J. Kivinen, X. Zhao, and P. Vainikainen, “Empirical characterization of wideband indoor radio channel at 5.3 GHz,” in *IEEE Transactions on Antennas and Propagation*, vol. 49, No. 8, August 2001.

[44] T. Kobayashi, H. Masui, S. Takahashi, K. Takahashi, and K. Kage, “Delay profile measurement system for microwave mobile communications and delay characteristics in an urban en-

vironment," in *Proceedings of the IEEE Radio and Wireless Conference (RAWCON)*, pp. 163–166, August 1999.

[45] W. C. Y. Lee, "Estimate of local average power of mobile radio signal," in *IEEE Transactions on Vehicular Technology*, vol. 34, No. 1, pp. 22-27, February 1985.

[46] Y. Li, L. J. Cimini, Jr., and N. R. Sollenberger, "Robust channel estimation for OFDM systems with rapid dispersive fading channels," in *IEEE Transactions on Communications*, vol. 46, no. 7, pp. 902-915, July 1998.

[47] U. Martin, "Echo estimation-deriving simulation models for the mobile radio channel," in *Proceedings of the Vehicular Technology Conference*, vol. 1, pp. 231-235, July 1995.

[48] J. Maurer, T. Fügen, and W. Wiesbeck, "Narrow-band measurement and analysis of the inter-vehicle transmission channel at 5.2 GHz," in *Proceedings of the Vehicular Technology Conference*, pp. 1274–1278, May 2002.

[49] H. Meyr, M. Moeneclaey, and S. A. Fechtel, Digital Communication Receivers: Synchronization, Channel Estimation, and Signal Processing, John Wiley & Sons, New York, 1998.

[50] A. N. Mody, "Signal Acquisition and Tracking for Fixed Wireless Access Multiple Input Multiple Output Orthogonal Frequency Division Multiplexing," Ph.D. Thesis, Georgia Institute of Technology, Atlanta, Georgia 2004.

[51] W. Mohr, "Modeling of wideband mobile radio channels based on propagation measurements," in *Proc. 16th International Symposium of Personal, Indoor, Mobile Radio Communications*, vol. 2, pp. 397-401, 1995.

[52] M. Morelli, A. N. D'Andrea, and U. Mengali, "Feedback frequency synchronization for OFDM applications," *in Proceedings of the IEEE Global Telecommunications Conference*, vol.5, pp. 2504-2507, 1999.

[53] Y. Morioka, T. Sota, T, and M. Nakagawa, "An anti-car collision system using GPS and 5.8 GHz inter-vehicle communication at an off-sight intersection," in *Proceedings of the IEEE Vehicular Technology Conference*, pp. 2019-2024, September 2000.

[54] P. H. Moose, "A technique for orthogonal frequency division multiplexing frequency offset correction," in *IEEE Transactions on Communications*, vol. 42, no. 10, pp. 2908-2914, October 1994.

[55] K. H. Mueller, and M. S. Muller, "Timing recovery in digital synchronous data receivers," in *IEEE Transactions on Communications*, vol. COM-24, pp. 516-531, May 1976.

[56] R. V. Nee and R. Prasad, *OFDM Wireless Multimedia Communications,* Norwood, MA: Artech House, 2000.

[57] M. Newton, D. Kitchener, and M. S. Smith, "Wideband channel dynamics (measurement and simulation)," in *Proc. of 11th International Antennas and Propagation Conf.*, pp. 428-431, April 2001.

[58] J. O. Nielsen, V. Afanassiev, and J. B. Andersen, "A dynamic model for the indoor channel," in *KAP Journal of Wireless Personal Communications*, vol. 19, pp. 91-120, 2001.

[59] H. Nogami and T. Nagashima, “A frequency and timing period acquisition technique for OFDM systems,” in *Proceedings of IEEE Personal, Indoor, and Mobile Radio Communication*, pp. 1010-1015, September 1995.

[60] Heo Nojeong and P. K. Varshney, “Energy-efficient deployment of intelligent mobile sensor networks,” *IEEE Transactions on Systems, Man and Cybernetics*, Vol. 35, No. 1, pp. 78–92, January 2005.

[61] K. K. Onodera and P. R. Gray, “A 75-mW 128-MHz DS-CDMA baseband demodulator for high-speed wireless applications,” in *IEEE Journal of Solid-State Circuits*, vol. 33, No. 5, pp. 753-760, May 1998.

[62] A. Papoulis, Probability, Random Variables, and Stochastic Processes, McGraw-Hill, New York, 1991.

[63] C. S. Patel, G. L. Stüber, and T. G. Pratt, “Simulation of Rayleigh faded mobile-to-mobile communication channels,” in *Proceedings of the IEEE Vehicular Technology Conference*, vol.1, pp. 163-167, October 2003.

[64] J. D. Parsons, D.A. Demery and A.M.D. Turkmani, “Sounding techniques for wideband mobile radio channels: a review,” in *IEE Proceedings*, pp. 437-446, Feb. 1991.

[65] T. Pollet, M. van Bladel, and M. Moeneclaey, “BER sensitivity of OFDM systems to carrier frequency offset and Wiener phase noise,” in *IEEE Transactions on Communications*, vol. 43, No. 2/3/4, pp. 191-193, February/March/April 1995.

[66] J. G. Proakis, *Digital Communications*, McGraw-Hill, New York, 1995.

[67] T. S. Rappaport, *Wireless Communications: Principles and Practice,* Prentice Hall PTR, Upper Saddle River, NJ, 1995.

[68] J. S. Sadowsky and V. Kafedziski, “On the correlation and scattering functions of the WSSUS channel for mobile communications,” in *IEEE Transactions on Vehicular Technology*, vol. 1, No. 1, pp. 270-282, February 1998.

[69] S. Salous, P. Pantzaris, and P. Green, “FMCW waveforms for UHF/SHF wideband channel sounders,” in *Proceedings of the IEE Colloquium on High Bit Rate UHF/SHF Channel Sounder Technology and Measurement*, digest No. 1993/233, pp. 2/1-2/5.

[70] M. Sandell, J.-J. van de Beek, and P. O. Börjesson, “Timing and frequency synchronization in OFDM systems using the cyclic prefix,” *in Proceedings of the International Symposium on Synchronization*, Essen, Germany, pp. 16-19, December 1995.

[71] H. Sari, G. Karam, and I. Jeanclaude, “Transmission techniques for digital terrestrial tv broadcasting,” in *IEEE Communications Magazine*, pp. 100-109, February 1995.

[72] T. M. Schnidl and D. C. Cox, “Robust frequency and timing synchronization for OFDM,” in *IEEE Transactions on Communications*, vol. 45, no. 12, pp. 1613-1621, December 1997.

[73] S. Simoens, V. Buzenac, and M. de Courville, “A new method for joint cancellation of clock and carrier frequency offsets in OFDM receivers over frequency selective channels,” in *Proceedings of the. 2000 IEEE Vehicular Technology Conference*, pp. 390-394.

[74] B. Sklar, “Rayleigh fading channels in mobile digital communication systems, part I: characterization,” in *IEEE Communications Magazine*, pp. 90-100, July 1997.

[75] B. Sklar, “Rayleigh fading channels in mobile digital communication systems, part II: mitigation,” in *IEEE Communications Magazine*, pp. 102-109, July 1997.

[76] M. Sliskovic, “Sampling frequency offset estimation and correction in OFDM systems,” in *Proceedings of the 2001 IEEE ICECS*, pp. 437-440, 2001.

[77] M. Sliskovic, “Signal Processing Algorithms in Multicarrier Systems,” Ph.D. Thesis, University of Zagreb, Croatia 2001.

[78] M. Speth, S. A. Fechtel, G. Fock, and H. Meyr, “Optimum receiver design for wireless broadband systems using OFDM — part I,” in *IEEE Transactions on Communications*, vol. 47, no. 11, pp. 1668-1677, November 1999.

[79] Spirent Communications SR5500 Wireless Channel Emulator Operations Manual. www.spirentcom.com (February, 2007).

[80] H. Steendam, M. Moeneclaey, “Sensitivity of orthogonal frequency-division multiplexed systems to carrier and clock synchronization errors,” in *Signal Processing,* vol.80, pp. 1217–1229, July 2000

[81] M. Steinbauer, The Radio Propagation Channel — A Non-Directional, Directional, and Double-Directional Point-of-View, Ph.D. Thesis, Fakultät für Elektrotechnik und Informationstechnik, Technische Universität Wien, Vienna, Austria November 2001.

[82] G. L. Stüber, *Principles of Mobile Communications*, Kluwer Academic Press, Boston 1996.

[83] Symmetricom, Inc., “Timing & time code reference,” application note. www.symmetricom.com (February, 2007).

[84] T. Tank and J. P. M. G. Linnartz, “Vehicle-to-vehicle communications for AVCS platooning,” in *IEEE Transactions on Vehicular Technology*, pp. 528-536, May 1997.

[85] R. Van Nee and R. Prasad, *OFDM for Wireless Multimedia Communications*, Artech House, Boston 2000.

[86] F. Vatalaro and A. Forcella, “Doppler spectrum in mobile-to-mobile communications in the presence of three-dimensional multipath scattering,” in *IEEE Transactions on Vehicular Technology*, pp. 213-219, February 1997.

[87] R. Wang and D. Cox, “Double mobility mitigates fading in ad hoc wireless networks,” in *Proceedings of the IEEE Antennas and Propagation Society International Symposium*, vol. 2, pp. 306-309, 2002.

[88] R. Wang and D. Cox, “Channel modeling for ad hoc mobile wireless networks,” in *Proceedings of the IEEE Vehicular Technology Conference*, pp. 21-25, Spring 2002.

[89] W. D. Warner and C. L. Leung, “OFDM/FM frame synchronization for mobile radio data communication,” in *IEEE Transactions on Vehicular Technology*, vol. 42, no. 3, pp. 302-313, August 1993.

[90] L. Williams and A. Kupetz, “The 4G soldier – new developments in military mobile communications,” RF Design, www.rfdesign.com (February, 2007), pp. 52-55, June 2003.

[91] X. Zhao, J. Kivinen, P. Vainikainen, and K. Skog, “Characterization of Doppler spectra for mobile communications at 5.3 GHz,” in *IEEE Transactions Vehicular Technology*, vol. 52, no. 1, pp. 14-23, 2003.

[92] T. Zwick, C. Fischer, and W. Wiesbeck, “A stochastic multipath channel model including path directions for indoor environments,” in *IEEE Journal of Selected Areas in Communications*, vol. 20, No. 6, pp. 1178-1192, August 2002.

VITA

Guillermo Acosta-Marum was born in Mexico City, Mexico, in 1962. He obtained his Bachelor of Engineering with Honors and Master of Engineering, both in Electrical Engineering, from Stevens Institute of Technology, Hoboken, New Jersey, in 1985 and 1987, respectively. He also obtained a Master of Business Administration with Honors from the *Instituto Tecnologico Autonomo de Mexico* (ITAM), Mexico City, Mexico, in 1996. Mr. Acosta has held technical and managerial positions in the recording, radio, and TV industries and in the Communications Ministry of Mexico. He has been an adjunct instructor in Electrical Engineering in the Instituto Tecnologico y Estudios Superiores de Monterrey - Campus Estado de Mexico (ITESM-CEM), the Universidad Iberoamericana, and Devry University. He has also been a graduate teaching assistant (class instructor) and a graduate research assistant at the Georgia Insitute of Technology. He is member of the IEEE, ASA, INCE, Tau Beta Pi, and Eta Kappa Nu, and he is a Robert G. Shackelford Graduate Student Fellowship Recipient.